THERMODYNAMICAL PROPERTIES OF FUNCTIONAL MATERIALS: NEUTRON SCATTERING AND LATTICE DYNAMICS STUDIES

By

Mayanak Kumar Gupta

Enrolment No. PHYS01201104011

Bhabha Atomic Research Centre, Mumbai

A thesis submitted to the
Board of Studies in Physical Sciences
In partial fulfillment of requirements
for the Degree of
DOCTOR OF PHILOSOPHY
of
HOMI BHABHA NATIONAL INSTITUTE

January 2016

Statement by Author

This dissertation has been submitted in partial fulfilment of requirements for an advanced degree at Homi Bhabha National Institute (HBNI) and is deposited in the Library to be made available to borrowers under rules of the HBNI.

Brief quotations from this dissertation are allowable without special permission, provided that accurate acknowledgement of source is made. Requests for permission for extended quotation from or reproduction of this manuscript in whole or in part may be granted by the Competent Authority of HBNI when in his or her judgment the proposed use of the material is in the interests of scholarship. In all other instances, however, permission must be obtained from the author.

(Mayanak Kumar Gupta)

Declaration

I, hereby declare that the investigation presented in the thesis has been carried out by me. The work is original and has not been submitted earlier as a whole or in part for a degree / diploma at this or any other Institution/University.

(Mayanak Kumar Gupta)

Declaration

I, hereby declare that minor suggestions of the examiners have been incorporated in the thesis.

Dr. R. Mittal

(Guide)

List of Publications

In Refereed Journal:

Related to Thesis

[1] *Phonon instability and mechanism of superionic conduction in Li_2O.*

M. K. Gupta, Prabhatasree Goel, R. Mittal, N. Choudhury and S. L. Chaplot

Phys. Rev. B 85, 184304 (2012).

[2] *Suppression of antiferroelectric state in $NaNbO_3$ at high pressure from in situ neutron diffraction.*

S. K. Mishra, **M. K. Gupta**, R. Mittal, S. L. Chaplot, and Thomas Hansen

Appl. Phys. Lett. 101, 242907 (2012).

[3] *Inelastic neutron scattering and ab-initio calculation of negative thermal expansion in Ag_2O*

M. K. Gupta, R. Mittal, S. L. Chaplot and S. Rols

Physica B 407, 2146 (2012).

[4] *Negative thermal expansion in cubic ZrW_2O_8: Role of phonons in entire Brillouin zone from ab-inito calculations*

M. K. Gupta, R. Mittal and S. L. Chaplot

Phys. Rev. B, **88**, 014303 (2013).

[5] *Phonon dynamics and inelastic neutron scattering of sodium niobate*

S. K. Mishra, **M. K. Gupta**, R. Mittal, M. Zbiri, S. Rols, H. Schober, and S. L. Chaplot

Phys. Rev. B 89, 184303 (2014).

[6] *Phonons, nature of bonding, and their relation to anomalous thermal expansion behavior of M_2O (M = Au, Ag, Cu).*

M. K. Gupta, R. Mittal, S. L. Chaplot, and S. Rols

Journal of Applied Physics, **115**, 093507 (2014).

[7] *Phonons lithium diffusion and thermodynamics of $LiMPO_4$ (M=Mn, Fe).*

Prabhatasree Goel, **M. K. Gupta**, R. Mittal, S. Rols, S. J. Patwe, S. N. Achary, A. K. Tyagi and S. L. Chaplot

J. Mater. Chem. A, **2** 14729 (2014).

[8] *Spin-phonon coupling, high-pressure phase transitions, and thermal expansion of multiferroic $GaFeO_3$: A combined first principles and inelastic neutron scattering study.*

M. K. Gupta, R. Mittal, M. Zbiri, Ripandeep Singh, S. Rols and S.L. Chaplot

Phys. Rev. B. 90, 134304 (2014).

[9] *Spin-phonon coupling and high-temperature phase transition in multiferroic material $YMnO_3$.*

M. K. Gupta, R. Mittal, M. Zbiri, Neetika Sharma, S. Rols, H. Schober and S. L.Chaplot

J. Mater. Chem. C 3, 11717 (2015).

[10] *Phonons and stability of infinite-layer iron oxides $SrFeO_2$ and $CaFeO_2$.*

M. K. Gupta, R. Mittal, S. L. Chaplot, Cedric Tassel and Hiroshi Kageyama

Solid State Communications 241, 43 (2016).

[11] *Spin-phonon coupling and high pressure phase transitions of $RMnO_3$ (R= Ca and Pr): An inelastic neutron scattering and first principle studies.*

S. K. Mishra, **M. K. Gupta**, R. Mittal, A. I. Kolesnikov and S. L. Chaplot

Phys. Rev. B 93, 214306 (2016).

[12] *Lattice dynamics and thermal expansion behavior in metal cyanides, MCN (M=Cu,Ag, Au): Neutron inelastic scattering and first principles calculations.*

M. K. Gupta, Baltej Singh, R. Mittal, S. Rols and S. L. Chaplot

Phys. Rev. B 93, 134307 (2016)

Note: In paper 1 and 7,the parts involving classical lattice dynamics calculations are not included here and forms part of the thesis of Dr. Prabhatasree Goel. Paper 2, 5 and 11 involve extension of previous work of Dr. S. K. Mishra in which the student has contributed significantly.

In Other Areas:

[1] *Anomalous Thermal Expansion in Framework Compounds.*

M. K. Gupta, R. Mittal and S. L. Chaplot

Chinese Journal of Physics 49, 316 (2011).

[2] *Inelastic neutron scattering and theoretical studies on strontium tungstate, $SrWO_4$.*

P. Goel, R. Mittal, **M. K. Gupta**, Mala N. Rao,S. L.Chaplot, S. Rols, A. K. Tyagi and Z. Petr

Chinese Journal of Physics 49, 308 (2011).

[3] *Phase transitions and thermodynamic properties of yttria, Y_2O_3: Inelastic neutron scattering shell model and first-principles calculations.*

Preyoshi P. Bose, **M. K. Gupta**, R. Mittal, S. Rols, S. N. Achary, A. K. Tyagi, and S. L. Chaplot

Phys. Rev. B 84, 094301 (2011).

[4] *Vibrational properties and phase transitions in II-VI materials: lattice dynamics, ab initio studies and inelastic neutron scattering measurements.*

Tista Basak, Mala N Rao, **M. K. Gupta** and Samrath L Chaplot

J. Phys.: Condens. Matter 24,115401 (2012).

[5] *Spin-Lattice Coupling in* $K_{0.8}Fe_{1.6}Se_2$ *and* KFe_2Se_2*: Inelastic Neutron Scattering and ab-initio Phonon Calculations.*

R. Mittal, **M. K. Gupta**, S. L. Chaplot, M. Zbiri, S. Rols, H. Schober, Y. Su, Th. Brueckel, T. Wolf

Phys. Rev. B 87, 184502 (2013).

[6] *Inelastic neutron scattering investigations of negative thermal expansion behavior in semiconductors and framework solid.*

Mala N. Rao, R. Mittal, Prabhatasree Goel, **M. K. Gupta**, S.K. Mishra, S.L. Chaplot

Neutron News 25, 34 (2014).

[7] *Phase transitions in delafossite* $CuLaO_2$ *at high pressures.*

Nilesh P. Salke, Alka B. Garg, Rekha Rao, S. N. Achary, **M. K. Gupta**, R. Mittal and A. K. Tyagi

Journal of Applied Physics, **115**, 133507 (2014).

[8] *Raman and ab initio investigation of negative thermal expansion material TaVO5: Insights into phase stability and anharmonicity.*

Nilesh P. Salke, **M. K. Gupta**, Rekha Rao, R. Mittal, Jinxia Deng, and Xianran Xing.

Journal of Applied Physics, **117**, 235902 (2015).

[9] *Structural and electrical properties of layered perovskite type PrTi2O7: experimental and theoretical investigations.*

Sadequa J. Patwe, Vasundhara Katari,Nilesh P. Salke,Sudhanshu K. Deshpande, Rekha Rao, **M. K. Gupta**, Ranjan Mittal, S. Nagabhusan Acharyand Avesh K. Tyagi.

Journal of Material Chemistry C 3, 4570 (2015)

[10] *Inelastic Neutron Scattering Studies of Phonon Spectra and Simulations of pressure induced amorphization in Tungstates, AWO4 (A = Ba, Sr, Ca and Pb).*

Prabhatasree Goel, **M. K. Gupta**, R. Mittal, S. Rols, S. N. Achary, A. K.Tyagi and S. L. Chaplot

Phys. Rev. B. 91, 94304 (2015).

(Mayanak Kumar Gupta)

Dedicated

To

My Parents

Acknowledgements

I would like to express my special appreciation and thanks to my advisor Dr. R. Mittal, Solid State Physics Division, Bhabha Atomic Research Centre. I would like to thank Dr. S. L. Chaplot former Director, Physics Group, Bhabha Atomic Research Centre, for encouraging my research and for allowing me to grow as a research scientist. Their advice on both research as well as on my career have been priceless. I would also like to thank my committee members Dr. D. M. Gaitonde and Dr. T. R. Ravindran whose useful suggestions have been very helpful. Special thanks to Dr. S. Basu, Head Solid State Physics Division, Bhabha Atomic Research Centre, for his support and encouragement.

I thank Dr. Narayani Choudhury, Dr. Mala. N. Rao, Dr. Prabhatasree Goel, Dr. S.K. Mishra, Dr. Amitabh Das and Dr. Ashok Arya with whom I shared discussions of my research work. I am also thankful to Mr. P.S.R. Krishna, Dr. Surendra Singh, Dr. Amit Kumar and Dr. Keka Chakraborty, for their constructive support during the period of my thesis work. I thank to my collaborators Dr. Stephane Rols, Dr. Mohamed Zbiri, Cédric Tassel, Hiroshi Kageyama and Dr. Alexander I. Kolesnikov for their scientific collaboration in various experiments.

I take the opportunity to thank all my friends, Baltej, Neetika, Dr. Sugam, Ripendeep, Swapnil, Nilesh and others who directly or indirectly have helped me in achieving my goals. My sincere thanks are due to all my colleagues in Solid State Physics Division, Bhabha Atomic Research Centre, for helping me in different ways.

I am very grateful to my parents. Their understanding and love encouraged me to work hard and to continue pursuing a Ph.D. project. Their firm and kind-hearted personality has affected me to be steadfast and never bend to difficulty. Last but not the least; I am greatly indebted to my wife Rashmi, son Anjaney, brother Bhupal and sisters Aarti, Anu, and Achala. They form the backbone and origin of my happiness. Their love and support without any complain or regret has enabled me to complete this Ph.D. project. Without their support and encouragement this would not have been easy. I owe my achievements to them.

Contents

Page No.

Homi Bhabha National Institute

Ph.D. Programme

1. **Name of the Candidate : Mayanak Kumar Gupta**
2. **Name of the constituent Institution : Bhabha Atomic Research centre**
3. **Enrolment No. : PHYS0120110411**
4. **Title of the thesis : Thermodynamical properties of functional materials: Neutron scattering and lattice dynamics studies**
5. **Board of studies : Physical Sciences**

Synopsis

The study of the vibrations of the atoms and molecules in a crystal is known as lattice dynamics. The temperature is interpreted in a material by its atomic vibrations. In order to have a complete picture of crystalline materials, a deep understanding of lattice dynamics is required. The propagation of sound waves in crystals, Raman scattering of light and absorption of certain frequencies in the infra-red spectral region are some of the experimental observations of lattice dynamics. Without lattice dynamics it is not possible to explain various thermodynamical properties such as phase transitions, thermal conductivity, thermal expansion etc. Further, atomic vibrations also contribute to free energy in the form of entropy besides vibrational energy itself. In crystalline solids the motion of atoms are not random but follow certain rules defined by the neighboring atoms in the system. In crystalline solids these well defined collective motions are quantized and are called as "phonons". To characterize and understand the various properties in solid, it is highly desirable to study these phonons with the help of theoretical tools and inelastic-neutron/light scattering experiments.

It is not always possible to perform experiment at high temperature and pressure conditions; in such cases, the simulation studies are used to predict the material properties under these extreme conditions. For this purpose, theoretical studies based on lattice dynamical methods are necessary for exploring the entire spectrum of thermal vibrations in crystals. The data obtained from experimental techniques are used to test and validate the theoretical methods. Once validated successfully, these methods may further be used to predict the thermodynamic properties at various thermodynamical conditions. The author has used the state of the art density functional theory methods to compute the total energy and forces, hence the phonons in entire Brillouin zone for various compounds. To validate the theoretical results, the author has also carried out inelastic neutron scattering experiments.

The thesis consists of eight chapters. Application of density functional theory to a variety of oxide materials to understand the role of phonons in their functional properties of negative thermal expansion (NTE), multiferroicity or super-ionic conduction is presented. The motivation for studying the various compounds, details of the work done and the significance of the results obtained are given below in the brief description of various chapters.

Chapter 1 describes the basic experimental and theoretical tools used to study the thermodynamical properties. The techniques of inelastic neutron scattering and lattice dynamics have been explained briefly. Lattice dynamical calculations of phonons may be carried out using either a quantum-mechanical *ab-initio* density functional theory (DFT) approach or an atomistic approach involving semi-empirical interatomic potentials. The work described in this thesis pertains mainly to the former approach. At low temperature the amplitude of atoms about their equilibrium positions are small and the interaction between atoms can be assumed to be harmonic in nature. The DFT method is used to calculate the total energy and force constants in the system for any given atomic configuration. The force-constants will follow the symmetry of the crystal, which are used to determine the lattice dynamics of the system. Inelastic neutron scattering is best suited to study the phonon behavior of solids. The wavelength of the thermal neutrons is comparable to the interatomic distances in a crystal, and energies are also of the same order as the energy of the phonons. The relation of the phonon frequencies with wave vector is called the phonon dispersion relation. On the other hand, the distribution of phonons of different energy in the entire Brillouin zone is known as the phonon density of states. Measurement of phonon on single crystal provides the information of the phonon dispersion relation while polycrystalline samples give information of the phonon density of states. The experimental technique used for the measurements of temperature dependence of phonon density of states using the IN4 time-of-flight spectrometer at high flux reactor of Institut Laue-Langevin, Grenoble, France is also described in this Chapter.

Chapter 2 describes the relation between nature of bonding and negative thermal expansion behavior in M_2O and MCN (M=Au, Ag and Cu) compounds. A comparative study of the dynamics of M_2O and MCN (M = Au, Ag and Cu) using first principle calculations based on the density functional theory is given. A good match between the calculated phonon density of states and that derived from inelastic neutron scattering measurements is obtained for Cu_2O and Ag_2O. The author performed experiments on Cu_2O and Ag_2O powder sample but not on Au_2O due to non-availability of sample. The calculated thermal expansions of Ag_2O and Cu_2O are negative, in agreement with available experimental data, while it is found to be positive for Au_2O. The low energy phonon modes responsible for this anomalous thermal expansion are identified. The charge density in the three compounds are calculated and it is found that the magnitude of the ionic character of the Ag_2O, Cu_2O, and Au_2O crystals is in decreasing order, with an Au-O bond of covalent nature strongly rigidifying the Au_4O tetrahedral units. Here for the first time it is seen that the nature of chemical bonding and open space in the unit cell are directly related to the magnitude of thermal expansion coefficient.

The author has carried out the temperature dependent measurements of phonon spectra in quasi one-dimensional metal cyanides MCN (M=Cu, Ag and Au) from 150 to 310 K. *Ab-initio* lattice dynamics calculations have been performed to interpret the phonon-spectra as well as to understand the anamolous thermal expansion behavior in these compounds. We bring out the differences in the phonon mode behavior to explain the differences in the thermal expansion behavior among the three compounds. The chain-sliding modes are found to contribute maximum to the negative thermal expansion along ‘c’ axis in the Cu- and Ag- compounds, while the same modes contribute to positive thermal expansion in the Au- compound. Several low energy transverse modes lead to positive thermal expansion along ‘a’ and ‘b’ axis in all the compounds. The calculated elastic constants and Born effective charges are correlated with the difference in nature of bonding among these metal cyanides.

Chapter 3 describes theoretical studies on ZrW_2O_8 about thermal expansion behavior and its origin. The author has performed ab-inito density functional theory calculation of phonons in cubic phase of ZrW_2O_8 in the entire Brillouin zone and identified specific anharmonic phonons that are responsible for large negative thermal expansion (NTE) in terms of translation, rotation and distortion of WO_4 and ZrO_6. The calculations have been used to interpret the experimental phonon spectra as a function of pressure and temperature. The phonons showing anharmonicty with temperature are not necessarily the same as those showing anharmonicity with pressure although both are of similar frequencies. Only the latter phonons are associated with NTE. Therefore the cubic and/or quartic anharmonicity of phonons is not relevant to NTE but just the volume dependence of frequencies.

Chapter 4 describes the experimental and theoretical studies on spin phonon coupling and pressure driven phase transition in multiferroic compound $GaFeO_3$ and $YMnO_3$. An extensive phonon study on multiferroic $GaFeO_3$ is described in this chapter. Inelastic neutron scattering measurements are performed over a wide temperature range, 150 to 1198 K. First principles lattice dynamical calculations are done for the sake of the analysis and interpretation of the observations. The phonon spectra are calculated in two ways namely with and without including the magnetic interactions. The two sets of calculations highlight pronounced difference due to magnetic interaction in the energy range of the vibrations of the Fe and O ions. Therefore, magnetism induced by the active spin degrees of freedom of Fe cations plays a key role in stabilizing the structure and dynamics of $GaFeO_3$. Moreover, the computed enthalpy in various phases of $GaFeO_3$ is used to gain deeper insights into the high pressure phase stability of this material.

In $YMnO_3$, the author has carried out temperature-dependent inelastic neutron scattering measurements over the temperature range 50 - 1303 K, covering both the antiferromagnetic to paramagnetic transition (70 K), as well as the ferroelectric to paraelectric transition (1258 K). Measurements are accompanied by first principles calculations of phonon spectra for the sake of interpretation and analysis of the measured phonon spectra in the room temperature ferroelectric (P6$_3$*cm*) and high temperature paraelectric (P6$_3$/*mmc*) hexagonal phases of $YMnO_3$. The comparison of the experimental and first-principles calculated phonon spectra highlight unambiguously a spin-phonon coupling character in $YMnO_3$. This is further supported by the pronounced differences in the magnetic and non-magnetic phonon calculations. The calculated atomistic partial phonon contributions of the Y and Mn atoms are not affected by inclusion of magnetic interactions, whereas the dynamical contribution of the O atoms is found to change. This highlights the role of the super-exchange interactions between the magnetic Mn cations, mediated by O bridges.

Chapter 5 describes our experimental and theoretical studies on stability of quasi two dimensional $CaFeO_2$ and $SrFeO_2$, spin phonon coupling and high temperature distortion. A detailed ab-initio lattice dynamical analysis of the Fe-O infinite-layer compounds $CaFeO_2$ and $SrFeO_2$ in various magnetic configurations is presented. These indicate strong spin-phonon coupling in $SrFeO_2$ in contrast to that in case of $CaFeO_2$. The available powder neutron inelastic scattering data on $SrFeO_2$ from 5 K to 353 K in the antiferromagnetic phase has been analyzed using the ab-initio calculations. These suggest distortion of the ideal infinite planer structure above 300 K. From ab-initio calculations in $SrFeO_2$ as a function of volume, it is seen that the distortion in $SrFeO_2$ above 300 K is similar to that in $CaFeO_2$ at ambient conditions. The distortion of the planer structure of $CaFeO_2$ involves doubling of the planer unit cell that may be usually expected to be due to a soft phonon mode at the M-point (1/2 1/2 0). However, ab-initio calculations show quite unusually that all the M-point (1/2 1/2 0) phonons are stable, but two stable M_3^+ and M_2^- modes anharmonically couple with an unstable B_u mode at the zone centre and lead to the cell doubling and the distorted structure. Magnetic exchange interactions in both the compounds have been computed on the basis of the ideal planar structure (*P*4/*mmm* space group) and with increasing amplitude of the B_u phonon mode. These reveal that the magnetic exchange interactions reduce significantly with increasing distortion. The ab-initio phonon calculations have been extended to high pressures, which reveal that, above 20 GPa of pressure, the undistorted planer $CaFeO_2$ becomes dynamically stable.

Chapter 6 describes the role of phonon and phase transition in perovskite structure compounds $NaNbO_3$, $PrMnO_3$ and $CaMnO_3$. Sodium niobate ($NaNbO_3$) exhibits an extremely complex sequence of structural phase transitions in the perovskite family and therefore, provides an excellent model system for understanding the mechanism of structural phase transitions. The author has performed the temperature dependence inelastic neutron scattering measurements and first principles lattice dynamical calculations in sodium niobate. The measurements are carried out in various crystallographic phases of this material at various temperatures from 300 K to 1048 K. The computed phonon density of states is found to be in good agreement with the experimental data. The calculations are useful to assign the characteristic Raman modes in the antiferroelectric phase, which are due to the folding of the T (ω=95 cm^{-1}) and Δ (ω=129 cm^{-1}) points of the cubic Brillouin zone, to the A_{1g} symmetry. Further, the author has also computed enthalpy in various phase of sodium niobate and found that the orthorhombic structure with space group Pbcm could transform to the Pbnm structure at high pressure. The calculated phase transition pressure is fairly close to the experimental value.

Further detailed lattice dynamical calculations of vibrational properties in $RMnO_3$ (R= Ca and Pr) is presented. The temperature dependence of phonon spectra in $RMnO_3$ has been measured by A. I. Kolesnikov of Oak Ridge National Laboratory, USA. The measurements performed in the temperature range from 7 K to 1251 K covered all the relevant characteristic transition temperatures in $CaMnO_3$, while for $PrMnO_3$ data was collected over 6-150 K covering the magnetic transition. The author performed the interpretation and analysis of the observed phonon spectra using ab-initio phonon calculations. The effect of pressure on the structural distortions in orthorhombic phase of $CaMnO_3$ and $PrMnO_3$ is discussed. On application of pressure, it is found that the variations of Mn-O distances are isotropic for $CaMnO_3$ and highly anisotropic for $PrMnO_{3.}$ The calculated structure as a function of pressure in $PrMnO_3$ shows that suppression of Jahn-Teller distortion as well as insulator to metal transition occurs simultaneously. The calculations show that this transition may not be associated with the occurrence of the tetragonal phase above 20 GPa as reported in the literature, since the tetragonal phase is found to be dynamically unstable although it is found to be energetically favored over the orthorhombic phase above 20 GPa. $CaMnO_3$ does not show any phase transition up to 60 GPa.

Chapter 7 describes our theoretical studies on superionic and battery materials Li_2O and $LiMPO_4$ (M=Mn, Fe). Studies on the vibrational and elastic behavior of lithium oxide, Li_2O around its superionic transition temperature has been described. Phonon frequencies calculated using the *ab-initio* density functional theory (DFT) are in excellent agreement with the reported experimental data. Further, volume dependence of phonon dispersion relation has been calculated, which indicate softening of zone boundary transverse acoustic phonon mode along [110] at volume corresponding to the superionic transition in Li_2O. This instability of phonon mode could be a precursor leading to the dynamical disorder of the lithium sub-lattice.

In $LiMPO_4$ (M=Mn, Fe), the author has performed ab-initio density functional theory calculations as a function of volume to understand the microscopic picture of Li sub-lattice. Here the aim has been to correlate the diffusion of lithium and dynamical instability in $LiMPO_4$. The lattice dynamics calculations indicate instability of zone-centre as well as zone-boundary phonon modes along [100] at unit cell volume corresponding to elevated temperature.

Chapter 8 of this thesis gives the summary and the future direction based on the work described in this thesis. The research work described in the thesis uses the techniques of lattice dynamics calculations and inelastic neutron scattering measurements to understand the thermodynamic properties of various compounds. The role of phonons in leading to various thermodynamical properties like thermal expansion, specific heat, temperature and pressure driven phase transitions and ionic conduction in various compounds is analyzed in detail. The nature of bonding and their relation with anomalous thermal expansion behavior has been studied. In addition, the spin-phonon coupling has been investigated in multiferroic and perovskite compounds. The various temperature and pressure driven phase transitions in multiferroic and perovskite structure compounds have been found to be associated with dynamical instabilities. Further, the correlation between phonon instability and conduction of Li ion in superionic and battery materials is established. The calculations have greatly aided the planning and execution of the various experimental measurements. The calculations enabled to understand the microscopic picture of the dynamics in various solids leading to the manifestations of several unique properties. The experience gained from the study of spin-phonon coupling, phase-transition mechanism and negative thermal expansion driven by phonons will be of immense help in understanding the physics as well as their application aspects. This experience gained would also be useful for studying the structure and dynamics of more complex geophysical and technologically important solids.

List of Figures

the energy transfer in order to describe the effect of energy resolution in the experiment. In order to compare with the experimental data the calculated spectrum is scaled by 6%.

Figure 5.4 Calculated partial densities of states of various atoms in $SrFeO_2$(P4/mmm),$CaFeO_2$ (P4/mmm) and $CaFeO_2$(P-42_1m).

Figure 5.5 Calculated dispersion relation of $SrFeO_2$ and $CaFeO_2$in P4/mmm space group.. The solid and dashed lines correspond to calculations at ambient pressure and 5 kbar, respectively. The Bradley-Cracknell notation is used for the high symmetry points along which the dispersion relations are obtained: Γ=(0, 0, 0), Z = (1/2, 0, 0) , M = (1/2, 1/2 , 0). A = (1/2, 1/2, 1/2), R = (0, 1/2, 1/2), X = (1/2, 0, 0).

Figure 5.6 Polarization vectors of selected zone center modes of $CaFeO_2$in P4/mmmFor each mode, the assignment and frequency are indicated in meV units. The 'i' after the phonon energy indicates that mode is unstable. The length of the arrows is related to the displacement of the atoms. The absence of an arrow on an atom indicates that the atom is at rest. The number after the mode assignment gives the phonon frequency. Key: Ca, blue spheres; Fe, golden spheres; O, red spheres (1 meV=8.0585 cm^{-1}).

Figure 5.7 The energy landscape of p-$CaFeO_2$ obtained by exciting the pair of phonons with different amplitude. (a) $A^{3+}$and B_u modes (b) M^{3+} and A^{3+} modes (c) M^{2-} andA^{3+} modes (d) $M^{3+}$and B_u modes and (e) $M^{2-}$and B_u modes. The energies E are per magnetic unit cell.

Figure 5.8 Energy barrier from the p-$CaFeO_2$ (P4/mmm) to the d-$CaFeO_2$ (P-42_1m). ζ corresponds to the distortion vector as obtained from the difference in atomic co-ordinates of the d-$CaFeO_2$ and p-$CaFeO_2$ structures phases as given in TABLE 5.4. The energies E is per magnetic unit cell.

Figure 5.9 (a) The calculated x and z-coordinate of the oxygen and z-coordinate of the calcium atom in the d-$CaFeO_2$ as a function of pressure. As given in Table 5.4 the oxygen and calcium atoms occupy the Wyckoff sites 4e(x+1/2, -x, -z) and (1/2 0 –z) respectively. (b) The calculated phonon dispersion of planer $CaFeO_2$ at ambient and 30GPa.

Figure 5.10 Calculated dispersion relations of $SrFeO_2$(P4/mmm) and $CaFeO_2$(P4/mmm)including the A, C, G antiferromagnetic and FM configurations.

Figure 5.11 The various J exchange interaction parameters in $SrFeO_2$ (P4/mmm) and p-$CaFeO_2$(P4/mmm).

Figure 5.12 The calculated magnetic exchange interaction parameters (J's) in $SrFeO_2$ (P4/mmm) and p-$CaFeO_2$(P4/mmm) compound at different amplitude of B_u phonon mode distortion.

Figure 6.1 Comparison of the calculated (filled circles) long-wavelength phonon frequencies with the available experimental data (stars)[17, 39, 40] for both the antiferroelectric (AFE) and the ferroelectric (FE) phases.

Figure 6.2 The temperature dependence of the phonon spectra of $NaNbO_3$ as observed by neutron inelastic scattering.

Figure 6.3 The experimental (dotted line at 303 K) and calculated (solid line at 0 K) phonon spectra for $NaNbO_3$ in the antiferroelectric phase (**Pbcm**). The calculated spectra have been convoluted with a Gaussian of FWHM of 15% of the energy transfer in order to describe the effect of energy resolution in the experiment.

Figure 6.4 The calculated partial density of states for various atoms and the total phonon density of states for $NaNbO_{3,}$ in both the antiferroelectric orthorhombic (Pbcm) phase (solid line) and the ferroelectric rhombohedral (R3c) phase (dashed line).

Figure 6.6 Computed phonon dispersion relations for cubic phase (**Pm-3m)** of $NaNbO_3$ compared to reported experimental inelastic neutron scattering (INS) single crystal data (red circles) (Ref. [43]).

Figure 6.7 Ab initio derived eigenvectors of selected zone-centre and zone-boundary unstable phonon modes at the Γ**,** M, R, T and X points for the cubic phase of $NaNbO_3$. The lengths of arrows are related to the displacements of the atoms. Key: Na, cyan; Nb, blue; O, brown.

Figure 6.8 The eigenvectors of the two antiferroelectric modes, at (a) ω=93 cm^{-1} and (b) 129 cm^{-1} of $NaNbO_3$, induced by the folding of the T (q= ½ ½ ¼) and Δ (q= 0 0 ¼) points of the Brillouin zone under the cubic phase, respectively. (Key: Na: violet spheres; Nb: blue spheres; O: brown spheres).

Figure 6.9 Enthalpy difference (ΔH) between the indicated ferroelectric (R3c), antiferroelectric (Pbcm), and paraelectric (Pbnm) phases of $NaNbO_3$ as calculated using ab-inito DFT calculation.

Figure 6.10 The neutron inelastic spectra of $CaMnO_3$ at low temperatures, the data were summed over (a) Q=0.5-7 $Å^{-1}$ and (b) Q=4-7 $Å^{-1}$ respectively. The peak at ~20 meV is due to spin-wave excitations, not due to phonons (1 meV=8.0585 cm^{-1}).

Figure 6.11 The (Q,E) contour plot of S(Q,E) data for $CaMnO_3$ at T=7 K measured at SEQUOIA with incident neutron energy of 110 meV is shown at top. Strong intensity excitations at low temperatures (7 K and 110 K) below E=20 meV and Q=3.5 $Å^{-1}$ are due to magnetic spin-wave excitations. The excitations around 30, 45, 55, 60, 65, 70, and 90 meV are due to phonons (their intensities increase with increasing Q).

Figure 6.12 The temperature dependence (above 300 K) of the neutron inelastic spectra of $CaMnO_3$, the data were summed over (a) Q=0.5-7 A^{-1} and (b) Q=4-7 A^{-1} respectively.

Figure 6.13 Comparison between the experimental (T=300 K) and calculated neutron inelastic spectra of $CaMnO_3$ using (a) local density approximation and (b) generalized gradient approximation. Experimental data are summed over 4-7 $Å^{-1}$. The phonon calculations are carried out in the fully relaxed magnetic (FM) configuration. The calculated phonon spectra have been convoluted with a Gaussian of FWHM of 4.5 meV to account for the effect of energy resolution in the experiment.

Figure 6.14 (a) The calculated partial phonon density of states of various atoms in $CaMnO_3$ with in LDA and GGA approximations. (b) The calculated partial density of states of $CaMnO_3$ in various configurations with in GGA. “FRM”, “FNM” and “PNM” refer to fully relaxed magnetic, fully relaxed non-magnetic and partially relaxed non magnetic calculations, respectively. The energies of unstable modes in PNM-GGA are plotted as negative energies.

Figure 6.15 Top panel: Temperature dependent neutron inelastic spectra of $PrMnO_3$ summed over various Q-range. Bottom panel: Contour plot of S(Q,E) spectra for $PrMnO_3$ measured at 6 K (right) and 150 K (left). A dispersed spin wave excitation is clearly seen below 20 meV and 1.5 A^{-1} at 6 K. In 150 K spectra, weakly dispersed magnetic excitation around 15 meV is observed.

Figure 6.16 (a) Comparison between the experimental (T= 150 K) and calculated phonon spectra in $PrMnO_3$. Experimental data are summed over 4-7 $Å^{-1}$. (b) The calculated partial phonon density of states of various atoms in $PrMnO_3$. The phonon calculations are carried out in the fully relaxed magnetic (FRM) configuration in the generalized gradient approximation (GGA).

Figure 6.17 (Color online) Pressure dependence of pseudocubic lattice parameters for (a) $CaMnO_3$ and (b) $PrMnO_3$ compared to reported experimental data for $CaMnO_3$ [70-72] and $PrMnO_3$ [28] respectively. Pressure dependence of Mn-O bond length and distortion of MnO_6 ochtahedra as calculated are shown in (c) $CaMnO_3$ and (d) $PrMnO_3$, respectively.

Figure 6.18. (a) Enthalpy difference (ΔH) between the orthorhombic (Pnma) and tetragonal (I4/mcm) phases of $PrMnO_3$ as calculated using ab-inito DFT calculation. (b) The computed phonon dispersion relations for $PrMnO_3$ in tetragonal phase

Figure 7.1 Phonon dispersion from first principles density functional theory under generalized gradient approximation (GGA-DFT). The full and dashed lines correspond to calculations performed at a= 4.57 Å and a= 4.88 Å respectively. The open symbols correspond to reported experimental[8] data.

Figure 7.2 Motion of individual atoms for zone boundary TA mode along [110] direction at lattice parameter corresponding to a= 4.88 Å. Key; O: red spheres, Li: blue spheres.

Figure 7.3 Softening of zone boundary transverse acoustic (TA) phonon along [110]. Δ**a** correspond to difference in lattice parameter from equilibrium. The equilibrium value of lattice parameter, a in GGA and LDA calculations are 4.57 Å, and 4.45 Å respectively.

Figure 7.4 Structure of $LiMPO_4$ (M=Mn, Fe) (orthorhombic Pnma space group) derived from xcrysden software at T = 0 K. Key; Li: Red spheres, M=Mn or Fe: Yellow spheres, P: Green spheres, O: Blue spheres.

Figure 7.5 The comparison of the calculated and experimental neutron inelastic scattering spectra for $LiMPO_4$ (M=Mn, Fe) available in the literature [18] at ambient pressure at 300 K. The ab-initio calculation is carried out at 0 K. The experimental spectra comprises of magnetic and phonon contribution, while computed results pertain to phonon contribution alone.The calculated spectra have been convoluted with a Gaussian of FWHM of 0.5 meV to 10% of the energy transfer in order to describe the effect of energy resolution in the experiment.

Figure 7.6 The calculated partial densities of states in $LiMPO_4$ (M=Mn,Fe). The solid and dashed lines correspond to the calculations carried out using ab-initio.

Figure 7.7 The Calculated phonon dispersion for $LiMPO_4$ (M=Mn, Fe) from ab-initio density functional theory under generalized gradient approximation (GGA-DFT).

Figure 7.8 The low-energy part of the phonon dispersion relation from ab-initio density functional theory under generalized gradient approximation (GGA-DFT). The full and dashed lines refer to the phonon dispersion corresponding to calculated unit cell parameters a=10.42(10.55) Å, b = 6.06 (6.17) Å, c = 4.75 (4.79) Å and a = 10.77 (10.66) Å, b = 6.20 (6.22) Å, c = 4.88 (4.83) Å for $LiFePO_4$ ($LiMnPO_4$). The zone-centre and zone-boundary phonon modes in $LiFePO_4$ and $LiMnPO_4$ soften at unit cell volume corresponding to the higher temperature. This region is hitherto defined by us as dynamically unstable regime. The thick lines shows the phonon branches undergoing large softening in the dynamically unstable regime.

Figure 7.9 Zone-boundary and zone-centre modes as a function of unit cell volume. The zone-centre and zone-boundary phonon modes in $LiFePO_4$ and $LiMnPO_4$ soften at unit cell volume corresponding to higher temperatures.

Figure 7.10 Motion of individual atoms for zone boundary and zone centre modes at unit cell volumes corresponding to ambient and dynamically unstable region. The numbers after the mode assignments give the phonon energies of mode in Fe(Mn) compound. i after the phonon energy indicates that mode is unstable. A 2×1×1 super cell of the primitive unit cell is shown for zone boundary mode at (0.5 0 0). The zone-centre and zone-boundary phonon modes in $LiFePO_4$ and $LiMnPO_4$ soften at unit cell volume corresponding to higher temperatures. Key; Li: Red spheres, M=Mn or Fe: Yellow spheres, P: Green spheres, O: Blue spheres.

List of Tables

temperature phases. The amplitude of the eigen vector of O1 is scaled to match with the distortion vector.

TABLE 5.1 Comparison of the calculated structural parameters of $SrFeO_2$ and $CaFeO_2$ with the experimental data. For isotropic temperature factors experimental data [14] and calculations are given at 293 K.

TABLE 5.2 (a) The calculated zone centre optic phonon modes for $SrFeO_2$ (P4/mmm) and d-$CaFeO_2$ (P-42_1m) in meV units. (1 meV=8.0585 cm^{-1}).

TABLE 5.2 (b) The calculated zone boundary modes for $CaFeO_2$ (P4/mmm) in meV units. (1 meV=8.0585 cm^{-1}). M_5^+, M_5^-, A_5^+ and A_4^- are doubly degenerate modes.

TABLE 5.3 Calculated Born effective charges (Z) as well as dielectric constants (ε) in various phases of $SrFeO_2$ and $CaFeO_2$.

TABLE 5.4 The calculated structures of d-$CaFeO_2$ (P-42_1m) and (√2×√2×1) super cell of p-$CaFeO_2$ (P4/mmm). The super cell (√2×√2×1) of p-$CaFeO_2$ is equivalent to the d-$CaFeO_2$. The distortion vector is obtained from the difference in atomic co-ordinates between d-$CaFeO_2$ and p-$CaFeO_2$ structures phases. The eigen vector of the unstable B_u and stable M_3^+ and M_2^- modes in the p-$CaFeO_2$ phase for the super cell is also given. A linear combination of Bu , M_3^+ and M_2^- modes with appropriate weight factor is used to generate the observed distortion vector as given in the last column of the table.

TABLE 5.5 Calculated lattice parameters and bond length of $CaFeO_2$ and $SrFeO_2$ in various magnetic configurations (A, C, G type antiferromagnetic and Ferromagnetic F).

Table-6.1: Experimental [35] and ab-initio calculated structural parameters of $NaNbO_3$ in the orthorhombic, antiferroelectric phase (Pbcm) and in the rhombohedral, ferroelectric phase (R3c). The structural information of ferroelectric (R3c) phase compared with the result obtained by reference [5] (second row) with the Wu and Cohen version of GGA.

TABLE 6.2. Comparison of experimental and theoretical structural parameters in the antiferromagnetic orthorhombic phase (space group: Pnma) of $CaMnO_3$. The Wyckoff sites of the atoms are given in the brackets. “FRM”, “FRNM” and “PNM” refer to fully relaxed magnetic, fully relaxed non-magnetic and partially relaxed non magnetic calculations, respectively.

List of Abbreviation

AFD	Antiferrodistortive
AFE	Antiferroelectric
DFPT	Density functional perturbation theory
DFT	Density functional theory
FD	Ferrodistortive
FE	Ferroelectric
FM	Fully relaxed magnetic
FNM	Fully relaxed non-magnetic
GGA	Generalized Gradient Approximation
HF	Hellman-Feynman
HK	Hohenberg–Kohn
HO	Harmonic oscillator
HT	High temperature
IFC	Interatomic force constants
INS	Inelastic neutron scattering
IR	Infrared spectroscopy
IXS	Inelastic X-ray scattering
JT	Jahn-Teller
KS	Kohn–Sham
LA	Longitudinal acoustic
LDA	Local–density approximation
LO-TO	Longitudinal optic and transverse optic
LT	Low temperature

ME	Magneto-electric
NTE	Negative thermal expansion
PAW	Projector-Augmented wave method
PBE	Perdew Burke Ernzerhof
PNM	Partially relaxed non-magnetic
TA	Transverse acoustic
VASP	Vienna Ab-initio Simulation Package
XAFS	X-ray absorption fine structure

Chapter 1

An Introduction to Lattice Dynamics, Density Functional Theory and Inelastic Neutron Scattering Techniques

1.1 Introduction

The understanding of thermodynamic properties of solids has important applications in diverse areas like condensed matter physics, materials science, mineralogy, geophysics, etc. It is of interest to undertake theoretical studies of materials to understand (i) how the structural changes across phase transitions manifest in the vibrational and thermodynamic properties and, (ii) the underlying physics that leads to improved material properties. Experimental studies at high pressures and temperatures are often quite limited. Thus the development of accurate models for theoretical studies of materials is of importance. An important requirement for the calculation of thermodynamic properties of solids is an accurate description of the phonon spectra. The phonon spectra can be directly measured using the inelastic neutron scattering technique. The experiment data can be analyzed using the lattice dynamical calculations. The calculated phonon spectra are used to derive the thermodynamic properties. The calculations are useful us to understand the microscopic origin of exotic material properties and their response to various thermodynamic conditions.

The organization of this chapter is as follows: The brief description about various types of materials studied is described in section 1.2. There are a few spectroscopic techniques which are used to measure phonons as well as other low energy excitation like magnons. We will be describing some of them with their merit and demerits in section 1.3.2. We have used the most powerful technique to measure phonon, *ie* neutron inelastic scattering technique which is described in detail in section 1.3.1. We have used the technique to measure density of states.

The theory of lattice vibrations is very well established. Various physical properties and thermodynamical properties of solids depend on their lattice-dynamical behavior. In section 1.4, we will describe the theory of lattice dynamics which is used to compute the various thermodynamical properties of the compound.

We have used the density functional theory (DFT) to study a variety of oxide materials to understand the role of phonons in their functional properties of negative thermal expansion (NTE), multiferroicity or super-ionic conduction In section 1.5, formalism of density functional theory has been discussed. The pseudopotential method, which is used to study all the compounds, is been briefly described in section 1.6. The section 1.7 is about the detailed of various software's. And finally conclusion of the chapter is drawn in section 1.8.

1.2 Functional Material

Functional materials are important due to their scientific interest and applications. Their properties can be tuned by external stimuli. Few specific examples include ferroelectric materials, magnetic materials, multiferroics, negative thermal expansion materials, semiconductors, piezoelectrics, ionic conductors and many more. We have studies two classes of functional materials, namely negative thermal expansion (NTE) materials and multiferroics. Negative thermal expansion materials exhibit volume contraction on heating. Multiferroics exhibit different kind of interactions simultaneously, which bring novel physical phenomena and offer possibilities for new device functions. The range of exploitable properties is very large, and includes, for example: semiconducting behavior, magnetism, dielectric properties, piezoelectricity, pyroelectricity, and the ability to alter refractive indices with electric field or stress, the ability to conduct ions in the solid state or store atoms for later use. The materials can be used in various applications including information and communications technology, energy generation and storage, transport, healthcare, defense, consumer goods etc. Many of the applications depend upon the use of multiple functional materials. A brief description of the class of compounds studied is given below.

1.2.1 Negative Thermal Expansion Materials

Usually materials expand on heating; however, some materials show anomalous thermal expansion behavior like volume contraction. Further, it has been observed that materials with large thermal expansion coefficients have very poor thermal shock resistance. The stability and integrity of materials subjected to high temperatures or large temperature fluctuations is a problem related to their thermal expansion properties. The issue of stability and integrity of material can be addressed using a composite of negative thermal expansion material with positive thermal expansion material. These materials have various usages in jet engine, mirrors in telescopes or waveguides etc, where dimensional stability is necessary for positioning in precision optics.

When we heat a material the changes in the lattice parameters is attributed to anharmonic nature of vibrational potential of atoms or molecule. In crystalline material, the vibration of the atoms are understood in terms of lattice vibrational modes *ie* phonons. Each phonon mode has different nature of atomic displacement pattern. Thermal expansion in solids cannot be fully appreciated by only considering the lengthening of bonds. Different bond lengths and bond strengths also affect the extent of thermal expansion. Hence the impact on the thermal behavior of a three-dimensional structure necessitates additional considerations. In solids, all the lattice vibrational modes must be considered. Some of the vibrational modes can lead to an increase in unit cell size, while other vibrational modes can result in a decrease. In addition, different vibrational modes of various energies are excited at different temperatures. Thermal expansion behavior of a solid, therefore, depends upon the energies of various vibrational modes.

In this category of functional materials, we have studied three different typres of compounds, namely ZrW_2O_8, M_2O (M=Ag, Au and Cu) and MCN (M=Ag, Au and Cu). The first two belongs to category of framework compounds. However MCN are quasi-one dimensional material. The author has performed temperature dependent measurement of inelastic neutron spectra of Ag_2O, Cu_2O, AgCN, AuCN, HT-CuCN and LT-CuCN compounds. The lattice dynamics calculations in all above compounds have also been carried out. The calculations are able to explain the origin of anomalous thermal expansion behavior and correlate this with low energy phonons, nature of bonding, open structure and elastic constants.

1.2.2 Ferroelectric, Magnetic and Multiferroic Materials

The progress in experimental and theoretical studies of ferroic materials has leads to a lot of interest in the investigation and design of functional materials with desired novel functionality. Functional properties arise from coupling of different interactions and external stimuli likes: stress, electric field, magnetic field. Due to vast technological application and scientific interest an attention has drawn on ferroic materials like: ferroelectric, ferromagnetic, piezoelectrics, and multiferroic. Among the functional properties, the electronic and magnetic properties have attracted much attention of scientific community due to its vast application. The rich physics and wide varieties of novel properties of magnetic materials are related to a delicate balance between charge, spin, and orbital degree of freedom.

Multiferroic material is defined as a material showing more than two ferroic properties in a single phase. The applicability of multiferroic materials is vaster than that of ferroelectric or ferromagnetic materials. Further, the magnetoelectric materials, whose characteristics, include the emergence of simultaneous electric and magnetic ordering, offer opportunities for multifunctional device application. This justifies the intense research going on this class of materials, and the keen interest they are subject to, at both the fundamental and practical sides [1-14]. Magnetism in transition metals containing materials is induced by the active spin components in the d-shell levels. On the other hand, ferroelectricity occurs generally in the absence of d-electrons. Hence it is intriguing to observe multiferroicity since this phenomenon involves a simultaneous emergence of both the properties. The classification of multiferroic is based on the nature of the fundamental mechanism though emergence of ferroelectricity. The emergence of ferroelectricity is associated with inversion-symmetry breaking. The field describing broken inversion-symmetry (e.g. polarization) depends on linearly on the degree of freedom relevant to transition is known as proper ferroelectric and if this dependence is nonlinear (quadratic or higher order) then it called as an improper ferroelectric. Ferroelectricity in $PbTiO_3$, $BaTiO_3$, $KNbO_3$, and $BiFeO_3$ is example of proper ferroelectric and associated with polar optical phonon. The example of improper ferroelectrics are: $YMnO_3$ (arises from combination of zone boundary and zone centre phonon), $LuFe_2O_4$ (arises due to superposition of two distinct charge-order state:

electronic in nature), $TbMnO_3$, YMn_2O_5 or $TbMn_2O_5$ (arises due to certain type of spin ordering and magnetic ferroelectric).

Khomskii [15] suggested a classification for magneto-electric multiferroic materials as type I and type II multiferroics. In the type I multiferroics the origin of magnetism and ferroelectricity are different and they possess a high ferroelectric transition temperature (Tc) and generally magnetoelectric coupling is weak. On the other hand for type II multiferroics the origin of ferroelectricity is governed by magnetism hence they exhibit strong magnetoelectric coupling but have low ordering temperature. We have listed below few examples of multiferroic and their classification according to Khomskii.

Type I mutiferroic

Lone-pair: Example: $BiFeO_3$, $BiMnO_3$, $PbVO_3$

Phonon driven Improper Ferroelectricity: example: $InMnO_3$ and $YMnO_3$

Improper-Ferroelectric from charge ordering: $Pr_{1-x}Ca_xMnO_3$, $LuFe_2O_4$

Type II mutiferroic

Magnetically Driven Improper Ferroelectricity: $TbMnO_3$, $Ni_3V_2O_8$

From Collinear magnetism (exchange Striction): YMn_2O_5

Phonon mediated linear magnetoelectric coupling: $TbMn_2O_5$, $GaFeO_3$, $AlFeO_3$

Understanding the mechanism of multiferrocity is of considerable importance for the design of new multiferroics at controllable conditions (temperature and pressure). Hence the electric and magnetic properties attributed to the dynamics of ions and electrons need to be studied and explored. In this thesis, we have studied various kinds of compounds ranging from magnetic, ferroelectric and multiferroic of type I and II. Our aim is to investigate the role of phonon in various phase transitions and their coupling with spin. The compounds namely: $GaFeO_3$, $YMnO_3$, $PrMnO_3$, $CaMnO_3$, $NaNbO_3$, $SrFeO_2$ and $CaFeO_2$ have been studied using combination of inelastic neutron scattering and first principles lattice dynamics simulations. The author has performed the lattice dynamics calculations in all the above compounds and explained the coupling of magnetic degree of freedom with the atomic degree of freedom, various pressure and temperature driven phase transition and role of phonon and its manifest on physical properties. The neutron inelastic measurement have been performed on $GaFeO_3$, $YMnO_3$ and $NaNbO_3$.

1.2.3 Superionic Compounds and Battery Materials

Fast ion conductors are one of the functional materials which possess high values of ionic conductivity at relatively modest temperatures. Such compounds find extensive technological applications in solid state batteries, gas sensors and fuel cells. The search for better solid electrolytes (i.e. higher ionic conductivities, higher power densities, lower cost, environmentally friendly, etc.) is a particularly active area of research. The author has performed first principles lattice dynamics simulation on superionic compounds and battery materials Li_2O, $LiMnPO_4$ and $LiFePO_4$. The author is able to correlate the specific phonon mode which may lead to onset of the superionic behavior in the compound. In other battery material $LiMPO_4$ (M=Mn, Fe), the lattice dynamics calculations indicate instability of zone-centre as well as zone-boundary phonon modes at unit cell volume corresponding to elevated temperature and may result in the onset of diffusion of Li in these compounds.

1.3 Theory of Inelastic Neutron Scattering

The inelastic scattering of any radiation from a system involves exchange of energy and momentum between the system and the probing radiation. Thermal neutrons as a probe can exchange a part of their energy and momentum with an excitation in the system. They may lose part of their energy in creating an excitation in the system or may gain energy by annihilation. Thus, the nature of the excitation can be probed by measuring the energy and momentum of the neutrons before and after the scattering event from a system. During the process the sum of energy and momentum of the neutron and system will remain conserve. This can be expressed mathematically by using following equations:

$$E_i - E_f = \hbar\omega(q, j) \tag{1.1}$$

$$\hbar(\mathbf{k}_\mathrm{i} - \mathbf{k}_\mathrm{f}) = \hbar\mathbf{Q} = \hbar(\mathbf{G} \pm \mathbf{q}) \tag{1.2}$$

where k_i, k_f are incident and the scattered neutron wavevectors and **Q** is the wavevector transfer (scattering vector) associated with the scattering process. **q** is the wavevector of the excitation with energy $\hbar\omega$ and **G** is a reciprocal lattice vector of the system under study, E_i and E_f are the incident and scattered neutron energies and $\hbar\omega$ is the energy transfer to the system in the scattering process. The +(-) sign indicates that the excitation is annihilated (created) in the scattering process. Hence, the experimental technique of neutron scattering to determine the nature of excitations in the system involves study of the inelastic spectrum of scattered neutrons. The energy and wavevector of neutrons are measured using a spectrometer.

In the scattering process, the inelastic scattering cross-section of the process is measured and this is directly proportional to the dynamical structure factor S(**Q**, ω) (characteristic of the system), which is the double Fourier transform of the space-time correlation function of the constituents of the system including the phonon. Peaks in S(**Q**, ω) correspond to these elementary excitations[16-18]. The measurements on single crystals give information about the **q** dependence of phonon (phonon dispersion relation), while polycrystalline samples provide frequency distribution of the phonons (phonon density of states g(ω)). The measurement of phonon dispersion relation is not always possible because a suitable single crystal may not be available. The complete phonon dispersion relation is often available only along high symmetry directions of the Brillouin zone. Therefore, in order to obtain a complete picture of the dynamics, it is useful to determine the phonon density of states.

The scattering from the sample can occur by creation or annihilation of one or more excitations (phonon) in the system. The neutron scattering structure factor[17, 19] [19,20] due to a one-phonon inelastic process is given by

$$S^{(1)}_{\mathrm{coh}}(\mathbf{Q},\omega) = A'\sum_{\mathbf{q}j}\frac{\hbar}{2\omega(\mathbf{q}j)}\{n(\omega)+\frac{1}{2}\pm\frac{1}{2}\}\left|F^{(1)}_{j}(\mathbf{Q})\right|^{2}\delta(\mathbf{Q}-\mathbf{G}\pm\mathbf{q})\delta(\omega\mp\omega(\mathbf{q}j)) \tag{1.3}$$

where,

$$F^{(1)}_{j}(\mathbf{Q}) = \sum_{k} b^{\mathrm{coh}}_{k}\frac{\mathbf{Q}.\xi(\pm\mathbf{q}j,k)}{\sqrt{m_k}}\exp\{-W_k(\mathbf{Q}))\exp(i\mathbf{G}.\mathbf{r}(k)) \tag{1.4}$$

where A' is the normalization constant and b_k, m_k and **r**(k), neutron scattering length, mass and the coordinate of the kth atom, respectively. ξ is eigenvector of excitation, $F^{(1)}_{j}(\mathbf{Q})$ is one-phonon structure factor, exp(-W_k(**Q**)) is the Debye-Waller factor. $\hbar\mathbf{Q}$ and $\hbar\omega$ are the momentum and energy transfer on scattering of the neutron, respectively, while $n(\omega)$ is the phonon- population factor.

The upper and lower signs (eq. 1.3) in $\pm$ or $\mp$ correspond to loss and gain of the energy of the neutrons, respectively. The two delta functions in eq. (1.3) stand for the conservation of momentum and energy. These two conditions allow the determination of the phonon dispersion relation $\omega_j(\mathbf{q})$. From a large number of such measurements on a single crystal, one can identify several points of the phonon dispersion relations.

From eq. (1.4) it is clear that phonon cross-sections depend strongly on **Q** and ω, apart from the atomic structure of the solid itself. For measuring a phonon having the eigenvector ξ, the scattering vector **Q** should be chosen such that it is aligned parallel to ξ as much as possible. Since $\mathbf{Q} = \mathbf{G} \pm \mathbf{q}$ and for longitudinal mode $\mathbf{q} \perp \xi$ one should chose $\mathbf{G} \perp \mathbf{q}$ for observation of a longitudinal mode. For transverse modes $\mathbf{q} \perp \xi$ and one requires $\mathbf{G} \perp \mathbf{q}$.

For simple structures, the eigenvectors may be determined entirely from the symmetry of the space group. Thus the structure factors $F_j(\mathbf{Q})$ may be entirely determined from the crystal structure. For more complex structures, the space-group symmetry only classifies the phonons into a number of irreducible representations. The number of phonons associated with each representation is same as that of number of symmetry vectors. The eigenvectors could be any linear combinations of the symmetry vectors associated with the irreducible representation. Calculation of individual structure factors can be done from the knowledge of the eigenvectors which can be obtained from the lattice dynamics calculation. These calculations help in identifying the regions in reciprocal space, where the neutron-scattering cross-sections are large.

1.3.1 Phonon Density of States Measurements Using IN4C Spectrometer

The time-of-flight spectrometer detects a large (**Q**, ω) space volume in a single run. This is done by the simultaneous use of several detectors equipped with the respective TOF electronics. The change in energy and the scattering vector **Q** is obtained by measuring the flight time and the scattering angle of the neutrons from a beam pulsing device (chopper) to the detectors. The energy of the neutrons is fixed before or after the scattering process. For measurement of phonon density of states the scattered neutrons from the sample are collected over a wide range of scattering angles. By choosing a suitable high incident neutron energy, measurement of the scattering function S(**Q**, ω) over a wide range of momentum and energy transfers can be undertaken and the data can be averaged over a wide range of **Q**.

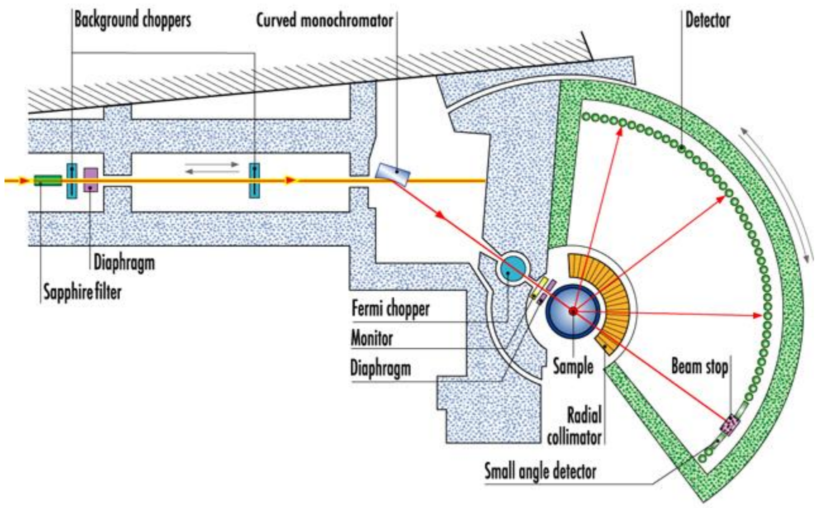

FIG 1.1 *Schematic diagram of the IN4 spectrometer at ILL, Grenoble, France (after www.ill.fr).*

IN4C is a time-of-flight spectrometer used for the study of excitations in condensed matter. It works in the thermal neutron energy range (10-100 meV). The instrument is consisting of two spectrometer units. The main component of the spectrometer is two background choppers, the double curvature mono-chromator with four faces and the Fermi chopper. The background choppers are rapidly pulsating beam shutters which act as a low-pass filter. Thus one can eliminate most of the fast neutrons and gamma rays from the beam that give rise to background noise in the spectra. A suitable energy is selected from the thermal neutron spectrum with the crystal monochromator. The monochromator, an assembly of 55 crystal pieces, concentrates the divergent incident beam onto a small area at the sample position. Hence the full use of the available solid angle gives a high incident flux. The Fermi chopper rotates at speeds of up to 40000 rpm. It transmits short neutron pulses (10- 50 µs) to the sample. The time-of-flight of neutrons between the chopper and the sample (1-5 ms) can be measured by using precise electronic circuitry. The sample environment is designed to accommodate standard cryostats and furnaces. A radial collimator around the sample position is used to cut the scattering from the sample environment. The secondary flight-path is in vacuum to avoid parasitic scattering of the transmitted neutrons. The detector bank (^{3}He detector tubes , length 300 mm, width 30 mm, elliptical section, pressure 6 bar) covers scattering angles from 10^o to 120°. The time-of-flight spectra measured at various angles are further treated in order to obtain the scattering function S(Q, w) that is characteristic of the properties of the sample. The measurements on polycrystalline samples of $GaFeO_3$, $YMnO_3$, MCN (M=Ag, Au and Cu), Ag_2O and Cu_2O is carried out by the author using the time-of-flight IN4 spectrometer (Fig. 1.1) at the Institut Laue Langevin (ILL), France.

1.3.2 Other Experimental Techniques

Inelastic X ray scattering (IXS) is a recently evolved technique and used to measure phonon in the entire Brillouin zone. The energy of the X-rays are in the order of KeV, however the energy of phonons is of the order of meV. Hence one would need a high resolution instrument. This can be done using perfect single crystal at the cost of huge intensity loss. Hence with the synchrotron radiation source, where the incident flux is very high, one can perform the IXS measurements. The IXS has following advantage over INS

- Large (Q,ω) space.
- Requires microgram samples hence suitable for high pressure experiments.
- Energy resolution that is independent of the energy transfer.
- Nearly no intrinsic backgrounds.

The first two advantages are probably the most significant. The first follows from the fact that x-ray energies (~20 keV) are much larger than the measured energy transfers (~1 to 200 meV), unlike neutrons where the probe energy is often very similar to the phonon energy, ~50 meV. The technique is especially important for the study of liquid samples where one would like access to large energy transfer at small momentum transfers[20], and is less important for crystalline materials where one can often work in higher Brillouin zones. The access to small samples, follows from the very high flux and brilliance of synchrotron radiation sources, with the option to focus beams easily to ~100 microns in diameter, and, with some losses, to ~10 microns. It means that one can investigate small samples, including samples at very high (e.g. earth's core) pressures in diamond anvil cells, and small crystals of new materials. The latter is especially important in the world of modern materials synthesis, where often the size of the single crystals are very small. . Neutrons remain advantageous when high - energy resolution is needed, as backscattering spectrometers provide sub-meV resolution, at least for smaller energy transfers. Neutrons remain extremely competitive when large single crystals of heavier materials are available, whereas, x-rays are limited by the short penetration length into the sample.

Raman scattering[21], is due to inelastic scattering of the incident photons whereby energy is transferred to or received from the sample due to changes in the vibrational or rotational modes of sample molecules, causing a change in the energy, and therefore the frequency of the scattered light. If the incident photon gives up energy to the sample it is scattered with a red shifted frequency and referred to as stokes shift. If the solid/molecule is already in an exited energy state, and gives energy to the scattered photon, the output has a blue-shifted frequency, and is referred to as anti-stokes shift. The selection rule governing Raman scattering is determined by changes in polarizibility during the vibration, which is different from another vibrational spectroscopic technique – infrared spectrometry (IR). In the case of IR spectroscopy[22, 23], the frequency of incident light has to match the energy differences between ground and excited vibrational states; and the subsequent energy loss of the incident light is detected. The molecular vibration where there is a change in dipole moment can only be observed in the IR spectroscopy. Raman scattering spectrum provides essentially the same type of information as the infrared (IR) absorption spectrum, namely, the energies of vibrational modes in solid.

Further, Brillouin light scattering[24, 25] is the inelastic scattering of an incident optical wave field by thermally excited elastic waves (usually called acoustic phonons). From an empirical point of view, the two types of scattering (Raman and Brillouin) differ only in the distinction that optical phonons are involved in Raman scattering and acoustic modes are involved in Brillouin scattering. Due to the small frequencies of acoustic phonons for small q vectors, the Brillouin lines are separated by small frequency shifts, of the order of less than 1 cm^{-1}, from the Rayleigh line. For this reason it is not possible to use a grating monochromator as for Raman scattering, but rather a Fabry-Perot interferometer must be used.

However, the above methods differ fundamentally in mechanism and selection rules, and each has specific advantages and disadvantages. The major disadvantage of optical spectroscopy techniques is due to large wavelength (~5000 A) of the incident radiation. That would allow to probe only a tiny region of the Brillouin zone close to zone centre. However various phase transitions and properties of the materials are contributed from entire Brillouin zone. Further selection rule for Raman and IR techniques restrict their applicability in few compounds, whereas there is no such limitation is neutron inelastic technique. We can measure any phonon mode in the entire Brillouin zone. The advantage of the Raman and IR techniques are that the radiation flux in these techniques is much higher than neutron, hence data can be collected in very short times. Moreover these techniques can easily be set up in small laboratories, whereas neutron inelastic requires major facility of reactor.

1.4 Theoretical Techniques

It is very important to analyze and interprete the measured data as well as understand the various physical and thermodynamical properties like elastic constant, specific heat, thermal expansion etc. The character and energy of atomic dynamics in solid as well as the individual atomic contribution to the spectra and other thermodynamical properties are difficult to obtain from measurements. Theory of lattice dynamics is a well established technique, it help us to understand the measured spectra and their atomic origin. Hence the theory of lattice dynamics plays a key role to simulate the observed spectra in various thermodynamical conditions. Also there are various thermodynamical conditions where direct measurement is not possible. The simulations are very useful to interpret the experimental data. Simulation and experimental techniques complement each other and provide complete information about a system. In following section we will be describing the lattice dynamics techniques to compute the vibrational spectra and derived thermodynamical quantities.

1.4.1 Theory of Lattice Dynamics

The theory of lattice dynamics is based on two basic approximation Born-Openheimer approximation and harmonic approximations. According to Born-Openheimer approximation in a system of electron and ion, we can treat the equation of motion of electron and ion separately since the electronic degree of freedom is much faster than ionic degree of freedom because of the mass difference. Here one can assume that electron will follow instantaneously the ionic motion. This is called Born- Openheimer approximation; this approximation will fail if the ionic and electronic motion becomes comparable.

Now the Hamiltonian of the crystalline system is given by:

$$H = \sum_i \frac{p_i^2}{2m_i} + \sum_{ll'kk'} \phi\begin{pmatrix} l & l' \\ k & k' \end{pmatrix} \tag{1.5}$$

Where Φ is the crystal potential energy of the system and given by $\phi = \sum_{ll'kk'} \phi\begin{pmatrix} l & l' \\ k & k' \end{pmatrix}$; where *l* and *l'* is a three dimensional crystal cell index and *k* and *k'* is atom index in l^{th} and l'^{th} cell respectively. Now if we can expand the total crystal potential ϕ in terms of atomic displacement $u_\alpha\begin{pmatrix} l \\ k \end{pmatrix}$ of k^{th} atom in l^{th} cell along α Cartesian direction.

$$\phi = \phi_0 + \sum_{\substack{ll',k,k'\\ \alpha}} \phi_\alpha \begin{pmatrix} l & l' \\ k & k' \end{pmatrix} u_\alpha \begin{pmatrix} l \\ k \end{pmatrix} + \frac{1}{2!} \sum_{\substack{ll',k,k'\\ \alpha\beta}} \phi_{\alpha\beta} \begin{pmatrix} l & l' \\ k & k' \end{pmatrix} u_\alpha \begin{pmatrix} l \\ k \end{pmatrix} u_\beta \begin{pmatrix} l' \\ k' \end{pmatrix} + \frac{1}{3!} \sum_{\substack{ll'l'',k,k',k''\\ \alpha\beta\gamma}} \phi_{\alpha\beta\gamma} \begin{pmatrix} l & l' \\ k & k' \end{pmatrix} u_\alpha \begin{pmatrix} l \\ k \end{pmatrix} u_\beta \begin{pmatrix} l' \\ k' \end{pmatrix} u_\gamma \begin{pmatrix} l'' \\ k'' \end{pmatrix} + Higher \tag{1.6}$$

In equilibrium configuration the force on every atom will be zero. Hence this will lead to the first derivative of potential energy to be precisely zero.

At low temperature if the amplitude of vibrations i.e. atomic displacements are not very large then we can ignore the higher order term beyond the quadratic term, this is called as harmonic approximation. We will see the pros and cons these approximations soon.

Using the Born-Openhiemer and harmonic approximation, one can solve the Hamiltonian. The equation of motion by solving the Hamiltonian is

$$m_k \ddot{u}_\alpha \begin{pmatrix} l \\ k \end{pmatrix}, t = \sum_{l',k',\beta} \phi_{\alpha\beta} \begin{pmatrix} l & l' \\ k & k' \end{pmatrix} u_\beta \begin{pmatrix} l \\ k \end{pmatrix}, t \tag{1.7}$$

In crystalline system, force constant will satisfy the translational sum rules. This sum rule is of great importance in practical calculations as it enables the determination of the “self force constant” $\phi_{\alpha\beta}\begin{pmatrix} 0 & 0 \\ k & k \end{pmatrix}$ and this is given by $\phi_{\alpha\beta}\begin{pmatrix} 0 & 0 \\ k & k \end{pmatrix} = -\sum'_{l,l',k,k'} \phi_{\alpha\beta}\begin{pmatrix} l & l' \\ k & k' \end{pmatrix}$

where the prime in summation implies the exclusion of the *l*=*l*’ and *k*=*k*’.

$$\sum_{l,l',k,k'} \phi_{\alpha\beta} \begin{pmatrix} l & l' \\ k & k' \end{pmatrix} = 0 \tag{1.8}$$

Any perturbation in the system of crystalline material, which is a three dimensional periodic system can be written in terms of plane waves. Hence atomic displacement of k^{th} atom of l^{th} unit cell at any instantaneous time *t* can be expanded as sum of plane waves

$$u_\alpha \begin{pmatrix} l \\ k \end{pmatrix}, t \Big) = \sum\nolimits_{\omega,q} \frac{u_\alpha(q,v)}{\sqrt{m_k}} \exp^{i(q.r(l,k)-\omega(q,v)t)} \tag{1.9}$$

Now using equation (1.9) in (1.7), we will get 3n simultaneous equations

$$\omega^2(q) U_\alpha(q,v) = \sum\nolimits_{k',\beta} D_{\alpha\beta} \begin{pmatrix} q \\ kk' \end{pmatrix} U_\beta(q,v) \tag{1.10}$$

Where α= x, y, z and k'=1, n (n is number of atoms in unit cell) and

$$D_{\alpha\beta} \begin{pmatrix} q \\ kk' \end{pmatrix} = \frac{1}{\sqrt{m_k m_{k'}}} \sum\nolimits_{l'} \phi_{\alpha\beta} \begin{pmatrix} l & l' \\ k & k' \end{pmatrix} \exp^{i(q.r(l,k)-q.(r(l',k')-\omega(q,v)t))} \tag{1.11}$$

The above equation can be written in matrix form

$$\Omega(q)U(q)=D(q)U(q) \tag{1.12}$$

where

$$D(q) = \begin{pmatrix} D\begin{pmatrix} q \\ 11 \end{pmatrix} & D\begin{pmatrix} q \\ 12 \end{pmatrix} \cdots & \cdots & D\begin{pmatrix} q \\ 1n \end{pmatrix} \\ D\begin{pmatrix} q \\ 21 \end{pmatrix} & D\begin{pmatrix} q \\ 22 \end{pmatrix} \cdots & \cdots & D\begin{pmatrix} q \\ 2n \end{pmatrix} \\ & \vdots & & \\ D\begin{pmatrix} q \\ n1 \end{pmatrix} & D\begin{pmatrix} q \\ n2 \end{pmatrix} \cdots & \cdots & D\begin{pmatrix} q \\ nn \end{pmatrix} \end{pmatrix} \tag{1.13}$$

$$U(q)=\begin{pmatrix} U_x(k=1|q) \\ U_y(k=1|q) \\ \vdots \\ U_z(k=n|q) \end{pmatrix} \tag{1.14}$$

D(q) is known as dynamical matrix and it is a Hermitian matrix. The diagonalization of above matrix will have the form

$$\left\|\left(D(q)-\omega^2(q)\right)1_{3n}\right\| \tag{1.15}$$

Solving the equation (1.15), 3n eigenvalues are obtained which are $\omega_j^2(\boldsymbol{q})$, (j=1,2,…,3n). Because, the dynamical matrix is Hermitian, the eigenvaues are real and its eigenvectors are orthogonal to each other. The components of the eigenvectors $\xi_j(\mathbf{q})$ determine the pattern of displacement of the atoms in a particular mode of vibration. Corresponding to every direction in **q**-space, there are 3n curves $\omega=\omega_j(\mathbf{q})$, (j=1,2,…3n). Such curves are called phonon dispersion relations. The index j, which distinguishes the various frequencies corresponding to the propagation vector, characterizes various branches of the dispersion relation. Dispersion relation must satisfy the crystal symmetry. Though, some of these branches are degenerate because of symmetry, in general they are distinct. The form of dispersion relation depends on the crystal structure as well as on the nature of the interaction between atoms. Because of the translational invariance three phonon frequencies are zero at q=0. These three branches are referred to as acoustic branches. The remaining (3n-3) branches have finite frequencies at $\boldsymbol{q}$=0, which are labeled as optic branches. This will give 3n eigenvalues and eigenvectors. The eigenvalues are the square of phonon frequency at given q, hence we have 3n phonon at any given q. For a stable system all the phonon frequencies at any q must be positive.

The distribution of ω(q) is known as density of states. Mathematically it can be represented as

$$g(\omega)=\frac{1}{3nN}\lim_{\Delta\omega\to 0}\sum_{j,q}\delta(\omega-\omega_j(q)) \qquad (1.16)$$

Here δ(x) is the Dirac delta function.

The eiqgenvector at any q point for given phonon mode will determine the direction and relative amplitude of atomic motion in a crystalline solids, it is also known as polarization vector.

1.4.2 Thermodynamical Functions

By knowing the phonon spectrum we can calculate the various thermodynamical quantities contributed from phonons. The theory of lattice dynamics described in previous section allows us to determine the phonon frequencies in the harmonic approximation. The theory is strictly valid in harmonic approximations; those properties which are consequence of anharmonic character of lattice vibrations cannot be accounted within this approximation like thermal conductivity, thermal expansion, specific heat at high temperature and multiphonon process etc.

The number of phonons excited in thermal equilibrium at any temperature is given by Bose-Einstein distribution $n(\omega)\left[=\frac{1}{\exp(\hbar\omega/k_B T)-1}\right]$. At high temperatures, $\hbar\omega_j(\mathbf{q}) \ll k_B T$, the number of phonons in a given state is directly proportional to the temperature and inversely proportional to their energy. Anharmonic effects are relatively small at low temperature. These effects become more important at high temperatures. This change at high temperatures affects physical properties of the crystal. In the quasiharmonic approximation (where, the vibrations of atoms at any finite temperature are assumed to be harmonic about their mean positions appropriate to the corresponding temperature), the thermodynamic properties of a crystal are based on the energy distribution of these phonon vibrations; however, in magnetic system the other low energy excitations like magnon will also play the role in determining these properties.

The partition function of a single harmonic oscillator is given by

$$Z_{HO} = \sum_n \exp - \left(\frac{((n + \frac{1}{2})\hbar\omega}{K_B T} \right) \tag{1.17}$$

$$Z_{HO} = \frac{\exp^{-(\hbar\omega_{jq}/2K_BT)}}{1 - \exp^{-(\hbar\omega_{jq}/K_BT)}} \tag{1.18}$$

In a crystalline system vibrational modes (phonon mode) are orthogonal to each other; hence the partition function of the system is given by

$$Z = \exp^{-\phi(V)} \prod_{j,q} \frac{\exp^{-(\hbar\omega_{jq}/2K_BT)}}{1 - \exp^{-(\hbar\omega_{jq}/K_BT)}} \tag{1.19}$$

Here the partition function of the crystalline system is written as a product of partition functions of single phonon; this is the major advantage of harmonic oscillator. This is only valid when the oscillators are independent. Various thermodynamic properties of the crystal derived from the partition function involve summations over the phonon frequencies in the entire Brillouin zone and can be expressed as averages over the phonon density of states. The Helmholtz free energy F and entropy S are given by

$$F = -k_B T \ln Z = \phi(V) + \int [\frac{1}{2}\hbar\omega + k_B T \ln\{1 - \exp(\frac{-\hbar\omega}{k_B T})\}] g(\omega) d\omega \qquad (1.20)$$

$$S = -\frac{dF}{dT} = k_B \int \{-\ln[1 - \exp(\frac{-\hbar\omega}{k_B T})] + \frac{(\frac{\hbar\omega}{k_B T})}{[\exp(\frac{\hbar\omega}{k_B T}) - 1]}\} g(\omega) d\omega \qquad (1.21)$$

The energy E of the crystal with volume V is

$$E = F - T\frac{dF}{dT} = \phi(V) + E_{vib} \qquad (1.22)$$

where ϕ (V) is the static lattice energy and E_{vib}, the vibrational energy at temperature T.

$$E_{vib} = \int \{n(\omega) + \frac{1}{2}\} \hbar\omega g(\omega) d\omega \qquad (1.23)$$

where n(ω) is the population factor given by

$$n(\omega) = \frac{1}{\exp(\hbar\omega / k_B T) - 1} \qquad (1.24)$$

The specific heat $C_v(T)$ is given by

$$C_v(T) = \frac{dE}{dT} = k_B \int (\frac{\hbar\omega}{k_B T})^2 \frac{e^{(\frac{\hbar\omega}{k_B T})}}{(e^{(\frac{\hbar\omega}{k_B T})} - 1)^2} g(\omega) d\omega \qquad (1.25)$$

The calculated phonon density of states can be used to compute the specific heat. While lattice dynamical calculations yield C_V, the specific heat at constant volume, experimental heat capacity data correspond to C_P, the specific heat at constant pressure. The difference C_P-C_V is given by

$$\mathrm{C_p(T) - C_v(T) = [\alpha_v(T)]^2 BVT} \tag{1.26}$$

where α_V is the volume thermal expansion and B is the bulk modulus defined as

$$B = -V\frac{dP}{dV} \tag{1.27}$$

Thermal expansion in materials is often expressed using the volume coefficient of thermal expansion (CTE). The volume CTE, α, is defined with the following relationship:

$$\alpha = \left(\frac{\partial \ln V}{\partial \ln T}\right)_P \tag{1.28}$$

where V is volume and T is temperature at constant pressure, P. Thermal expansion is always in the direction of increasing entropy and this can be expressed by applying a Maxwell relation to equation (1.28) as follows:

$$\alpha = -\frac{1}{V}\left(\frac{\partial S}{\partial P}\right)_T = \frac{1}{B_T}\left(\frac{\partial S}{\partial V}\right)_T \tag{1.29}$$

where S is entropy and $\mathrm{B_T}$ is the isothermal bulk modulus, which is always positive and signifies the change in volume with increasing temperature is always in the direction of increasing disorder. The sign of α is related to that of $\left(\frac{\partial S}{\partial V}\right)_T$. A positive sign for α shows increasing entropy with increasing volume; while a negative sign for α denotes increasing disorder when the volume decreases at constant temperature. As pressure increases and volume decreases under non-isothermal conditions, entropy decreases in materials exhibiting normal thermal expansion and α is positive in these compounds. NTE is anomalous in this limited scope as materials with NTE show increasing entropy with decreasing volume. Using thermodynamical relations it can be shown that

$$\alpha = \frac{1}{B_T}\left(\frac{\partial P}{\partial T}\right)_V = -\left(\frac{\partial \ln V}{\partial P}\right)_T \left(\frac{\partial P}{\partial T}\right)_V \tag{1.30}$$

$$\left(\frac{\partial P}{\partial T}\right)_V = \left(\frac{C_v}{V_0}\right)\gamma \tag{1.31}$$

$$\alpha(T) = \gamma C_v(T) / B_T V_0 \tag{1.32}$$

Here γ is known as Gruniesen parameter and defined as

$$\gamma = \left(\frac{\partial P}{\partial (U/V)}\right)_V = -\left(\frac{\partial \ln T}{\partial \ln V}\right)_S \tag{1.33}$$

$$\gamma = -\frac{\partial \ln \omega}{\partial \ln V)} \tag{1.34}$$

The procedure of the calculation of thermal expansion is applicable when explicit anharmonicity of phonons is not very significant, and the thermal expansion arises mainly from the implicit anharmonicity, i.e., the change of phonon frequencies with volume. Due to very large Debye temperatures in most of these systems the quasiharmonic approximation seems to be suitable up to fairly high temperatures. We have discussed the role of implicit and explicit anharmonicity as well as validity of quasiharmonic approximation is Chapters 2-3.

The various ground state properties of a material are derivatives of the total energy at T=0 or free energy F at finite temperature. In Table 1.1 we have shown the variable on left side and the corresponding properties on right side.

TABLE 1.1 *Various physical variable (left) and corresponding physical properties obtained from derivatives of total energy with respect to these physical variables.*

Second derivative of E_{tot} or F wrt	**Physical property**
di, dj *Atomic displacement*	*Force constant (Phonons)*
Ei, Ej *Electric field*	*Dielectric tensor*
ε_{ij}, ε_{kl} *Strain*	*Elastic constants matrix*
E_i, ε_{jk} *Electric field, strain*	*Piezoelectric coefficient*
E_i,d_j *Electric field, Atomic displacement*	*Born dynamical charges*
d_i, ε_{ij} *Atomic displacement, strain*	*Strain phonon coupling*
H_i,H_j *Magnetic field*	*Magnetic susceptibility*
E_i,H_j *Electric field, Magnetic field*	*Electromagnetic coupling*
H_i, ε_{jk} *Magnetic field, strain*	*Piezomagnetic coefficient*

By calculating the total energy at different thermodynamical conditions one can calculate the various properties of the materials. In the next section we will be discussing about density functional theory (DFT) method to compute the total energy.

1.4.3 Flow Chart of Phonon Calculation

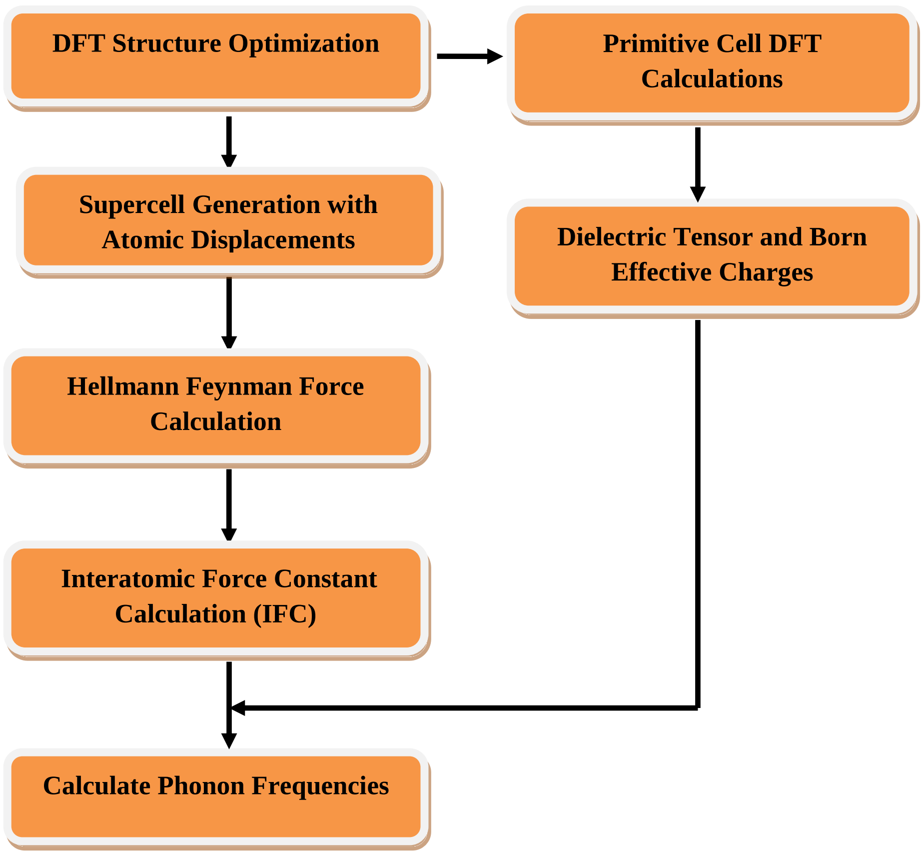

FIG. 1.2 *Flow chart of PHONON calculation using DFT methods.*

Fig 1.2 shows the flow chart of phonon calculation. Using DFT methods (The computer codes will be discussed later) the structure of a given compound is optimized (*i.e.* atomic position and lattice parameter such that the force on individual atom is less than 0.001 eV/Å). Further, the relaxed structure is used to compute the response function like dielectric tensor and Born effective charges. In the supercell approach of phonon frequencies calculation, a supercell of appropriate dimension is generated using the optimized structure parameters. Further, different atomic configuration of a given supercell is generated using the symmetry adapted displacement of individual atoms along various high symmetry directions. Now using the DFT method Hellman-Feynaman forces of individual atom in supecell is obtained for each configuration. The interactomic force constant of pair of atoms are calculated using the Hellman-Feynman forces. The phonon frequencies in the entire Brillouin zone are calculated using the interatomic force constants. The dielectric constants and Born effective charges can be used to calculate to longitudinal optical and transverse optic modes splitting. In next section we will describe the basics of ab-initio density functional theory.

The Born effective charge is defined as the derivative of the energy with respect to atomic displacements and electrical field. When studying materials with long-ranged force constants, such as oxides or semiconductors, one needs to consider the effect of long-range interaction on phonon frequencies. This is incorporated with Born effective charge tensor and dielectric constants.

In quantum mechanics, the force is the derivative of expectation value of Hamiltonian with respect to the atomic coordinates, this requires the three first derivative terms. Hellmann-Feynman theorem[26] says that the first derivative of the Hamiltonian with respect the atomic coordinates is equal to the expectation value of derivative of Hamiltonian. This is known as Hellmann-Feynman (HF) forces.

1.5 Ab-initio Density Functional Theory

The Density functional theory method is known to calculate the total energy from first principles. This technique does not necessarily require any experimental input like structure, bond length, lattice parameters and phonon frequencies etc. Usually it is difficult to predict the minimum energy crystal structure among a large number of possibilities; therefore the known structure is used as the starting point for further optimization. Ab-initio density functional theory is proven to be most accurate technique till now to compute the total energy at T=0K. The theory is based on solving the Hamiltonian of the system including electron and ions together. The valence electrons are the fundamental entity controlling the nature of bonding, volume, charge and various other properties. The theory in principle is exact however in practice it includes approximations at the level of exchange and correlation. We will discuss the detail of these approximations in next sections.

The behavior of electron in the vast environment of other electrons, ions and electromagnetic field controls the many physical and chemical and thermodynamical properties of the material. The many–body Hamiltonian operator that governs the behavior of a system of interacting electrons and nuclei in atomic units takes the form

$$\hat{H} = -\frac{1}{2}\sum_i \nabla_i^2 - \sum_{i,I} \frac{Z_I}{|r_i - R_I|} + \frac{1}{2}\sum_{i\neq j} \frac{1}{|r_i - r_j|} - \sum_I \frac{\nabla_I^2}{M_I} + \frac{1}{2}\sum_{I\neq J} \frac{Z_I Z_J}{|R_I - R_J|} \qquad (1.35)$$

The summations over *i* and *j* correspond to electrons, and summations over *I* and *J* correspond to nuclei of the system r_i, R_I and Z_I is ith electron spatial coordinate, position and charge on Ith nuclei respectively. Examining Eq. (1.35), we find that it basically consists of five terms being in order namely the kinetic energy of the electrons, the attractive electron–

nuclei interaction, the electron–electron repulsive interaction, the kinetic energy of the nuclei, and the nuclei–nuclei repulsive interaction. This further can be written in a compact form in the following manner:

$$\hat{H} = \hat{T}_e(r) + \hat{V}_{eN}(r,R) + \hat{V}_{ee}(r) + \hat{T}_I(R) + \hat{V}_{NN}(R) \tag{1.36}$$

Where the various kinetic and potential operators depend on the positions of the electron and nuclei positions r and R, respectively. Eq. (1.35) would be much more tractable to solve if it were separable in electron and ion coordinates, but the electron–nuclei interaction term V_{eN} prevents this as it depends explicitly on both the positions of the electrons *r* as well as the positions of the nuclei *R*. However the mass of an electron is negligible in comparison to the atomic masses in the system. Thus the nuclei can be assumed to remain stationary from the point of view of an electron. As the spatial configuration of nuclei might change, we assume electrons will instantly find themselves adjusted to the new spatial configuration of nuclei. Furthermore, in fixing the nuclei positions, the potential energy from the nuclei–nuclei interaction becomes constant. This is known as the Born–Oppenheimer, or adiabatic, approximation as already discussed in section 1.3.4. Now we are also effectively disregard the kinetic energy of the nuclei because of the heavy mass. Now the Hamiltonian becomes:

$$\hat{H} = \hat{T}_e(r) + \hat{V}_{eN}(r,R) + \hat{V}_{ee}(r) + \hat{V}_{NN}(R) = \hat{H}_e + E_{NN} \tag{1.37}$$

The $\hat{H}_e$ is known as the electronic Hamiltonian, as it describes the motion of electrons in a fixed environment of atomic nuclei. It can be further broken down into having terms of internal and external character by writing

$$\hat{H}_e(r) = \hat{T}_e(r) + \hat{V}_{\text{int}}(r) + \hat{V}_{ext}(r, R) \tag{1.38}$$

We need a formulation of an actual problem we can try to solve, and ideally, this problem is a connection to how the real world behaves, and the solution to which tells us something about the behavior of electrons in the real world.

$$\hat{H}_e \psi = E\psi \tag{1.39}$$

This is an eigenvalue problem. This equation connects the electronic hamiltonian operator $\hat{H}_e$ for a system of electrons with its stationary solutions E_e. These stationary solutions turn out to be the eigen solutions to the above equation, where each eigenfunction solution Ψ is known as a many–body electronic wavefunction. The electronic wavefunction Ψ describes the state of all electrons in the system, and is a function of the set of the spatial locations of each electron $\{r_i\}$. The electronic energy associated with each solution wavefunction also depends implicitly on nuclei positions:

$$\psi = \psi\left(\{r_i\};\{R_0\}\right), \quad E_e = E_e\left(\{R_0\}\right) \tag{1.40}$$

Now we assume implicitly the parametric dependence of the wavefunction and energies on the positions of the nuclei $\{R_I\}$, and we omit this from our expressions.

From Eq. (1.38) we have a Hamiltonian operator which dictates the behavior for a given system of N electrons moving about a fixed arrangement of atomic nuclei. These set of N electrons are described by their locations in space by the set of their spatial coordinates

$\{r_i\}$. The electrons are fermions; we have to also include information about their spin state. To incorporate this property, we add an additional spin degree of freedom ***s*** to the spatial coordinate ***r*** of an electron, and we can then write general coordinate of the electron is x given by

$$x = \{r_, s\} \tag{1.41}$$

We are now able to fully describe the electrons in the many–body wavefunction in terms of the augmented coordinates x. We will use it to enforce a property that electrons obey, known as the Pauli exclusion principle. This principle says that no two electrons can possess the same quantum state. In other words, they may not occupy both the same position in space and have the same spin state. Hence in order to include the effect of spin, the wave–function of the electrons is constructed such that it is anti–symmetric. Thus an interchange of any two electrons in the system would change the sign of the wavefunction in the following manner:

$$\Psi(r_1, r_2, ...r_N) = -\Psi(r_2, r_1, ...r_N) \tag{1.42}$$

Another condition imposed on the many–body wavefunction is the normalization of the wave function, i.e. for a wave function describing N electrons we have

$$\int |\Psi(r_1, ...r_N)|^2 dr_1....dr_N = 1 \tag{1.43}$$

and thus N electrons are described to exist in the system with unit probability. The single particle density in N electron system is defined as

$$n(r) = N\int |\psi(r, r_2....r_N)|^2 dr_2....dr_N \tag{1.44}$$

which yields the intuitive result that integrating the single–particle density over all of space will yield the total number of particles in the system, i.e.

$$\int n(r)dr = N \tag{1.45}$$

Determining the ground state wave–function for the Schrödinger Eq. (1.39) in terms of the many–body electron wave function Eq. (1.40) is only really tractable for simple systems with relatively very few electrons. One approach that transforms the many–body Schrödinger wave equation into a simple one–electron equation is known as the density functional theory formalism, or DFT. A central property of DFT is that it recasts the basic variable of our equations from being the ground state electronic wave function $\Psi(r_1, r_2, ...r_N)$ to that of the ground state electron density $n_0(r)$, where

$$n_0(r) = N\int \left|\Psi_0(r, r_2, ...r_N)\right|^2 dr_2....dr_N \tag{1.46}$$

and hence it effectively reduces the 3N degrees of freedom to just 3 for an N–electron system. Density functional theory is able to predict the ground state energy and wavefunction of the system, all the ground state properties of systems can be determined using the theory. In principle DFT is an exact theory of the ground state of a system, however due to lack of the exact form the exchange–correlation functional, the theory works on certain assumptions and approximations to this functional. This can have varying levels of sophistication and numerical overhead in calculation, while still providing acceptable results. However the approximated exchange–correlation functional would reflect the behavior of the true functional as much as possible.

Density functional theory is based on two pillars, one is known as Hohenberg and Kohn theorem and another is Kohn-Sham theorem.

1.5.1 Hohenberg–Kohn Theorem

$$\begin{tikzcd}
\hat{V}_{ext}(r)+C \arrow[d] & n_0(r) \arrow[l, "\textbf{HK}"'] \\
\Psi_i(\{r\}) \arrow[r] & \Psi_0(\{r\}) \arrow[u]
\end{tikzcd}$$

FIG 1.3 *Visualizing the Hohenberg–Kohn implications, where C denotes a constant.*

Hohenberg–Kohn Theorem 1.

For any system of multiple interacting particles in an external potential $V_{ext}(r)$, the potential $V_{ext}(r)$ is determined uniquely, except for a constant C, by the ground state particle density $n_0(r)$.

Hohenberg–Kohn Theorem 2.

A universal functional for the energy E[n] in terms of the density n(r) can be defined, valid for any external potential $V_{ext}(r)$. For any particular $V_{ext}(r)$, the exact ground state energy of the system is the global minimum value of this functional, and the density n(r) that minimizes the functional is the exact ground state density $n_0(r)$.

If we consider N electrons in an external potential $\hat{V}_{ext}\left(r,R_0\right)$ as defined in the electronic hamiltonian $\hat{H}_e$ from Eq. (1.38) and the many body wavefunction is given by Ψ(r) = Ψ(r_1; r_2; … r_N), we can define the functional

$$F[n]=\min\nolimits_{\psi\to n(r)}\left\langle\psi\left(r\right)\middle|\hat{T}_e\left(r\right)+\hat{V}_{\text{int}}\left(r\right)\middle|\psi\left(r\right)\right\rangle \tag{1.47}$$

where the minimum is taken over all wavefunctions Ψ(r) that construct the density n(r). The functional ***F*** is a universal in the sense that it does not depend on the system details we are dealing with nor of the external potential $\hat{V}_{ext}\left(r,R_0\right)$, i.e. it is independent of R_0. If we name E_0 and n_0(r) to be the ground state energy and density, respectively, then the above said two basic theorems of DFT are

$$E[n]=\int\hat{V}_{ext}\left(r,R_0\right)n(r)dr+F[n]\geq E_0 \tag{1.48}$$

for all n(r), and

$$\int\hat{V}_{ext}\left(r,R_0\right)n_0\left(r\right)dr+F[n_0]=E_0 \tag{1.49}$$

In order to prove the variational principle in Eq. (1.48), we introduce the notation $\psi^n_{\min}(r)$ for an electronic wave function that minimizes Eq. (1.47) such that

$$F[n]=\min\nolimits_{\psi\to n(r)}\left\langle\psi^n_{\min}\middle|\hat{T}_e\left(r\right)+\hat{V}_{\text{int}}\left(r\right)\middle|\psi^n_{\min}\right\rangle \tag{1.50}$$

Writing

$$V_{ext}\left(r,R_0\right)=\sum_i V_{ext}\left(r_i,R_0\right)$$

$$\int \hat{V}_{ext}\left(r,R_0\right)n\left(r\right)dr+F[n]=\left\langle \psi_{\min}^{n}\left|\hat{T}_e\left(r\right)+\hat{V}_{\text{int}}\left(r\right)+\hat{V}_{ext}\left(r,R_0\right)\right|\psi_{\min}^{n}\right\rangle \geq E_0 \tag{1.51}$$

This proves the first theorem of **Hohenberg- Kohn** theorem in Eq. (1.48). Further using the property of the ground state once again, we have

$$E_0=\left\langle \psi_0\left|\hat{T}_e\left(r\right)+\hat{V}_{\text{int}}\left(r\right)+\hat{V}_{ext}\left(r,R_0\right)\right|\psi_0\right\rangle \leq \left\langle \psi_{\min}^{n_0}\left|\hat{T}_e\left(r\right)+\hat{V}_{\text{int}}\left(r\right)+\hat{V}_{ext}\left(r,R_0\right)\right|\psi_{\min}^{n_0}\right\rangle \tag{1.52}$$

By subtracting the external potential from both the sides we have

$$\left\langle \psi_0\left|\hat{T}_e\left(r\right)+\hat{V}_{\text{int}}\left(r\right)\right|\psi_0\right\rangle \leq \left\langle \psi_{\min}^{n_0}\left|\hat{T}_e\left(r\right)+\hat{V}_{\text{int}}\left(r\right)\right|\psi_{\min}^{n_0}\right\rangle \tag{1.53}$$

However from (1.50) definition of $\psi_{\min}^{n_0}$ tells us

$$\left\langle \psi_0\left|\hat{T}_e\left(r\right)+\hat{V}_{\text{int}}\left(r\right)\right|\psi_0\right\rangle \geq \left\langle \psi_{\min}^{n_0}\left|\hat{T}_e\left(r\right)+\hat{V}_{\text{int}}\left(r\right)\right|\psi_{\min}^{n_0}\right\rangle \tag{1.54}$$

which is only possible if both sides of the expression are equal, i.e.

$$\left\langle \psi_0\left|\hat{T}_e\left(r\right)+\hat{V}_{\text{int}}\left(r\right)\right|\psi_0\right\rangle = \left\langle \psi_{\min}^{n_0}\left|\hat{T}_e\left(r\right)+\hat{V}_{\text{int}}\left(r\right)\right|\psi_{\min}^{n_0}\right\rangle \tag{1.55}$$

Hence finally we can write the ground state energy

$$E_0 = \int \hat{V}_{ext}(r,R_0)\,n(r)\,dr + \left\langle \psi_0 \middle| \hat{T}_e(r) + \hat{V}_{\text{int}}(r) \middle| \psi_0 \right\rangle$$

$$= \int \hat{V}_{ext}(r,R_0)\,n(r)\,dr + \left\langle \psi^{n_0}_{\min} \middle| \hat{T}_e(r) + \hat{V}_{\text{int}}(r) \middle| \psi^{n_0}_{\min} \right\rangle$$

$$= \int \hat{V}_{ext}(r,R_0)\,n(r)\,dr + F[n] \tag{1.56}$$

And this proves the second theorem of Hohenberg-Kohn. Hence all the ground state properties can be derived by knowing the functionals of the ground state density. This also proves that the density n(r) is a basic variable, rather than the electronic wave function Ψ(r). However the Hohenberg-Kohn theorem did not tell us about the form of functional in Eq. (1.47). If we can construct a satisfying approximation to the true functional F[n], for Eq. (1.48), we can then perform a minimization of this equation, and can accordingly obtain approximations to both the true ground state energy E_0 and the true ground state density $n_0(r)$.

1.5.2 Kohn–Sham Approach

Another breakthrough in the field of DFT is led by the famous theorem of Kohn-Sham. The philosophy of the Kohn–Sham (KS) approach is to map the many–body system to a one body system that will have the same solution, but be easier to solve.

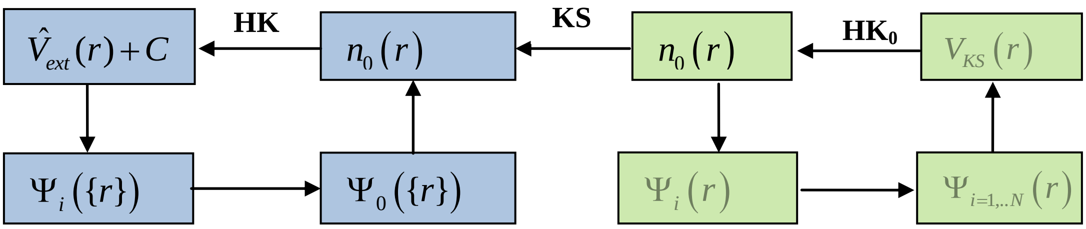

FIG 1.4 *Visualizing the KS ansatz that bridges the true multi–particle wave function system on the left with the auxiliary system on the right based on single–particle wave functions.*

The KS ansatz is the assumption that the ground state density of the fully interacting multi–body system is equal to that of some other fictitious system where the electrons do not interact. This reduces the complexity of treating a system of N mutually interacting electrons to that of treating N individual non–interacting electrons. Since the electrons in the mapped system do not interact hence we can solve this as a single electron problem in an effective field. The KS ansatz is based on the following two assumptions:

KS Ansatz 1. The precise ground state density of a system can be represented by the ground state density of an auxiliary system whose electrons do not interact. This first assumption is visualized in Fig. 1.4 which connects the ground state density $n_0(r)$ found for a non–interacting system with the true ground state density of a fully interacting many–body system.

KS Ansatz 2. The auxiliary hamiltonian is formed such that it contains the regular kinetic energy operator $\widehat{T} = -\frac{1}{2}\nabla^2$, but the potential is replaced by an effective potential $\widehat{V}_{eff}$.

An extremely useful simplification that can be made in the second assumption is that of using an effective potential $\widehat{V}_{eff}$ that is local. That is to say, an electron at point r will only 'feel' its local neighborhood. To see how the single–electron KS approach ties in that of many–electron HK theory, we start with the KS energy functional. The energy functional from the KS approach is

$$E_{KS}[n] = \hat{T}_0[n] + \int n(r)\left[V_{ext}(r) + \frac{1}{2}V_{Hartree}(r)\right]dr + E_{xc}[n] \tag{1.57}$$

where $\hat{T}_0$ is the kinetic energy of a system with density n and lacking electron–electron interactions. The term $\hat{V}_{Hartree}$ is the classical Coulomb potential for electrons, also known as the Hartree potential. Finally, E_{XC} is the so–called exchange–correlation energy. The first term and integral can be calculated exactly, while the last term, the exchange–correlation functional, incorporates both the exchange and correlation energies, as well as the 'remainder' of electron kinetic energy and anything else that might be lacking in order for the energy functional E_{KS} to be the true energy functional E from Eq. (1.48). It is only this term for which we need to construct a satisfying, approximate functional, since the form of the true functional is not known.

The major problem with DFT is that the exact exchange and correlation functional are not known except for the free electron gas. However, great progress has been made with remarkably simple approximations. One of the simplest exchange–correlation functional applied in DFT is the local–density approximation (LDA) functional, first used and developed by Kohn and Sham[27]. This functional approximates the exchange–correlation energy of a point in a system to being the same as that of a point in a homogenous electron gas of the same density. It turns out that the kinetic energy term $\hat{T}_0$ for the non–interacting electrons can account for a large part of the full kinetic energy term $\hat{T}_e$ for the many–body interacting system[28]. Thus only a relatively small part of the energy contributed to the functional E_{KS} comes from E_{XC}, and thus our calculated ground state properties become relatively well approximated despite a rough estimate of the exchange–correlation energy. If we apply the variational principle[28] to Eq. (1.57), we get

$$\frac{\delta E_{KS}[n]}{\delta n(r)} = \frac{\delta \hat{T}_0}{\delta n(r)} + \hat{V}_{ext}(r) + \hat{V}_{Hartree}(r) + \frac{\delta E_{xc}[n]}{\delta n(r)} = \mu \tag{1.58}$$

where μ is the Lagrange multiplier associated with the constraint of keeping the number of electrons in the system constant. We can now compare this with a similar equation, but where we neglect electron–electron interactions, getting

$$\frac{\delta E_{KS}[n]}{\delta n(r)} = \frac{\delta \hat{T}_0}{\delta n(r)} + \hat{V}_{eff}(r) = \mu \tag{1.59}$$

where we have $\hat{V}_{eff}(r)$ as an effective potential that not only incorporates the nuclei and external effects, but also the so–called effective potential of the other electrons, although no explicit interaction is given. The equations Eq. (1.58) and Eq. (1.59) are identical, provided

$$\hat{V}_{eff}(r) = \hat{V}_{ext}(r) + \hat{V}_{Hartree}(r) + \frac{\delta E_{xc}[n]}{\delta n(r)} \tag{1.60}$$

whose solution we can find by solving a set of single–particle Schrodinger equations for noninteracting particles for each electron in the system

$$\left[\hat{T} + \hat{V}_{eff}(r)\right]\psi_i(r) = \varepsilon_i \psi_i(r) \quad ,i = 1,2,3,....N \tag{1.61}$$

with the density being constructed up from each electron's fictitious wave function $\psi_i(r)$ and given as

$$n(r) = \sum_{i=1}^{N} \left|\psi_i(r)\right|^2 \tag{1.62}$$

Thus we can present an overview of the KS single–particle equations, for which we solve for the ground state density $n_0(r)$, in Eqs. (1.63)–(1.65).

$$V_{eff}(r) = \hat{V}_{ext}(r) + \hat{V}_{Hartree}(r) + \hat{V}_{XC}(r) \qquad (1.63)$$

$$\hat{H}_{KS}(r) = \hat{T}(r) + V_{eff}(r) \qquad (1.64)$$

$$\hat{H}_{KS}(r)\psi_i(r) = \varepsilon_i \psi_i(r) \qquad (1.65)$$

One unanswered issue is that the effective potential from Eq. (1.63) depends on the average location of the electrons in the system, and this is not known a priori. As we will see in the following section, determining this is done via a self–consistent approach, using an initial guess of the density n(r).

In order to treat the problem of dealing with the Schrödinger equation and its associated wavefunction on a computer, the wavefunction itself is expanded into components of a basis set $\{\varphi_n\}$ comprised of a total of n basis functions.

$$\Psi(r) = \sum_{j=1}^{n} c_j \varphi_j(r) \qquad (1.66)$$

The original wavefunction can then described as a column vector of coefficients with respect to the set of n basis functions like this:

$$\Psi(r) \equiv c = \{c_1, c_2, c_3, c_4, c_5, \ldots . c_5\}^T \qquad (1.67)$$

where the superscript (T) denotes transposition.

In principle, for an arbitrary wave function $\Psi(r)$ to be able to be described exactly by a basis set expansion, a complete set of basis functions $\{\varphi_\infty\}$ would be needed, and thus an infinite number of coefficients c_i would describe $\Psi(r)$. Since this is not practical for implementation, a finite basis set is utilized, and the wave function would be described exactly only in terms of the subspace that the finite basis set would define. If we look at how this affects the Schrödinger equation, either in Eq. (1.39) or Eq. (1.65), we substitute Eq. (1.66) into either one and obtain

$$\sum_{j=1}^{n} c_j \hat{H} \varphi_j(r) = \varepsilon \sum_{j=1}^{n} c_j \varphi_j(r) \tag{1.68}$$

We multiply both sides by $\varphi_i^*(r)$ where the superscript (*) denotes complex conjugation, getting

$$\sum_{j=1}^{n} \varphi_i^*(r) c_j \hat{H} \varphi_j(r) = \varepsilon \sum_{j=1}^{n} \varphi_i^*(r) c_j \varphi_j(r) \tag{1.69}$$

We then integrate both sides over r to get

$$\int \sum_{j=1}^{n} \varphi_i^*(r) c_j \hat{H} \varphi_j(r) dr = \int \varepsilon \sum_{j=1}^{n} \varphi_i^*(r) c_j \varphi_j(r) dr \tag{1.70}$$

$$\sum_{j=1}^{n} \int \varphi_i^*(r) c_j \hat{H} \varphi_j(r) dr = \varepsilon \sum_{j=1}^{n} c_j \int \varphi_i^*(r) \varphi_j(r) dr \tag{1.71}$$

which we rewrite as

$$\sum_{j=1}^{n} H_{ij} c_j = \varepsilon \sum_{j=1}^{n} S_{ij} c_j \tag{1.72}$$

where the Hamiltonian matrix H's elements are

$$H_{ij} = \int \varphi_i^*(r) c_j \hat{H} \varphi_j(r)\, dr \tag{1.73}$$

and the overlap matrix S's elements

$$S_{ij} = \int \varphi_i^*(r) \varphi_j(r)\, dr \tag{1.74}$$

The main result is that Eq. (1.73) shows us that we have transformed our operator–based Schrödinger equation to the following matrix–based generalized eigenvalue problem:

$$Hc = \varepsilon Sc \tag{1.75}$$

From Eq. (1.74), we can see that if the chosen basis set $\{\varphi\}$ is orthogonal, the overlap matrix S reduces to the identity matrix I, and Eq. (1.75) reduces to the regular eigenvalue problem $Hc = \varepsilon c$. In figure 1.5 the flow chart of DFT calculation scheme is shown.

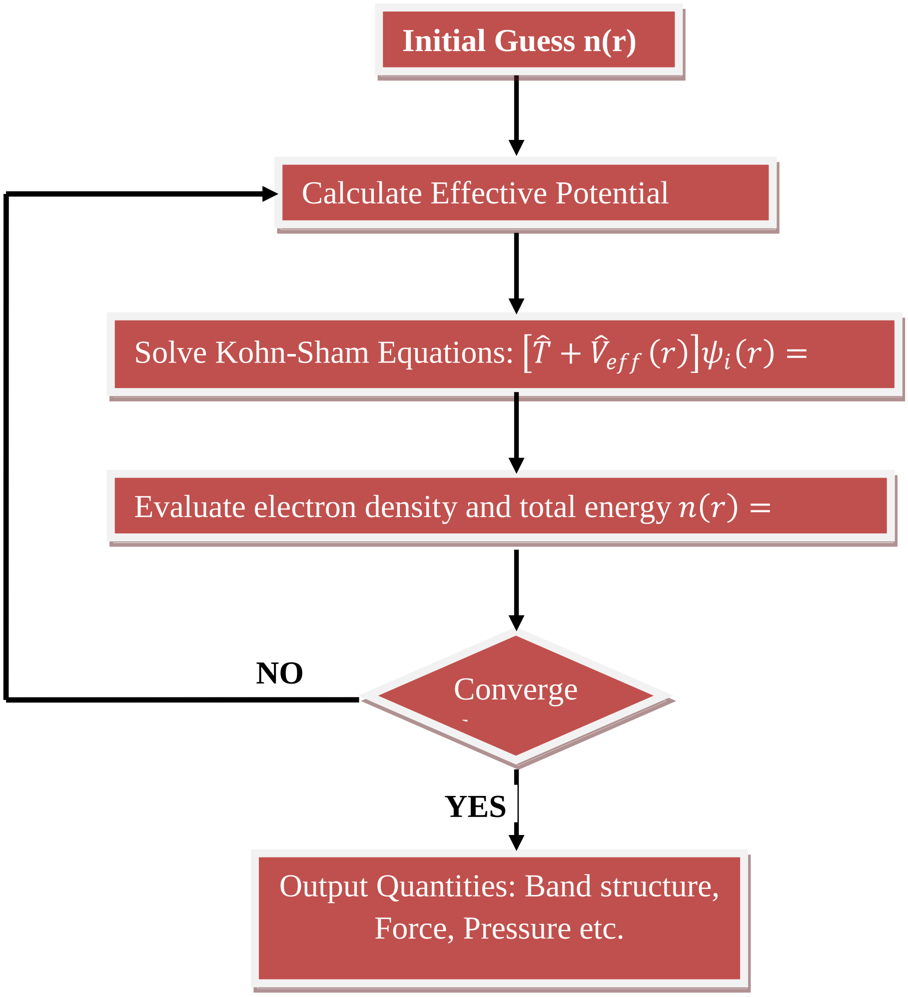

FIG 1.5 *Flow chart of DFT calculation scheme.*

1.6 Pseudopotential

In planewave basis set DFT calculations, the main problem arises when dealing with rapidly fluctuating electron densities in the vicinity of atomic cores. One needs a very large number of plane waves in order to describe such fluctuations properly. The only possibility to save a purely planewave basis set is to discard core states. The exclusion of the core states from the direct consideration means that one has to deal in the following not with the effect of bare nuclei potentials, but rather with the potentials screened by the core electrons. This potential is more smooth and shallow than the true one. This simplification gives rise to a family of pseudopotential methods in contrast to the all-electron methods (i.e., those where all electrons, valence and core electrons, are treated in the same way). Historically, the pseudopotential approach is related to the orthogonalized plane wave method (OPW), in which the basis set consists of plane waves, orthogonalized to lower - lying core states .The most straightforward way of screening the true potential with a fixed core density is not practically used. The Coulomb field of a not fully compensated bare charge remains singular at the nuclei. Moreover, a true valence wavefunction must have nodes in the intra-atomic region for ensuring its orthogonality to the core states. The description of these nodes by plane waves needs high cutoffs. In reality, one works with smooth node-free pseudofunctions generated in a shallow pseudopotential. The construction of a pseudopotential typically starts with the choice of an appropriate reference configuration (e.g., Fe3*d*74*s*1) and pseudopotential radii *rc*, which can be different for different *l*-channels. As a rule, the following conditions are imposed:

- The pseudofunction must have no nodes (in order to avoid wiggles that would demand for higher cutoff).
- The pseudofunction matches the all-electron one beyond the cutoff radius.
- Norm conservation, meaning that the charge contained within the pseudopotential radius is the same for the pseudofunction and the all-electron one. Otherwise, deviations from this rule give rise to ultrasoft pseudopotentials.
- The eigenvalues corresponding to pseudofunctions must be equal to those of the all-electron solution at least for the reference configuration.

Now-a-days, pseudopotentials being in use are usually of *ab-initio* nature. They are generated (with the use of certain approximations and criteria) from the true (all-electron) solutions for free atoms or ions. As it was mentioned above, there can be some deviations from the rule of norm conservation for pseudopotentials. Namely, Vanderbilt (Vanderbilt, 1990) suggested to abandon the norm-conservation condition, that would allow to make the pseudolization radius *rc* essentially larger (see Fig. 1.6), limited only by the condition that the spheres of this radius centered on different atoms must not overlap in a simulation. A big advantage would be that pseudopotentials generated with larger *rc* are much softer and hence a much lower planewave cutoff is needed.

The ultrasoft pseudopotentials can be characterized by some important features:

- The cutoff radius *R*, beyond which all all-electron and pseudo-properties (wavefunctions, potential) coincide, is only limited by next-neighbor distance.
- The necessary plane wave cutoff for the plane wave basis is drastically reduced.
- The amount of computational work (in the generation of pseudopotential) is increased. But most of these additional efforts need not to be repeated in the course of iterations.
- If the local potential in the sphere varies in the course of iterations, it can be considered as part of pseudopotential, so the pseudopotential develops itself as the calculation proceeds (similar to all-electron methods).
- The main area of application of ultrasoft pseudopotentials is for large systems, where the relative cost of the pseudopotential generation is relatively low, as compared to solving the electronic structure problem. For the latter, a low planewave cutoff is a major advantage.

1.6.1 Projector-Augmented Wave Method

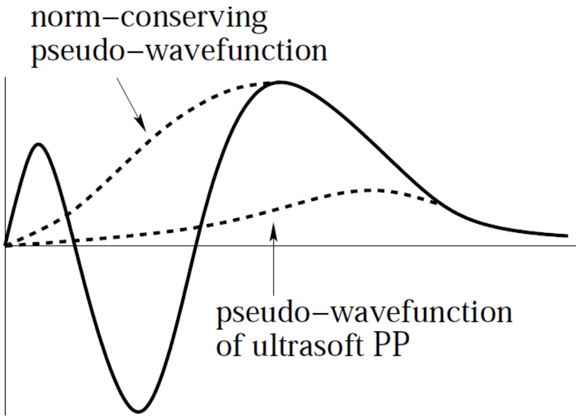

FIG 1.6 *Schematic representation of the pseudo-wavefunction of an ultrasoft pseudopotential compared to the pseudo-wavefunction of a norm-conserving pseudopotential.*

The Projector-Augmented wave method (PAW) has been developed by Peter Blochl in 1994 [29]. The new method was needed to enhance the accuracy and computational effciency of the plane wave pseudopotential approach and to provide the correct wave functions, rather than the ficticious wave functions provided by the pseudopotential approach. The PAW method describes the wave functions by a superposition of different terms: There is a plane wave part, the pseudo wave function, and expansions into atomic and pseudo-atomic orbitals at each atom. On one hand, the plane wave part has the flexibility to describe the bonding and tail region of the wave function, but fails to describe correctly all the oscillations of the wave function near the nuclei. On the other hand, the expansions into atomic orbitals are well suited to describe the nodal structure of the wave function near the nuclei, but the local orbitals lack flexibility to describe the bonding and tail regions. The PAW method combines the virtues of both numerical representations in one well-defined basis set. In order to avoid solving two electronic structure calculations, i.e., one with plane waves and one using atomic orbitals, the PAW method does not determine the coefficients of the atomic orbitals variationally. Instead, they are unique functions of the plane wave coefficients. The PAW method is in principle able to recover rigorously the density functional total energy, if plane wave and atomic orbital expansions are complete. This provides a systematic way to improve the basis set errors.

1.6.2 Local Density Approximation (LDA) and Generalized Gradient Approximation (GGA)

Two famous approximations used in density functional theory to account the exchange correlation effect of many body system to effective one body problem of Kohn-Sham approach are known as the local density approximation (LDA) already discussed in sec 1.3.7.2 and gradient density approximation (GGA). In local density approximation the exchange correlation is a functional of local density ρ only. This is known as simplest exchange correlation functional. It was used for a generation in material science, but is not accurate enough for many chemical proposes. Typical calculated discrepancy observed using LDA approximations are overestimated binding energy, underestimated lattice parameters, incorrect phase stability order etc. To address this issue the gradient of the electron density is also considered as a functional variable of exchange correlation. This is known as generalized gradient approximation (GGA). GGA greatly reduce bond dissociation energy error and generally improve transition state barrier. Typically but not always this is more accurate than LDA. But, unlike LDA, there is no single universal form. GGA requires knowledge of two variable densities and gradient of density. LDA works well with nice covalent systems and simple metal. However GGA give good result for molecules, H-bonded materials, and highly varying densities.

1.7 Software's

1.7.1 Quantum ESPRESSO

Quantum ESPRESSO[30] is an integrated suite of Open-Source computer codes for electronic-structure calculations and materials modeling at the nanoscale. It is based on density-functional theory, plane waves, and pseudopotentials. It can calculate the phonon in a crystalline material using density functional perturbation method (DFPT)[31] or supercell approach. The author has used this software to calculate the phonon dispersion relation of Li_2O using DFPT methods.

1.7.2 Vienna Ab-initio Simulation Package (VASP)

The Vienna Ab initio Simulation Package (VASP) [32, 33] is a computer program for atomic scale materials modeling, e.g. electronic structure calculations and quantum-mechanical molecular dynamics, from first principles. The total energy of the system and Hellman Feynman forces is computed by solving the Kohn-Sham equations. In VASP, central quantities, like the one-electron orbitals, the electronic charge density, and the local potential are expressed in plane wave basis sets. The interactions between the electrons and ions are described using norm-conserving or ultrasoft pseudopotentials, or the projector-augmented-wave method.

We have used the software to compute the total energy, pressure, Born dynamical charges, charge density and Hellman Feynman forces for ZrW_2O_8, M_2O, MCN (M=Ag, Au and Cu), $GaFeO_3$, $YMnO_3$, $AFeO_2$ (A=Ca and Sr), $NaNbO_3$, $RMnO_3$ (R=Ca and Pr) and $LiMPO_4$ (M=Fe and Mn).

1.7.3 PHONON 5.10

PHONON-5.10 is a software developed by K. Parlinski [34] for calculating phonon dispersion curves, and phonon density spectra of crystals from a set of Hellmann-Feynman forces calculated within an *ab-initio* program. One can use VASP, Wien2k or any other software package to compute the Hellmann-Feynman forces. Phonon builds a crystal structure, using one of the 230 crystallographic space groups, finds the force constant from the Hellmann-Feynman forces, builds the dynamical matrix, diagonalizes it, and calculates the phonon dispersion relations. It also calculates the polarization vectors, and the irreducible representations (Gamma point) of phonon modes, and calculates the total and partial phonon density of states. For polar crystals the LO/TO mode splitting can be included. This software has been used to compute the phonon dispersion relation and density of states calculation for ZrW_2O_8, M_2O, MCN (M=Ag, Au and Cu), $GaFeO_3$, $YMnO_3$, $AFeO_2$ (A=Ca and Sr), $NaNbO_3$, $RMnO_3$ (R=Ca and Pr) and $LiMPO_4$ (M=Fe and Mn).

1.8 Conclusions

This thesis is focused to understand the role of phonons in the functional properties of materials. We have given the details of the formalism to determine the frequency and wavevector of the phonon modes. The method consists of taking a Taylor expansion of the crystal potential in terms of atomic displacements, using Newton's second law and the translational invariance of the crystal, and solving the resulting equations. The neutron inelastic techniques have been used to measure the inelastic spectra of all the compounds. Besides these we have also discussed other experimental techniques with their merits and demerits.

[1] P. Silvia and E. Claude, Journal of Physics: Condensed Matter **21**, 303201 (2009).

[2] G. Catalan and J. F. Scott, Advanced Materials **21**, 2463 (2009).

[3] C.-W. Nan, M. I. Bichurin, S. Dong, D. Viehland and G. Srinivasan, Journal of Applied Physics **103**, 031101 (2008).

[4] V. V. Pavlov, A. R. Akbashev, A. M. Kalashnikova, V. A. Rusakov, A. R. Kaul, M. Bayer and R. V. Pisarev, Journal of Applied Physics **111**, 056105 (2012).

[5] W. Eerenstein, N. D. Mathur and J. F. Scott, Nature **442**, 759 (2006).

[6] J. H. Lee, L. Fang, E. Vlahos, X. Ke, Y. W. Jung, L. F. Kourkoutis, J.-W. Kim, P. J. Ryan, T. Heeg, M. Roeckerath, V. Goian, M. Bernhagen, R. Uecker, P. C. Hammel, K. M. Rabe, S. Kamba, J. Schubert, J. W. Freeland, D. A. Muller, C. J. Fennie, P. Schiffer, V. Gopalan, E. Johnston-Halperin and D. G. Schlom, Nature **466**, 954 (2010).

[7] T. Kimura, T. Goto, H. Shintani, K. Ishizaka, T. Arima and Y. Tokura, Nature **426**, 55 (2003).

[8] B. B. Van Aken, T. T. M. Palstra, A. Filippetti and N. A. Spaldin, Nat Mater **3**, 164 (2004).

[9] R. Ramesh and N. A. Spaldin, Nat Mater **6**, 21 (2007).

[10] N. Hur, S. Park, P. A. Sharma, J. S. Ahn, S. Guha and S. W. Cheong, Nature **429**, 392 (2004).

[11] N. Ikeda, H. Ohsumi, K. Ohwada, K. Ishii, T. Inami, K. Kakurai, Y. Murakami, K. Yoshii, S. Mori, Y. Horibe and H. Kito, Nature **436**, 1136 (2005).

[12] D. V. Efremov, J. van den Brink and D. I. Khomskii, Nat Mater **3**, 853 (2004).

[13] M. Zbiri, H. Schober, N. Choudhury, R. Mittal, S. L. Chaplot, S. J. Patwe, S. N. Achary and A. K. Tyagi, Applied Physics Letters **100**, 142901 (2012).

[14] T. Kimura, S. Kawamoto, I. Yamada, M. Azuma, M. Takano and Y. Tokura, Physical Review B **67**, 180401 (2003).

[15] D. Khomskii, Physics **2**, (2009).

[16] J. M. Carpenter and D. L. Price, Physical Review Letters **54**, 441 (1985).

[17] D. L. Price and K. Skold, Neutron scattering. (Academic Press, Orlando, 1986).

[18] P. Bruesch, Phonons: Theory and experiments II. (Springer Berlin Heidelberg, New York, 1986).

[19] S. L. Chaplot, N. Choudhury, S. Ghose, M. N. Rao, R. Mittal and P. Goel, European Journal of Mineralogy **14**, 291 (2002).

[20] E. Burkel and H. Sinn, Journal of Physics: Condensed Matter **6**, A225 (1994).

[21] D. Gardiner, Practical Raman Spectroscopy, (Springer Berlin Heidelberg, 1989), pp. 1.

[22] B. H. Stuart, Infrared Spectroscopy: Fundamentals and Applications, (John Wiley & Sons, Ltd, 2005), pp. 1.

[23] B. H. Stuart, Infrared Spectroscopy: Fundamentals and Applications, (John Wiley & Sons, Ltd, 2005), pp. 15.

[24] L. Brillouin, Ann. Phys **17**, (1922).

[25] E. Gross, Nature **129**, (1932).

[26] R. P. Feynman, Physical Review **56**, 340 (1939).

[27] W. Kohn and L. J. Sham, Physical Review **140**, A1133 (1965).

[28] R. O. Jones and O. Gunnarsson, Reviews of Modern Physics **61**, 689 (1989).

[29] P. E. Blöchl, Physical Review B **50**, 17953 (1994).

[30] G. Paolo, B. Stefano, B. Nicola, C. Matteo, C. Roberto, C. Carlo, C. Davide, L. C. Guido, C. Matteo, D. Ismaila, C. Andrea Dal, G. Stefano de, F. Stefano, F. Guido, G. Ralph, G. Uwe, G. Christos, K. Anton, L. Michele, M.-S. Layla, M. Nicola, M. Francesco, M. Riccardo, P. Stefano, P. Alfredo, P. Lorenzo, S. Carlo, S. Sandro, S. Gabriele, P. S. Ari, S. Alexander, U. Paolo and M. W. Renata, Journal of Physics: Condensed Matter **21**, 395502 (2009).

[31] S. Baroni, S. de Gironcoli, A. Dal Corso and P. Giannozzi, Reviews of Modern Physics **73**, 515 (2001).

[32] G. Kresse and J. Furthmüller, Computational Materials Science **6**, 15 (1996).

[33] G. Kresse and D. Joubert, Physical Review B **59**, 1758 (1999).

[34] K. Parlinksi,PHONON5.11, Software, (2003).

Chapter 2

Nature of Bonding and Negative Thermal Expansion Behavior in M_2O and MCN (M=Ag, Au, Cu) Compounds

2.1 Introduction

The phenomenon of large negative thermal expansion (NTE) in ZrW_2O_8 over a wide range of temperatures has lead to extensive research [1-17] in this area since last two decades. In fact, the phenomenon was observed long back in water. The polyhedral framework compounds with large open structure are mostly found to exhibit this phenomenon e.g ZrV_2O_7, TaV_2O_5, $Sc_2(MoO_4)_3$, HfV_2O_7 etc. The discovery of colossal thermal expansion behavior in metal cyanides compounds [15, 18, 19] has further accelerated the research in this field. The discovery of NTE has lead to industrial applications of these compounds in various areas like fiber optics, coatings, electronics and mirror substrates to tooth fillings etc.

Most of the compounds exhibiting negative thermal expansion behavior consist of rigid polyhedral units around metal ions. The polyhedral units are mutually connected via terminal oxygen's. The terminal oxygen plays an important role in governing the thermal expansion behavior in such compounds. ZrW_2O_8 is very popular compound in this category. It shows isotropic negative thermal expansion behavior from 0.3 K to 1050 K. Its structure remains cubic up to 1050 K, however there is an order-disorder transition around 450 K. The low energy transverse phonon modes in the compound are found to be very anharmonic in nature, which led to transverse displacement of oxygen and causes NTE in ZrW_2O_8[20-23]. The other frame work compounds such as ZrV_2O_7, HfV_2O_7 also show similar behavior although there structures are different than that of ZrW_2O_8. A number of experimental and theoretical studies have been performed on such compounds. These studies suggest that the transverse vibration of oxygen and distortions of polyhedron units are mainly responsible for negative thermal expansion.

In the case of M_2O (M=Ag, Cu and Au)[24-26] compounds, the metal ion M acts as terminal atom to connect M_4O polyhedral and plays important role in NTE behavior. The difference in the thermal expansion behaviour in these compounds mainly arises due to the difference in nature of bonding. The phonon calculations show that NTE in oxygen mediated compound is mainly supported by the structure *i.e.* open structure. However in compounds where metal atoms play the role of terminal entity, the nature of bonding between metal atom and oxygen is also found to be important in governing the thermal expansion behavior.

Recently metal cyanides have gained attention. $Zn(CN)_2$ was the first compound in this category[27]. The structure consists of tetrahedral framework of Zn connected with four cyanide units. The tetrahedral units are connected through CN, which provide the flexibility to bend the tetrahedra and results in NTE behaviour. The isostructural cyanide $Cd(CN)_2$ also exhibit NTE behavior. The magnitude of negative thermal expansion coefficient is found to be larger[17] in comparison to $Zn(CN)_2$. NTE has been explained in terms of rotations, translations and deformations of $M(C/N)_4$ coordinated tetrahedra[28, 29]. The compounds consist of polyhedra units connected via C≡N, and are known to provide more flexibility in comparison to those where polyhedrals are connected via oxygens. It seems the structure consisting of -C≡N- units provide much flexibility for the bending motion, which is found to be one of the major causes of NTE behavior in cyanides. In this chapter, results obtained on compounds M_2O and MCN (M=Ag, Au, Cu) are given in sections 2.2 and 2.3 respectively.

2.2 M_2O (M=Au, Ag, Cu) Compounds

The compounds M_2O (M=Ag, Cu and Au) [25, 26] crystallize in a simple cubic lattice (space group Pn-3m). The M atoms are linearly coordinated by two oxygen atoms, while oxygen is tetrahedrally coordinated by M atoms. Ag_2O shows a large isotropic negative thermal expansion (NTE) over its entire temperature range of stability, i.e. up to ~ 500 K, while Cu_2O only shows a small NTE below room temperature. At the moment, no experimental data are found in the literature for Au_2O, but we anticipate that our simulations on this isostructural system will generate effort in this direction. Extensive experimental data including specific heat measurements[30, 31], Raman and IR detection of long-wavelength optically active phonons[32, 33] together with neutron derived phonon dispersion relations and phonon density of states[34, 35] have been reported for Cu_2O while the calculations of the volume thermal expansion in Ag_2O and Cu_2O have also been published[35, 36]. EXAFS measurements on Ag_2O and Cu_2O[37-40] indicate that the mechanism at the origin of their NTE involves deformations of the M_4O tetrahedral units (M = Ag, Cu), rather than simple rigid units vibrations. Also it has been suggested[40] that the large difference between the NTE coefficient of Ag_2O and Cu_2O not only originates from a mass effect but also from differences from the chemical interaction

Here we present the neutron measurements of the phonon density of states of Ag_2O and Cu_2O, and ab-initio calculations of all three metal oxides. Much insight into the physics at play in the NTE properties of these systems can be derived from a systematic study of the series Cu, Ag, Au. This implies using the same simulation technique and the same experimental apparatus. We find that Ag_2O and Cu_2O have a NTE while we find that Au_2O

has a large positive expansion with increasing temperature. In the next sections, we discuss the origins for these large differences in the amplitude and sign of the thermal expansion coefficients between these isostructural compounds. Using the density functional perturbation approach we calculate the Born effective charge dielectric constant and other properties. We find that Au_2O has a less ionic character than Ag_2O and Cu_2O and discuss the consequences of tighter Au-O bonds on the lattice expansion and anharmonicity of the crystal.

Polycrystalline samples of Cu_2O and Ag_2O (99.9% purity purchased from Sigma Aldrich) were wrapped inside a thin Aluminum foil and fixed at the end of an orange cryostat stick for the measurements. The measurements were done in the neutron-energy-gain mode using the incident neutron energy of 14.2 meV (2.4 Å) at 320 K.

The calculation of phonon is performed using supercell method implemented in PHONON 5.10 software[41]. The Hellman-Feynman forces were calculated by the finite displacement method (displacement 0.04 Å) using a 2×2×2 super cell. Total energies and Hellman-Feynman forces calculations were performed using Vienna ab-initio simulation package (VASP)[42, 43]. The plane wave pseudo-potential with plane wave kinetic energy cutoff of 880 eV, 1000 eV and 1200 eV for Ag_2O, Cu_2O and Au_2O respectively was used. The integrations over the Brillouin zone were sampled on a 8×8×8 grid of k-points generated by the Monkhorst-pack method[44] for all three compounds. The calculated unit cell parameters for Ag_2O and Cu_2O are in agreement with the experimental data[25] (see TABLE 2.1), while the calculated lattice parameter for Au_2O is in agreement with previous calculations[45, 46].

2.2.1 Results and Discussion

2.2.1.1 Phonon Spectra

As expected for isostructural compounds, the dispersion curves below 10 meV in Ag_2O and Au_2O are found to be similar, while in Cu_2O these modes are shifted to higher energies, which can be understood considering the smaller mass of Cu Fig 2.1. In general, we find a very good agreement between both our calculations for Cu_2O and those of Bohnen et al.[35], together with their experimental dispersion curves reported in their paper, and with the measured phonon spectra measured (Fig. 2.2) in this study for Cu_2O and Ag_2O[47]. The latter observations validate our approach using ab-initio calculations, and give us confidence into the properties we derive from them, especially those extended to Au_2O.

The computed partial densities of states are shown in Fig. 2.3. These are obtained by atomic projections of the one-phonon eigenvectors and reflect the contribution of the different atoms to the spectrum. The contributions due to Ag, Cu or Au are located below 20 meV, the lightest atom Cu (63.54 amu) having its contributions extending up to the larger frequency. The masses of Ag (107.87 amu) and Au (197.97 amu) being different, one would also expect a renormalization of the phonon frequencies. However the first two peaks in the density of states are at nearly the same energies i.e. 3 meV and 6 meV. This observation suggests that the chemical bonds in Ag_2O and Au_2O are of different strength. The oxygen vibrations in all the three compounds extend over the entire phonon spectral range with maximum weight for frequencies above 50 meV. The M-O stretching modes in Cu_2O, Au_2O and Ag_2O are up to 75 meV, 70 meV and 65 meV respectively.

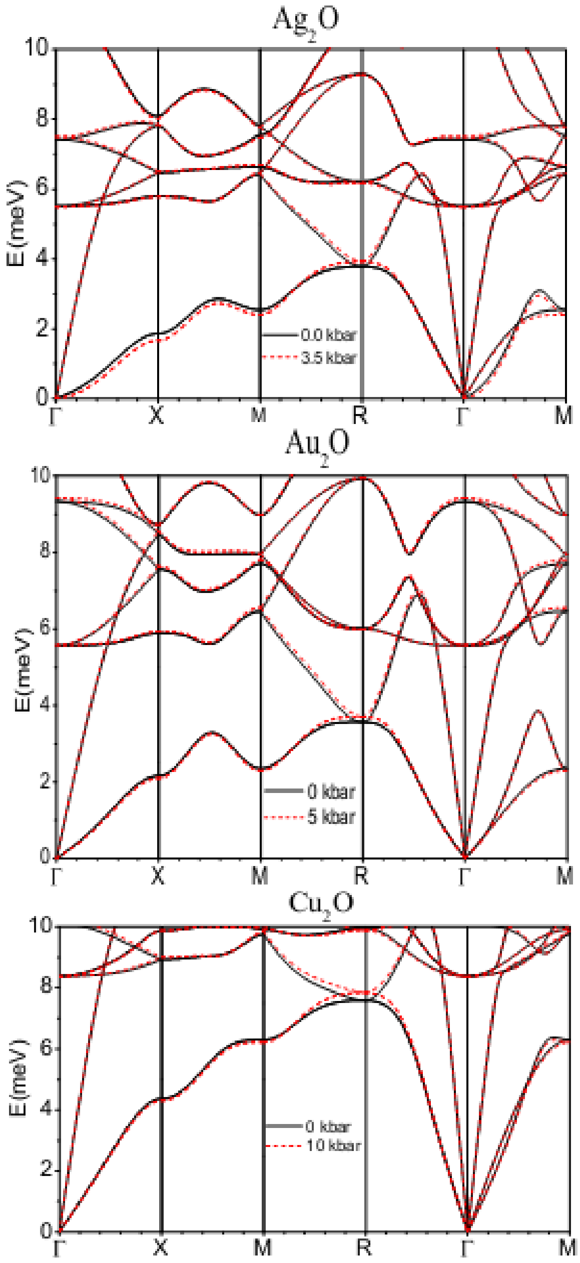

FIG 2.1 *The calculated low energy part of the phonon dispersion relation of M_2O (M=Ag, Au and Cu). The Bradley-Cracknell notation is used for the high-symmetry points along which the dispersion relations are obtained. Γ=(0,0,0); X=(1/2,0,0); M=(1/2,1/2,0) and R=(1/2,1/2,1/2).*

The different spectral range for these modes may reflect the different M-O bond lengths and difference in nature of M-O bonding. The smallest Cu-O bond (1.866 Å) results in shifting of energies up to the highest spectral range of 75 meV. However Ag-O and Au-O bond lengths 2.082 Å and 2.078 Å respectively in Ag_2O and Au_2O are similar but the stretch mode of Au is at larger frequencies. This suggests that the Au-O bond may have a more covalent nature as compared to the Ag-O bond for which an ionic nature dominates.

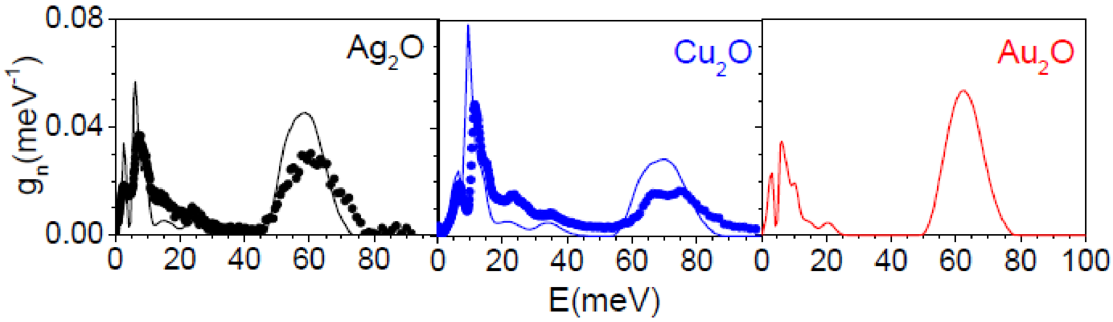

FIG 2.2 *Experimental (symbols plus line) and calculated (solid line) neutron-weighted phonon density of state of M_2O (M=Ag, Au and Cu) compounds. The calculated spectra have been convoluted with a Gaussian of FWHM of 15% of the energy transfer in order to describe the effect of energy resolution in the experiment.*

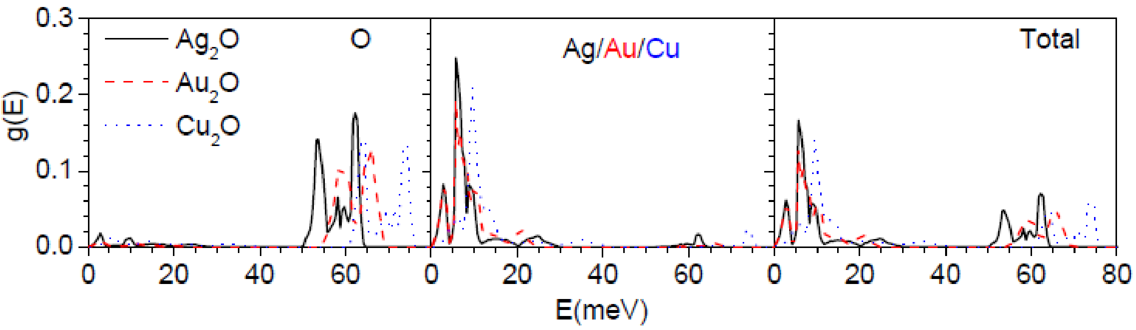

FIG 2.3 *Normalized partial density of states of various atoms and total one-phonon density of states in M_2O (M=Ag, Au and Cu) compounds.*

Finally, the lowest transverse acoustic modes in Ag_2O and Au_2O give rise to the first peak in the density of states at about 3 meV, clearly observed in the phonon spectra (see Fig. 2.2 and 2.3). The equivalent peak in the Cu_2O spectrum is observed at 6 meV.

2.2.1.2 Pressure Dependence of Phonon Modes and Thermal Expansion Behavior

In the quasi-harmonic approximation the volume thermal expansion coefficient[48] of a crystalline material, is given by the following relation: $\alpha_V = \frac{1}{BV}\sum_i \Gamma_i C_{Vi}(T)$. Here $\Gamma_i = -\frac{V}{E_i}\frac{dE_i}{dV}$ is the mode Grüneisen parameter, which is a measure of the volume/pressure dependence of the phonon frequency. $C_{Vi}(T)$ is the specific heat contribution of the i^{th} phonon mode (of energy E_i) at temperature T, while B and V stand for the volume and the bulk modulus of the compound, respectively. In the above relation, all the quantities but Γ_i are positive at all temperatures. Therefore the sign and magnitude of Γ_i govern the thermal expansion of the lattice, while the phonon energy range over which Γ_i is negative determines the temperature range over which the material will show NTE.

The calculated elastic constants and bulk modulus are given in TABLE 2.1. The experimental data [49] are only available for Cu_2O which agree very well with our calculated values. The calculated pressure dependence of the phonon dispersions (see Fig. 2.1) shows that in case of the Ag_2O and Cu_2O crystals, the lowest energy modes along Γ-X-M and Γ-M line soften with pressure in contrast to the modes along the M-R and Γ-R line. The softening is found to be negligible in Au_2O. The low energy optic modes in Ag_2O also soften in contrast to the case of Au_2O, where these modes harden on increasing the pressure. The pressure dependence of the phonon spectra have been calculated in the entire Brillouin zone to allow for the calculation of the energy dependence of the Grüneisen parameter Γ(E) (Fig. 2.4 and Fig. S2[24]) and further processed to obtain the thermal expansion coefficient $\alpha_V(T)$ (Fig. 2.5) as discussed below. For Ag_2O and Au_2O, the energy range for negative Γ(E) extends up to ~3.5 meV. However the magnitude is much larger for the former compound, reaching a value of -40 for the lowest modes, while for Au_2O the maximum negative Γ(E) reaches -10. For Cu_2O the phonons below 6.5 meV have negative Γ(E) with a maximum negative value of -4.5. The latter results are completely coherent to those obtained by Bohnen et al.[35] using the same approach. The calculated volume thermal expansion coefficient $\alpha_V(T)$ is plotted on Fig. 2.5 as a function of temperature.

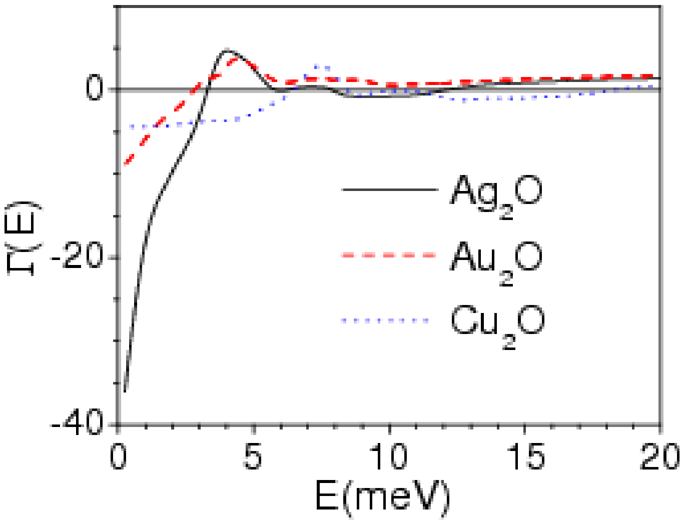

FIG 2.4 *The calculated Grüneisen Parameter of M_2O (M=Ag, Au and Cu). The calculations for Ag_2O are shown here for comparison with Au_2O and Cu_2O.*

Negative thermal expansion is calculated in Ag_2O over its temperature range of stability of about 500 K, while Cu_2O and Au_2O have negative $\alpha_V(T)$ below room temperature and below 16 K, respectively. The most negative $\alpha_V(T)$ values for Ag_2O (-44×10^{-6} K^{-1}) and Cu_2O (-8×10^{-6} K^{-1}) are respectively obtained at 40 K and 75K. The maximum negative value of $\alpha_V(T)$ for Au_2O is much reduced compared to the other two compounds and reaches ~ -2×10^{-6} K^{-1} at T ~ 8 K. As mentioned in the previous section, one understand the absence

TABLE 2.1 *Comparison of the calculated structural parameters and elastic constants of M_2O (M=Ag, Au, Cu) with the experimental data. The experimental data of lattice parameters for Ag_2O and Cu_2O is at 15 K and 293 K respectively, while the calculations are performed at 0 K. The values in the brackets give the experimental data of the lattice constants[25] and elastic constants and bulk modulus[49].*

	Calc. a (Å)	**C_{11}(GPa)**	**C_{44}(GPa)**	**C_{12}(GPa)**	**B(GPa)**
Ag_2O	4.81 (4.745)	80.0	0.6	70.8	73.8
Au_2O	4.80	101.1	2.4	94.9	97.1
Cu_2O	4.31 (4.268)	127.2 (121)	6.3 (10.9)	105.4 (105)	112.7 (112)

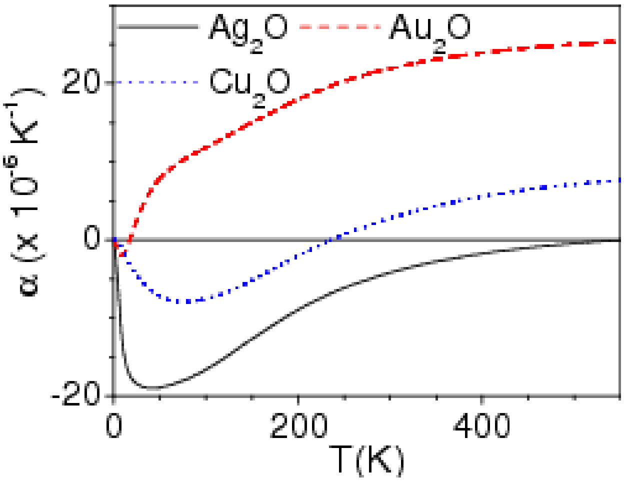

FIG 2.5 *Volume thermal expansion (α_V) coefficient as a function of temperature in M_2O (M=Ag, Au and Cu). The calculations for Ag_2O are shown here for comparison with Au_2O and Cu_2O.*

of NTE in the Au_2O lattice as resulting from the combination of two effects: 1) reduced absolute values of negative Γ(E) (compared to Ag_2O) and 2) reduced energy range for the phonon modes with negative Γ(E) (compared to Cu_2O). The comparison between the available experimental data of volume thermal expansion along with our calculations is shown in Fig 2.6. We have also calculated (Fig. 2.7) contributions of phonons as a function of energy E to the volume thermal expansion at 300 K. As shown in Fig. 2.7 the maximum negative contribution to volume thermal expansion coefficient is from the modes of energy around 4 to 5 meV. The nature of the low energy phonon modes contributing to the NTE can be visualized through animations[45, 46].

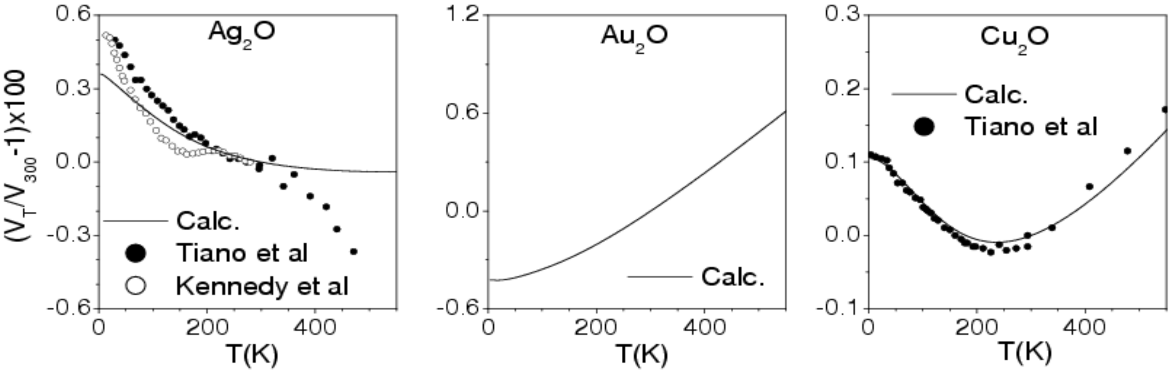

FIG 2.6 *The calculated and experimental [25, 26] volume thermal expansion of M_2O (M=Ag, Au and Cu).*

The eigenvectors of a selection of them have also been plotted on Fig. 2.8. The lowest Γ-point optical mode corresponds to the rotation of M_4O tetrahedral and the lowest X and M point modes have negative Grüneisen parameter in all the three compounds. X-point mode involves bending of M-O-M chains. The M atoms connected to various M_4O have different displacements indicating significant distortion of M_4O tetrahedra. This mode seems to contribute maximum to NTE in Ag_2O. The M-point mode involves rotation, translation as well as distortion of the M_4O tetrahedra, while for R-point the amplitude of all the atoms is similar and it indicates translational motion of M_4O as a rigid unit.

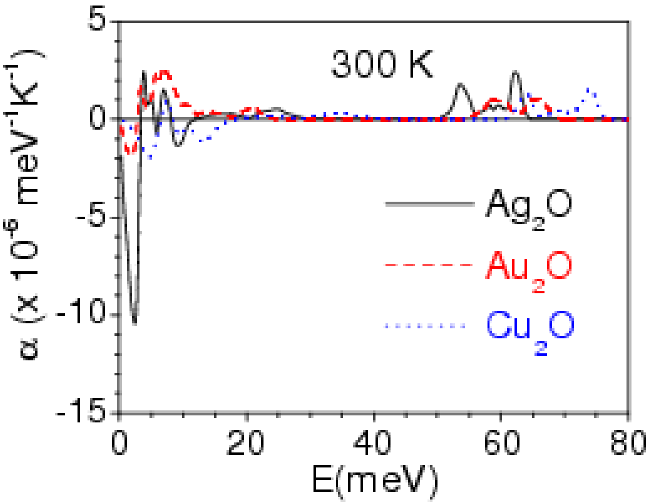

FIG 2.7 *Volume thermal expansion (α) coefficient contributed from phonons of energy E.*

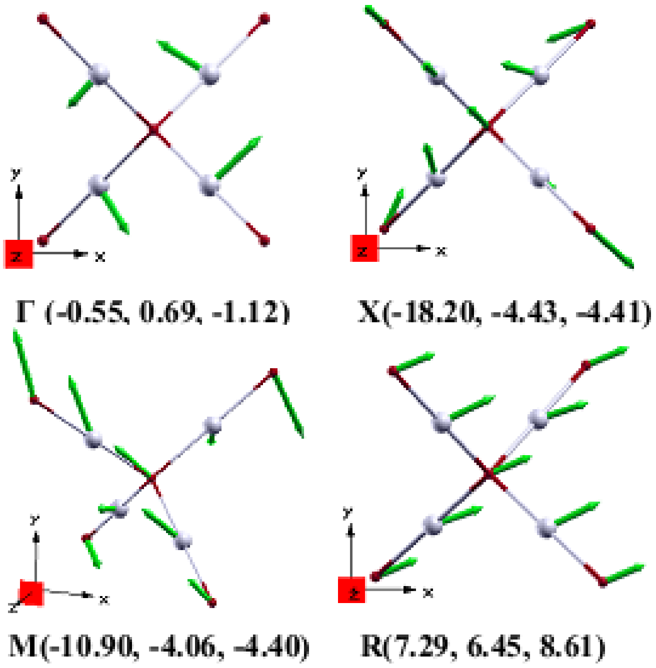

Γ (-0.55, 0.69, -1.12)

X(-18.20, -4.43, -4.41)

M(-10.90, -4.06, -4.40)

R(7.29, 6.45, 8.61)

FIG 2.8 *Polarization vectors of selected phonon modes in M_2O (M=Ag, Au and Cu). The numbers after the wave vector (Γ, X, M and R) gives the Grüneisen parameters of Ag_2O, Au_2O and Cu_2O respectively Key: M, grey spheres; O, brown spheres.*

2.2.1.3 Specific Heat and Mean Squared Thermal Amplitudes

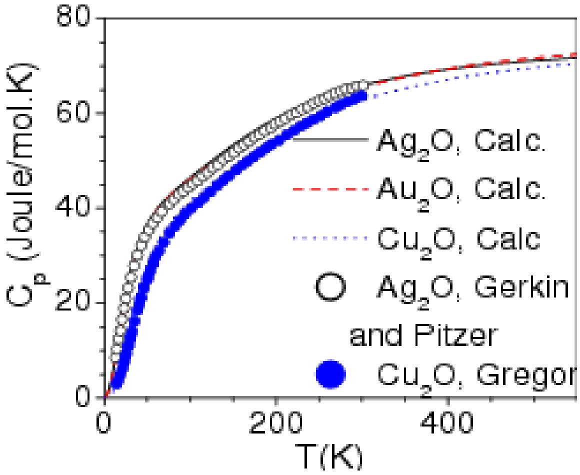

FIG 2.9 *Calculated and experimental[30, 31] specific heat as a function of temperature of M_2O (M=Ag, Au and Cu).*

We have used the calculated total and partial phonon density of states to calculate the temperature dependence of the specific heat C_p (Fig. 2.9) and the mean squared displacement $<u^2>$ of the atoms (Fig 2.10) of the three compounds. The calculated C_p agrees very well with the experimental data. In particular, the sharp rise at low temperatures is correctly reproduced, which proves again that the low-energy part of the calculated phonon spectra is reliable, at least for the Cu_2O and Ag_2O lattices. Also, the calculated specific heats of Ag_2O and Au_2O are nearly same which is consistent with the similarity of the low energy part of the phonon spectra of both the compounds (Fig. 2.3). Also, our calculations reproduce very well the lower specific heat at low temperatures of the Cu compound, which is a consequence of the general energy up shift of the singularities in the phonon spectra of Cu_2O compared to Ag_2O (and Au_2O).

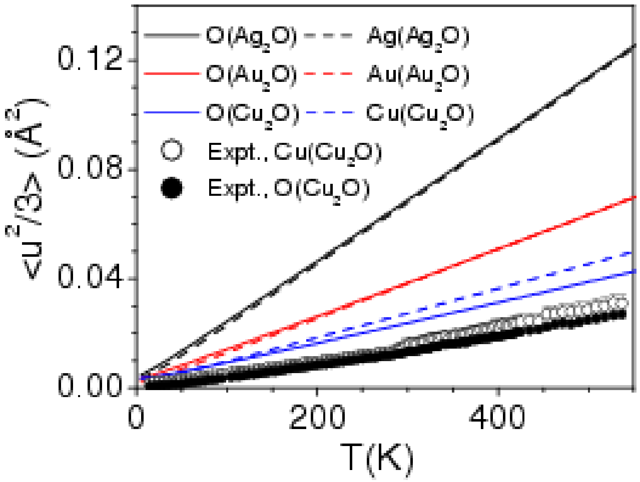

FIG 2.10 *The calculated mean square amplitudes of various atoms in M_2O (M=Ag, Au and Cu). The experimental data of Cu_2O are from Ref. [50].*

For Ag_2O, we calculate that both the Ag and O atoms have similar $<u^2>$ values at all T (see Fig. 2.10), and that these values are much larger than those calculated for the Au_2O and Cu_2O compounds for the same T. In particular, they are found to be twice those calculated for Au_2O, an effect that can easily be understood considering the mass ratio between Ag and Au for a similar density of states. We calculate that the $<u^2>$ values are the smallest for the Cu_2O compound, as resulting from its phonon spectrum renormalized to higher frequencies. For comparison the experimental data[50] of $<u^2>$ of atoms in Cu_2O are also shown, which are in qualitative agreement with our calculations, although with even smaller $<u^2>$.

2.2.1.4 Bonding in M_2O (M=Ag, Au, Cu)

It is clear that the large difference in the thermal expansion that we calculated for the three M_2O compounds reflects a difference in the bonding from one compound to the other. In addition, the presence of large voids in the unit cell renders the structure even more sensitive to subtle differences in bond strength. In order to understand the nature of the M—O bonding we have calculated the charge density for the three compounds (Fig. 2.11). We find that the bonding character of the Ag-O bond is more ionic than that of the Cu-O bond. We find that the Au-O bond is highly directional with the charge density elongated towards the O atom *i.e.* indicating a covalent nature, as suggested by previous studies[51]. The change of bonding from an ionic to a covalent character is due to different intra-atomic hybridization between the d, s and p states[45, 46]. The computed Born effective charges (see TABLE 2.2) for oxygen atoms in Ag_2O, Cu_2O and Au_2O are -1.28, -1.18 and -0.54 respectively. The latter values also reflect the larger ionic character for the Ag-O bond compared to Au-O. The compounds Ag_2O and Au_2O have an almost identical lattice parameter (Ag_2O =4.81 Å and Au_2O =4.80 Å) and similar Ag/Au-O bond lengths. However, the covalent and directional Au-O bond rigidifies the Au_4O tetrahedra, making them less susceptible to distortion, bending or rotation than their Ag_4O counterpart. This is revealing the microscopic origin of the large NTE in Ag_2O. As discussed in the previous sections, we found that Ag_2O shows a large softening of its transverse acoustic modes along the Γ-X-M line with increasing pressure while in Au_2O this softening is not observed. Also in case of Ag_2O high energy optical modes also show softening in contrast to Au_2O, where these modes become hard with pressure. Now if we compare the Cu_2O and Ag_2O cases, for which the nature of bonding is almost similar, we find that both compounds exhibit negative thermal expansion. However there is a large difference in the magnitude of the thermal expansion coefficient. The Cu-O

(1.87 Å) bond length is much smaller than the Ag-O (2.08 Å) bond. The Cu_4O tetrahedral units are therefore much more compact than Ag_4O, rendering distortion less favorable in Cu_4O as compared to Ag_4O. In addition, the difference in the open space in the unit cell between the two compounds leads to differences in the magnitude of the distortions and hence difference in the NTE coefficient. Here the open structure nature of the lattice regulates the extent of the NTE.

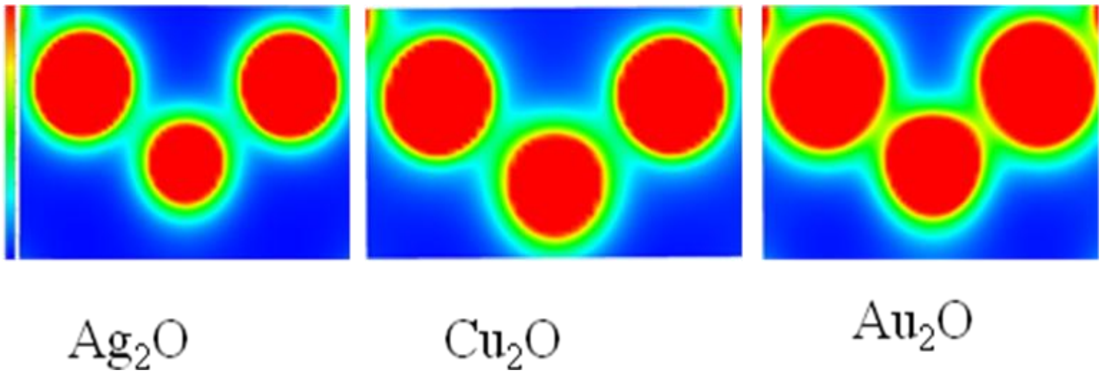

FIG 2.11 *The calculated charge density for Ag_2O, Cu_2O and Cu_2O in (011) plane.*

TABLE. 2.2 *Calculated Born effective charges (Z) in M_2O (M=Ag, Au, Cu).*

Atom	**Z_{xx}**	**Z_{xy}**	**Z_{xz}**	**Z_{yx}**	**Z_{yy}**	**Z_{yz}**	**Z_{zx}**	**Z_{zy}**	**Z_{zz}**
Ag_2O									
O	-1.28	0	0	0	-1.28	0	0	0	-1.28
Ag	0.64	0.63	0.63	0.63	0.64	0.63	0.63	0.63	0.64
Au_2O									
O	-0.54	0	0	0	-0.54	0	0	0	-0.54
Au	0.27	0.92	0.92	0.92	0.27	0.92	0.92	0.92	0.27
Cu_2O									
O	-1.18	0	0	0	-1.18	0	0	0	-1.18
Cu	0.59	0.44	0.44	0.44	0.59	0.44	0.44	0.44	0.59

2.3 MCN (M=Ag, Au and Cu) Compounds

The thermal expansion behavior in low dimension MCN (M=Cu, Ag and Au) compounds shows anisotropic thermal expansion behavior. The structure of the compounds has been determined by various groups[10, 52-57]. X-ray powder diffraction measurements have been performed[52] over a temperature range of 90-490 K. The structure of the cyanides is chain like and resembles a quasi one dimension structure. These chains consist of C≡N units connected via metal ions (M-C≡N-M). The structure seems to be simple, however the compounds shows C/N disorder along the chain in terms of random flipping of C/N sequence. The higher dimension cyanides like $Cd(CN)_2$, $Ni(CN)_2$ and $Zn(CN)_2$ are also known to show C/N disorder behavior.

CuCN crystallizes in two different structures named as low temperature and high temperature phase at ambient condition depends on the method of synthesis. The low temperature (orthorhombic, $C222_1$) and high temperature (hexagonal, R3m) phase of CuCN in the manuscript are termed by LT- CuCN and HT-CuCN, respectively. The low temperature phase is a modulated structure of the high temperature phase. The modulation in LT-CuCN[57] is observed from previous neutron diffraction study. The structure of LT-CuCN consists of long Cu-C≡N-Cu modulated chains, each containing five crystallographically distinct Cu atoms, which form a wave consisting of nine CuCN units.

At ambient condition, AgCN and HT-CuCN crystallizes in hexagonal R3m (space group no. 160) cell. However AuCN crystallizes in P6mm (space group no. 183) structure. The unit cell of AgCN and HT-CuCN consist of three formula units. However the structure of AuCN consists of single formula unit. All the three compounds have three atoms in their primitive unit cell. The crystal structures as shown in Fig. 2.12 indicates that in AuCN all chains (M-C≡N-M) are parallel along to c-axis while in HT-CuCN and AgCN the adjacent parallel chains are shifted by an amount of c/3 along c-axis.

Earlier reverse Monte Carlo simulations of the diffraction data have been performed to understand the local structure of these cyanides[52]. The buckling in the M-C≡N-M chains is found[52] to increase with temperature. The magnitude of buckling is governed by nature of bonding between metal ions and C≡N unit. The analysis suggests that HT-CuCN have large distortion perpendicular to the chain direction. Similar behavior is also observed in AgCN and AuCN; however, the magnitude of such distortion is very small in AuCN. The magnitude of distortion in all three compounds increases with temperature and found to be correlated[52] with the thermal expansion coefficient along the chain direction (α_c). The thermal expansion coefficient is positive in the a-b plane, however large NTE is found along the chain. The coefficient of negative thermal expansion along the chain direction for HT-CuCN, LT-CuCN, AgCN and AuCN is -27.9×10^{-6} K^{-1}, -53.8×10^{-6} K^{-1}, -14.8×10^{-6} K^{-1} and -6.9×10^{-6} K^{-1} respectively[52, 57].

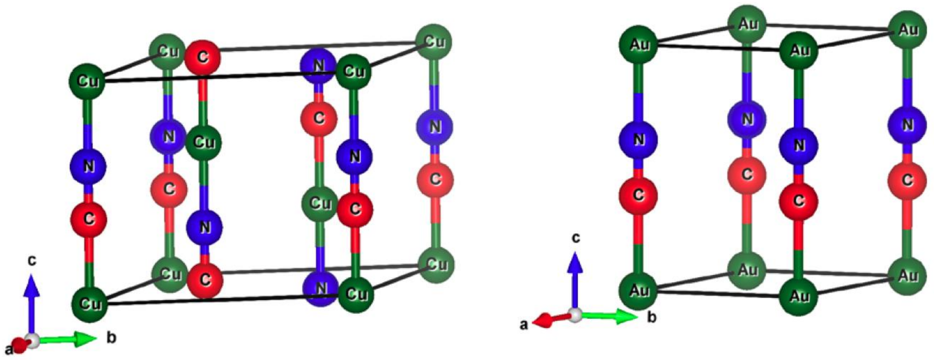

HT-CuCN/AgCN

AuCN

FIG 2.12 *The structure of AuCN and HT-CuCN/AgCN as used in the ab-intio calculations. Key: C, red sphere; N, blue sphere; Cu/Ag/Au green sphere*

Raman and infrared measurements have also been done[56] on MCN compounds. These measurements are limited to zone centre, hence they do not provide complete information about dynamics of the compounds. Here we present the temperature dependent inelastic scattering measurements on these cyanides. The measured spectra have contributions from all phonon modes from entire Brillouin zone. Our studies provide vibrational properties of these cyanides and the analysis of vibrational spectra using ab-initio phonon calculations is useful to understand the thermal expansion behavior of these cyanides. The inelastic neutron scattering measurements of all three MCN (M=Ag, Au and C) compounds were performed at three temperatures from 150 K, 240 K and 310 K. About 1 cc of polycrystalline samples of MCN have been used for the measurements. The low temperature measurements were performed using a helium cryostat. For these measurements we have used an incident neutron wavelength of 2.4 Å (14.2 meV) in neutron energy gain setup.

The phonon calculations for HT-CuCN, AgCN and AuCN are performed considering the periodic lattice model using the experimental structure parameters as given in Table 2.3. The model is an approximation of the real situation where we have neglected the C/N disorder. The low temperature phase of CuCN is a modulated structure of the high temperature phase. The required supercell to perform the calculations makes it computationally very expensive. Our interest is to understand the differences in thermal expansion behavior in terms of vibration, elastic constants and nature of bonding in these quasi one-dimensional metal cyanide systems, hence we have performed theoretical analysis on linear systems only.

There are 3 atoms in the primitive unit cell of HT-CuCN, AgCN (R3m) and AuCN (P6mm) phase, which gives 9 degree of freedom. The 9 displacement patterns are required to compute the phonon frequencies. For accurate force calculations we displaced the atoms in both the direction (±x,±y,±z) hence the number of displacements are double (18). The energy cutoff is 580 eV and a 8 ×8 × 8 k point mess have been used to obtain energy convergence in total energy of the order of meV, which is sufficient to obtain the required accuracy in phonon energies. The Monkhorst Pack method is used for k point generation[44]. The exchange-correlation contributions were approached within PBE generalized gradient approximation (GGA)[58]. The phonon spectra have been calculated in partially relaxed configuration. In partially relaxed only atomic coordinates are relaxed at fixed lattice parameter obtained from neutron diffraction data at 10 K and 310 K[52, 55, 57, 59].

TABLE 2.3 *The structure of various cyanides[55, 59] (T=10 K) as used in the ab-initio calculations of phonon spectra. The 'a' and 'c' lattice constants and atom coordinates in the hexagonal unit cell are given.*

	HT-CuCN(R3m)	**AgCN(R3m)**	**AuCN(P6mm)**
a(Å)	5.912	5.905	3.343
c(Å)	4.849	5.291	5.098
V($Å^3$)/Z	49.407	53.481	49.828
M (Cu, Ag Au)	1/3,2/3,1/3	1/3,2/3,1/3	0,0,0
C	1/3,2/3,0.714	1/3,2/3,0.724	0,0,0.387
N	1/3,2/3,0.952	1/3,2/3,0.942	0,0,0.613

.

2.3.1 Results and Discussion

2.3.1.1 Temperature Dependence of Phonon Spectra

We have measured (Figs. 2.13 and 2.14) the inelastic neutron spectra of MCN (M=Cu, Ag and Au) at 150 K, 240 K and 310 K. As mentioned above the measurements are carried out in the energy gain mode which has allowed us to measure only the external modes. The C≡N stretching modes appear around 250 meV and would not be possible to measure due to the paucity of high energy phonons in the temperature range of the measurements. The phonon spectra of AgCN show peaks (Fig. 2.13) at about 4 meV, 16 meV, 36 meV and 55 meV. Further we observe the peak about 36 meV soften with temperature. However the peak at about 55 meV becomes more diffusive as temperature increases from 150 to 310 K. The intensity of these peaks decrease as the temperature rises. The increase in temperature will enhance the vibrational mean square amplitude of atoms; hence the Debye Waller factor would in turn reduces the intensity of the peaks. Also the C/N disorder is known to increase[52] with temperature which will further reduce the sharp features in the phonon spectra.

Further the measured spectra of AuCN show (Figs. 2.13 and 2.14) much broad features rather than sharp peaks as seen in spectra of other compounds. The lowest peak is about 4 meV and the others peaks are observed around 20 meV, 35 meV, 50 meV and 75 meV. We could not observe any significant softening of phonon modes in AuCN with temperature. However in case of HT-CuCN we observe (Figs. 2.13 and 2.14) that the lowest peak in the phonon spectra is at about 7 meV and other peaks are around 20 meV, 45 meV and 70 meV. The lowest energy modes are shifted to high energies in comparison to AgCN. This could be partly due to the difference of mass of Cu (63.54 amu) and Ag (107.87 amu).

We observe significant softening with temperature for phonon modes around 45 meV. The magnitude of softening in HT-CuCN is larger than that in AgCN.

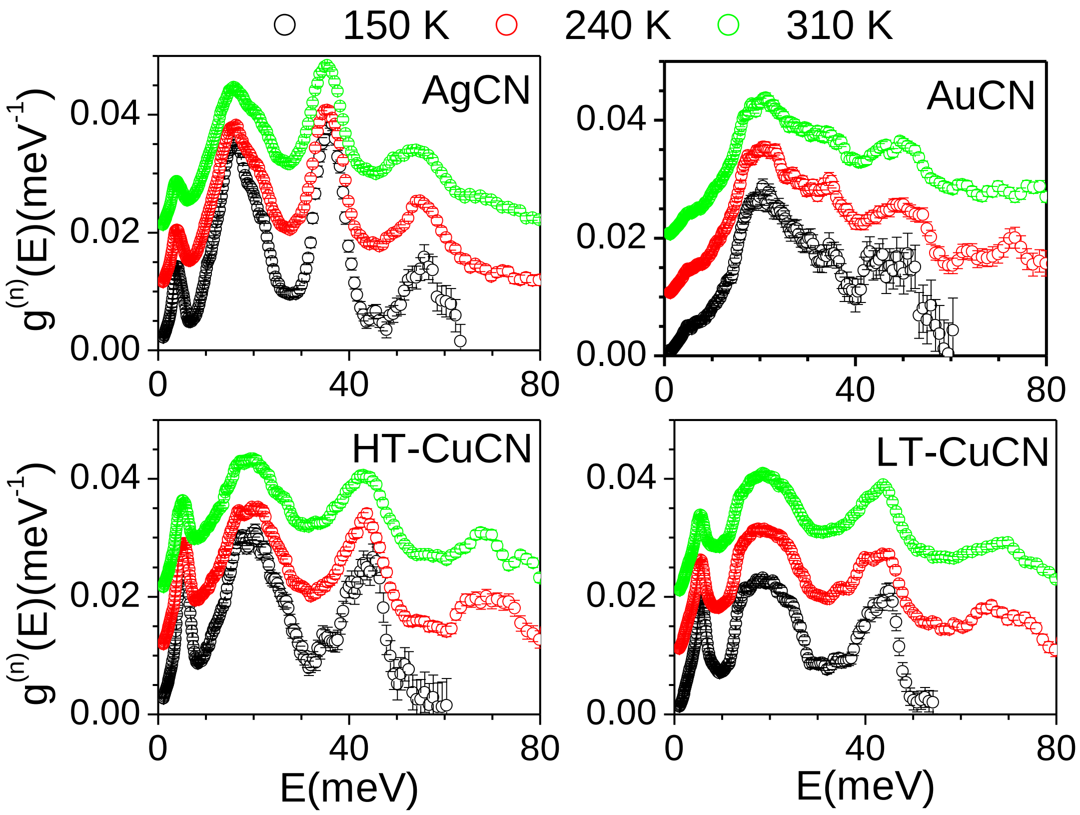

FIG 2.13 *The measure neutron inelastic spectra MCN (M=Cu, Ag and Au) at 150 K, 240 K and 310 K.*

In Fig. 2.14(b) we have shown the neutron inelastic scattering spectra measured at 150 K for high temperature and low temperature phases of CuCN. We find that the peak at around 20 meV in LT-CuCN seems to be broader in comparison to that in HT-CuCN, while at 300 K (Fig. 2.14(a)) the width of peaks in both the compounds seems to be same. The larger width at low temperature in LT-CuCN may be due to the fact that low temperature phase is a modulated structure of the high temperature phase. It seems at higher temperature the effect due to the CN disorder and anharmonicity dominate and the inelastic spectra as measured in both the phases appear similar.

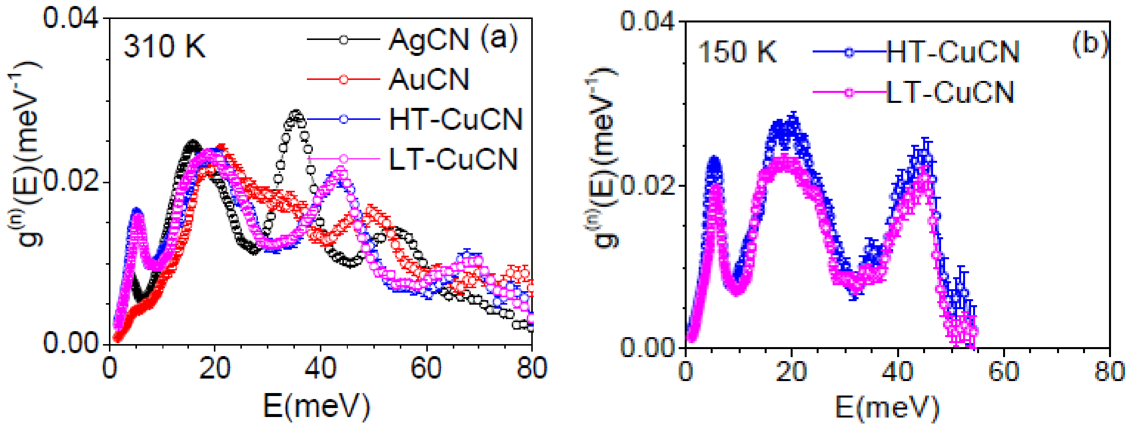

FIG 2.14 *(a) Comparison of the experimental phonon spectra for MCN (M=Cu, Ag and Au) at 310 K. (b) Comparison of the experimental phonon spectra for LT and HT phases of CuCN at 150 K.*

2.3.1.2 Calculated Phonon Spectra and Elastic Constants

The crystal structure of all three metal cyanides is known to show C/N disorder [52]. The C-N are randomly oriented along the c direction. The ideal structure of HT-CuCN and AgCN consists of chains of -M-CN-M- along c-axes. The ab-initio phonon calculations are carried out considering the ordered structure of these compounds. The phonon spectra have been calculated at fixed lattice parameters corresponding to experimental structures [52, 55, 59] at 10 K and 310 K.

We have also calculated the phonon dispersion (Fig 2.16) relation of all three compounds along various high symmetry directions namely [100], [001] and [110]. We find that in all the three compounds transverse acoustic modes along [001] are unstable. The mode involves transverse motion of C and N atoms in the a-b plane. The C/N disorder in the compounds might be responsible for stability of the crystal.

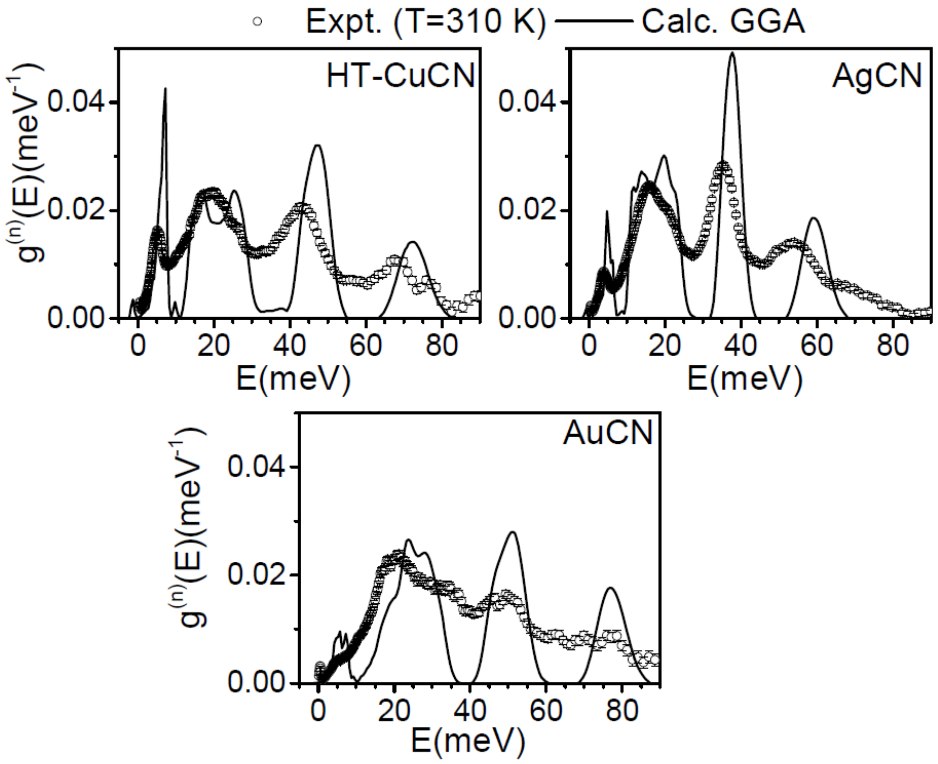

FIG 2.15 *The comparison between the measured (310 K) and calculated phonon spectra of MCN (M=Cu, Ag and Au).*

The comparison between the experimental and calculated phonon spectra is shown in Fig. 2.15. The calculated spectra are able to reproduce all the major features of the observed spectra. The structural disorder could lead to a variation of the M-C, M-N and C-N bond lengths, which would in turn broadens the peaks as observed in the experimental spectra.

This might be one of the reasons for difference in the calculated and experimental spectra of MCN. We notice that for HT-CuCN and AgCN elastic instability is observed along [100] and [110]. However, for AuCN these modes are found to be stable. The slopes of the transverse acoustic phonon branches (Fig. 2.16) are very low. Hence small errors in the calculation of phonon energies may result in large errors in the calculated elastic constants.

TABLE 2.4 *The various elastic constants of metal cyanides MCN (M=C, Ag and Au) in unit of GPa at T=0 K.*

	C_{11}	**C_{33}**	**C_{44}**	**C_{66}**	**C_{12}**	**C_{13}**
HT-CuCN	14.0	536.0	4.0	0.4	6.1	11.0
AgCN	18.5	387.0	5.2	-0.3	8.1	16.0
AuCN	28.4	755.3	6.5	2.2	15.3	14.0

So the elastic constant of MCN are calculated (TABLE 2.4) using the symmetry-general least squares method[60] as implemented in VASP5.2 and were derived from the strain−stress relationships obtained from six finite distortions of the lattice. The calculated elastic moduli include contributions of distortions with rigid ions and ionic relaxations. The elastic constants C_{11} and C_{33} are related to the longitudinal phonons polarized along x and z axis. It can be seen that there is a large difference in the values of the C_{11} and C_{33} elastic constants in all the compounds. This indicates large difference in the nature of bonding in a-b plane and along c-axis. This is in agreement with the analysis of experimental diffraction data which also shows strong one dimensional nature of these compounds. The values of C_{33} for HT-CuCN, AgCN and AuCN are 536 GPa, 387 GPa and 755 GPa respectively. Large value of C_{33} in AuCN (~755 GPa) in comparison to the other two compounds indicates that bonding between the atoms of -Au-CN-Au- chains is much stronger in comparison to that in Ag and Cu compounds.

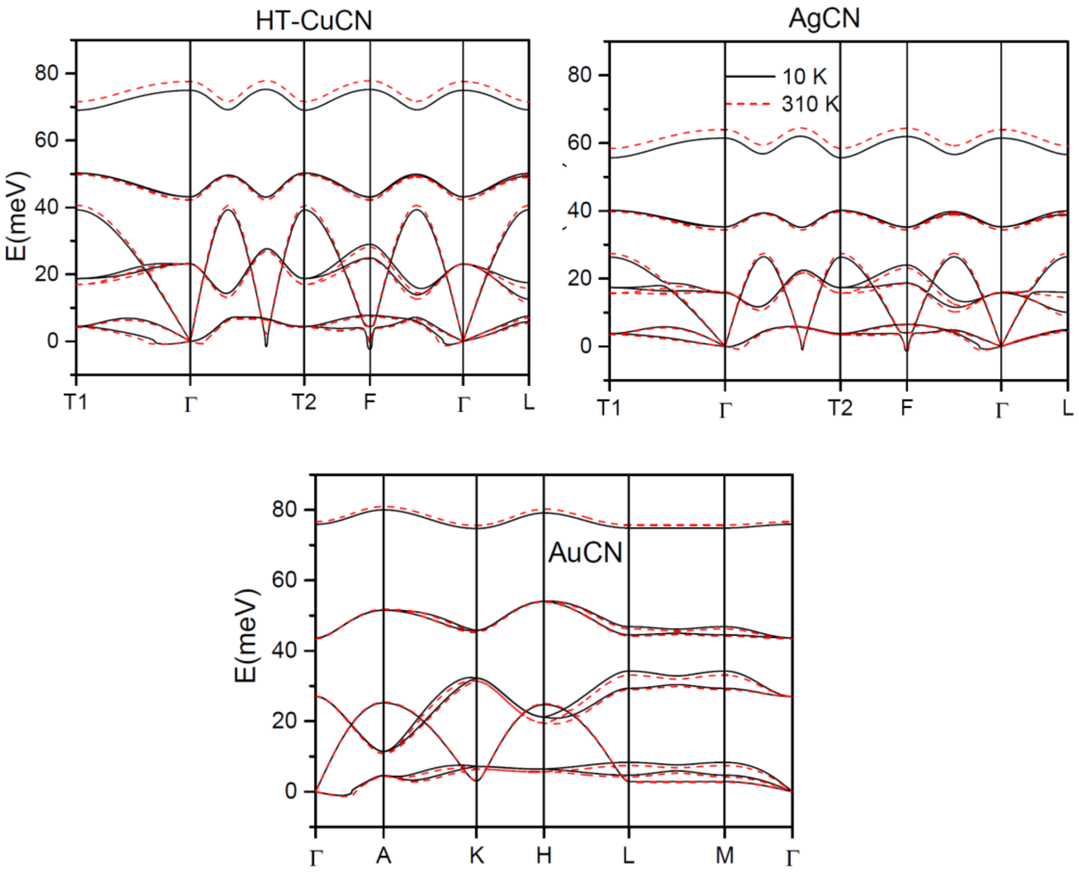

FIG 2.16 *The calculated dispersion relation along various high symmetry direction of MCN (M=Cu, Ag and Au) at lattice constant at 10 K (black) and 310 K (red). The C-N stretching modes at about 270 meV are not shown. The Bradley-Cracknell notation is used for the high-symmetry points. HT-CuCN/AgCN:* $T1(1/2,1/2,-1/2)_R \equiv (0, 1, 1/2)_H$, $\Gamma(0,0,0)_R \equiv (0, 0, 0)_H$, $T2(1/2,1/2,1/2)_R \equiv (0, 0, 3/2)_H$, $F(1/2,1/2,0)_R \equiv (0, 1/2, 1)_H$, $L(0,1/2,0)_R \equiv (-1/2, ½ ½)_H$; *In AuCN:* $\Gamma(0,0,0)_H$, $A(0\ 0\ 1/2)_H$, $K(1/3,1/3,0)_H$, $H(1/3\ 1/3\ 1/2)_H$, $L(1/2\ 0\ 1/2)_H$ *and* $M(1/2,1/2,0)_H$. *Subscript R and H correspond to rhombohedral and hexagonal notation respectively.*

The C_{66} elastic constant in all three compounds is very small. All these suggest that CuCN and AgCN are close to instability in plane against shear strain. However the AuCN shows significant stability against the shear strain. On increasing temperature, the magnitude of strain arising due to the vibrational amplitude of atoms perpendicular to chain will depend on the bond strength of -M-CN-M-. The calculated elastic constants as given in TABLE 2.4 indicates that nature of bonding in AuCN is strongest among all the three cyanides. This is consistence with the reverse Monte Carlo analysis of the diffraction data, which indicates that AuCN does not show any shear distortion even up to 450 K; however, significant distortion is observed in HT-CuCN and AgCN.

2.3.1.3 Partial Phonon Density of States

The partial density of states provide the contributions of the individual atoms to the total phonon spectra. We have calculated (Fig. 2.17) the partial density of states by projecting the eigenvector on different atoms. The contribution from M (Cu, Ag and Au) atoms is spread up to 35 meV; however, it is most significant contribution only below 10 meV. The C and N atoms contribute in the entire energy range up to 280 meV. We observed band gap in the phonon spectra from 80 meV to 280 meV. The CN stretching modes are at around 280 meV. The low energy peak in the partial density of states of Cu (63.54 amu), Ag (107.87 amu) and Au (197.97 amu) are at 7 meV, 5.2 meV and 5.2 meV respectively. The shift in the peak position is partly due to the mass renormalization. It should be noted that volume per primitive cell of HT-CuCN and AuCN compounds is nearly the same at 49.41 Å^3 and 49.82 Å^3 respectively. The lowest energy peak in the Au compound does not follow the mass effect. This indicates that the nature of bonding for the AuCN (P6mm) is stronger in comparison to HT-CuCN and AgCN (both in R3m). The difference in ionic radii of Cu (0.73 Å), and Au

(1.37 Å) along with the similarity in volume per primitive cell of these compounds further supports the idea of difference in nature of bonding.

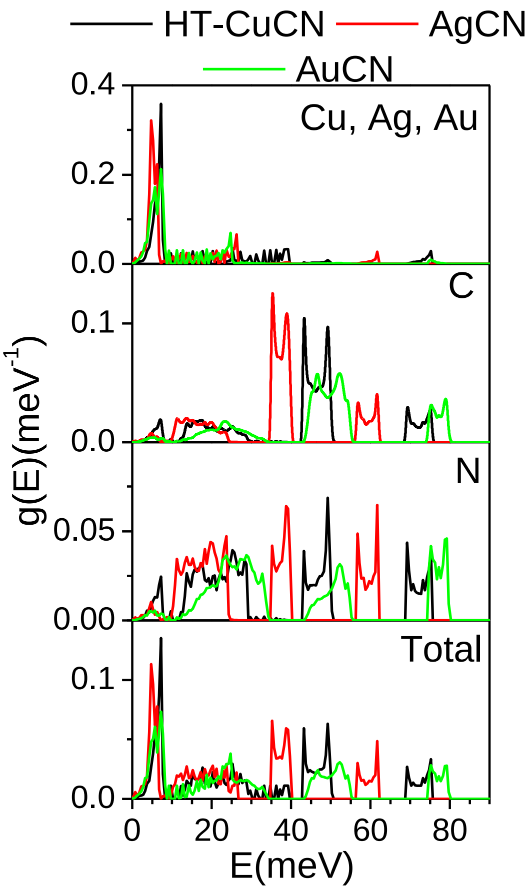

FIG 2.17 *The calculated phonon partial density of states of various atoms in MCN (M=Cu, Ag and Au) for structure at 10 K. The x-scale the C-N stretching modes at about 270 meV are not shown.*

The partial contributions due to C and N atoms in the HT-CuCN (49.41 Å^3) and AgCN (53.48 Å^3) in the external mode region (below 80 meV) are up to 75 meV and 62 meV respectively. As expected the difference in the energy range of the external modes in the two compounds seems to follow the volume effect. The volume of the primitive unit cell of AuCN is 49.82 Å^3. We find that external modes in AuCN extend up to 80 meV.

Comparisons of the energy range of the external modes of the three compounds suggest that force constants are stiffer in AuCN in comparison to other two compounds. The calculated C-N bond lengths (Table 2.6) are 1.174 Å, 1.169 Å and 1.163 Å in HT-CuCN, AgCN and AuCN respectively. As expected (Fig. 2.17) the energies of the phonon modes in the internal mode region simply follow the considerations due to change in C-N bond lengths. From the above analysis we can conclude that the nature of bonding along -Au-CN-Au- is stronger than that in -Ag-CN-Ag- and -Cu-CN-Cu-. This is consistent with the calculated Born effective charges as discussed in Section 2.5.4.

2.3.1.4 Born Effective Charges

The computed Born effective charges in all three compounds are listed in Table 2.5. We observe that the values of the charge of carbon, nitrogen and M (Cu, Ag and Au) atoms in all three compound are different and anisotropic. This anisotropic behavior of the Born effective charge suggest difference in nature of bonding along a- and c-axis. We find that for M atoms the values of the Born-effective charges along a-axis is large in comparison to that along c-axis. However, for C and N atoms this trend is reverse. It is interesting to note that for Cu and Ag compounds, the magnitude of Born effective charges along the chain (c-axis) has small finite value however in Au compound the value is zero. This suggests a large difference in nature of bonding in along M-CN-M chain among various MCN. This could be due to the difference in electronegativity of Cu(1.9), Ag(1.93) and Au(2.54) atoms. The zero magnitude of Born effective charge for Au compound along c-axis means that bonding along the chain may be either metallic or covalent. However, MCN are known to be insulator, hence the bonding between Au and CN may be covalent in nature.

TABLE 2.5 *The Born effective charges of various atoms in unit of e.* ($Z_{yy}=Z_{xx}$; $Z_{xy}=Z_{xz}=Z_{yx}=0$)

Atom	Zxx	Zzz
C(HT-CuCN/AgCN/AuCN)	-0.3/-0.4/-0.5	1.4/0.8/1.5
N(HT-CuCN/AgCN/AuCN)	-0.6/-0.6/-0.5	-1.1/-1.2/-1.5
Cu/Ag/Au	0.9/1.0/1.0	-0.3/0.4/0.0

TABLE 2.6 *The various bond length in metal cyanides MCN (M=C, Ag and Au) in unit of Å.*

Bond length	HT-CuCN	AgCN	AuCN
C-N	1.174	1.169	1.163
C-M	1.841	2.040	1.960
N-M	1.835	2.081	1.976

Further for AuCN (Table 2.4) the magnitude of C_{33} and C_{44} elastic constants, which are related to the longitudinal and transverse phonon frequencies along c-axis, is larger in comparison to the values for CuCN and AgCN. This also suggests that nature of boding in AuCN is stronger in comparison to CuCN and AgCN.

2.3.1.5 Thermal Expansion Behavior

The lattice parameter as a function of temperature has been reported from neutron diffraction measurements at temperature ranging from 90 K to 450K[52]. The measurements show that the *c* lattice parameter decreases with increase in temperature, however, lattice parameter *a* (=*b)* shows positive expansion behaviour. The overall volume thermal expansion is found to be positive in all three cyanides and has similar magnitude. The negative thermal expansion behavior along c axis is largest in CuCN and least in AuCN. So also, the positive expansion along a and b-axis is largest in CuCN and least in AuCN. We have computed the thermal expansion behavior using the quasiharmonic approximation. Each phonon mode of energy E_i contributes to the volume thermal expansion coefficient[48] given by $\alpha_V = \frac{1}{BV}\sum_i \Gamma_i C_{Vi}(T)$, where V is the unit cell volume, B is the bulk modulus, Γ_i (= -$\partial \ln E_i/\partial \ln V$) are the mode Grüneisen parameters and C_{Vi} the specific-heat contributions of the phonons in state i (= **q**j) of energy E_i. The volume dependence of phonon frequency is used to calculate the thermal expansion behavior. The phonon spectra in the entire Brillouin zone have been calculated at two volume corresponding to the experimental structures at 10 K and 310 K. The calculated Grüneisen parameters are shown in Fig.2.18(a).

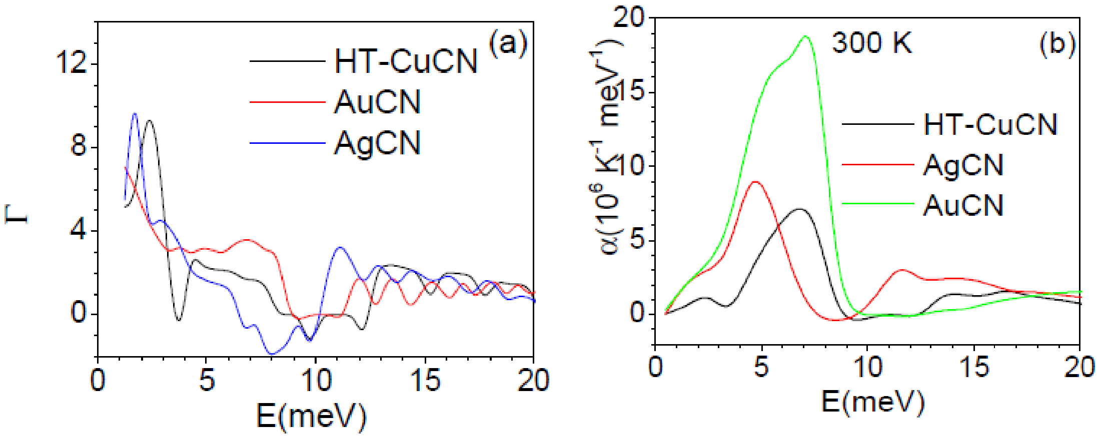

FIG 2.18 *(a) The calculated average Grüneisen parameters Γ(E) averaged over various phonon of energy E in the whole Brillouin zone. (b) The contribution of phonons of energy E to the volume thermal expansion coefficient (α_V) as a function of E at 300 K.*

It can be seen that low energy modes below 4 meV have large positive Grüneisen parameters. The calculated partial density of states shows that the contribution at such low energies is mainly from the M(=Cu, Ag and Au) atoms. As shown in Fig. 2.16 the calculated transverse acoustic modes in HT-CuCN and AgCN and AuCN are unstable. For the thermal expansion calculation the phonon energies have been calculated at 8000 q points (72000 phonon modes) in the entire Brillouin zone. We find that among these 72000 modes, the number of unstable modes in HT-CuCN and AgCN and AuCN are 558, 453 and 75 respectively, which is less than 1%. The temperature dependence of the unit cell volume is calculated without including the unstable modes. The calculations are qualitatively in good agreement with the observed thermal expansion behavior in AuCN, but underestimated the experimental magnitude in other two compounds (Fig 2.19). The underestimate might be related to the C/N disorder as discussed below.

The experimental[52, 57] value of the coefficient of negative thermal expansion (NTE) along the chain direction (α_c) for HT-CuCN, AgCN and AuCN is -27.9×10^{-6} K^{-1}, -14.8×10^{-6} K^{-1} and -6.9×10^{-6} K^{-1} respectively, while positive thermal expansion (PTE) in the a-b plane (α_a) is 74.8×10^{-6} K^{-1}, 65.7×10^{-6} K^{-1} and 57.4×10^{-6} K^{-1} respectively. As noted above, among the three compounds HT-CuCN has the highest C/N disorder and it has also the highest positive as well as negative thermal expansion coefficients. AuCN has the least C/N disorder and has the smallest values of NTE and PTE coefficients. As mentioned above, the ab-initio calculations performed with the ordered structures exhibit the highest number of unstable modes for HT-CuCN, while AuCN show the least number of unstable modes. It seems C/N disorder stabilizes the structure. Among cyanides, nickel cyanide $Ni(CN)_2$ has a long-range ordered structure in two dimensions (*a-b* plane) but a high degree of stacking disorder in the third dimension. The compound exhibits[61] NTE in two dimensions ($\alpha_a = -7\times10^{-6}$ K^{-1}) along with a very large PTE coefficient ($\alpha_c = 61.8\times10^{-6}$ K^{-1}) perpendicular to the layers. Here again it can be seen that disorder along c-axis results in large overall volume thermal expansion ($\alpha_V = 48.5\times10^{-6}$ K^{-1}). It appears that the C/N disorder contributes towards positive thermal expansion behavior. The order disorder transition at around 400 K in ZrW_2O_8 reduces[21] the overall NTE coefficient.

As noted above, the linear thermal expansion coefficient along 'a-' and 'c-' axis are found to be positive and negative respectively. We are interested to find the modes which have large negative and positive Grüneisen parameters and contribute towards thermal expansion behavior. The estimated Grüneisen parameters (Γ_i) and the specific-heat contribution of modes (C_{Vi}) from the ab-*initio* calculations have been used to estimate the contribution of the various phonons to the thermal expansion (Fig. 2.18(b)) as a function of phonon energy at 300 K. The maximum contribution to α_V seems to be from the low-energy modes below 10 meV. The calculated volume dependence of phonon dispersion curves for HT-CuCN, AgCN and AuCN are shown in Fig. 2.16. The displacement pattern of a few zone boundary phonon modes, has been plotted (Fig. 2.20).

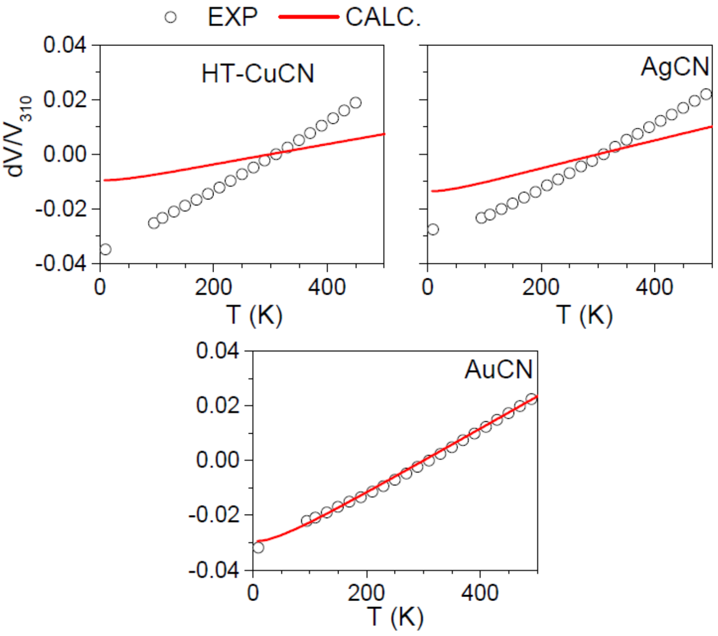

FIG 2.19 *The calculated and experimental thermal expansion behavior of MCN (M=Cu, Ag and Au).*

The mode assignments, phonon energies and Grüneisen parameters are given in the figures. As mentioned above, HT-CuCN and AgCN crystallize in the same space group (R3m), hence the eigen vector pattern for symmetrically equivalent phonon modes would be similar. The investigation of the displacement pattern of the eigenvectors shows that the phonon modes have mainly two kinds of dynamics. One which involves atom vibration along the chain and the other in which atoms vibrate perpendicular to the chain. For HT-CuCN and AgCN, the adjacent -M-C≡N-M- chains are shifted by ±c/3 along c-axis. We find that lowest zone-boundary modes at F and LD points in the Brillouin zone are found to be unstable. For the LD point mode (Fig. 2.20), within a chain, the M and C≡N move with equal displacements. The movement of atoms in the adjacent chains is found to be out-of-phase with each other. The motion of the atoms in F-point mode is similar to that in LD-point mode. However for F-point mode there is a small component of displacement in the a-b plane. Both the modes are found to become more unstable on compression of the lattice. Such type of modes would contribute maximum to the NTE along c-axis. However in case of AuCN, the K point mode (Fig. 2.20) also shows sliding of -M-C≡N-M- chains out-of-phase with each other. The mode is found to have small positive Γ of 1.1. It seems that the chain sliding modes mainly contribute to negative α_c in HT-CuCN and AgCN compounds and this contribution is not seem in AuCN. The vibrational amplitude along the chain would depend on the nature of bonding between metal and cyanide (-C≡N-) as well as on the atomic mass of metal ion. As mentioned above, this bonding in HT-CuCN and AgCN seems to be similar. The smaller mass of Cu (63.54 amu) would lead to large amplitude of thermal vibration along the chain in comparison to Ag (107.87 amu) compound, which indicates that the contraction along the -M-C≡N-M- chain would be more in the HT-CuCN in comparison to the AgCN, which is qualitatively in agreement[52] with the observed NTE behavior in these compounds. Several modes in which the atoms move perpendicular to the chain have positive Grüneisen parameters and would be responsible for positive thermal expansion behavior.

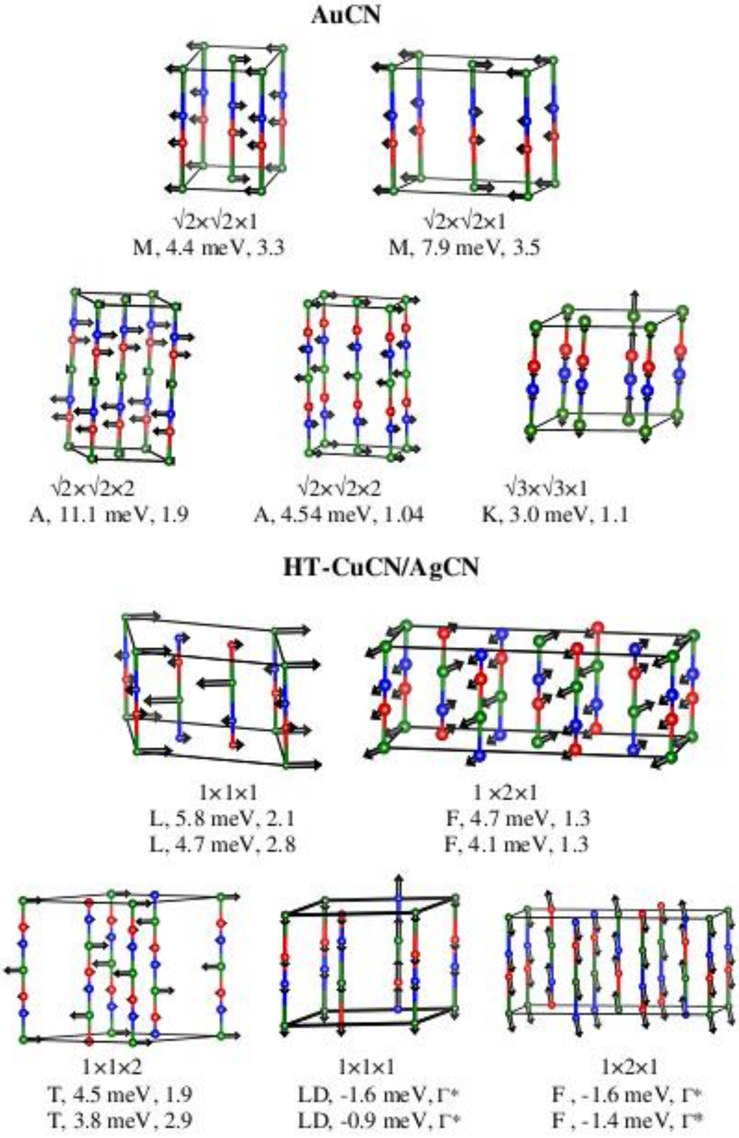

FIG 2.20 *The calculated displacement pattern of various phonon modes in AuCN and HT-CuCN and corresponding Grüneisen parameters. The first line below each figure represents the size of the supercell. The second line below the figure give the high symmetry point, phonon energies and Grüneisen parameters, respectively. In the bottom panel (HT-CuCN and AgCN) the second and third line below the figure corresponds to HT-CuCN and AgCN respectively. Key: C, red sphere; N, blue sphere; Cu/Ag/Au green sphere.*

**The Grüneisen parameters values of unstable F and LD-point modes are not given. The modes are found to become more unstable on further compression of the lattice. Such type of modes would contribute maximum to the NTE along c-axis.*

2.4 Conclusions

We have reported temperature dependent inelastic neutron scattering measurements of phonon spectrum for Ag_2O, Cu_2O, AgCN, AuCN and MCN. A comparative ab-initio calculations of phonon spectra as well as thermal expansion behavior in M2O and MCN is presented. The calculations are in good agreement with the experimental inelastic neutron scattering phonon spectra. The calculated thermal expansion behavior of these compounds is in agreement with the available experimental data. We find that although low energy phonon modes of similar energies are present in all the M_2O compounds, the nature of bonding as well as open space in the unit cell are important in governing the thermal expansion behavior.

In MCN (M=Cu, Ag and Au), the calculated thermal expansion behavior is found to be in qualitative agreement with the available experimental data. We have also identified the phonon modes responsible for the anomalous thermal expansion behavior in these cyanides. The nature of the chemical bonding is found to be similar in HT-CuCN and AgCN, which is significantly different from that in AuCN. The computed elastic constants and Born effective charges are correlated with the difference in nature of bonding in metal cyanides.

[1] J. C. Hancock, K. W. Chapman, G. J. Halder, C. R. Morelock, B. S. Kaplan, L. C. Gallington, A. Bongiorno, C. Han, S. Zhou and A. P. Wilkinson, Chemistry of Materials **27**, 3912 (2015).

[2] M. S. Senn, A. Bombardi, C. A. Murray, C. Vecchini, A. Scherillo, X. Luo and S. W. Cheong, Physical Review Letters **114**, 035701 (2015).

[3] L.-F. Huang, P.-L. Gong and Z. Zeng, Physical Review B **91**, 205433 (2015).

[4] J. Chen, L. Hu, J. Deng and X. Xing, Chemical Society Reviews **44**, 3522 (2015).

[5] L. Wang, C. Wang, Y. Sun, K. Shi, S. Deng, H. Lu, P. Hu and X. Zhang, Journal of Materiomics **1**, 106 (2015).

[6] V. J. Härkönen and A. J. Karttunen, Physical Review B **89**, 024305 (2014).

[7] H. Fang, M. T. Dove and A. E. Phillips, Physical Review B **89**, 214103 (2014).

[8] F. Bridges, T. Keiber, P. Juhas, S. J. L. Billinge, L. Sutton, J. Wilde and G. R. Kowach, Physical Review Letters **112**, 045505 (2014).

[9] P. Hermet, J. Catafesta, J. L. Bantignies, C. Levelut, D. Maurin, A. B. Cairns, A. L. Goodwin and J. Haines, The Journal of Physical Chemistry C **117**, 12848 (2013).

[10] J. Grant Hill, A. O. Mitrushchenkov and K. A. Peterson, The Journal of Chemical Physics **138**, 134314 (2013).

[11] H. Fang, M. T. Dove, L. H. N. Rimmer and A. J. Misquitta, Physical Review B **88**, 104306 (2013).

[12] J. Hu and Y. P. Chen, Physical Review E **87**, 062104 (2013).

[13] H. Fang and M. T. Dove, Physical Review B **87**, 214109 (2013).

[14] V. Gava, A. L. Martinotto and C. A. Perottoni, Physical Review Letters **109**, 195503 (2012).

[15] A. M. Chippindale, S. J. Hibble, E. J. Bilbé, E. Marelli, A. C. Hannon, C. Allain, R. Pansu and F. Hartl, Journal of the American Chemical Society **134**, 16387 (2012).

[16] T. Klimczuk, H. C. Walker, R. Springell, A. B. Shick, A. H. Hill, P. Gaczyński, K. Gofryk, S. A. J. Kimber, C. Ritter, E. Colineau, J. C. Griveau, D. Bouëxière, R. Eloirdi, R. J. Cava and R. Caciuffo, Physical Review B **85**, 174506 (2012).

[17] V. E. Fairbank, A. L. Thompson, R. I. Cooper and A. L. Goodwin, Physical Review B **86**, 104113 (2012).

[18] A. L. Goodwin, M. Calleja, M. J. Conterio, M. T. Dove, J. S. O. Evans, D. A. Keen, L. Peters and M. G. Tucker, Science **319**, 794 (2008).

[19] K. W. Chapman, P. J. Chupas and C. J. Kepert, Journal of the American Chemical Society **128**, 7009 (2006).

[20] M. G. Tucker, A. L. Goodwin, M. T. Dove, D. A. Keen, S. A. Wells and J. S. O. Evans, Physical Review Letters **95**, 255501 (2005).

[21] T. A. Mary, J. S. O. Evans, T. Vogt and A. W. Sleight, Science **272**, 90 (1996).

[22] M. K. Gupta, R. Mittal and S. L. Chaplot, Physical Review B **88**, 014303 (2013).

[23] T. R. Ravindran, A. K. Arora and T. A. Mary, Physical Review Letters **84**, 3879 (2000).

[24] M. K. Gupta, R. Mittal, S. L. Chaplot and S. Rols, Journal of Applied Physics **115**, 093507 (2014).

[25] W. Tiano, M. Dapiaggi and G. Artioli, Journal of Applied Crystallography **36**, 1461 (2003).

[26] B. J. Kennedy, Y. Kubota and K. Kato, Solid State Communications **136**, 177 (2005).

[27] K. W. Chapman and P. J. Chupas, Journal of the American Chemical Society **129**, 10090 (2007).

[28] D. Pei, E. J. Liang, J. Yu and Z. Y. Du, Journal of Physics: Condensed Matter **20**, 275224 (2008).

[29] J. W. Zwanziger, Physical Review B **76**, 052102 (2007).

[30] L. V. Gregor, The Journal of Physical Chemistry **66**, 1645 (1962).

[31] R. E. Gerkin and K. S. Pitzer, Journal of the American Chemical Society **84**, 2662 (1962).

[32] Y. Petroff, P. Y. Yu and Y. R. Shen, Physical Review B **12**, 2488 (1975).

[33] K. Reimann and K. Syassen, Physical Review B **39**, 11113 (1989).

[34] M. M. Beg and S. M. Shapiro, Physical Review B **13**, 1728 (1976).

[35] K.-P. Bohnen, R. Heid, L. Pintschovius, A. Soon and C. Stampfl, Physical Review B **80**, 134304 (2009).

[36] R. Mittal, S. L. Chaplot, S. K. Mishra and P. P. Bose, Physical Review B **75**, 174303 (2007).

[37] P. Fornasini, G. Dalba, R. Grisenti, J. Purans, M. Vaccari, F. Rocca and A. Sanson, Nuclear Instruments and Methods in Physics Research Section B: Beam Interactions with Materials and Atoms **246**, 180 (2006).

[38] S. a. Beccara, G. Dalba, P. Fornasini, R. Grisenti, A. Sanson and F. Rocca, Physical Review Letters **89**, 025503 (2002).

[39] M. Dapiaggi, W. Tiano, G. Artioli, A. Sanson and P. Fornasini, Nuclear Instruments and Methods in Physics Research Section B: Beam Interactions with Materials and Atoms **200**, 231 (2003).

[40] A. Sanson, F. Rocca, G. Dalba, P. Fornasini, R. Grisenti, M. Dapiaggi and G. Artioli, Physical Review B **73**, 214305 (2006).

[41] K. Parlinksi, (2003)

[42] G. Kresse and J. Furthmüller, Computational Materials Science **6**, 15 (1996).

[43] G. Kresse and D. Joubert, Physical Review B **59**, 1758 (1999).

[44] H. J. Monkhorst and J. D. Pack, Physical Review B **13**, 5188 (1976).

[45] A. Filippetti and V. Fiorentini, Physical Review B **72**, 035128 (2005).

[46] H. Shi, R. Asahi and C. Stampfl, Physical Review B **75**, 205125 (2007).

[47] M. K. Gupta, R. Mittal, S. Rols and S. L. Chaplot, Physica B: Condensed Matter **407**, 2146 (2012).

[48] G. Venkataraman, L. A. Feldkamp and V. C. Sahni, Dynamics of perfect crystals (MIT Press, Cambridge, 1975).

[49] J. Hallberg and R. C. Hanson, physica status solidi (b) **42**, 305 (1970).

[50] W. Schäfer and A. Kirfel, Applied Physics A **74**, s1010 (2002).

[51] S. W. Fei Pei, Gang Wang, Ming Xu, Song-You Wang, Liang-Yao Chen and Yu Jia Journal of Korean Physical Society **55**, (2009).

[52] J. Hibble Simon, B. Wood Glenn, J. Bilbé Edward, H. Pohl Alexander, G. Tucker Matthew, C. Hannon Alex and M. Chippindale Ann, Zeitschrift für Kristallographie Crystalline Materials, **225**, 457 (2010)

[53] G. A. Bowmaker, B. J. Kennedy and J. C. Reid, Inorganic Chemistry **37**, 3968 (1998).

[54] S. J. Hibble, S. M. Cheyne, A. C. Hannon and S. G. Eversfield, Inorganic Chemistry **41**, 1042 (2002).

[55] S. J. Hibble, A. C. Hannon and S. M. Cheyne, Inorganic Chemistry **42**, 4724 (2003).

[56] C. Romao, M. M. Barsan, D. F. R. Gilson and I. S. Butler, AIP Conference Proceedings **1267**, 253 (2010).

[57] S. J. Hibble, S. G. Eversfield, A. R. Cowley and A. M. Chippindale, Angewandte Chemie International Edition **43**, 628 (2004).

[58] J. P. Perdew, K. Burke and M. Ernzerhof, Physical Review Letters **77**, 3865 (1996).

[59] S. M. Cheyne, Ph.D. Thesis, University of Reading UK, 2004.

[60] Y. Le Page and P. Saxe, Physical Review B **65**, 104104 (2002).

[61] A. L. Goodwin, M. T. Dove, A. M. Chippindale, S. J. Hibble, A. H. Pohl and A. C. Hannon, Physical Review B **80**, 054101 (2009).

Chapter 3

Negative Thermal Expansion in Cubic ZrW_2O_8: Role of Phonons in Entire Brillouin Zone from Ab-inito Calculations

3.1 Introduction

The discovery of large isotropic negative thermal expansion (NTE) in cubic phase of ZrW_2O_8 two decades ago has lead to great excitement in the field of material science. Since then anamolous thermal expansion behavior has been found in large number of open frame work compounds [1-3]. ZrW_2O_8 has M-O-M' (M, M'= Zr, W) type of linkages and show[1] negative volume thermal expansion coefficient of -29×10^{-6} K^{-1} at 300 K. Increasing flexibility in the structure has lead to the discovery of compounds exhibiting[4] colossal positive and negative thermal expansion. The compounds find applications in forming the composites with tailored thermal expansion coefficients useful for applications such as in fiber optic communication systems.

At ambient pressure ZrW_2O_8 crystallizes [1] in cubic structure ($P2_13$, Z=4) that consists of ZrO_6 octahedral and WO_4 tetrahedral units. Diffraction, spectroscopic as well as computer simulation techniques [5-13] have been used to understand the thermodynamic behaviour of ZrW_2O_8. All these works show that anharmonicity of low energy phonon modes has major contribution to the observed thermal expansion behavior. X-ray absorption fine structure (XAFS) measurements [13] led to a suggestion that NTE in ZrW_2O_8 could be due to the translational motion of WO_4 tetrahedra along <111> axis along with correlated motion of three nearest ZrO_6 octahedra. The reverse Monte Carlo analysis of the neutron total scattering data suggested [10] that WO_4 as well as ZrO_6 polyhedra rotate and translate as rigid units. Earlier a rigid unit mode model [11] was also used to understand NTE behaviour of ZrW_2O_8. Hancock et al [12] proposed other modes involving translation and rotation of polyhedra. It seems all the phonon modes identified from various techniques could contribute to NTE.

Earlier neutron scattering data [9] as well as theoretical [8] estimates of the anharmonicty of the phonons in ZrW_2O_8 using interatomic potential model indicated that modes of energy below 8 meV are responsible for observed NTE. However, estimates based on Raman spectroscopy showed [8] that several modes upto 50 meV contribute to NTE. The large disagreement in the energy range as well as nature of the low-energy modes in previous works indicated the need for understanding of NTE behaviour in ZrW_2O_8 using ab-inito calculations. Recently ab-initio calculations of zone center phonon modes have been published [6]. However the authors concluded [6] that one should fully explore the nature of the phonons in the entire Brillouin zone for understanding the mechanism of NTE. Here we report such a comprehensive calculations and identify specific zone-boundary modes that are highly anharmonic. The calculations are able to reproduce the observed NTE as well as anomalous trends of the phonon spectra with increase in temperature and pressure.

Important soft modes were identified in cubic ReO_3 [14] and ScF_3 [15] at M and R-points in the Brillouin zone respectively. These modes show simultaneously both large negative Grüneisen parameter as well as large quadratic anharmonicity, the former leading to NTE and latter to the temperature dependence. In case of ZrW_2O_8, we find that the modes that show large negative Grüneisen parameter and contribute to NTE are not necessarily the same as those showing cubic and/or quartic anharmonicity and significant temperature dependence. This finding means that the modes found anharmonic in temperature dependent measurements are not necessarily relevant to NTE.

The first-principle calculations of lattice dynamics have been performed using Vienna Ab-initio Simulation Package (VASP) [16-19] and PHONON5.2 software's [20].The details are given in reference [21]. The calculations reproduce the equilibrium crystal structural parameters, elastic constants and mean squared amplitude of various atoms quite satisfactorily as given in Table SI and SII of the reference [21].

3.2 Result and Discussion

The calculated phonon spectrum is found to be in excellent agreement with the experimental phonon spectrum [5] as shown in Fig. 3.1. The calculated energies of all the zone-centre modes are also shown in Fig. 3.1. The calculated partial density of states of various atoms shows (Fig. S1 of [21]) that vibrations due to Zr atoms span only up to 50 meV, while vibrations due to W and O span the entire energy range. The W-O stretching modes lie in the energy range from 85 -130 meV. The calculated phonon dispersion relation along the high symmetry directions is shown in Fig. S2 [21]. The low energy range of phonon dispersion up to 50 meV contains large number of non-dispersive phonon branches, which give rise to several peaks in density of states. To emphasis the anharmonic nature of low energy phonons, we have also shown the phonon dispersion up to 10 meV (Fig. 3.2) at 0 and 1 kbar. We find that several phonon branches soften with increasing pressure. The lowest optic mode is calculated at 40 cm^{-1} (~5 meV), which is in excellent agreement with the experimental value of 40 cm^{-1} from Raman [7] as well as infra-red measurements [6]. The optic modes along with several phonon branches give rise to the first peak in the calculated phonon density of states at 4.5 meV which is observed at 3.8 meV in neutron scattering experiments [5]. The low-energy peak also leads to a sharp increase in the specific heat at low temperatures (Fig. S3 [21]). The optic modes along with several phonon branches give rise to the first peak in the calculated phonon density of states at 4.5 meV which is observed at 3.8 meV in neutron scattering experiments [5]. The low-energy peak also leads to a sharp increase in the specific heat at low temperatures (Fig. S3 [21]).

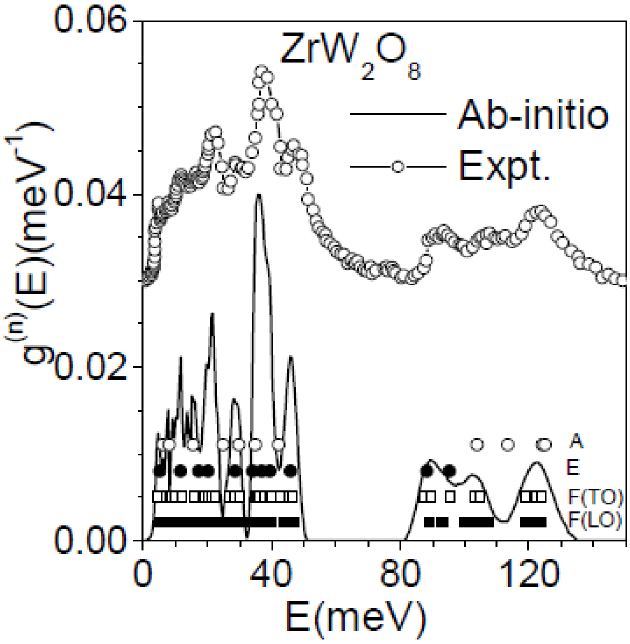

FIG 3.1 *The calculated (0 K) and experimental (300 K) [5] neutron-weighted phonon spectra in ZrW_2O_8. For better visibility the experimental phonon spectra[5] is shifted along the y-axis by 0.03 meV^{-1}.The calculated zone-centre optic modes, A, E, F(TO) and F(LO) are also shown.*

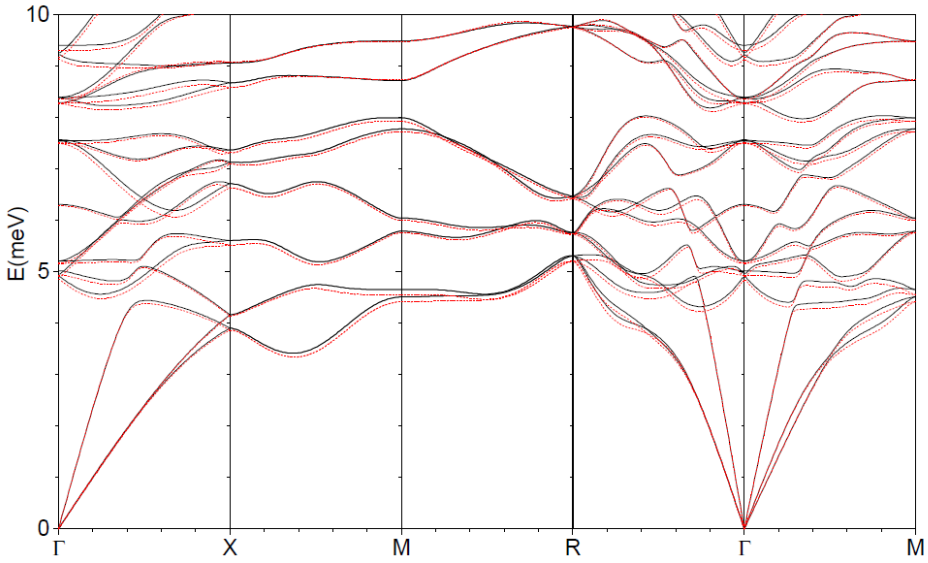

FIG 3.2 *Calculated low-energy part of the pressure dependent dispersion relation for ZrW_2O_8. The solid and dashed lines correspond to the calculations at ambient pressure and 1 kbar. Γ=(0,0,0); X=(1/2,0,0); M=(1/2,1/2,0) and R=(1/2,1/2,1/2).*

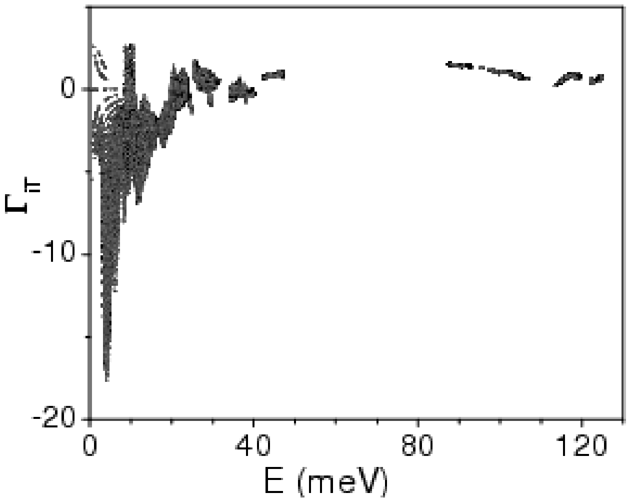

FIG 3.3 *The calculated Grüneisen parameters as a function of phonon energy.*

The calculation of thermal expansion is carried out using the quasi-harmonic approximation. Each phonon mode of energy E_i contributes to the volume thermal expansion coefficient [22] that is given by the relation $\alpha_V = \frac{1}{BV}\sum_i \Gamma_{iT} C_{Vi}(T)$, where V is the unit cell volume, B is the bulk modulus, Γ_{iT} (=-∂lnE$_i$/∂lnV) are the mode Grüneisen parameters and C_{Vi} the specific-heat contributions of the phonons of energy E_i. The index i run over the various phonon branches and all the wave vectors in the Brillouin zone. The Grüneisen parameters Γ_{iT} (Fig. 3.3), are numerically calculated from the pressure dependence of phonon modes around ambient pressure.

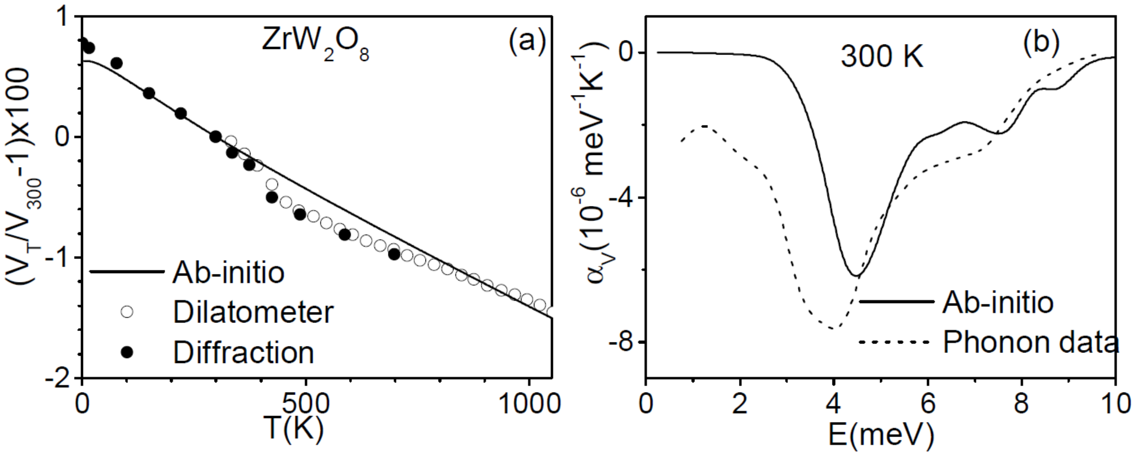

FIG 3.4 (a) *The calculated and experimental[1] relative volume thermal expansion for* ZrW_2O_8, *(*V_T/V_{300}*-1) × 100 % ,* V_T *and* V_{300} *being the cell volumes at temperature T and 300 K respectively. (b) The contribution of phonons of energy E to the volume thermal expansion as a function of E at 300 K from the ab-initio calculation as well as phonon data [9].*

The calculated α_V at 300 K from ab-initio calculation is -22.5 × 10^{-6} K^{-1}, while the experimental value [1] is about -29 × 10^{-6} K^{-1}. The calculated relative volume thermal expansion is shown in Fig. 3.4(a). The discontinuity in the experimental data at about 400 K is associated with an order-disorder phase transition. We find that there is a slight deviation between the experimental data [1] and the calculations at low temperatures due to underestimation of the contribution from low energy phonon modes. Similar underestimation of the anharmonicity of low energy phonon modes is also found in cases of $Zn(CN)_2$ [23] as well as $Ag_3M(CN)_6$ (M=Co,Fe) [24]. The properties of the low energy phonon modes are very sensitive to volume of the crystal. DFT calculations overestimate or underestimate crystal volume depending on the exchange correlation functional.

TABLE 3.1 *The calculated change in energy of selected phonon modes on increase of temperature from 0 to 300 K.* E_i *and* Γ_{iT} *are the phonon energy at 0 K and Grüneisen parameter.* ΔE_V *and* ΔE_A *are the change in the phonon energy due to change in volume (implicit anharmonicity), and due to increase in thermal amplitudes of atoms (explicit anharmonicity) respectively, and* ΔE_T *is the total change in the phonon energy. All the energy values are in meV units.*

Wave vector	E_i	Γ_{iT}	ΔE_V	ΔE_A	ΔE_T
Γ	4.93	-7.0	-0.22	0.15	-0.07
Γ	5.21	-5.7	-0.19	0.16	-0.03
X	3.90	-5.7	-0.14	0.22	0.08
X	4.16	-2.4	-0.06	0.68	0.62
M	4.51	-12.7	-0.36	0.42	0.06
M	4.65	-12.8	-0.37	0.55	0.18
R	5.29	-11.7	-0.39	-0.38	-0.77

The contribution of phonon density of states at energy E to the thermal expansion has been determined (Fig. 3.4(b)) as a function of phonon energy at 300 K. We find that the maximum contribution to α_V is found to be from phonon modes of energy 4.5 ± 1 meV, which is consistent with the previous analysis of high pressure inelastic neutron scattering measurements [9] as well as diffraction data [5]. The eigenvectors of a few of the low energy modes (Table 3.1) that contribute most to NTE have also been plotted (Fig. 3.5 and S4 [21]). The nature of these phonons can be best understood by the animations [21]. The lowest Γ-point mode of 4.93 meV (Γ_{iT} = -7.0) involves out-of-phase translation of two chains consisting of WO_4 and ZrO_6, while the Γ-point mode of 5.21 meV (Γ_{iT} = -5.7) show out-of-phase rotation of WO_4 and translation of ZrO_6 in two different chains. These modes also involve significant distortion of WO_4 tetrahedra formed around W1 and W2.

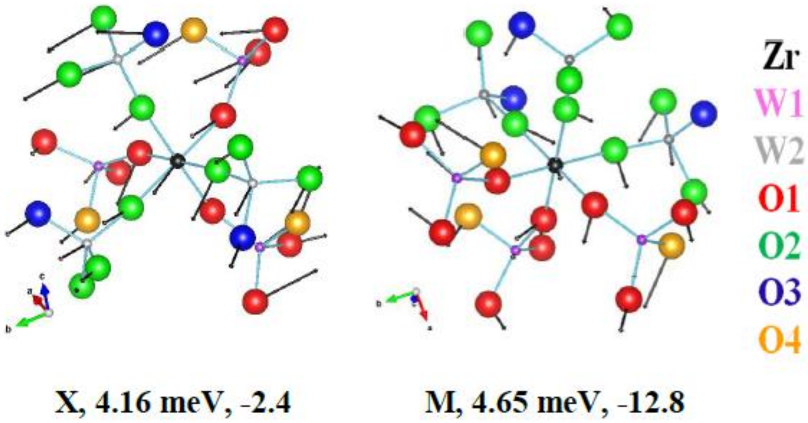

FIG 3.5 *Polarization vectors of selected phonon modes in ZrW_2O_8. The numbers after the wave vector (X and M) give the phonon energies and Grüneisen parameters respectively. The lengths of arrows are related to the displacements of the atoms. The atoms are labeled as indicated in Ref.[1].*

Hancock et al [12] proposed two types of modes for understanding the mechanism of NTE. In one of the mode both ZrO_6 as well as WO_4 in a chain rotate and also translate along the <111> axis. As discussed above, for the two lowest optic modes we have not found simultaneous rotational motion of both the ZrO_6 as well as WO_4. However we find that for the X-point modes of 3.90 meV (Γ_{iT} = -5.7) and 4.16 meV (Γ_{iT} = -2.4), the motion of polyhedral units is similar to that proposed by Hancock et al [12]. The modes show in-phase translation and rotation of WO_4 and ZrO_6 in a single chain. The motion of tetrahedral and octahedral units in two different chains is also in-phase. While the two modes seem to be of similar nature, the relative amplitudes of Zr, W atoms and O atoms are found to be different.

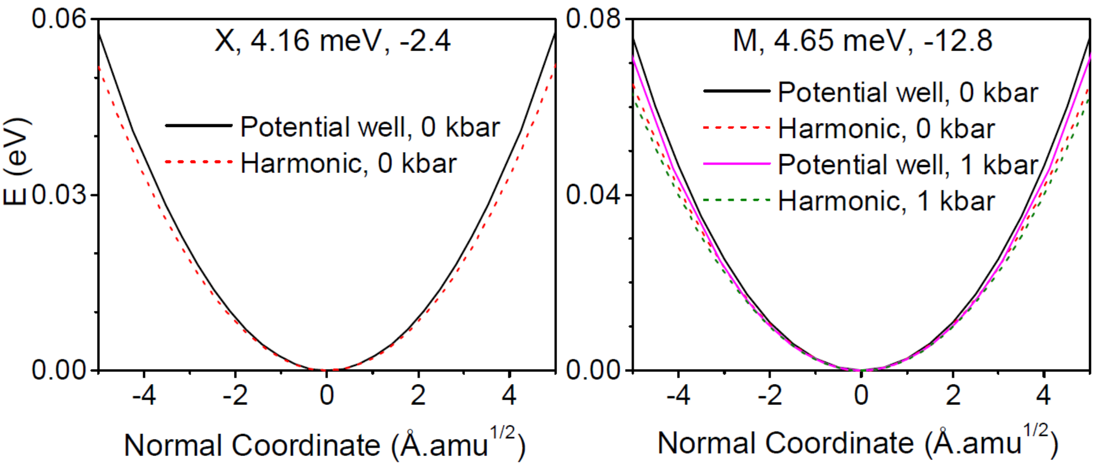

FIG 3. 6 *Calculated potential wells of selected phonon modes in ZrW_2O_8. The numbers after the wave vector (X and M) give the phonon energies and Grüneisen parameters respectively.*

The second mode proposed by Hancock et al [12] indicates that ZrO_6 octahedron rotates opposite to the WO_4 tetrahedra. We find that R-point (0.5 0.5 0.5) mode of 5.29 meV with Γ_{iT} value of -11.7 show similar behaviour. The two WO_4 around W1 and W2 in a chain rotate in-phase while ZrO_6 rotate out-of phase. In general we find that in most of the modes, amplitude of the free oxygens O3 and O4 are larger as compared to that of shared oxygen's O1 and O2. This means that rotation of WO_4 and ZrO_6 is accompanied by distortion of these polyhedra.

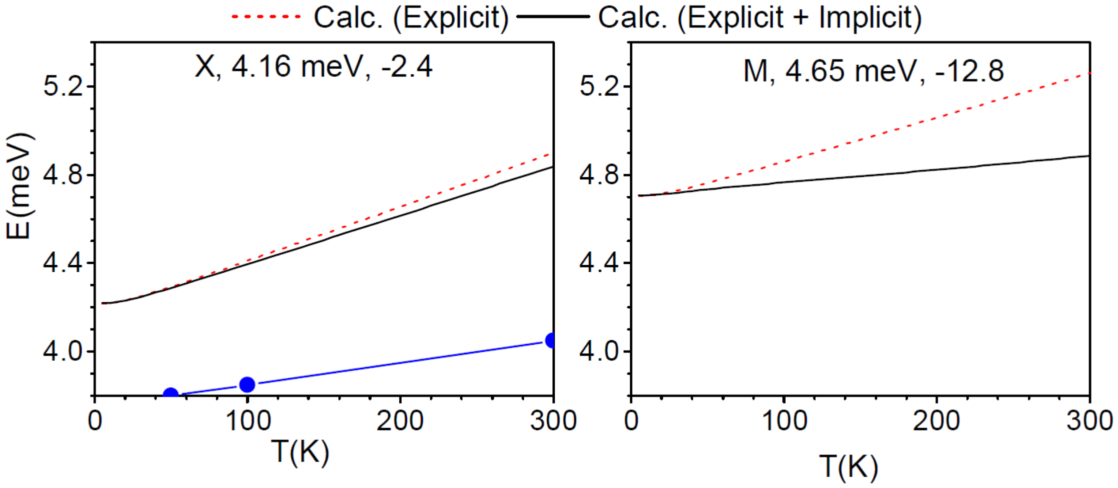

FIG 3.7 *Calculated temperature dependence of selected phonon modes in ZrW_2O_8. The numbers after the wave vector (X and M) give the phonon energies and Grüneisen parameters respectively. For comparison, the experimental temperature dependence of phonon peak at 3.8 meV in the density of states[5] is also shown, which involves average over entire Brillouin zone.*

The M-point modes of 4.51 meV and 4.65 meV energy have negative Grüneisen parameter Γ_{iT} value of about -12.7 and -12.8 respectively. The mode at 4.51 meV involves in-phase translation and bending of WO_4 and ZrO_6 network. The mode is very similar to that previously described by Cao et al [13], where a correlated motion between WO_4 and it nearest ZrO_6 is shown to lead NTE. However, for 4.65 meV mode we find out-of-phase translation of WO_4 and ZrO_6 in two chains.

The temperature dependence of phonon density of states of ZrW_2O_8 shows [5] hardening of the peak at 3.8 meV to 4.05 meV on increase of temperature from 50 K to 300 K. On the other hand, the same peak is found to soften with pressure [9] although both increase in pressure and temperature involve compression of the lattice. Temperature and pressure variation of the phonon energy is known to occur due to anharmonicity of the interatomic potential. The change in phonon energies is due to two effects. The so called "implicit" anharmonicity, refers to the volume dependence of the phonon spectra that can be calculated in the quasiharmonic approximation. The second is the "explicit" anharmonicity, which refer to the changes in phonon frequencies due to large thermal amplitude of atoms. The change in phonon energies with temperature is due to both the "implicit" as well as "explicit" anharmonicities, while the pressure effect only involves the implicit part. We would also call the "implicit" and "explicit" parts as volume and amplitude effects respectively.

In a complex crystal it is quite difficult to estimate the anharmonic effects rigorously. However, one can make certain simplifying assumptions and arrive at qualitative trends in the shifts of selected phonons as a function of temperature. The potential wells of a few of the phonon modes at high symmetry points in the cubic Brillouin zone have been calculated and used to estimate the temperature dependence of the phonon frequencies. The detailed procedure for calculation of explicit part of the temperature dependence of phonon modes can be found in reference [21] as well as in Refs.[25-27].

The potential wells (Fig.3.6 and S5 [21]) of the seven modes of energy around 4.5 meV, along the high symmetry points namely Γ, X, M and R in the cubic Brillouin zone, have been calculated. The energy of modes may increase or decrease with increase of temperature, depending on the nature of anharmonicity. The potential wells for Γ point mode of energy at 4.93 and 5.21 meV (Table SIII [21]) have cubic as well as quadratic anharmonicity, while all the remaining five modes have only quadratic anharmonicity. The potential well for M point mode of 4.65 meV with Grüneisen parameter Γ_{iT} value of about -12.7 has also been plotted at 1 kbar. As expected the width of the well is slightly increased due to softening of phonon mode on compression.

The anharmonicity parameters (Table SIII [21]) as obtained from fitting of equation (S1 [21]) to the potential well are used for calculating the temperature dependence of phonon modes. We find (Fig. 3.7 and S6 [21]) that zone boundary mode of energy 4.16 meV (0 K) at X-point shows maximum hardening and shifts to 4.78 meV on increase of temperature to 300 K. The low energy Γ-point modes do not respond to temperature and remain nearly invariant with temperature. The R-point mode of energy 5.29 meV shows normal behaviour of decrease of phonon energy with increase of temperature. The calculated energy shift for low energy modes on increase of temperature from 0 to 300 K is given in Table 3.1. Ab-initio calculations are able to qualitatively explain the experimentally observed [5] temperature dependence of low energy phonon spectra of ZrW_2O_8 (Fig. 3.7).

We would like to draw attention to the fact that the modes at M and R point show large implicit anharmonicity. These modes are important for understanding the NTE behaviour. However as far as temperature dependence is concerned, the X-point mode having low negative Grüneisen parameter Γ_{iT} value of -2.4 shows maximum temperature dependence. Recently in case of NTE compounds ScF_3 [15] and ReO_3 [14] respectively, R-point and M-point modes are found to show large pressure as well as temperature dependence. The authors also found large quadratic anharmonicity for the same modes. We would like to say that quadratic anharmonicity is useful to explain the large temperature dependence of R-point and M-point modes and is not relevant to NTE.

3.3 Conclusions

To summarize, the ab-initio density functional calculations of phonons modes of ZrW_2O_8 have been reported in the entire Brillouin zone. Certain phonon modes are found to be highly anharmonic in nature. The calculations agree quite well with the reported NTE behavior of ZrW_2O_8. We have also been able to explain the observed anomalous pressure as well as temperature variation of the energies of phonon modes. The increase of the frequency with temperature essentially results from the cubic and/or quadratic anharmonic part of the phonon potential, which is able to explain the temperature dependence of low energy modes as reported in the literature.

[1] T. A. Mary, J. S. O. Evans, T. Vogt and A. W. Sleight, Science **272**, 90 (1996).

[2] B. K. Greve, K. L. Martin, P. L. Lee, P. J. Chupas, K. W. Chapman and A. P. Wilkinson, Journal of the American Chemical Society **132**, 15496 (2010).

[3] C. Lind, A. P. Wilkinson, Z. Hu, S. Short and J. D. Jorgensen, Chemistry of Materials **10**, 2335 (1998).

[4] A. L. Goodwin, D. A. Keen, M. G. Tucker, M. T. Dove, L. Peters and J. S. O. Evans, Journal of the American Chemical Society **130**, 9660 (2008).

[5] G. Ernst, C. Broholm, G. R. Kowach and A. P. Ramirez, Nature **396**, 147 (1998).

[6] V. Gava, A. L. Martinotto and C. A. Perottoni, Physical Review Letters **109**, 195503 (2012).

[7] T. R. Ravindran, A. K. Arora and T. A. Mary, Physical Review Letters **84**, 3879 (2000).

[8] R. Mittal and S. L. Chaplot, Physical Review B **60**, 7234 (1999).

[9] R. Mittal, S. L. Chaplot, H. Schober and T. A. Mary, Physical Review Letters **86**, 4692 (2001).

[10] M. G. Tucker, A. L. Goodwin, M. T. Dove, D. A. Keen, S. A. Wells and J. S. O. Evans, Physical Review Letters **95**, 255501 (2005).

[11] K. A. P. Alexandra, D. H. Kenton, T. D. Martin, H. Volker, D. G. Julian and C. W. Michele, Journal of Physics: Condensed Matter **8**, 10973 (1996).

[12] J. N. Hancock, C. Turpen, Z. Schlesinger, G. R. Kowach and A. P. Ramirez, Physical Review Letters **93**, 225501 (2004).

[13] D. Cao, F. Bridges, G. R. Kowach and A. P. Ramirez, Physical Review Letters **89**, 215902 (2002).

[14] T. Chatterji, P. G. Freeman, M. Jimenez-Ruiz, R. Mittal and S. L. Chaplot, Physical Review B **79**, 184302 (2009).

[15] C. W. Li, X. Tang, J. A. Muñoz, J. B. Keith, S. J. Tracy, D. L. Abernathy and B. Fultz, Physical Review Letters **107**, 195504 (2011).

[16] G. Kresse and J. Furthmüller, Computational Materials Science **6**, 15 (1996).

[17] G. Kresse and D. Joubert, Physical Review B **59**, 1758 (1999).

[18] J. P. Perdew, K. Burke and M. Ernzerhof, Physical Review Letters **77**, 3865 (1996).

[19] J. P. Perdew, K. Burke and M. Ernzerhof, Physical Review Letters **78**, 1396 (1997).

[20] K. Parlinksi, (2003)

[21] M. K. Gupta, R. Mittal and S. L. Chaplot, Physical Review B **88**, 014303 (2013).

[22] G. Venkataraman, L. A. Feldkamp and V. C. Sahni, Dynamics of perfect crystals (MIT Press, Cambridge, 1975).

[23] R. Mittal, M. Zbiri, H. Schober, E. Marelli, S. J. Hibble, A. M. Chippindale and S. L. Chaplot, Physical Review B **83**, 024301 (2011).

[24] R. Mittal, M. Zbiri, H. Schober, S. N. Achary, A. K. Tyagi and S. L. Chaplot, Journal of Physics: Condensed Matter **24**, 505404 (2012).

[25] N. Choudhury, S. L. Chaplot and K. R. Rao, Physical Review B **33**, 8607 (1986).

[26] B. Kuchta and T. Luty, Chemical Physics Letters **92**, 462 (1982).

[27] B. Kuchta and T. Luty, The Journal of Chemical Physics **78**, 1447 (1983).

Chapter 4

Spin-Phonon Coupling and Phase Transitions in Multiferroic Compounds $GaFeO_3$ and $YMnO_3$

4.1 Introduction

Materials showing more than two ferroic properties (magnetism, electricity, and elasticity) simultaneously come under the umbrella of multiferroics whose characteristics include the emergence of simultaneous electric and magnetic orderings, offering therefore opportunities for multifunctional device applications. This justifies the intense research going on this class of materials, and the keen interest they are subject to, at both the fundamental and practical sides [1-15]. Magnetism in transition metals containing materials is induced by the active spin components in the d-shell levels. On the other hand, ferroelectricity occurs generally in the absence of d-electrons. Hence it is intriguing to observe multiferroicity since this phenomenon involves a simultaneous emergence of both the properties. Over the last few decades, various multiferroic materials have been discovered which exhibit magnetoelectric (ME) coupling. However, most of the magnetoelectric multiferroics possess magnetic and ferroelectric transition temperatures far from the ambient one. For example in the case of $BiMnO_3$ [14], the Curie temperature, $T_{C,}$ is about 100 K while the Neel temperature, $T_{N,}$ is close to 750 K. This results in a weak magnetoelctric coupling at the ambient conditions.

Practically, the weak coupling materials are not potentially useful. However, there are few mechanisms allowing to tune these properties simultaneously; like magnetic ferroelectricity induced by frustrated magnetism, lone pair effect, charge-ordering, and local non-centrosymmetry. For instance, the charge ordering driven magnetic ferroelectricity is observed in a large number of rare earth oxides [11, 12]. Understanding the mechanism of multiferrocity is of considerable importance for the design of new multiferroics at controllable conditions (temperature and pressure). Hence the electric and magnetic properties attributed to the dynamics of ions and electrons need to be studied and explored. In this chapter, results obtained on multiferroic compounds $GaFeO_3$ and $YMnO_3$ are given in sections 4.2 and 4.3 respectively.

4.2 $GaFeO_3$

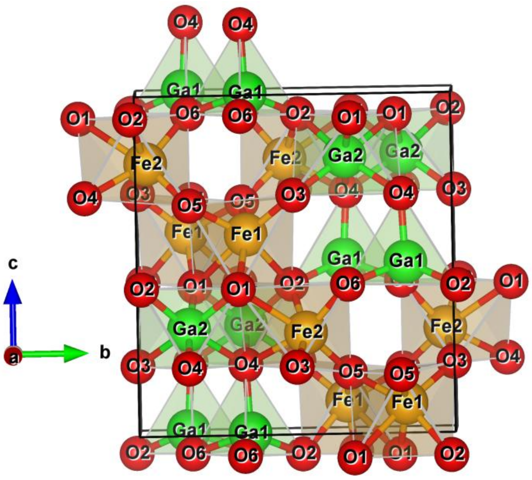

FIG 4.1 *Crystal structure of $GaFeO_3$ in the $Pc2_1n$ space group. The atoms are labeled following Table 4.1.*

$GaFeO_3$ belongs to the class of multiferroic compounds and shows a ME coupling at low temperature. It does not contain lead or bismuth species, making it ecologically and biologically attractive. At room temperature the structure [15] is chiral orthorhombic ($Pc2_1n$), while its parental oxides Fe_2O_3 and Ga_2O_3 occur [16] in the rhombohedral and monoclinic phases, respectively. The orthorhombic structure of $GaFeO_3$ has eight formula units per unit-cell, with two different symmetry inequivalent sites of iron and gallium atoms; Fe1, Fe2, and Ga1 and Ga2, respectively. The tetrahedral sites are occupied by Ga1, while Ga2, Fe1 and Fe2 occupy all the octahedral sites (Fig. 4.1). The electric polarization is found [15] to be along the b axis at ambient conditions. Ideally, the magnetic structure of $GaFeO_3$ is expected to reflect an antiferromagnetic ordering, since the magnetic moments of Fe1 and Fe2 cations are antiparallel. However due to the observed disorder on the Fe and Ga sites [15], a ferri-magnetic transition is observed below 225 K, instead [15, 17]. The magnetization axis was found to be along c-axis.

In a first principles study, authors [18, 19] suggest that distorted octahedra, GaO_6 and FeO_6, in $GaFeO_3$ lead to a noncentrosymmetric structure, which might be responsible for the electric polarization. The authors also showed that the site disorder involving the interchange of Fe and Ga2 sites is highly probable and consistent with the presence of the observed Fe disorder [15] with the Ga2 site. They indicate that the minimum of total energy is reached when adopting an antiferromagnetic spin configuration. However, anti site disorder of Fe and Ga atoms between octahedral Ga and Fe sites lead to a finite magnetic moment, and $GaFeO_3$ behaves like a ferrimagnet. It has been concluded that significant orbital magnetic moment of Fe ions is attributed to the local distortion of oxygen octahedra and the off centering of the iron atoms. Interestingly, the unequal distribution of Fe spins in $GaFeO_3$ is due to the Ga-Fe disorder. This material is known to exhibit piezoelectricity and ferrimagnetism, with a Curie temperature, $T_{C,}$ of about 225 K. This could be enhanced by a site disorder between Ga and

Fe. It has been shown that the T_C could be enhanced [20] to ~ 350 K by increasing the Fe content to about 40% ($Ga_{2-x}Fe_xO_3$ (x=1.40). The magnetic structure and magnetoelectric properties of $Ga_{2-x}Fe_xO_3$ ($0<x<1.1$) were extensively studied by T. Arima and coworkers [15]. The authors found that the saturated magnetization as well as the ferrimagnetic phase transition temperature increases with increase in Fe content, while the coercive force decreases. The linear and quadratic ME coefficients measurements show that the electric polarization is largely modulated when a magnetic field is applied parallel to the direction of the spontaneous magnetization. However it has a negligible effect when the field is applied parallel to the spontaneous polarization axis. Thin films of $GaFeO_3$ are reported to exhibit [21, 22] ferroelectricity at room temperature, which makes them practically useful at the nano-level. We note also that the ball milling transforms [23] the structure of $GaFeO_3$ from orthorhombic to rhombohedral (R3c).

First Principle studies of zone centre phonon modes and Raman measurements were reported on the isostructural compound $AlFeO_3$ by Kumar and coworkers [24]. The Raman measurements have been performed in the temperature range 5 - 315 K. The observed spectra showed that the intensity of the Raman mode at 1230 cm^{-1} vanishes to zero above 250 K. It was concluded that this mode originates from a two magnon Raman process. The authors also reported first principles calculation of the zone center phonon modes in magnetic ordered and disordered structure. They found a strong interaction between spin and lattice vibrations [24]. X-Ray as well as neutron diffraction, dielectric, Raman and IR measurements have been reported on $GaFeO_3$ [25-30]. No structural phase transition was observed [30] in the temperature range 14 - 1368 K. A dielectric anomaly [26] has been observed at the magnetic transition temperature. A spin-phonon coupling is reported [28] to take place below 210 K by observing the discontinuity in the peak position of the Raman mode at 374 cm^{-1}. Raman and Mossbauer spectroscopic studies on $GaFeO_3$ have also been reported [29].

TABLE 4.1 *Comparison between the experimental (4 K) and calculated (0 K) structural parameters of* $GaFeO_3$ *(orthorhombic phase, space group* $Pc2_1n$*).*

		Expt.	**FM(GGA)**	**FM(LDA)**	**PNM(LDA)**	**FNM(LDA)**
	a (Å)	8.7193	8.8516	8.6610	8.6610	8.4791
	b (Å)	9.3684	9.5232	9.2923	9.2923	8.7713
	c (Å)	5.0672	5.1491	5.0355	5.0355	4.9999
O1	*x*	0.3228	0.3221	0.3233	0.3154	0.3255
	y	0.4262	0.4268	0.4291	0.4405	0.4517
	z	0.9716	0.9825	0.9836	0.9860	0.9802
O2	*x*	0.4864	0.4868	0.4857	0.4853	0.4789
	y	0.4311	0.4323	0.4330	0.4413	0.4555
	z	0.5142	0.5190	0.5190	0.5331	0.5312
O3	*x*	0.9979	0.9970	0.9969	0.9877	0.9851
	y	0.2022	0.2022	0.2014	0.2091	0.2216
	z	0.6541	0.6579	0.6564	0.6599	0.6605
O4	*x*	0.1593	0.1615	0.1621	0.1564	0.1590
	y	0.1974	0.1996	0.2005	0.2049	0.2123
	z	0.1480	0.1570	0.1575	0.1684	0.1662
O5	*x*	0.1695	0.1683	0.1677	0.1667	0.1651
	y	0.6717	0.6726	0.6742	0.6820	0.7001
	z	0.8437	0.8422	0.8447	0.8245	0.8309
O6	*x*	0.1736	0.1671	0.1664	0.1658	0.1632
	y	0.9383	0.9391	0.9394	0.9365	0.9509
	z	0.5166	0.5180	0.5217	0.5247	0.5372
Fe1	*x*	0.1538	0.1539	0.1549	0.1678	0.1709
	y	0.5831	0.5834	0.5836	0.5894	0.6049
	z	0.1886	0.1857	0.1883	0.1691	0.1689
Fe2	*x*	0.0346	0.0316	0.0308	0.0269	0.0186
	y	0.7998	0.7956	0.7961	0.8000	0.8168
	x	0.6795	0.6721	0.6739	0.6772	0.6785
Ga1	*x*	0.1500	0.1520	0.1510	0.1503	0.1462
	y	0.0	0.0	0.0000	0.0000	0.0000
	z	0.1781	0.1749	0.1770	0.1789	0.1873
Ga2	*x*	0.1593	0.1608	0.1607	0.1561	0.1589
	y	0.3073	0.3089	0.3095	0.3139	0.3204
	z	0.8106	0.8167	0.8160	0.8189	0.8181

The authors observed a disordered nature of the compound. The peak width of the phonon mode at 700 cm^{-1} shows an anomalous large broadening around the Curie temperature, which is a measure of anharmonicity. The data was interpreted within the context of coupling of phonons and the Fe spins. Further, the stability of $GaFeO_3$ has been studied [31] under pressure; up to about 65 GPa. The compound undergoes a phase transition [31] from $Pc2_1n$ to Pbnm phase at about 25 GPa. Increasing further the pressure to 53 GPa, the Pbnm phase also undergoes first order phase transition due to quenching of the Fe magnetic moment. Spin waves measurements have been reported by inelastic neutron scattering [32-34] in similar systems ($TmFeO_3$, $ErFeO_3$, YFeO3 and $TbFeO_3$). It comes out that an incommensurate phase was evidenced [34] in $TbFeO_{3,}$ upon applying a magnetic field.

The various studies available on $GaFeO_3$ are based on structural and electronic considerations. A limited amount of work on phonon dynamics has been reported, but it was restricted to the zone centre phonon modes. Presently, we provide a detailed analysis of lattice dynamics and spin phonon coupling in $GaFeO_3$, where both the zone-centre and zone-boundary modes are covered. A better understanding of the dynamics governing the thermodynamical aspects of this promising multiferroic looks necessary for future fundamental and practical developments. In this context, we have measured the phonon density of states over a wide temperature range 150-1198 K. We have computed the phonon spectrum from first principles density functional theory to quantitatively explore the dynamics. The study is done in the ordered phase, by first considering the magnetic interactions and then neglecting them to better explore the possible interplay and effect of the spin degrees of freedom on the lattice dynamics [35, 36]. Further, the total energy and enthalpy is estimated in various phases to determine the relative phase stability of $GaFeO_3$. The equation of state has been calculated and compared with the available experimental data.

The measurements were performed at several temperatures in the range 150-1198 K at IN4C spectrometer at the Institut Laue Langevin (ILL), France. The low temperature measurements were performed using a standard orange cryostat. For the high temperature range, the sample was put into a quartz tube insert and mounted into a furnace. The other end of the quartz tube was kept open in the air. For these measurements we have used an incident neutron wavelength of 2.4 Å (14.2 meV), performing in the up-scattering mode (neutron energy gain). The momentum transfer, Q, extends up to 7 $Å^{-1}$.

The plane wave energy cutoff for density functional theory calculations were set to 620, 720 and 740 eV, with soft pseudopotentials, then including only the Ga semi core electrons, and also with semi core electrons of both Ga and Fe, respectively using VASP [37, 38]. A 4×4×4 k-points mesh for the Brillouin zone integration was found to be suitable for the required convergence. Total energies were calculated for 60 generated structures resulting from individual displacements of the symmetry inequivalent atoms in the orthorhombic ($Pc2_1n$) phase, along the six inequivalent Cartesian directions ($\pm x$, $\pm y$ and $\pm z$). Phonons are extracted from subsequent calculations using the direct method as implemented in the Phonon software [39]. The free energy calculations of $GaFeO_3$ are also done in the Pbnm and R3c phases. The GGA was formulated by the Perdew–Burke–Ernzerhof (PBE) density functional[40]. The LDA was based on the Ceperly–Alder parametrization by Perdew and Zunger [41]. The valence electronic configurations of Ga, Fe and O as used in calculations for pseudo potential generation are s^2p^1, d^7s^1 and s^2p^4, respectively. Both non-spin-polarized and spin polarized calculations were performed. The magnetic calculations have been carried out for the A-type antiferromagnetic ordering in the $Pc2_1n$ phase. Moreover, since $GaFeO_3$ is known to be a Mott insulator, the on-site Hubbard correction is applied using the Dudarev approach [42] using U_{eff}=4 eV [43-47]. Both full (lattice constants and atomic positions) and partial (only atomic positions) geometry relaxations were carried out. Hereafter, the labeling

“FM” and “FNM” refer to fully relaxed magnetic and fully relaxed non-magnetic calculations. Further, “PNM” refers to the partially relaxed non-magnetic calculation, where we used the structure obtained from “FM” and relaxed only the atomic positions without magnetic ordering. The structural details relevant to the present calculations are summarized in Table 4.1. Further, we performed fully relaxed magnetic calculations (labeled as FM_Ga_SC) including the semi core electrons of the Ga atoms having the electronic configuration $d^{10}s^2p^1$. The equation of states as well as the free energy of $GaFeO_3$ has also been evaluated in the fully relaxed magnetic calculations (labeled as FM_GaFe_SC) by considering $d^{10}s^2p^1$ and $p^6d^7s^1$ electronic configuration for Ga and Fe atoms, respectively.

4.2.1 Results and Discussion

4.2.1.1 Temperature Dependence of Phonon Spectra

The phonon spectra of $GaFeO_3$ (Fig. 4.2) were measured up to 1198 K, across the magnetic transition (~ 225 K)**.** The magnetic signal is expected to be more pronounced at low Q, and to vanish at high Q, following the magnetic form factor. Therefore, two Q-domains were considered; i.e., high-Q (4 to 7 Å^{-1}) and low-Q (1 to 4 Å^{-1}). The temperature dependence of the Bose factor corrected S(Q,E) plots of $GaFeO_3$ are shown in Fig 4.2. At low temperatures (upto 315 K), the low-Q data shows a larger elastic line as compared to the high-Q spectra. Presently, given the lack of detailed magnetic measurements, we speculate that this quasi-elastic scattering may originates from spin fluctuations which disappear at high temperatures. In the high temperature range, only phonons contributes significantly to the spectra, and therefore the width of the elastic line is similar in both the Q ranges.

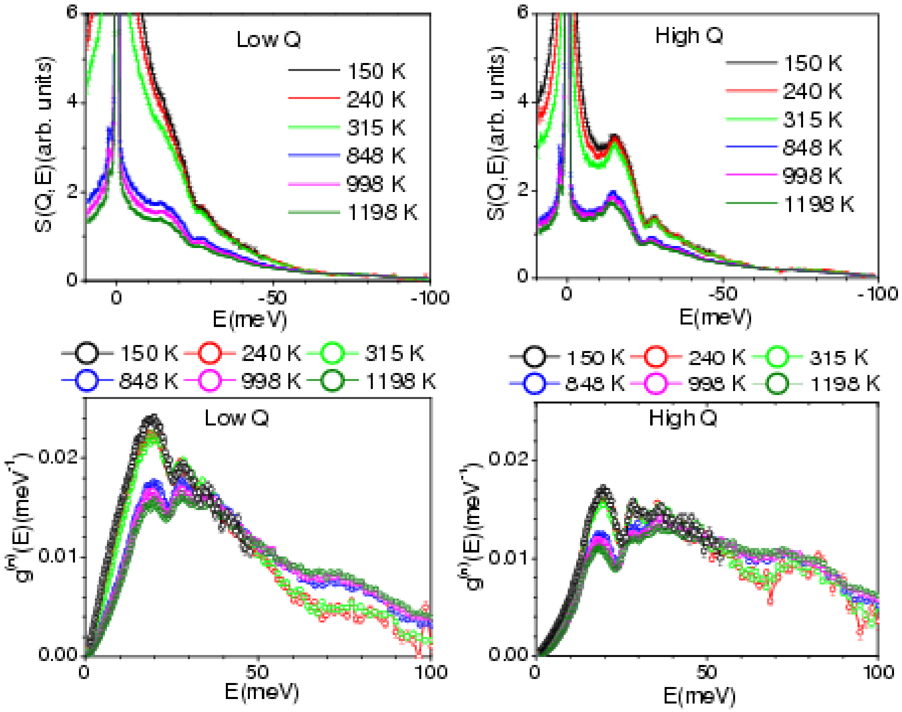

FIG 4.2 *Temperature dependent inelastic neutron spectra of* $GaFeO_3$*. Top panel: the low-Q and high-Q Bose factor corrected S(Q,E), where both the energy loss (0 - 10 meV) and the energy gain (-100 - 0 meV) sides are shown. Bottom panel: the low-Q and high-Q, unity-normalized, phonon density of states,* $g^{(n)}(E)$*, inferred from the neutron energy gain mode S(Q,E) data, within the incoherent approximation.*

The phonon spectra inferred from the S(Q,E) data, within the incoherent approximation, are also shown in Fig. 4.2. The phonon spectra consist of several peaks located around 20, 30, 55 and 80 meV. We find that both the high Q as well as the low Q data show large variation in the intensity as a function of temperature. At low energy (below 40 meV), the low Q data are more intense in comparison to the high Q data. Further for the low Q part, at 150 K below the magnetic transition temperature (~225 K), there is a large intensity of the low energy inelastic spectra (~ 20 meV) as compared to the data collected at higher temperatures. This is expected to be due to a strong magnetic signal. At 848 K, it is found that in both the low Q as well the high Q data, there is a considerable decrease of the intensity of the low energy peaks around 20 meV. Although $GaFeO_3$ undergoes a paramagnetic to ferri-magnetic transition [15] around 225 K, a paramagnetic scattering persists in the low energy range around 20 meV, at 240 and 315 K. The intensity in the higher energy range, above 55 meV, of the high Q data does not show significant temperature dependence, confirming a pure phonon contribution in these spectral regime. Above 848 K, there is a loss of intensity, due to paramagnetic scattering, and only phonons contribute in this range. $GaFeO_3$ does not show any structural phase transition at high temperature. However polyhedral (GaO_4, GaO_6, FeO_6) distortions are found to increase upon heating up to 1198 K [30]. This might be an additional reason for the broadening of the phonon spectra above 60 meV at high temperatures, besides the increased thermal amplitudes.

4.2.1.2 Magnetic Ordering and Calculated Phonon Spectra

The microscopic origin of the polarization in multiferroic materials is attributed to the hybridization of the electronic orbitals producing a polar charge distribution and ionic displacements from the related centro-symmetric positions. Hence, it is important to study the lattice dynamics in order to understand the ME properties of multiferroics. Detailed electronic structure calculations of $GaFeO_3$ are reported in the literature [18, 19, 44]. However, phonon studies over the whole Brillouin zone are missing. Calculations of (electronic) structure and dynamics would help to gain newer and deeper insights into the various physical properties and possible phase transitions of this kind of materials.

The calculated Fe magnetic moment in the equilibrium structure in the $Pc2_1n$ phase at Fe1 and Fe2 sites are 4.1 μ_B and 4.1 μ_B, respectively, which is in agreement with the reported experimental values [15] of 3.9 μ_B, 4.5 μ_B. Neglecting the spin degrees of freedom in the calculations leads to a collapse of the b-lattice parameter, with a value decreasing from 9.29 Å to 8.77 Å. However by considering Fe magnetism, the calculated value of b-lattice parameter is brought to agreement with the observation (Table 4.1).

Fig. 4.3 compares the experimental and calculated phonon spectra. The "FNM" calculation results in a shift of all the modes to higher energies. This is due to the fact that the b-axis is underestimated in FNM calculations, leading to an overestimation of the phonon energies. Interestingly, the model calculations "FM" and "PNM" provide a very good agreement with the experimental spectra. We notice however some differences in the low energy part of the phonon spectra. The difference comes in fact from the value of the Fe magnetic moment in the two numerical models. The main effect of the Fe spin degrees of freedom is to soften the calculated phonon energies around 30 meV, bringing them hence closer to the experimental values. This demonstrates the role of magnetic interactions in $GaFeO_3$, in a similar way to other recent phonon studies in other systems [35, 36].

The "FM"-based calculated phonon spectra (Fig. 4.3) lead to peaks centered around 20, 30, 55 and 80 meV. The experimental spectra show peaks at 20 and 30 meV and clear humps at 55 and 80 meV. $GaFeO_3$ is known to have a Ga-Fe disorder, from diffraction measurements [15]. However our phonon calculations were done in the ordered phase (Table 4.1). The structural disorder could lead to a large variation of the Ga/Fe-O bonds, and would then result in a broadening of the peaks, as experimentally observed.

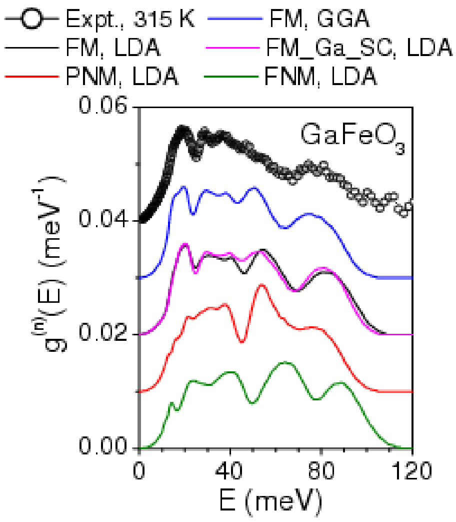

FIG 4.3 *The calculated and experimental neutron inelastic scattering spectra of* $GaFeO_3$. *The experimental data consist of the "High Q" data collected at 315 K. The calculated spectra have been convoluted with a Gaussian of FWHM of 15% of the energy transfer in order to describe the effect of energy resolution in the experiment.*

The difference in the phonon spectra (Fig. 4.3) from the various calculations can be understood from the estimated atomistic contributions in terms of the partial density of states from LDA calculations (Fig. 4.4). The difference is primarily due to the nature of the chemical bonding, in the magnetic and nonmagnetic configurations, as well as the related volume effect. We find that vibrations of Fe and Ga atoms extend up to 45 meV, while the dynamics of the oxygen atoms spreads over the entire spectral range, up to 100 meV. The vibrational aspects due to the two Ga symmetry inequivalent atomic sites remain nearly invariant in all the three calculation types, while the Fe vibrations show a considerable change. The intensity of vibrational density of states of the Fe2 atoms is enhanced around 20 meV. The vibrations of Fe1 as calculated around 30 meV in the non-magnetic calculations are found to soften magnetically, and exhibit a peak around 20 meV. "FNM" calculations predict the oxygen vibrations to extend up to about 100 meV. The overestimation in the range of vibrations is primarily due to the non-inclusion of the Fe magnetic moment which results in a contraction of the unit cell. The “FM” and “PNM” model calculations show that the vibrations of all the oxygen atoms soften in the energy range 60 - 100 meV.

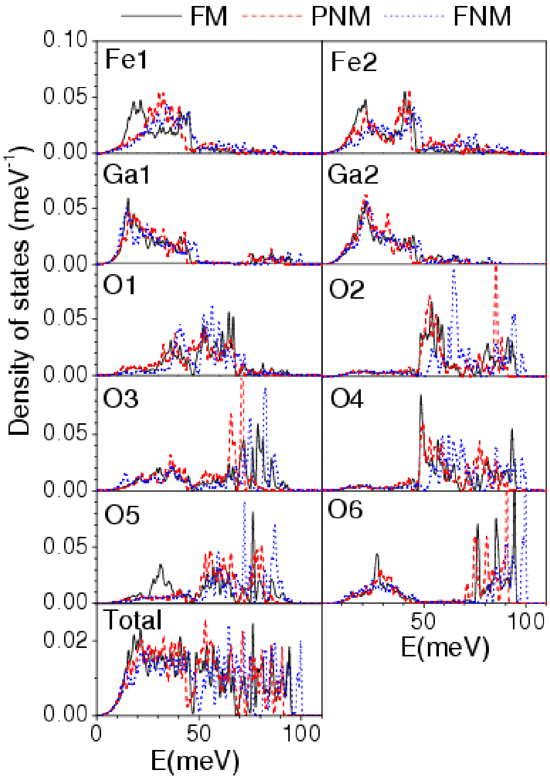

FIG 4.4 *The calculated partial phonon density of states of various atoms in* $GaFeO_3$ *within the local density approximation* (*LDA*)*. The atoms are labeled following Table 4.1. “FM”, “FNM” and “PNM” refer to fully relaxed magnetic, fully relaxed non-magnetic and partially relaxed non magnetic calculations, respectively.*

A further interesting finding consists of the vibrations of the O5 atoms, as extracted from the “FM” calculation type. The O5 atoms are connected only to the Fe1 and Fe2 atoms (Figure 4.1). The O5 vibrations (Figure 4.4) around 60 meV are related to the Fe magnetism. This dynamics is found to shift to lower energies at about 30 meV in the “FM” calculations. Given the known effect of the density functional approximation (LDA or GGA) on the volume description (LDA tends to underestimate the volume value and GGA shows the opposite trend), we compare the “FM” calculated phonon spectra from LDA and GGA approaches. The unit cell volume from LDA and GGA calculations is estimated to be 405.3 Å^3 and 434 Å^3, respectively. The experimental value is 413.9 Å^3 [15].

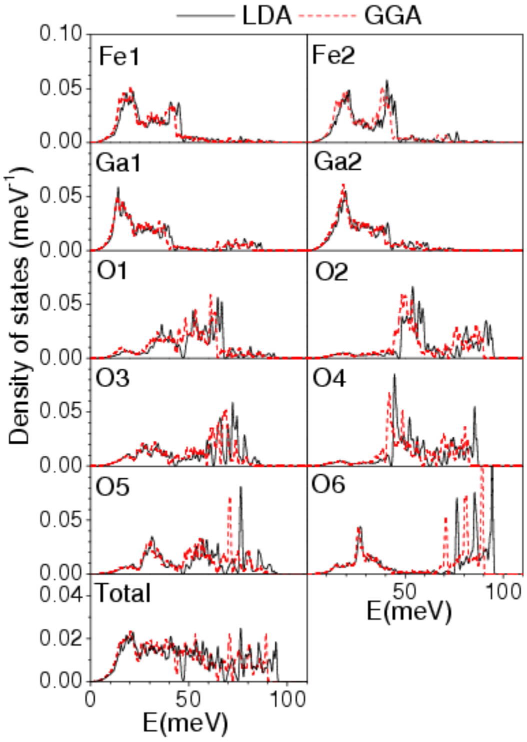

FIG 4.5 *The calculated partial phonon density of states of various atoms in GaFeO$_3$ within the local density approximation* (*LDA*) *and the generalized gradient approximation (GGA) in the fully relaxed magnetic (FM) structure in Pc2$_1$n space group. The atoms are labeled following Table 4.1.*

The low energy part of the phonon spectra, which is sensitive to Fe magnetism, is nearly the same in both LDA and GGA (Figures 4.3 and 4.5). Above 50 meV, some variations are however noticed. The GGA calculated phonons above 50 meV are found to be slightly at lower energies as compared to LDA calculated phonons. Both the exchange-correlation methods lead to an overall good matching with the observations.

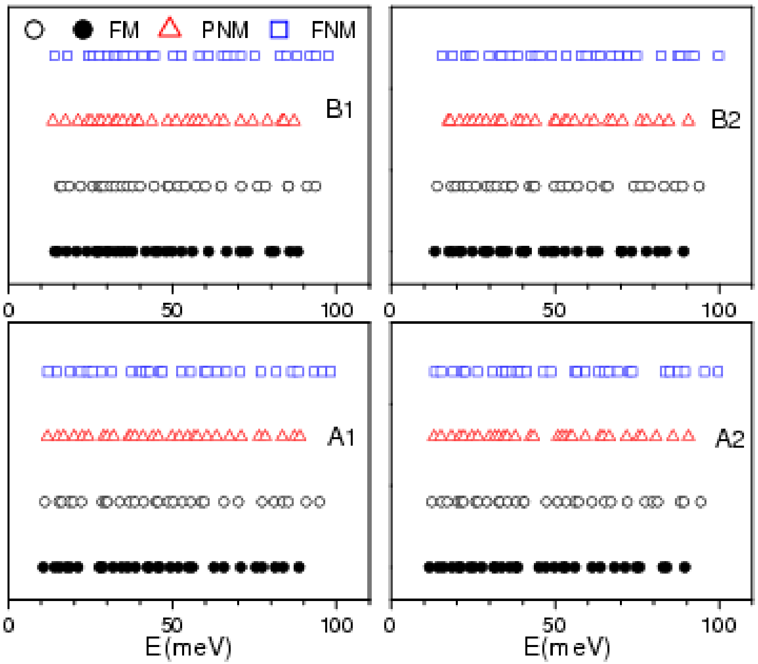

FIG 4.6 *The calculated zone centre phonon modes of GaFeO$_3$ (orthorhombic phase, space group Pc2$_1$n). Open and closed symbols correspond to calculations performed within the local density approximation (LDA) and generalized gradient approximation (GGA), respectively. A1, A2, B1 and B2 correspond to the group theoretical representations of the system symmetry.*

Under the orthorhombic (Pc2$_1$n) symmetry, GaFeO$_3$ possesses 120 zone centre modes corresponding to the irreducible representations: $\Gamma = 30A_1+30A_2+30B_1 +30B_2$. Figure 4.6 compares the determined zone centre phonon modes from the various calculation types. The LDA and GGA approximations lead basically to the same phonon energies. Several modes are found to significantly differ when comparing the magnetic and non magnetic cases. This confirms a spin-phonon coupling behavior. The change in energies of the modes below 25 meV is mainly due to the magnetic interactions, while the high energy phonons are influenced by the volume effect.

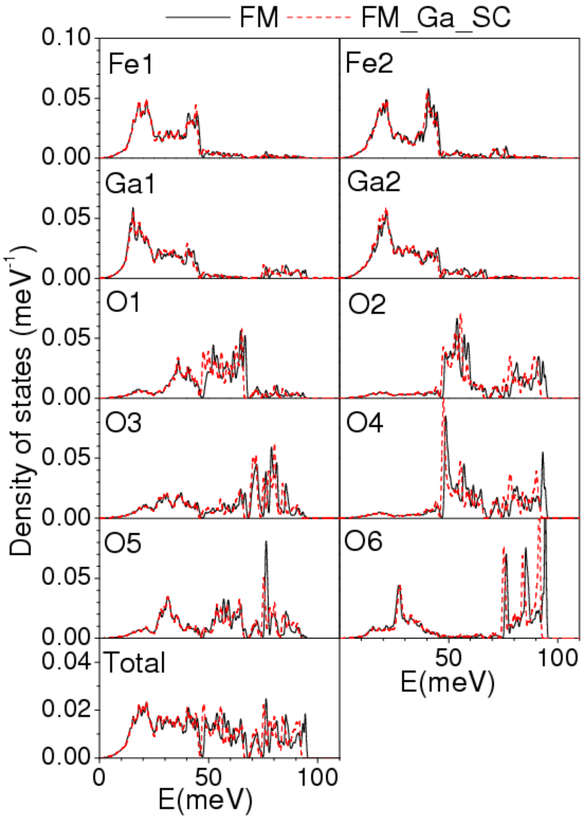

FIG 4.7 *The calculated partial phonon density of states of various atoms in $GaFeO_3$ within the local density approximation (LDA) in $Pc2_1n$ space group. "FM_Ga_SC" and "FM" refer to the fully relaxed magnetic calculations with and without the semi core electrons of the Ga atoms respectively. The atoms are labeled following Table 4.1.*

Further, fully relaxed magnetic calculations (FM_Ga_SC) including the semi core electrons of the Ga atoms ($d^{10}s^2p^1$) are performed. The detailed comparison of the "FM" and "FM_Ga_SC" calculated phonon spectra (Fig. 4.3 and Fig. 4.7) shows that the low energy phonons below 40 meV are not affected by the inclusion of the semicore d-shell electrons of the Ga atoms. The only noticeable difference is detected in the high energy modes which soften by about 1 meV. Both the calculations are in good agreement with the experimental data. The calculated partial densities of states (Fig. 4.7) indicated that the changes in the high-energy range are associated with the change in the partial contribution of O atoms.

4.2.1.3 High Pressure Phase Stability of $GaFeO_3$

The high pressure measurements [31], up to 70 GPa (increasing and decreasing cycles), revealed a very rich phase diagram of $GaFeO_3$. Arielly and coworkers reported the emergence of a new orthorhombic phase (space group Pbnm) above 25 GPa, upon increasing pressure. The transition was found to fully establish at 45 GPa. In this phase all the Ga atoms have eight co-ordinations. However in the $Pc2_1n$ phase, two different Ga sites are distinguishable; one with a six-fold symmetry, and the other possessing a four-fold coordination. Increasing further the pressure to about 53 GPa results in another first order transition with significant drop of the volume. However, the system remains in the same orthorhombic space group (Pbnm). At this pressure value (53 GPa), the magnetic interactions weaken due to the broadening of the iron d-bands. Mossbauer measurement reveals that the Neel temperature is close to 5 K, at about 77 GPa. Further decreasing the pressure to the ambient value, the hexagonal R3c phase was found to be the stable one, which is different from the originally starting orthorhombic $Pc2_1n$ phase, at ambient conditions. In the literature [31], only the lattice parameters of $GaFeO_3$ are available in the Pbnm and R3c phases. The related atomic co-ordinates are missing. We have therefore started from the atomic co-ordinates of $LuFeO_3$ and $LiNbO_3$, as provided in Refs. [48] and [49] respectively. Mossbauer spectroscopy reveals the existence of magnetic ordering in $GaFeO_3$ [31] even at high pressures. The crystal structure of $GaFeO_3$ in Pbnm and R3c phases has been calculated by relaxing the atomic co-ordinates as well as lattice parameters. The total energy has been calculated in both the phases in various antiferromagnetic configurations represented by the

TABLE 4.2 *The calculated structural parameter of $GaFeO_3$ in the orthorhombic (Pbnm) and hexagonal (R3c) phases within* the *local density* approximation (LDA) in the *fully relaxed magnetic structure (FM). In the orthorhombic phase the O1, O2, Fe and Ga atoms are located at 4c (x, 1/4, z), 8d (x, y, z), 4b(1/2, 0, 0) and 4c (x, 1/4, z), respectively, while in the hexagonal phase O, Fe and Fe occupy the positions 36f (x, y, z), 12c (0, 0, z) and 12c (0, 0, z), respectively. The experimental lattice parameters are from Ref.[31].*

Orthorhombic Pbnm phase			
		Expt. (25.7 GPa)	**Calc. (25 GPa)**
	a	4.948(4)	4.793
	b	5.165(20)	4.965
	c	7.0000(8)	7.241
O1	*x*		0.413
	y		0.250
	z		0.142
O2	*x*		0.323
	y		0.076
	z		0.672
Fe	*x*		0.500
	y		0.000
	z		0.000
Ga	*x*		0.059
	y		0.250
	z		0.987
Hexagonal R3c phase			
		Expt. (0.2 GPa)	**Calc. (0 GPa)**
	a	5.036(2)	4.981
	b	5.036(2)	4.981
	c	13.585(7)	13.425
O	*x*		0.969
	y		0.333
	z		0.080
Fe	*x*		0.000
	y		0.000
	z		0.018
Ga	*x*		0.000
	y		0.000
	z		0.309

A, C, and G ordering types. Computationally, we found that the Pbnm phase is the most stable when adopting the G-type antiferromagnetic ordering, while the R3c phase stabilizes with the A-type antiferromagnetism. The calculated structural details under the Pbnm and R3c phases at 25 GPa and ambient pressure, respectively, are given in Table 4.2. Therein the available experimental lattice parameters are also shown.

TABLE 4.3 *The calculated elastic constants (in GPa units) of* $GaFeO_3$ *in the orthorhombic phase (space group* $Pc2_1n$*)* in the *fully relaxed magnetic structure (FM) at ambient pressure.*

Elastic Constant	**GGA**	**LDA**
C_{11}	291.8	344.6
C_{12}	137.2	163.3
C_{13}	119.8	148.4
C_{22}	257.5	300.0
C_{23}	127.0	159.0
C_{33}	250.3	284.6
C_{44}	62.5	72.7
C_{66}	83.7	95.1

Presently, the high-pressure equation of state, total energy (Φ) and enthalpy ($H=\Phi+PV$) of various phases of $GaFeO_3$ were estimated for the fully relaxed magnetic (FM) configuration. The GGA calculated enthalpy showed that the high-pressure Pbnm phase is more stable than the $Pc2_1n$ phase at ambient pressure. Fig. 4.8(a) presents the enthalpy difference from LDA calculations, for the $Pc2_1n$ and R3c phases with respect to the Pbnm phase. Above 23 GPa, the Pbnm phase is found to be stable when comparing to $Pc2_1n$. The application of pressure leads to a change in the correlation between the electronic motions and affects the magnetic interaction. A quenching of the Fe magnetic moment in the Pbnm phase is found at 47 GPa, which triggers a sudden drop of the volume and increases the total energy (Fig. 4.8(b)). This is in agreement with the high pressure data [31] which shows a similar behaviour around 53 GPa. The values of the magnetic moments on the Fe-atoms remain about 4.1 μ_B from ambient pressure to below 47 GPa and then decrease to 1.0 μ_B at this transition.

The calculated phase diagram is qualitatively in a good agreement with the observation. It should be mentioned that it is difficult to identify experimentally the high pressure equilibrium phases, due to the large hysteresis. Fig. 4.9 shows the comparison between the LDA-calculated and experimental relative change of the unit cell volume in various phases of $GaFeO_3$ as a function of pressure. A very good agreement is noticed between our calculations and the measurements [31] in the $Pc2_1n$ and R3c structures; however, the volume in the Pbnm phase is underestimated. Table 4.3 gathers the LDA and GGA calculated elastic constants. The estimated bulk modulus values from LDA and GGA calculations, in the $Pc2_1n$ phase, are 207 and 178 GPa, respectively. The LDA determined value is found to be in a better agreement with the experimental bulk modulus value (226 GPa) [31]. As expected, the GGA underestimates the elastic constants by about 15% with respect to LDA, given that GGA tends to overestimate the calculated unit cell volume. This results in lowering the calculated bulk modulus values.

Further, the total energy (Φ) and enthalpy ($H=\Phi+PV$) of various phases of $GaFeO_3$ are estimated from LDA for the fully relaxed magnetic (FM_Ga_SC) configuration including the semi core electrons of the Ga atoms. Here again we found that computationally the Pbnm and R3c phases are most stable when adopting the G-type antiferromagnetic ordering and A-type antiferromagnetism respectively. The FM_Ga_SC calculated enthalpy difference in the various phases shows that the Pbnm phase is stable above 30 GPa (Fig. 4.8(c)) when comparing to $Pc2_1n$. The pressure increase leads to a quenching of the Fe magnetic moment in the Pbnm phase at 36 GPa, resulting in an increase of the total energy (Fig. 4.8(d)) and a sudden drop of the volume. We also find that the Fe magnetic moment is quenched in the R3c phase, when the pressure is raised to 45 GPa. The FM_Ga_SC calculated relative change of the unit cell volume as a function of pressure (Fig. 4.9) in various phases is found to be in a qualitative agreement with the experimental data [31].

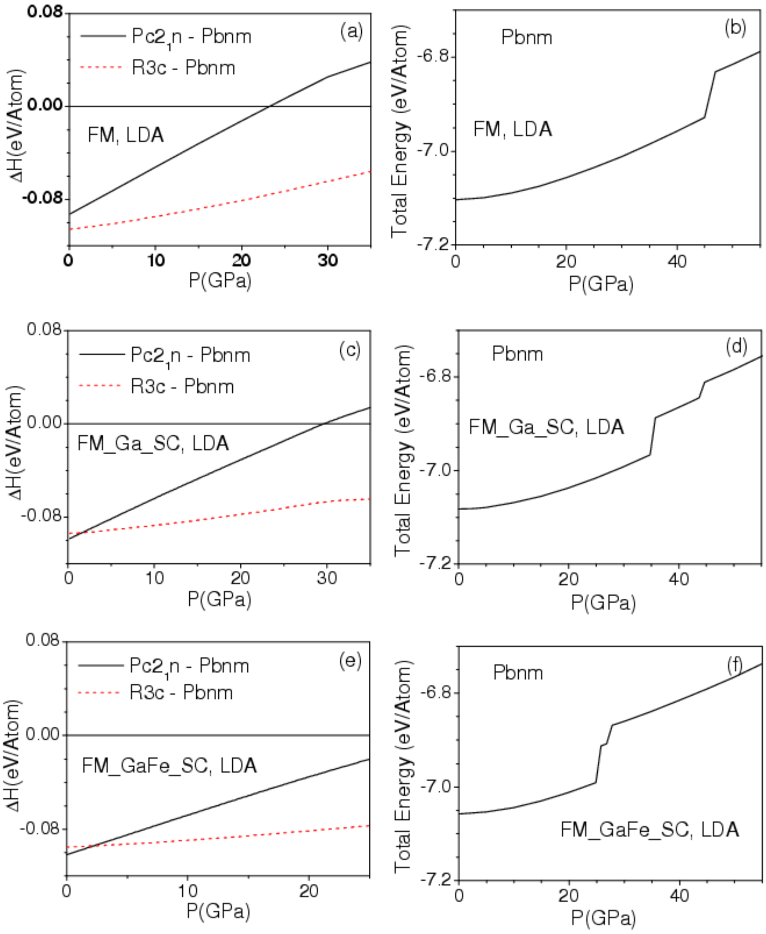

FIG 4.8 *(a, c, e) The calculated enthalpy (H=Φ+PV) difference in the* $Pc2_1n$ *and R3c phases with respect to the Pbnm phase of* $GaFeO_3$ *as a function of pressure within* the *local density approximation (LDA). (b, d, f) The calculated total energy (Φ) in the Pbnm phase of* $GaFeO_3$ *as a function of pressure within the* LDA. The *explanation of the labeling FM, FM_Ga_SC, FM_GaFe_SC is described in Section III.*

Environment of the Fe in $GaFeO_3$ is strongly asymmetric, therefore polarization of the low-lying semi core states could influence the total energy. In this context, we have also calculated total energy (Φ) and enthalpy (H=Φ+PV) within LDA framework for the fully relaxed magnetic configuration (FM_GaFe_SC) including the semi core electrons of both the Ga and Fe atoms. As in the above two types of calculations, the G-type and A-type antiferromagnetic ordering is found to be stable for Pbnm and R3c phases respectively. The comparison of the enthalpy of the $Pc2_1n$ and Pbnm phases shows (Fig. 4.8(e)) that the former phase is stable up to 26 GPa. Further increase in pressure leads to stability of $GaFeO_3$ in the Pbnm phase. This is due to quenching of the Fe magnetic moment which leads to an increase of the total energy and a sudden drop of the volume. In the R3c phase, the Fe magnetic moment is also found to quench at 28 GPa. A comparison of the experimental [31] and calculated equation of state from FM_GaFe_SC calculations is shown in Fig. 4.9.

The equation of state is found (Fig. 4.9) to be qualitatively different as obtained from calculations performed in FM, FM_Ga_SC, FM_GaFe_SC configurations. We find that comparison of enthalpy in the $Pc2_1n$ and Pbnm phases, in the FM and FM_Ga_SC calculations, reveals a stability of $GaFeO_3$ in the Pbnm phase above 36 and 26 GPa, respectively, while no such phase transition is found in the FM_GaFe_SC calculations. As shown in Fig. 4.9, quenching of the magnetic moment at high pressure in the Pbnm structure induces a number of phase transitions in the different calculations. However, in the R3c phase no quenching of Fe magnetic moment was found in FM calculations. While we notice that Fe moment was found to quench (Fig. 4.9) in both FM_Ga_SC, FM_GaFe_SC calculations, and leading to a phase transition.

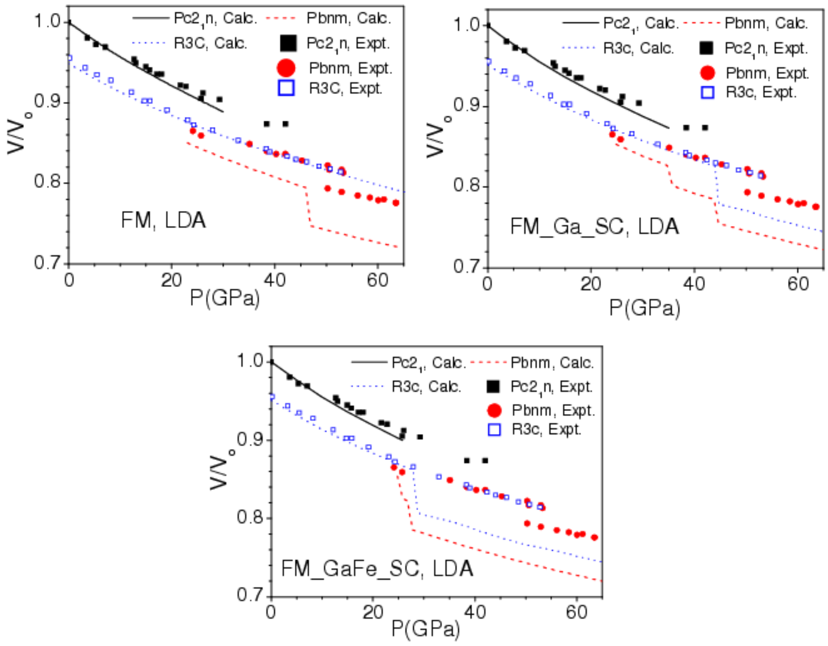

FIG 4.9 *The LDA-calculated equation of state of various phases of $GaFeO_3$ and a comparison with available experimental data [31]. V refers to the volume per formula unit at pressure P. V_o refers to the volume per formula unit of $Pc2_1n$ phase at ambient pressure.* The *explanation of the labeling FM, FM_Ga_SC, FM_GaFe_SC" is described in Section 4.1.*

The FM calculated enthalpy value under the $Pc2_1n$ phase is -7.196 eV/atom, while in the R3c phase this is estimated to be -7.209 eV/atom, indicating that the R3c phase is more stable as compared to $Pc2_1n$. The calculated energy difference between the two phases is rather small (~13 meV/atom). On the other hand the FM_Ga_SC and FM_GaFe_SC LDA calculated enthalpy values indicate that, at ambient pressure, the $Pc2_1n$ phase is energetically favorable by ~4 meV/atom and ~6 meV/atom in comparison to the R3c phase. However the $Pc2_1n$ phase is found to be stable only below 2 GPa. As discussed and highlighted above, the inclusion of the semi core electrons in the atomistic pseudo potentials has only a minor influence on the obtained dynamical properties, while these seem to induce some qualitative changes in the equation of state.

4.3 YMnO$_3$

Yttrium Manganese oxide (YMnO$_3$) keeps attracting a keen interest as it is known to exhibit ferroelectricity and antiferromagnetism simultaneously [50]. At ambient conditions the compound has a hexagonal P6$_3$*cm* structure. Above 1258 ±14 K, a ferroelectric to paraelectric phase transition occurs, and the system crystallizes [51] under the hexagonal P6$_3$/*mmc* space group (Fig. 4.10). Below 70 K, YMnO$_3$ has an A-type antiferromagnetic ordering. The ferroelectric phase consists of six formula units of YMnO$_3$. The structure is a framework network of MnO$_5$ bipyramids and YO$_7$ units. The MnO$_5$ units are tilted with respect to the c-axis and Y^{3+} ions are shifted by $\pm\delta$ from *a-b* plane along the c-axis. The high-temperature phase has two formula units of YMnO$_3$. The Mn^{3+} ions are coordinated by five oxygens, whereas the Y^{3+} ions are coordinated by six symmetrically equivalent oxygens, forming MnO$_5$ bipyramids and YO$_6$ units, respectively. All Y^{3+} ions lie in the *a-b* plane. The ferroelectric P6$_3$*cm* phase is connected to the high-temperature *P*6$_3$*/mmc* structure by the tripling of the corresponding unit cell. Moreover there is a loss of the mirror symmetry perpendicular to the *c* axis due to the tilting and distortion of the MnO$_5$ bipyramids and the displacement of the Y atoms. This triggers the emergence of the spontaneous electric polarization of the system. The exact nature of this ferroelectric transition is still under debate [8, 52-60]. Compounds [61, 62] with reduced rare-earth ionic radius (Ho, Er, Tm, Yb, Lu and Y) crystallize in a hexagonal structure (space group P6$_3$*cm*), whereas an orthorhombic (space group *Pnma*) phase is reported for compounds with larger rare-earth ionic radius (La, Ce, Pr, Nd, Sm, Eu, Gd, Tb and Dy). A hexagonal-to-orthorhombic structural phase transition [63] can take place at elevated temperatures, under pressure.

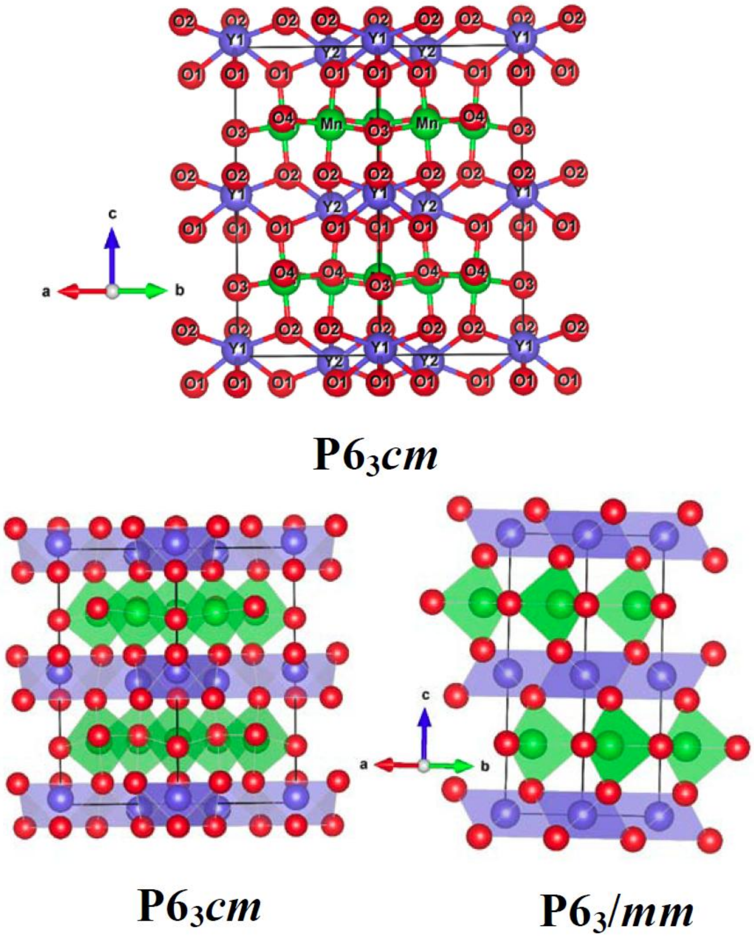

$P6_3cm$

$P6_3cm$ $P6_3/mm$

FIG 4.10 *Schematic representation of the crystal structure of the room -temperature (space group P6*$_3$*cm) and the high-temperature (space group P6*$_3$*/mmc) phases of YMnO*$_3$*. The atoms are labeled following Table 4.4. Key: Y, blue spheres; Mn, green spheres; and O, red spheres.*

Although ferroelectricity in $YMnO_3$ is believed to be due to the tripling of the unit cell, there is however an ambiguity about a second transition observed at ~ 920 K in this material. It was suggested [64] that this transition can be considered as a hidden order in which a residual symmetry, displayed by [64] the trimerization order parameter, is spontaneously broken. In this context, a generic $P6_3cm$ ↔ $P3c1$ ↔ $P\text{-}3c1$ phase diagram was proposed, corresponding to the observation in another isostructural compound ($InMnO_3$). High-resolution powder neutron diffraction investigation [51] of the structural behavior of the multiferroic hexagonal polymorph of $YMnO_3$ has been reported over the temperature range 300 - 1403 K. These measurements showed that on heating the ambient-temperature polar $P6_3cm$ structure undergoes a centrosymmetric $P6_3/mmc$ transition at 1258 ±14 K. This corroborated the absence of the previously suggested [56] intermediate phase with space group $P6_3/mcm$. Further, the measurements also provided evidence for an isosymmetric phase transition (i.e., $P6_3cm$ to $P6_3cm$) at $\approx$ 920 K, which involves a sharp decrease in polarization.

Most of the dynamical probes of manganites are based on Raman and infrared techniques [65, 66]. These are limited to the zone centre modes. Available INS measurements on single crystals are limited to low energies, below 20 meV [67, 68]. However a better understanding of thermodynamical behavior of a material requires a complete description of phonon spectra in the entire Brillouin zone (zone-centre and zone-boundary). Therefore INS can be used to probe phonons in the entire Brillouin zone. In this context, we present temperature-dependent measurements of phonon spectra in $YMnO_3$, over the temperature range 50 - 1303 K .i.e. in the low-temperature ($P6_3cm$), as well as in the high-temperature ($P6_3/mmc$) phase of $YMnO_3$. Our measurements are accompanied by first principles density functional-based magnetic lattice dynamics calculations for the sake of analysis and interpretation of the neutron data. Phonon dispersion relations in the entire Brillouin zone have been calculated in both the high- and low-temperature hexagonal phases of $YMnO_3$. Unstable phonon modes in the high-temperature phase are related to the stabilization of the low-temperature phase.

The inelastic neutron scattering measurements were carried out, at several temperatures in the range 70 - 1303 K, using the direct-geometry thermal neutron time-of-flight IN4C spectrometer at the Institut Laue-Langevin (ILL), France. The low-temperature measurements were performed using a standard orange cryostat. For the high-temperature range, the sample was put into a quartz tube, and mounted in a furnace. The other end of the quartz tube was kept open in the air. An incident neutron wavelength of 2.4 Å (14.2 meV) was used, performing in the up-scattering mode (neutron energy gain). The momentum transfer, Q, extends up to 7 $Å^{-1}$.

The calculations were carried out with and without considering the magnetic interactions using VASP. This is for the sake of understanding the effect of the spin degrees of freedom on the lattice dynamics [35, 36, 69]. The A-type antiferromagnetic ordering, in both the hexagonal phases, was adopted in the magnetic calculations. The on-site Coulomb interaction was accounted for within the Dudarev approach [42] using $U_{\mathrm{eff}} = U - J = 7.12$ eV [70, 71]. The labels; 'FM', 'PNM' and 'FNM' are aberrative of fully magnetic, partially nonmagnetic and fully non magnetic as explained in section 4.1. An energy cutoff of 800 eV and a 6×6×2 k-points mesh for the Brillouin zone integration are used and found to satisfy the required numerical convergence. Total energies were calculated for 24 generated structures resulting from individual displacements of the symmetry inequivalent atoms in the room temperature hexagonal ($P6_3cm$), and high temperature ($P6_3/mmc$) phases, along the six inequivalent Cartesian directions (±x, ±y and ±z). Phonons are extracted from subsequent calculations using the direct method as implemented in the Phonon software [39].

4.3.1 Results and Discussion

4.3.1.1 Temperature Dependence of Phonon Spectra

The INS measurements are performed across the magnetic and structural transition temperatures. In addition to the temperature dependence of the INS spectra, we present the data in terms of the Q-dependence as well, in order to map out both magnetic and lattice (phonon) excitations. The magnetic signal is expected to increase as Q decreases, following the magnetic form factor [72]. However, in the case of phonons, the form factor exhibits a Q^2– like dependence (multiplied by the Debye-Waller factor exp(-2W(Q)), hence the intensity of the phonon signal increases with Q in the range of our measurements up to 7 $Å^{-1}$.

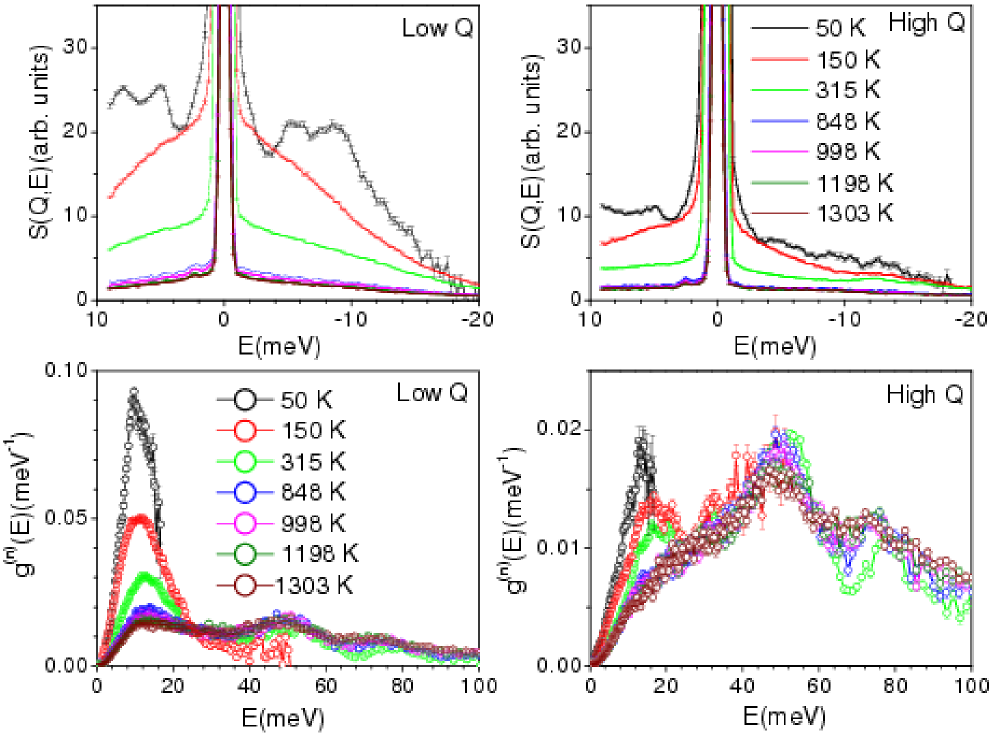

FIG 4.11 *Temperature dependent neutron inelastic spectra of* $YMnO_3$*. Top panel: the low-Q and high-Q Bose factor corrected S(Q,E), where both the energy loss (0 - 10 meV) and the energy gain (-20 - 0 meV) sides are shown. Bottom panel: the low-Q and high-Q, unity-normalized, neutron inelastic spectra,* $g^{(n)}(E)$*, inferred from the neutron energy gain mode S(Q,E) data, within the incoherent approximation.*

So also, the phonon signal increases with temperature due to increased population of the phonons. On the other hand, the magnetic signal decreases with increase of temperature. Hereafter the Q-dependence is limited to compare INS spectra in the low-Q (1 - 4 Å^{-1}) and high-Q (4 - 7 Å^{-1}) regions. The measured temperature dependence of the dynamical scattering function S(Q,ω) within the low-Q and high-Q regions is shown in Fig. 4.11(a) and Fig 4.11(b), respectively. At 50 K the observed peak around 10 meV is of magnetic nature, given its Q-dependence (stronger at low-Q and absent at high-Q). Above 70 K the compound undergoes [50, 73] a paramagnetic transition. Our data at 150 and 315 K show an appreciable broadening of the elastic peak which may results from the paramagnetic scattering. The increase in the temperature would lead to a decay of the paramagnetic fluctuations, which reduces the width of the elastic peak. Above 848 K the width of the elastic line stays close to the instrumental resolution, indicating that the paramagnetic scattering vanishes at high temperatures. The neutron inelastic spectra are depicted in Fig. 4.11(c) and Fig. 4.11(d), for the low-Q and high-Q regions, respectively. For the low-Q data, the low-energy excitations below 20 meV show a pronounced change as a function of the temperature. However such a trend is not observed in the high-Q data, confirming a more phonon-like character in this spectral range. Both the magnetic and phonon excitations are present in the low-Q part, whereas the high-Q data contains mainly phonon contributions. A prominent peak is observed in the low-Q data of the neutron inelastic spectra at 50 K and decaying strongly with temperature. The INS measurements [67, 68] carried out on a single crystal of $YMnO_3$ indicate that the dispersion of spin waves lies within the energy range 5 - 15 meV. This is in agreement with our measurements where we also find a large change in the intensity in the low-Q data, across the Neel temperature (T_N~70 K). The stretching modes (Fig. 4.11) around 80 meV, at 315 K, are found to soften as the temperature increases to 848 K. This might primarily be due to the increase of the Mn-O bond lengths leading to such a softening. The crystal structure and the phonon spectrum of the compound (Fig. 4.11(d) do not show large changes even above the Neel temperature of 70 K when the antiferromagnetic ordering is destroyed, which suggests that some kind of local magnetic order persists above 70 K. Our earlier work on $GaFeO_3$ shows [74] that magnetic signal is present well above the magnetic ordering temperature of 225 K. We therefore believe that in $YMnO_3$ also above 70 K in the paramagnetic phase local magnetic order as well as paramagnetic fluctuations may be present which give rise to the magnetic signal in the low-Q region at 150 K and 315 K.

The structural phase transition ($P6_3cm$ to $P6_3/mmc$) in $YMnO_3$, occurring at 1258 ±14 K, involves a structural distortion and a ferroelectric to paraelectric transition. It is well know that the phase transition from ferroelectric to paraelectric is driven by a softening of a zone boundary phonon mode at the K-point. We did not observe any significant change across the transition (up to 1303 K). It should be noted that the neutron inelastic spectra measurements were performed on a polycrystalline sample, and are averaged over the whole Brillouin zone. Therefore it would be crucial to detect small changes in specific dispersion branches, which may only be measured efficiently using a single crystal.

4.3.1.2 Effect of the Magnetic Ordering on the Calculated Phonon Spectra

The purpose of the three model calculations (“FM”, “FNM”, and “PNM”) described in Section III is to study the effect of the cell volume and magnetic interactions on the phonon spectra. The comparison between the relaxed and the experimentally refined structural parameters are gathered in TABLE 4.4. Further, a comparison between calculated and refined [51] bond lengths is provided in TABLE 4.5. The calculated magnetic moment per Mn atom is 3.99 μ_B and 3.95 μ_B, from LDA and GGA, respectively. However neutron diffraction measurements [75, 76] reported that, below T_N, the Mn moment has a value of ~ 3 μ_B. $YMnO_3$ is a non collinear magnetically frustrated two dimensional system [50]. The Mn-Mn distance in the *a-b* plane and along c-axis is 3.5 Å and 6.05 Å respectively. Therefore, the magnetic interaction in the *a-b* plane is much stronger than that along c-axis, which indicates low dimensionality of the magnetic structure in $YMnO_3$. The nearest neighbor antiferromagnetic exchange interaction and hexagonal magnetic lattice in the a-b plane results in a magnetically frustrated [77] spin configuration. The spin frustration parameter (θ_{CW}/T_N, θ_{CW} and T_N are Curie-Weiss (CW) and Neel temperature respectively) [53] for $YMnO_3$ is close to 10. The large value of spin frustration parameter for $YMnO_3$ [78] can be partly due to the low dimensionality of the Mn networks in addition to the geometrical frustration effects. The deviation from the calculated value might be due to magnetic fluctuations associated with frustration and/or low dimensionality.

The calculated phonon spectra are compared with the measured ones (at 315 K) in Fig. 4.12. The "FM" type calculation using GGA reproduces the low energy features of the measured phonon spectra. The peak in the experimental spectra at about 52 meV is estimated around 45 meV. Further the Mn-O stretching modes are underestimated around 67 meV, while experimentally these are observed around 80 meV. The GGA determined structural parameters clearly show that both the 'a' and 'c' lattice parameters are overestimated by ~ 2 %. This results in the overestimation of the various Mn-O bond lengths, which leads to the underestimation of the energies of the Mn-O stretching modes. Results of the FM-LDA calculations are found to be close to the experimental data. This is in agreement with the correct estimation of the structural parameters as well as bond lengths using this model calculation (TABLE 4.4 and 4.5). Consequently in the following we adopt the LDA density functional.

TABLE 4.4 *Comparison between the calculated and room temperature experimental[51] structural parameters of YMnO$_3$ (Hexagonal phase, space group P6$_3$cm). The experimental structure (space group P6$_3$cm) consists of Y1 and O3 atoms at 2a(x,y,z), Y2 and O4 at 4b(x,y,z), and Mn, O1, and O2 at 6c(x,y,z) Wyckoff site. "FM", "FNM" and "PNM" refer to fully relaxed magnetic, fully relaxed non-magnetic and partially relaxed non magnetic calculations, respectively.*

		Expt.	**FM(GGA)**	**FM(LDA)**	**PNM(LDA)**	**FNM(LDA)**
	a (Å)	6.14151	6.236	6.095	6.095	5.838
	b (Å)	6.14151	6.236	6.095	6.095	5.838
	c (Å)	11.4013	11.599	11.416	11.416	12.013
O1	*x*	0.3074	0.308	0.306	0.307	0.302
	y	0.0000	0.000	0.000	0.000	0.000
	z	0.1626	0.164	0.164	0.169	0.161
O2	*x*	0.6427	0.641	0.640	0.640	0.636
	y	0.0000	0.000	0.000	0.000	0.000
	z	0.3355	0.336	0.336	0.342	0.339
O3	*x*	0.000	0.000	0.000	0.0000	0.0000
	y	0.000	0.000	0.000	0.0000	0.0000
	z	0.4744	0.475	0.476	0.4876	0.475
O4	*x*	0.3333	0.333	0.333	0.333	0.333
	y	0.6667	0.667	0.667	0.667	0.667
	z	0.0169	0.021	0.021	0.028	0.020
Mn	*x*	0.3177	0.333	0.333	0.336	0.333
	y	0.0000	0.000	0.000	0.000	0.000
	z	0.0000	0.000	0.000	0.000	0.000
Y1	*x*	0.0000	0.000	0.000	0.000	0.000
	y	0.0000	0.000	0.000	0.000	0.000
	z	0.2728	0.274	0.275	0.276	0.274
Y2	*x*	0.6667	0.667	0.667	0.667	0.667
	y	0.3333	0.333	0.333	0.333	0.333
	z	0.7325	0.732	0.731	0.731	0.733

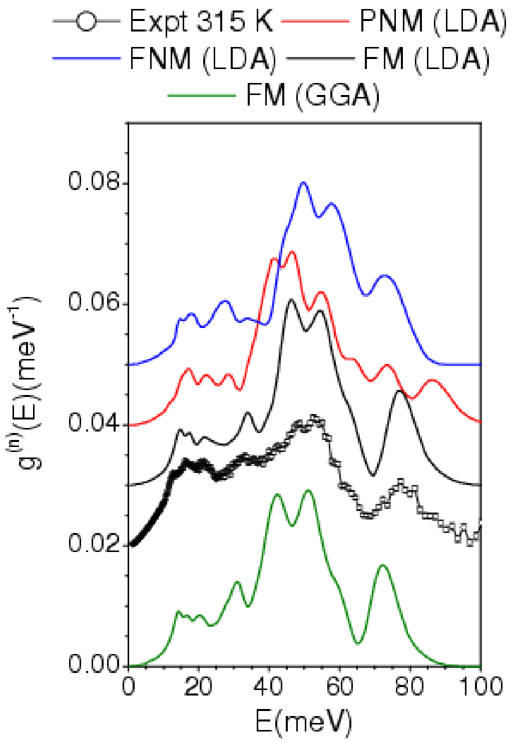

FIG 4.12 *The calculated and experimental neutron inelastic spectra of* $YMnO_3$*. The experimental data were collected at 315 K, and averaged over the high-Q region. The calculated phonon spectra have been convoluted with a Gaussian of FWHM of 10% of the energy transfer in order to describe the effect of energy resolution in the experiment. For better visibility, the experimental and calculated phonon spectra are shifted vertically with respect to each other. Multiphonon as calculated using the Sjølander formalism has been subtracted for comparison with the calculations.*

The calculated phonon spectra (Fig. 4.12), using the three model calculations PNM, FM, FNM, are closely similar up to ~ 25 meV. A significant change is observed at higher energies. To gain deeper insights into the phonon spectra, we extracted the atomistic partial contributions to the calculated phonon density of states (Fig. 4.13). The Y and Mn atoms are found to contribute mainly below 50 meV, while the O atoms are dynamically active within the range 40 - 90 meV. In all the three model calculations the contributions from Y and Mn atoms remain nearly unperturbed in the entire energy range. On the other hand, the differences in the phonon spectra are found to originate from the dynamics of the oxygen atoms. Such differences from the various calculations are primarily due to the nature of the chemical bonding, in the magnetic and nonmagnetic configurations, as well as a volume effect in this case as well. By comparing the FNM and FM phonon calculations we highlighted an effect of magnetism and cell volume on the phonon spectra.

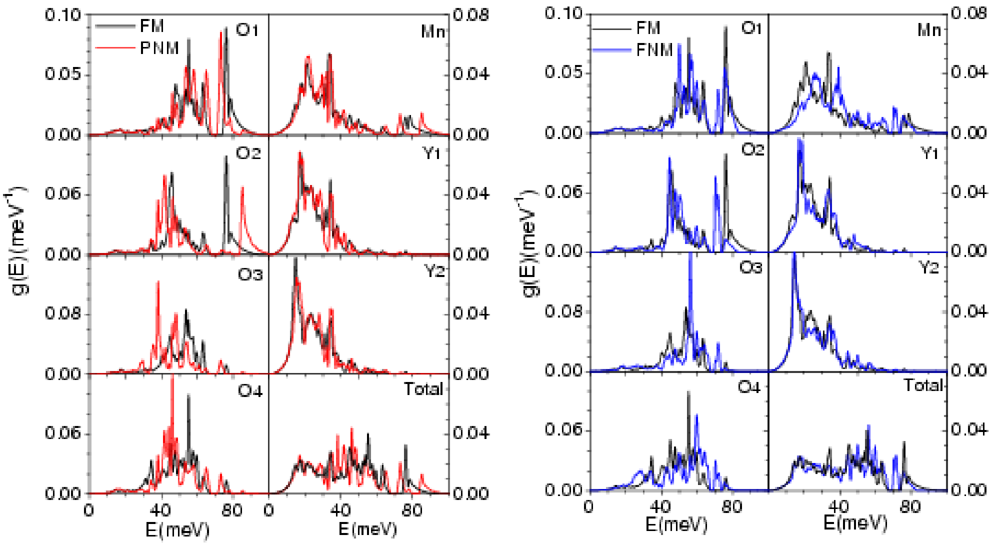

FIG 4.13 *The calculated atomistic partial phonon density of states (Y, Mn and O) in the low temperature phase (space group P6$_3$cm) of YMnO$_3$, within the local density approximation* (*LDA*).

By comparing the FM and PNM calculated phonon spectra we can identify the specific modes sensitive to magnetic interactions. In both FM and PNM, the calculated lattice parameters (TABLE 4.4) are similar. However there are slight changes in the related atomic positions. We find that the calculated Mn-O1 and Mn-O2 bond lengths show a large difference in both the calculations (TABLE 4.5). The FM calculated bond lengths are closer to the experimentally refined ones. The calculated values of Mn-O2 are 1.879 Å and 1.806 Å in "FM" and "PNM", respectively. The significant shortening of the Mn-O2 bond length as compared to the refined value of 1.891 Å [51], results in a hardening of the modes (Fig. 4.13) around 80 meV in the "PNM" calculations. The overestimation (TABLE 4.5) of Mn-O1 bond lengths in the "PNM" calculations leads to a softening of the modes involving O atoms, in comparison with "FM" calculations. Further, we find that the PNM-calculated low-energy modes around 40 meV for the planar O3 and O4 atoms soften significantly in comparison (Fig. 4.13) to the "FM" calculations. The difference in the calculated phonon spectra in both FM and PNM is due to the fact that in the PNM calculations the Mn^{3+} magnetic moment is zero, while the FM calculated magnetic moment of Mn^{3+} is 3.99 μ_B. Therefore, the super exchange interactions between Mn cations, mediated by O atoms, influence the partial phonon spectra involving oxygens. It it worth to notice that the Mn phonon modes seems to be insensitive to the magnetic moment exhibited on the Mn site. The FNM calculated structure (TABLE 4.5) shows that the "c" lattice parameter has a value of 12.01 Å, while the experimentally refined value is 11.40 Å [51]. The "a" lattice parameter is found to be underestimated (5.838 Å) in comparison to the experimental value of 6.1415 Å. All the four FNM calculated Mn-O bond lengths (TABLE 4.5) are more isotropic. This leads to an underestimation of the energies of the Mn-O stretching modes (Fig. 4.13) around 80 meV in the "FNM" calculations in comparison to the "FM" calculations. Fig. 4.14 shows the change in the energy of the estimated zone centre modes in the PNM and FNM configuration, with respect to FM calculations. There is a noticeable deviation when comparing energies from magnetic and non-magnetic calculations. The maximum shift in phonon energies is observed for high energy Mn-O stretching modes. This supports a spin-phonon coupling behavior, that is, the coupling of the magnetic structure with phonons. The change in the energies of the modes around 30 meV is mainly due to magnetic interactions, while the high energy stretching modes are most influenced by the estimated Mn-O bond lengths.

TABLE 4.5 *Comparison between the calculated and room temperature experimental[51](293 K) bond lengths (in Å units) in* $YMnO_3$ *(Hexagonal phase, space group* $P6_3cm$*). "FM", "FNM" and "PNM" refer to fully relaxed magnetic, fully relaxed non-magnetic and partially relaxed non magnetic calculations, respectively.*

Bond	**Expt.**	**GGA (FM)**	**LDA(FM)**	**LDA(PNM)**	**LDA(FNM)**
Mn-O1	1.855	1.911	1.881	1.940	1.934
Mn-O2	1.891	1.901	1.880	1.806	1.939
Mn-O3	1.973	2.099	2.051	2.051	1.968
Mn-O4	2.106	2.091	2.045	2.049	1.961
Y1-O1	2.268	2.304	2.255	2.232	2.244
Y1-O2	2.308	2.351	2.302	2.322	2.256
Y1-O3	2.299	2.334	2.290	2.418	2.389
Y2-O1	2.275	2.302	2.255	2.231	2.220
Y2-O2	2.300	2.340	2.292	2.331	2.261
Y2-O4	2.458	2.451	2.403	2.323	2.556
Mn-Mn	3.632	3.599	3.519	3.507	3.372
Mn-Y1	3.243	3.346	3.272	3.277	3.320
Mn-Y2	3.701	3.399	3.681	3.677	3.755
Y1-Y1	5.701	5.799	5.708	5.708	6.006
Y1-Y2	3.575	3.634	3.555	3.556	3.410
Y2-Y2	3.546	3.600	3.519	3.519	3.371

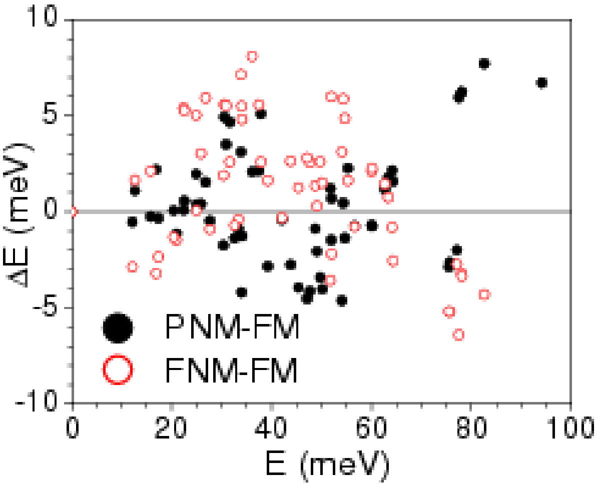

FIG 4.14 *The calculated shift of the zone centre optic phonon modes in "PNM" and "FNM" configurations with respect to the "FM" model calculation.*

4.3.1.3 Phonon Spectra in the Room Temperature ($P6_3cm$) and High-Temperature ($P6_3/mmc$) Hexagonal Phases

The calculated phonon spectra of $YMnO_3$ were subject of previous works [60, 70, 79]. The estimated phonon dispersions have been reported [79] in the entire Brillouin zone, at room temperature in the $P6_3cm$ hexagonal phase. However, only calculations of phonon modes at the zone centre and K-point were reported [60] in the high-temperature hexagonal phase ($P6_3/mmc$). The group theoretical analysis along with the first-principles phonons calculations at zone centre is used to understand [60] the mechanism of multiferroicity in $YMnO_3$. Alina et al. [80] calculated the zone-centre phonon modes using LDA, and they reassigned the Raman modes. We went beyond obtaining only the zone-centre modes by extracting also phonon dispersion relations (Fig. 4.15), in the entire Brillouin zone and along various high-symmetry directions in both the hexagonal phases (*P6$_3$cm* and P6$_3$/*mmc*). We discuss also the relationship between the phonon modes at the ferroelectric (*P*6$_3$*cm*) to the paraelectric (*P*6$_3$/*mmc*) phase transition.

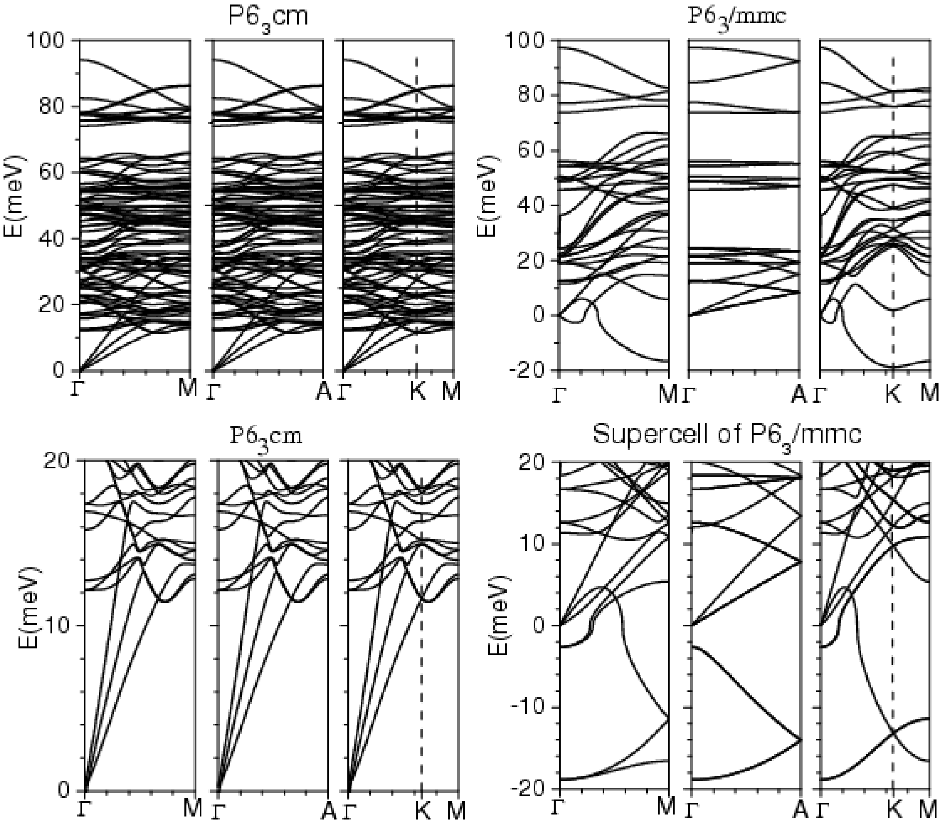

FIG 4.15 *The calculated phonon dispersion relations along the high-symmetry directions of the ambient-temperature (space group P6$_3$cm) and the high-temperature (space group P6$_3$/mmc) hexagonal phases of YMnO$_3$. The zoom of the calculated phonon dispersion relations in the ambient temperature (P6$_3$cm) and high temperature phase (P6$_3$/mmc) with a super cell of √3×√3×1 are also shown. The high-symmetry points are: K (1/3 1/3 0), A (0 0 1/2) and Γ (0 0 0). The size of the hexagonal unit cell is nearly same in the P6$_3$cm and super cell of P6$_3$/mmc.*

TABLE 4.6 *The calculated structures in the ambient temperature and super cell* $(\sqrt{3}\times\sqrt{3}\times1)$ *of high temperature phase. The super cell* $(\sqrt{3}\times\sqrt{3}\times1)$ *of high temperature phase is equivalent to the room temperature hexagonal phase* ($P6_3cm$)*. The distortion vector is obtained from the difference in atomic co-ordinates of the ambient temperature* ($P6_3cm$) *and super cell of high temperature phases. The amplitude of the eigen vector of O1 is scaled to match with the distortion vector.*

		Ambient temperature phase (*$P6_3cm$*)	**Supercell of high temperature phase (P6$_3$/*mmc*)**	**Distortion vector in fractional coordinates**	**Eigen vector of the unstable K3 mode in the high temperature phase (*$P6_3/mmc$*)**
	a (*Å*)	6.095	6.165		
	b (*Å*)	6.095	6.165		
	c (*Å*)	11.416	11.223		
O1	*x*	0.306	0.333	-0.027	-0.027
	y	0.000	0.000	0.000	0.000
	z	0.164	0.1665	-0.003	0.000
O2	*x*	0.640	0.667	-0.027	-0.027
	y	0.000	0.000	0.000	0.000
	z	0.336	0.334	0.002	0.000
O3	*x*	0.000	0.000	0.000	0.000
	y	0.000	0.000	0.000	0.000
	z	0.476	0.500	-0.024	-0.039
O4	*x*	0.333	0.333	0.000	0.000
	y	0.667	0.667	0.000	0.000
	z	0.021	0.000	0.021	0.020
Mn	*x*	0.333	0.333	0.000	0.000
	y	0.000	0.000	0.000	0.000
	z	0.000	0.000	0.000	0.000
Y1	*x*	0.000	0.000	0.000	0.000
	y	0.000	0.000	0.000	0.000
	z	0.275	0.250	0.025	0.019
Y2	*x*	0.667	0.667	0.000	0.000
	y	0.333	0.333	0.000	0.000
	z	0.731	0.750	-0.019	-0.018

The calculated phonon dispersion relations in both the room-temperature (space group $P6_3cm$) and the high-temperature (space group $P6_3/mmc$) phases are shown in Fig. 4.15. The phonon modes are found to be stable in the entire Brillouin zone, in the low-temperature phase. However, phonon instability is clearly noticed in the high-temperature phase, at the symmetry point K (1/3 1/3 0). The unstable mode is highly anharmonic in nature, and it become stable at higher temperatures due to anharmonicity. It has been proposed [52, 67] that the condensation of the unstable phonon mode at K point drives the transition to the low-temperature structure of $YMnO_3$. This mode is not polar in nature. However, ferroelectricity

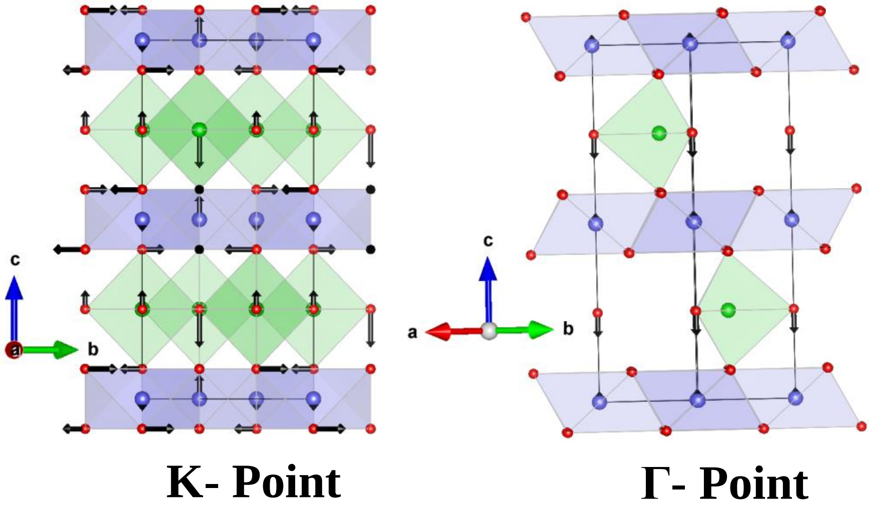

K- Point **Γ- Point**

FIG 4.16 *The displacement patterns of the lowest phone mode at K and Γ points in the high-temperature phase (space group* $P6_3/mmc$*) of* $YMnO_3$*. The lengths of arrows are related to the displacements of the atoms. Key: Y, blue spheres; Mn, green spheres; and O, red spheres.*

in the improper ferroelectric $YMnO_3$ arises from the coupling of the unstable K-point mode with a stable mode at the Γ-point. The latter is polar in nature and, therefore, contributing to the ferroelectricity in the room -temperature phase. The eigenvectors of these modes have been extracted from our ab-initio calculations. The displacement pattern of unstable mode at the K point is shown in Fig 4.16. At the K-point, the mode consists of an unequal displacement of two Y atoms in opposite direction, along with an out-of-phase rotation of MnO_5 bipyramid units, around the c-axis. The unequal amplitude of motions of the O atoms induces a distortion of the MnO_5 units. The displacement pattern of the stable mode at the Γ-point consists of a motion of O atoms belonging to the plane formed by the Mn atoms of the MnO_5 units. We have also calculated the phonon dispersion relation of high temperature phase ($P6_3/mmc$) of $YMnO_3$ (Fig. 4.15) with a super cell of √3×√3×1 which is equivalent to room temperature hexagonal phase ($P6_3cm$). The structure as used in the phonon calculations is given in TABLE 4.6. The comparison of the two structures show that in the room temperature phase ($P6_3cm$) atomic positions are slightly distorted in comparison to the structure obtained from the √3×√3×1 super cell of the high temperature phase ($P6_3/mmc$). The group theoretical classification at zone centre of low temperature phase ($P6_3cm$) is $10A_1+5A_2+5B_1+10B_2+30E_1+30E_2$ while the classification at K point in the high temperature phase ($P6_3/mmc$) is given by $2K_1+2K_2+3K_3+3K_4+12K_5+8K_6$. The freezing of unstable K point mode in the high temperature phase will lead to transition to the room temperature phase. Group theoretical analysis shows that the unstable modes at the K-point (1/3 1/3 0) and K*-point (-1/3 -1/3 0) [of imaginary energy = 18.7 i meV] belong to the K_3 representation in $P6_3$/mmc and condenses into stable modes of A1 [of energy =21.0 meV] and B2 [of energy =16.9 meV] representations at the Gamma point in the room temperature phase ($P6_3cm$). A symmetry-based correlation between the zone centre modes in the low-temperature phase and the K-point modes in the high-temperature phase is given in Fig 4.17. The difference in the atomic co-ordinates of room temperature phase ($P6_3cm$) and the √3×√3×1 super cell of the high temperature phase ($P6_3/mmc$) is a measure of the distortion required to stabilize the ambient temperature phase. The eigen vectors of the unstable K3 mode of high temperature phase ($P6_3$/mmc) for the super cell is given in Table 4.6. The eigen vector of the K3 mode is in good agreement with the distortion vector, which corroborates the previous results [51, 60] that freezing of the unstable K3 mode is responsible for phase transition to the ambient temperature phase.

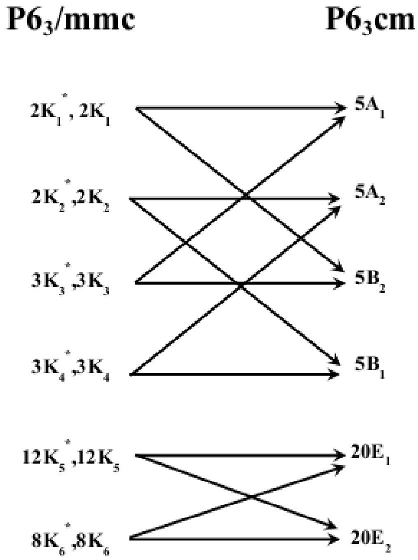

FIG 4.17 *A symmetry-based correlation between the zone centre modes in the low-temperature phase (P6$_3$cm) and the K-point (1/3,1/3,0) and K*-point (-1/3,-1/3,0) modes in the high-temperature phase (P6$_3$/mmc).*

4.4 Conclusions

We have reported measurements of neutron inelastic scattering spectra of the multiferroic material $GaFeO_3$ and $YMnO_3$ over a wide temperature range covering all the relevant characteristic transition temperatures. In $GaFeO_3$, across the magnetic transition temperature, at 225 K, there is an increase of the intensity of the low energy phonons around 20 meV, associated with the dynamics of the Fe atoms. The low energy vibrations exhibit a significant Q dependence up to about 848 K, indicating a persistence of the paramagnetic spin fluctuations up to very high temperatures. $GaFeO_3$ is not subject to any structural high-temperature phase transition. However, the increase of the distortion amplitudes of the various polyhedral units might be at the origin of the gradual broadening of the stretching modes around 60 meV. The ab-initio phonon calculations highlighted unambiguously a spin-phonon coupling in $GaFeO_3$. The enthalpy calculations in various phases showed that the quenching of the Fe magnetic moment leads to the observed high pressure structural phase transition at 47 GPa.

In $YMnO_3$, the room temperature phase is found to be subject to a strong spin-phonon coupling. The calculated phonon dispersion relations in the entire Brillouin zone indicate phonon instability in the high-temperature ($P6_3/mmc$) hexagonal phases of $YMnO_3$, at the symmetry point K (1/3 1/3 0). Unstable phonon modes may lead to a stabilization of the low-temperature ($P6_3cm$) phase.

[1] P. Silvia and E. Claude, Journal of Physics: Condensed Matter **21**, 303201 (2009).

[2] G. Catalan and J. F. Scott, Advanced Materials **21**, 2463 (2009).

[3] C.-W. Nan, M. I. Bichurin, S. Dong, D. Viehland and G. Srinivasan, Journal of Applied Physics **103**, 031101 (2008).

[4] V. V. Pavlov, A. R. Akbashev, A. M. Kalashnikova, V. A. Rusakov, A. R. Kaul, M. Bayer and R. V. Pisarev, Journal of Applied Physics **111**, 056105 (2012).

[5] W. Eerenstein, N. D. Mathur and J. F. Scott, Nature **442**, 759 (2006).

[6] J. H. Lee, L. Fang, E. Vlahos, X. Ke, Y. W. Jung, L. F. Kourkoutis, J.-W. Kim, P. J. Ryan, T. Heeg, M. Roeckerath, V. Goian, M. Bernhagen, R. Uecker, P. C. Hammel, K. M. Rabe, S. Kamba, J. Schubert, J. W. Freeland, D. A. Muller, C. J. Fennie, P. Schiffer, V. Gopalan, E. Johnston-Halperin and D. G. Schlom, Nature **466**, 954 (2010).

[7] T. Kimura, T. Goto, H. Shintani, K. Ishizaka, T. Arima and Y. Tokura, Nature **426**, 55 (2003).

[8] B. B. Van Aken, T. T. M. Palstra, A. Filippetti and N. A. Spaldin, Nat Mater **3**, 164 (2004).

[9] R. Ramesh and N. A. Spaldin, Nat Mater **6**, 21 (2007).

[10] N. Hur, S. Park, P. A. Sharma, J. S. Ahn, S. Guha and S. W. Cheong, Nature **429**, 392 (2004).

[11] N. Ikeda, H. Ohsumi, K. Ohwada, K. Ishii, T. Inami, K. Kakurai, Y. Murakami, K. Yoshii, S. Mori, Y. Horibe and H. Kito, Nature **436**, 1136 (2005).

[12] D. V. Efremov, J. van den Brink and D. I. Khomskii, Nat Mater **3**, 853 (2004).

[13] M. Zbiri, H. Schober, N. Choudhury, R. Mittal, S. L. Chaplot, S. J. Patwe, S. N. Achary and A. K. Tyagi, Applied Physics Letters **100**, 142901 (2012).

[14] T. Kimura, S. Kawamoto, I. Yamada, M. Azuma, M. Takano and Y. Tokura, Physical Review B **67**, 180401 (2003).

[15] T. Arima, D. Higashiyama, Y. Kaneko, J. P. He, T. Goto, S. Miyasaka, T. Kimura, K. Oikawa, T. Kamiyama, R. Kumai and Y. Tokura, Physical Review B **70**, 064426 (2004).

[16] K. Kelm and W. Mader, Zeitschrift für anorganische und allgemeine Chemie **631**, 2383 (2005).

[17] R. B. Frankel, N. A. Blum, S. Foner, A. J. Freeman and M. Schieber, Physical Review Letters **15**, 958 (1965).

[18] M. J. Han, T. Ozaki and J. Yu, Physical Review B **75**, 060404 (2007).

[19] S. Daniel, Journal of Physics: Condensed Matter **24**, 185502 (2012).

[20] J. P. Remeika, Journal of Applied Physics **31**, S263 (1960).

[21] S. Mukherjee, A. Roy, S. Auluck, R. Prasad, R. Gupta and A. Garg, Physical Review Letters **111**, 087601 (2013).

[22] A. Thomasson, S. Cherifi, C. Lefevre, F. Roulland, B. Gautier, D. Albertini, C. Meny and N. Viart, Journal of Applied Physics **113**, 214101 (2013).

[23] R. Saha, A. Shireen, S. N. Shirodkar, M. S. Singh, U. V. Waghmare, A. Sundaresan and C. N. R. Rao, Inorganic Chemistry **50**, 9527 (2011).

[24] P. Kumar, A. Bera, D. V. S. Muthu, S. N. Shirodkar, R. Saha, A. Shireen, A. Sundaresan, U. V. Waghmare, A. K. Sood and C. N. R. Rao, Physical Review B **85**, 134449 (2012).

[25] U. Staub, Y. Bodenthin, C. Piamonteze, S. P. Collins, S. Koohpayeh, D. Fort and S. W. Lovesey, Physical Review B **82**, 104411 (2010).

[26] Z. H. Sun, B. L. Cheng, S. Dai, L. Z. Cao, Y. L. Zhou, K. J. Jin, Z. H. Chen and G. Z. Yang, Journal of Physics D: Applied Physics **39**, 2481 (2006).

[27] S. Kavita, V. R. Reddy, K. Deepti, G. Ajay, A. Banerjee and V. G. Sathe, Journal of Physics: Condensed Matter **22**, 146005 (2010).

[28] M. Somdutta, G. Ashish and G. Rajeev, Journal of Physics: Condensed Matter **23**, 445403 (2011).

[29] S. Kavita, V. R. Reddy, G. Ajay, S. D. Kaushik and V. Siruguri, Journal of Physics: Condensed Matter **24**, 376001 (2012).

[30] S. K. Mishra, R. Mittal, R. Singh, M. Zbiri, T. Hansen and H. Schober, Journal of Applied Physics **113**, 174102 (2013).

[31] R. Arielly, W. M. Xu, E. Greenberg, G. K. Rozenberg, M. P. Pasternak, G. Garbarino, S. Clark and R. Jeanloz, Physical Review B **84**, 094109 (2011).

[32] S. E. Hahn, A. A. Podlesnyak, G. Ehlers, G. E. Granroth, R. S. Fishman, A. I. Kolesnikov, E. Pomjakushina and K. Conder, Physical Review B **89**, 014420 (2014).

[33] S. M. Shapiro, J. D. Axe and J. P. Remeika, Physical Review B **10**, 2014 (1974).

[34] S. Artyukhin, M. Mostovoy, N. P. Jensen, D. Le, K. Prokes, V. G. de Paula, H. N. Bordallo, A. Maljuk, S. Landsgesell, H. Ryll, B. Klemke, S. Paeckel, K. Kiefer, K. Lefmann, L. T. Kuhn and D. N. Argyriou, Nat Mater **11**, 694 (2012).

[35] Z. Mohamed, M. Ranjan, R. Stéphane, S. Yixi, X. Yinguo, S. Helmut, L. C. Samrath, R. J. Mark, C. Tapan, I. Yasunori, M. Satoru, H. Hideo and B. Thomas, Journal of Physics: Condensed Matter **22**, 315701 (2010).

[36] R. Mittal, M. K. Gupta, S. L. Chaplot, M. Zbiri, S. Rols, H. Schober, Y. Su, T. Brueckel and T. Wolf, Physical Review B **87**, 184502 (2013).

[37] G. Kresse and J. Furthmüller, Computational Materials Science **6**, 15 (1996).

[38] G. Kresse and D. Joubert, Physical Review B **59**, 1758 (1999).

[39] K. Parlinksi, (2003)

[40] J. P. Perdew, K. Burke and M. Ernzerhof, Physical Review Letters **77**, 3865 (1996).

[41] J. P. Perdew and A. Zunger, Physical Review B **23**, 5048 (1981).

[42] S. L. Dudarev, G. A. Botton, S. Y. Savrasov, C. J. Humphreys and A. P. Sutton, Physical Review B **57**, 1505 (1998).

[43] I. A. Vladimir, F. Aryasetiawan and A. I. Lichtenstein, Journal of Physics: Condensed Matter **9**, 767 (1997).

[44] M. J. Han, T. Ozaki and J. Yu, Physical Review B **73**, 045110 (2006).

[45] M. P. J. Punkkinen, K. Kokko, W. Hergert and I. J. Väyrynen, Journal of Physics: Condensed Matter **11**, 2341 (1999).

[46] G. Rollmann, A. Rohrbach, P. Entel and J. Hafner, Physical Review B **69**, 165107 (2004).

[47] A. Bandyopadhyay, J. Velev, W. H. Butler, S. K. Sarker and O. Bengone, Physical Review B **69**, 174429 (2004).

[48] H. Boysen and F. Altorfer, Acta Crystallographica Section B **50**, 405 (1994).

[49] R. Mittal, S. L. Chaplot and N. Choudhury, Progress in Materials Science **51**, 211 (2006).

[50] E. F. Bertaut and M. Mercier, Physics Letters **5**, 27 (1963).

[51] A. S. Gibbs, K. S. Knight and P. Lightfoot, Physical Review B **83**, 094111 (2011).

[52] A. S. K. I. G. Ismailzade, Sov. Physc. Solid State **7**, (1965).

[53] T. Katsufuji, S. Mori, M. Masaki, Y. Moritomo, N. Yamamoto and H. Takagi, Physical Review B **64**, 104419 (2001).

[54] T. Katsufuji, M. Masaki, A. Machida, M. Moritomo, K. Kato, E. Nishibori, M. Takata, M. Sakata, K. Ohoyama, K. Kitazawa and H. Takagi, Physical Review B **66**, 134434 (2002).

[55] G. R. Nenert, Y.; Stokes, H. T.; Palstra, T. T. M. , arxiv:condmat/ 05045465 (2005).

[56] G. Nénert, M. Pollet, S. Marinel, G. R. Blake, A. Meetsma and T. T. M. Palstra, Journal of Physics: Condensed Matter **19**, 466212 (2007).

[57] J. Kim, K. C. Cho, Y. M. Koo, K. P. Hong and N. Shin, Applied Physics Letters **95**, 132901 (2009).

[58] J. Kim, Y. M. Koo, K.-S. Sohn and N. Shin, Applied Physics Letters **97**, 092902 (2010).

[59] T. Lonkai, D. G. Tomuta, U. Amann, J. Ihringer, R. W. A. Hendrikx, D. M. Többens and J. A. Mydosh, Physical Review B **69**, 134108 (2004).

[60] C. J. Fennie and K. M. Rabe, Physical Review B **72**, 100103 (2005).

[61] M. Gilleo, Acta Crystallographica **10**, 161 (1957).

[62] F. Moussa, M. Hennion, J. Rodriguez-Carvajal, H. Moudden, L. Pinsard and A. Revcolevschi, Physical Review B **54**, 15149 (1996).

[63] V. E. Wood, A. E. Austin, E. W. Collings and K. C. Brog, Journal of Physics and Chemistry of Solids **34**, 859 (1973).

[64] A. Cano, Physical Review B **89**, 214107 (2014).

[65] M. N. Iliev, H. G. Lee, V. N. Popov, M. V. Abrashev, A. Hamed, R. L. Meng and C. W. Chu, Physical Review B **56**, 2488 (1997).

[66] C. Toulouse, J. Liu, Y. Gallais, M. A. Measson, A. Sacuto, M. Cazayous, L. Chaix, V. Simonet, S. de Brion, L. Pinsard-Godart, F. Willaert, J. B. Brubach, P. Roy and S. Petit, Physical Review B **89**, 094415 (2014).

[67] S. Petit, F. Moussa, M. Hennion, S. Pailhès, L. Pinsard-Gaudart and A. Ivanov, Physical Review Letters **99**, 266604 (2007).

[68] S. Pailhès, X. Fabrèges, L. P. Régnault, L. Pinsard-Godart, I. Mirebeau, F. Moussa, M. Hennion and S. Petit, Physical Review B **79**, 134409 (2009).

[69] R. Mittal, M. Zbiri, S. Rols, Y. Su, Y. Xiao, H. Schober, S. L. Chaplot, M. Johnson, T. Chatterji, S. Matsuishi, H. Hosono and T. Brueckel, Physical Review B **79**, 214514 (2009).

[70] J. E. Medvedeva, V. I. Anisimov, M. A. Korotin, O. N. Mryasov and A. J. Freeman, Journal of Physics: Condensed Matter **12**, 4947 (2000).

[71] O. Gunnarsson, O. K. Andersen, O. Jepsen and J. Zaanen, Physical Review B **39**, 1708 (1989).

[72] G. E. Bacon, Neutron diffraction. (Oxford University Press, Oxford, 1975).

[73] T. Chatterji, S. Ghosh, A. Singh, L. P. Regnault and M. Rheinstädter, Physical Review B **76**, 144406 (2007).

[74] M. K. Gupta, R. Mittal, M. Zbiri, R. Singh, S. Rols, H. Schober and S. L. Chaplot, Physical Review B **90**, 134304 (2014).

[75] A. Muñoz, J. A. Alonso, M. J. Martínez-Lope, M. T. Casáis, J. L. Martínez and M. T. Fernández-Díaz, Physical Review B **62**, 9498 (2000).

[76] P. J. Brown and T. Chatterji, Journal of Physics: Condensed Matter **18**, 10085 (2006).

[77] X. Fabrèges, S. Petit, I. Mirebeau, S. Pailhès, L. Pinsard, A. Forget, M. T. Fernandez-Diaz and F. Porcher, Physical Review Letters **103**, 067204 (2009).

[78] J. Park, J. G. Park, G. S. Jeon, H.-Y. Choi, C. Lee, W. Jo, R. Bewley, K. A. McEwen and T. G. Perring, Physical Review B **68**, 104426 (2003).

[79] K. Z. Rushchanskii and M. Ležaić, Ferroelectrics **426**, 90 (2012).

[80] A. Prikockytė, D. Bilc, P. Hermet, C. Dubourdieu and P. Ghosez, Physical Review B **84**, 214301 (2011).

Chapter 5

Phonons and Stability of Infinite-Layer Iron Oxides $SrFeO_2$ and $CaFeO_2$

5.1 Introduction

Low-dimensional magnetic systems have received much attention due to their exotic magnetic and electronic properties. Iron forms a large number of oxides with FeO_4 tetrahedral, FeO_5 pyramidal or FeO_6 octahedral configurations. The gillespite mineral $BaFeSi_4O_{10}$ was the first example with iron in square planar coordination [1], which is stabilized by four-member rings of SiO_4. The compounds $AFeO_y$ (A = Sr, Ca; $y \sim 2.5$) adapt a brownmillerite structure consisting of tetrahedral and octahedral layers [2]. Later the synthesis of a metastable phase $SrFeO_2$ using a topochemical reaction of $SrFeO_y$ was reported [3]. $SrFeO_2$ is distinct (from $BaFeSi_4O_{10}$) in that square-planar FeO_4 units are connected with each other to form extended FeO_2 layers that are separated by strontium atoms (Fig. 5.1). The resultant structure is isostructural with the infinite-layer structure $SrCuO_2$ ($P4/mmm$).The Fe^{2+} ion is in a high spin state ($S = 2$) with the electronic configurations of $(d_{z2})^2(d_{xz},d_{yz})^2(d_{xy})^1(d_{x2-y2})^1$ [4]. $SrFeO_2$ is an AFM insulator with a high ordering temperature T_N of 473 K, while at high pressure it undergoes a spin transition to $S = 1$ accompanied by a transition to a ferromagnetic (FM) half-metallic state[5]. Magnetic properties of $SrFeO_2$ have been examined by density functional theory (DFT) band structure and total energy calculations[4, 6]. Recently high pressure study [7] on $SrFeO_2$ based on first principles DFT simulation is performed to explain the antiferromagnetic to ferromagnetic phase transition at high pressure. In the last decade plenty of studies [7-20] have been reported on planer $AFeO_2$ (A = Ca, Sr) and their derivatives.

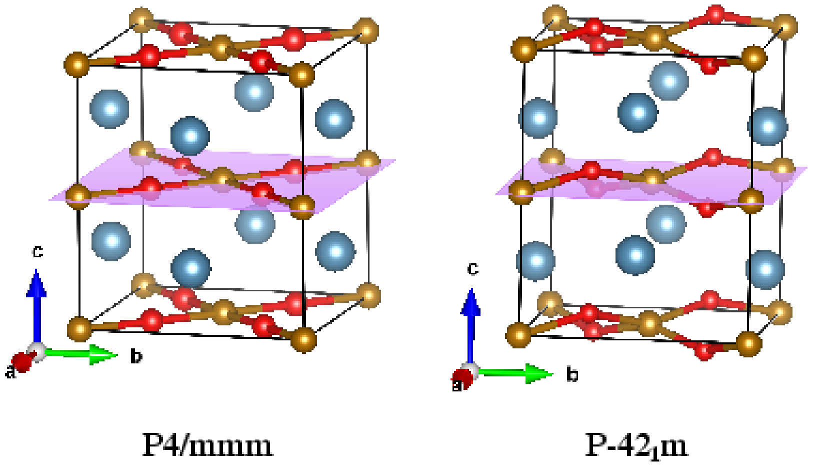

FIG 5.1 *Structures of planer* $CaFeO_2$ *(P4/mmm) and distorted* $CaFeO_2$*(P-42*$_1$*m). The ab plane in these structure are depicted by violate sheet. Supercell's compatible to the magnetic unit cell are shown, i.e. a √2× √2 × 2 supercell of the P4/mmm structure and 1×1×2 supercell of P-42*$_1$*m structure.The oxygen atoms in the distorted structure are shifted along z axis by ±δ. Key: Ca, blue spheres; Fe, golden spheres; O, red spheres.*

When Sr is replaced by Ca with a smaller ionic radius, the infinite-layer structure becomes corrugated [21]. In $CaFeO_2$ (P-42$_1$$m$), oxygen atoms move along the z direction to distort FeO_4 square planar unit toward a tetrahedral shape. This distortion affects the exchange interaction and leads to a reduction in T_N (420 K). The origin of this distortion in $CaFeO_2$ is discussed in terms of phonons. Ab-initio density functional perturbation theory (DFPT) calculation of the zone centre phonon modes has also been reported [6, 21]. For $CaFeO_2$ assuming the *P*4/*mmm* space group, two unstable phonon modes are indicated, one of which involves out-of-plane translation motion of the oxygen atoms along z-axis, while the other zone boundary mode shows in-plane rotation of the FeO_4 squares. Recently, a high-resolution neutron diffraction study at various temperatures [22] has demonstrated that even in $SrFeO_2$ the ideal infinite-layer structure is destabilized upon approaching to the Neel temperature (473 K). The analysis shows a local transverse mode creates buckling in the FeO_4 planes, resulting in lowering the tetragonal symmetry. Such transverse distortion created by local structural instability significantly weakens the exchange interactions.

In order to obtain further insight into structural instability of $SrFeO_2$ and $CaFeO_2$ as well as its effect on exchange parameters, we have performed the *ab-initio* phonon calculations for planar $SrFeO_2$ ($P4/mmm$) and both planar and distorted $CaFeO_2$ ($P4/mmm$ and $P\text{-}42_1m$), termed here after by p-$CaFeO_2$ and d-$CaFeO_2$, respectively, in various magnetic configurations in the entire Brillouin zone. The longitudinal and transverse optic (LO-TO) splitting has been taken into account in the calculations of phonon frequencies. These calculations are useful to interpret the measured spectrum and able to explain the origin of distortion in $CaFeO_2$ as well as high-pressure stability of $CaFeO_2$. Our calculations show that $SrFeO_2$ ($P4/mmm$) and d-$CaFeO_2$ ($P\text{-}42_1m$) are dynamically stable with the G-type AFM structure, while p-$CaFeO_2$ ($P4/mmm$) is dynamically unstable at ambient pressure. The calculated phonon density of states of $SrFeO_2$ has been compared with the powder inelastic neutron scattering result.

The inelastic neutron scattering experiments were performed by Hiroshi Kageyama of Kyoto University, Japan using the MARI time of flight spectrometers at ISIS, UK. The measurements were done in the neutron-energy-loss mode using incident neutron energy of 120 meV at several temperatures from 5 to 353 K.

The Vienna *ab initio* simulation package (VASP) [23, 24] was used for calculations. The plane wave pseudo-potential with plane wave kinetic energy cutoff of 400 eV was used for both compounds. The integrations over the Brillouin zone were sampled on a 4×4×4 grid of k-points generated by Monkhorst-pack method [25]. The generalized gradient approximation (GGA) exchange correlation given by Perdew, Becke and Ernzerhof [26, 27] with projected-augmented wave method has been used. Since the compounds contain localized Fe 3*d* electrons at ambient pressure, we have used the simplified approach to the LSDA+U, introduced by Dudarev *et al*. [28]. The onsite interaction term U was taken to be 4.0 eV for *d* electrons of iron. We have included the G-type AFM magnetic ordering in both compounds.

Phonon spectra for $SrFeO_2$ and $CaFeO_2$ were extracted using the PHONON software [29]. All the phonon calculations are carried out in the fully relaxed configuration. The relaxed unit cell parameters are given in TABLE 5.1. We have also carried out an additional calculation of phonon modes in $SrFeO_2$ and p-$CaFeO_2$ (*P*4/*mmm*) as described in Section IV. The exchange parameter has been calculated using a Heisenberg spin Hamiltonian with forth neighbour interaction. To determine the magnetic ground state and discuss the magnetic properties of $SrFeO_2$, we considered four more ordered spin structures besides the FM state, namely, the AF1 state with q= (½ ½ ½), the AF2 state with q = (0 0 ½), the AF3 state with q = (½ ½ 0) and the AF4 state with q = (½ 0 ½).

5.2 Results and Discussion

5.2.1 Experimental and Calculated Phonon Spectra of Planar $SrFeO_2$

The measured neutron inelastic spectra of $SrFeO_2$ over a temperature range from 5K to 353 K shown in Fig 5.2. $SrFeO_2$ exhibits the G-type AFM order below 473 K. The data were averaged over a high-Q regime of 9-10Å^{-1} to avoid paramagnetic contributions to the phonon data. In Fig 5.3, we have shown the computed neutron weighted phonon spectra together with experimental spectra at T=5K. Here, the measured spectra were corrected from multiphonon contributions as calculated using Sjolander formalism[30]. In order to probe the individual atomic contribution, we also calculated the neutron weighted partial density of states. The calculations were done under GGA approximation. The GGA is expected to overestimate the lattice parameters and in turn underestimate the phonon frequencies. When the calculated energy spectrum is scaled by 6%, we obtained an excellent agreement between theory and experiment (Fig. 5.3), which partially justifies the use of our theoretical tool for other thermodynamical properties.

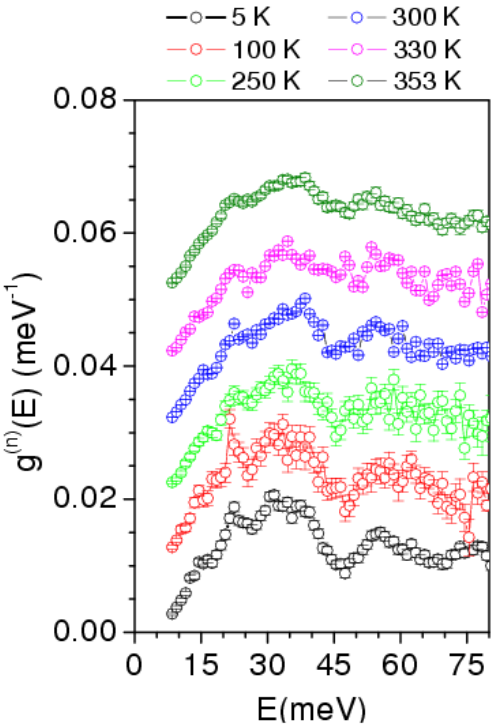

FIG 5.2 *Experimental phonon spectra of $SrFeO_2$ (P4/mmm) at various temperatures in the antiferromagnetic phase.*

We have also calculated the partial phonon density of states associated with various atoms (in Figure 5.4). This helps to assign the peaks in the experimental spectra. We note that the first peak around 15 meV (Fig. 5.4) has contributions from Sr atoms. The peaks around 25 meV, 30 meV and 40meV have large contributions from oxygen and iron atoms. The phonon spectra above 40 meV have mainly contributions from oxygen atoms. At higher temperature (Fig. 5.2), one can observe that the peaks about 15 meV and 25 meV retain their spectral features, while the peak about 30 meV shifts to higher energy. Furthermore, the peaks are significantly broadened above 300 K, which might be related[22] to the distortion in the planer structure of $SrFeO_2$, which is discussed later in this chapter .

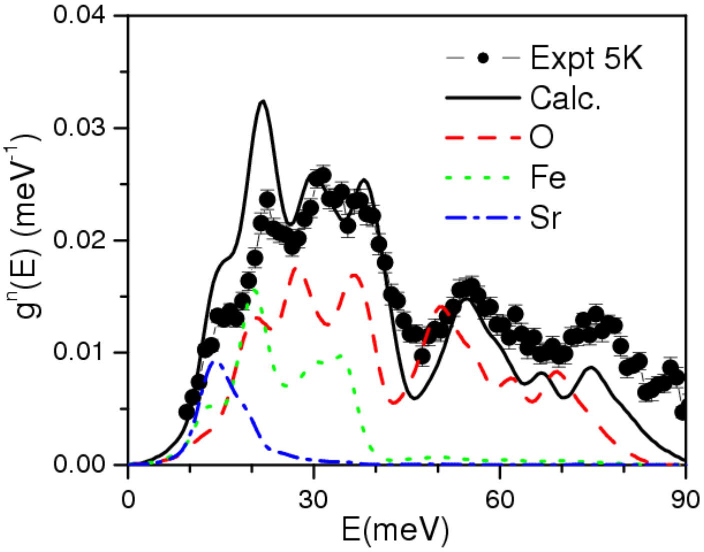

FIG 5.3 *Experimental and calculated phonon spectra of* $SrFeO_2$ *(P4/mmm).The partial atomic contributions to total neutron weighted phonon density of states are shown with dotted lines. The calculated spectra have been convoluted with a Gaussian of FWHM of 7meV of the energy transfer in order to describe the effect of energy resolution in the experiment. In order to compare with the experimental data the calculated spectrum is scaled by 6%.*

5.2.2 Phonon Spectra in $SrFeO_2$ and $CaFeO_2$

We have calculated the phonon spectra of $SrFeO_2$ and d-$CaFeO_2$ and p-$CaFeO_2$ in a relaxed geometry. The calculated lattice constants and experimental values are given in Table 5.1. In Fig. 5.4, we show the calculated partial and total density of states for $CaFeO_2$ and $SrFeO_2$. We find that the p-$CaFeO_2$ is dynamically unstable as observed in the previous study[21]. It may be noted that Ref.[21] provides the calculations of phonon modes at few selected points in the Brillouin zone. However our calculations of phonon spectra in entire Brillouin zone successfully give a complete picture of dynamics. They allow one to understand the differences in the calculated phonon spectra of d-$CaFeO_2$ and p-$CaFeO_2$ and compare with those of $SrFeO_2$.

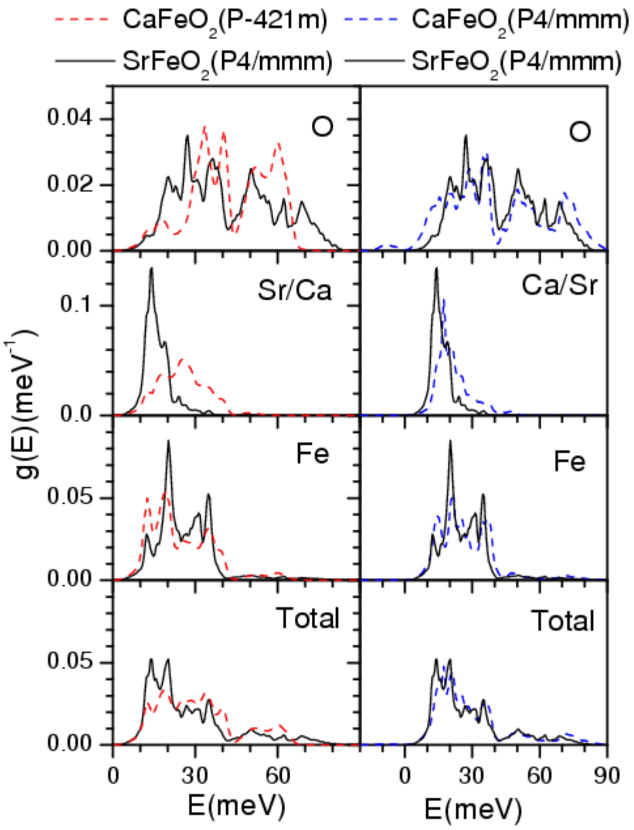

FIG 5.4 *Calculated partial densities of states of various atoms in $SrFeO_2$(P4/mmm),$CaFeO_2$ (P4/mmm) and $CaFeO_2$(P-42_1m).*

The calculated phonon spectra of d-$CaFeO_2$ and $SrFeO_2$ are significantly different (left panel Fig. 5.4). In $SrFeO_2$, the contribution from oxygen is extended in the entire spectral range up to 80 meV, while in d-$CaFeO_2$ it ranges up to 70 meV. Given the larger unit cell of $SrFeO_2$, one would naively expect that the phonon spectra in d-$CaFeO_2$ are broader than those in$SrFeO_2$, which is in contrast to the calculated result. This difference is understood in terms of the difference in bonding nature in Fe-O: the Fe-O stretching bond is stronger in planer geometry than that of distorted one. The A-site contribution in $SrFeO_2$ is limited to 35 meV, while in $CaFeO_2$ this extends up to 45 meV, which seems to follow the mass difference of Ca (40.08 amu) and Sr(87.62 amu). No major difference is observed in the Fe spectra. A further comparison of calculated phonon spectra in p-$CaFeO_2$ and $SrFeO_2$, as shown in the right panel of Fig. 5.4, reveals that it simply follows the volume consideration. In the p-$CaFeO_2$, the oxygen partial density of states extends from 10*i* to 90 meV, while the unstable modes in p-$CaFeO_2$ are found to be stable in the d-$CaFeO_2$. It seems that oxygen dynamics plays an important role in stabilizing the distorted structure.

TABLE 5.1 *Comparison of the calculated structural parameters of $SrFeO_2$ and $CaFeO_2$ with the experimental data. For isotropic temperature factors experimental data [14] and calculations are given at 293 K.*

	$SrFeO_2$, *P*4/*mmm* Expt. [3]	$SrFeO_2$ *P*4/*mmm* Calc.	$CaFeO_2$, *P*-42_1*m* Expt [6]	$CaFeO_2$ *P*-42_1*m* Calc.
a(Å)	3.991	4.042	5.507	5.550
c(Å)	3.474	3.497	3.355	3.443
B_{iso}(Sr/Ca) Å^2	0.470	0.440	0.485	0.580
B_{iso}(Fe) Å^2	0.470	0.380	0.590	0.490
B_{iso}(O) Å^2	0.790	0.610	0.909	0.660
Volume/ atom	13.83	14.28	12.72	13.26

TABLE 5.3 *Calculated Born effective charges (Z) as well as dielectric constants (ε) in various phases of $SrFeO_2$ and $CaFeO_2$.*

	Z_{xx}	Z_{xy}	Z_{yx}	Z_{yy}	Z_{zz}
$SrFeO_2$(*P*4/*mmm*) $\varepsilon_{xx} = 5.02$, $\varepsilon_{zz} = 5.82$					
Sr	2.29	0	0	2.29	2.97
Fe	2.97	0	0	2.97	0.35
O	-3.16	0	0	-2.10	-1.66
p-$CaFeO_2$(*P*4/*mmm*) $\varepsilon_{xx} = 5.80$, $\varepsilon_{zz} = 6.35$					
Ca	2.35	0	0	2.35	2.78
Fe	2.82	0	0	2.82	0.63
O	-3.03	0	0	-2.14	-1.71
d-$CaFeO_2$ ($P\text{-}42_1m$) $\varepsilon_{xx} = 4.97$, $\varepsilon_{zz} = 4.94$					
Ca	2.26	-0.07	-0.07	2.26	2.65
Fe	2.79	-0.13	0.13	2.79	0.74
O	-2.53	0.41	0.41	-2.53	-1.69

The partial densities of states have been used for the calculation of the mean square amplitude for various atoms at different temperatures. The comparison between the calculated values and the experimental data at 300 K is given in Table 5.1. The calculated temperature factors for Sr/Ca, Fe and O are similar in both compounds. The difference in nature of the in-plane and out-of-plane bonding may result in large anisotropic values of u^2 along the *x* and *z* axis. The observation is in agreement with the recent measurements[22] of u^2 in $SrFeO_2$.The larger values of u^2 of various atoms in d-$CaFeO_2$ in comparison with$SrFeO_2$may be due to smaller unit cell of d-$CaFeO_2$in addition to the difference in bonding nature.

In order to compare the nature of bonding in d-$CaFeO_2$, p-$CaFeO_2$ and $SrFeO_2$, we have computed the Born dynamical charge tensor (Table 5.3). Thanks to the high local site symmetry of Ca/Sr, Fe and O atoms, the Born effective charge tensors in planar structure (*P*4/*mmm*) have only few non-zero diagonal elements, namely in-plane ($Z_{xx} = Z_{yy}$) and out-of-plane (Z_{zz}) components. The calculated components of Born effective charges for p-$CaFeO_2$ and $SrFeO_2$ are very close. However, we observed a large difference in the Fe charges along *z* direction (Z_{xx} component) between p-$CaFeO_2$ and $SrFeO_2$. This might be due to difference in inter-planar separation of FeO_4 layers in p-$CaFeO_2$ and $SrFeO_2$ along the *c* direction, attributed to the difference in ionic radii between Ca and Sr. Furthermore, a comparison of the Born effective charge tensors in p-and d-$CaFeO_2$ reveals that Born effective charges for Ca and Fe are nearly the same. The out-of-plane (Z_{zz}) component for O atoms is nearly same, while there is a large difference in the in-plane (Z_{xx}, Z_{yy}) components. This indicates that the nature of Fe-O bonding in the *x*-*y* plane in planer and distorted structure is quite different.

The p-$CaFeO_2$ and $SrFeO_2$ (*P*4/*mmm*) has 4 atoms in unit cell, which results in 12 vibrational modes for each wave vector. Group theoretical symmetry analysis[29] was carried out to classify the phonon modes belonging to various representations. The group theoretical decomposition of the phonon modes at the zone centre (Γ point) and zone boundary (M and A points) are given by:

$$\Gamma=3A_{2u} + B_u + 4E_u$$

$$M= M_1^{+}+ M_2^{+}+M_3^{+} +M_4^{+}+ 2M_5^{+}+M_2^{-}+ M_3^{-}+ 4M_5^{-}$$

$$A= A_1^{+}+ A_2^{+}+A_3^{+} +2A_4^{+}+ 4A_5^{+}+ A_3^{-}+ 2A_5^{-}$$

At the Γ point, all the modes are infrared active. For d-$CaFeO_2$ ($P\text{-}42_1m$), the classification of modes at the Γ point is given by:

$$\Gamma=3A_1 + A_2 + 2B_1 + 4B_2 + 7E$$

TABLE 5.2 (a) *The calculated zone centre optic phonon modes for* $SrFeO_2$ *(P4/mmm) and d-*$CaFeO_2$ *(P-*42_1*m) in meV units. (1 meV=8.0585* cm^{-1}*).*

	$SrFeO_2$ (*P*4/*mmm*)	$CaFeO_2$ (*P*4/*mmm*)	$CaFeO_2$ (*P*-42_1*m*)	
A_u	23.7 44.7	24.9 44.4	A_1	15.2 26.9 35.7
B_u	9.4	13.7*i*	A_2	65.4
E_u	21.2 35.0 62.6	23.1 33.9 71.4	B_1	20.2 44.6
			B_2	25.2 48.9 60.5
			E	16.0 27.8 29.7 38.9 41.6

In this case, all the modes are Raman active, with the B_2 and E modes being also infra-red active. The calculated zone centre modes are given in Table 5.2(a). The lowest energy B_u mode (9.43 meV) in $SrFeO_2$ is smaller than the lowest A_1 mode (15.16 meV) in $CaFeO_2$, which should arises from the larger unit cell volume in $SrFeO_2$ in comparison with $CaFeO_2$. The zone boundary modes for p-$CaFeO_2$ (*P*4/*mmm*) have also been calculated (Table 5.2(b)).

TABLE 5.2 (b) *The calculated zone boundary modes for $CaFeO_2$ (P4/mmm) in meV units. (1 meV=8.0585 cm^{-1}). M_5^+, M_5^-, A_5^+ and A_4^- are doubly degenerate modes.*

$CaFeO_2$ (*P*4/*mmm*)			
M_3^+	8.2	A_3^+	11.5*i*
M_5^+	12.6	A_5^+	17.9
M_2^-	13.7	A_3^-	19.9
M_5^-	19.1	A_4^+	29.5
M_3^-	21.9	A_5^+	30.4
M_5^-	43.0	A_5^-	36.8
M_2^+	48.6	A_2^+	46.4
M_4^+	56.7	A_4^+	50.2
M_1^+	73.1	A_1^+	68.6

5.2.3 Dynamical Instabilities in Planer $CaFeO_2$ and Stabilization of Distorted $CaFeO_2$ at Ambient Pressure

The calculated phonon dispersion relations along various high symmetry directions in $SrFeO_2$, p- and d-CaFeO2 are shown in Fig. 5.5. All the modes in the entire Brillouin zone are found to be stable in $SrFeO_2$ and d-$CaFeO_2$, while in p-$CaFeO_2$ the low energy B_u mode at the zone centre and A_3^+ mode at A(½½½) point are unstable. We have performed the amplitude mode analysis[31], which indicates that the distortion in p-$CaFeO_2$ is induced by

B_u, M_3^+ and M_2^- phonon modes. Our calculation of phonon dispersion relation in high symmetry phase of p-$CaFeO_2$ gives stable phonons at M(½½ 0) point.

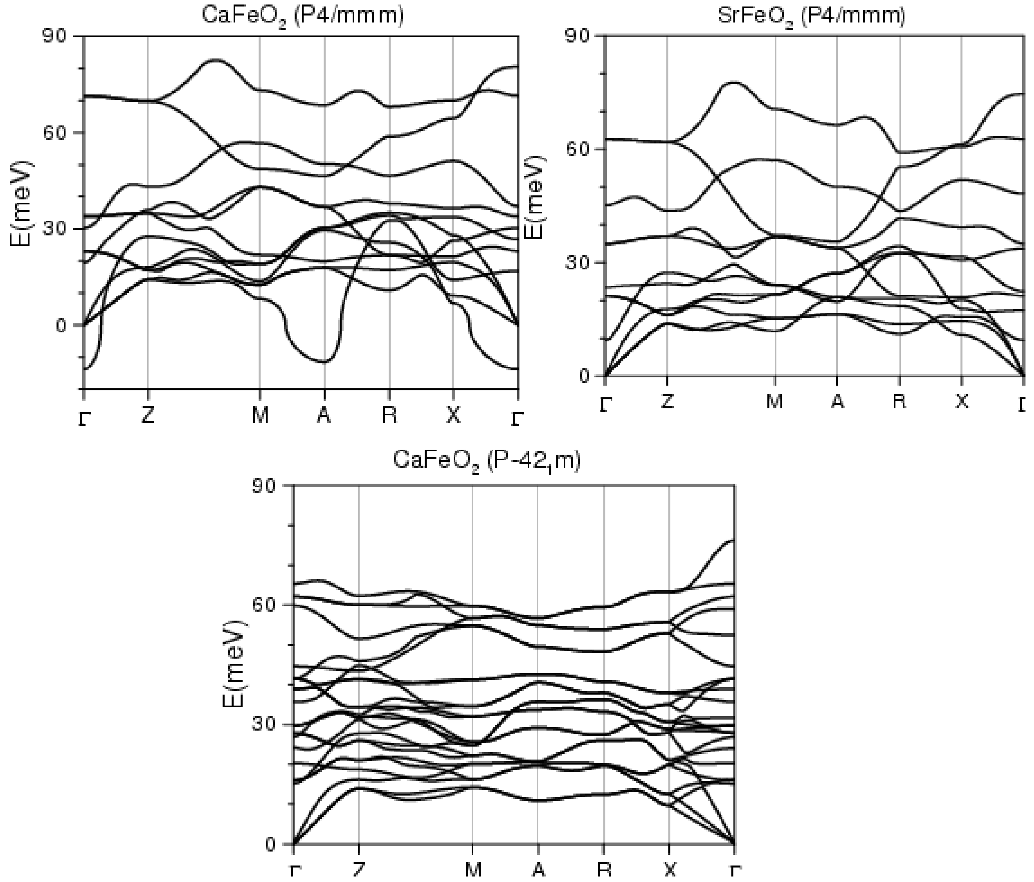

FIG 5.5 *Calculated dispersion relation of $SrFeO_2$ and $CaFeO_2$in P4/mmm space group.. The solid and dashed lines correspond to calculations at ambient pressure and 5 kbar, respectively. The Bradley-Cracknell notation is used for the high symmetry points along which the dispersion relations are obtained: Γ=(0, 0, 0), Z = (1/2, 0, 0) , M = (1/2, 1/2 , 0). A = (1/2, 1/2, 1/2), R = (0, 1/2, 1/2), X = (1/2, 0, 0).*

The M_3^+ mode involves the in-phase rotation of FeO_4 units about *z* axis, while the M_2^- mode involves the out-of-phase displacement of neighbouring Ca atoms along *z*. The unstable B_u mode at zone centre involves the displacement of oxygen atom along ±z direction and another unstable A_3^+ mode at A(½ ½ ½) involves the out-of-phase rotation of FeO_4 about *z* direction in the alternative layer. In summary, M_3^+, B_u and A_3^+ modes could be responsible for the shifting of oxygen positions, while M_2^- mode is responsible for the shifting of Ca position. The strong coupling between the low energy phonon modes in p-$CaFeO_2$ has been also discussed in Ref.[21]. These characteristic phonon modes are represented in Fig. 5.6.

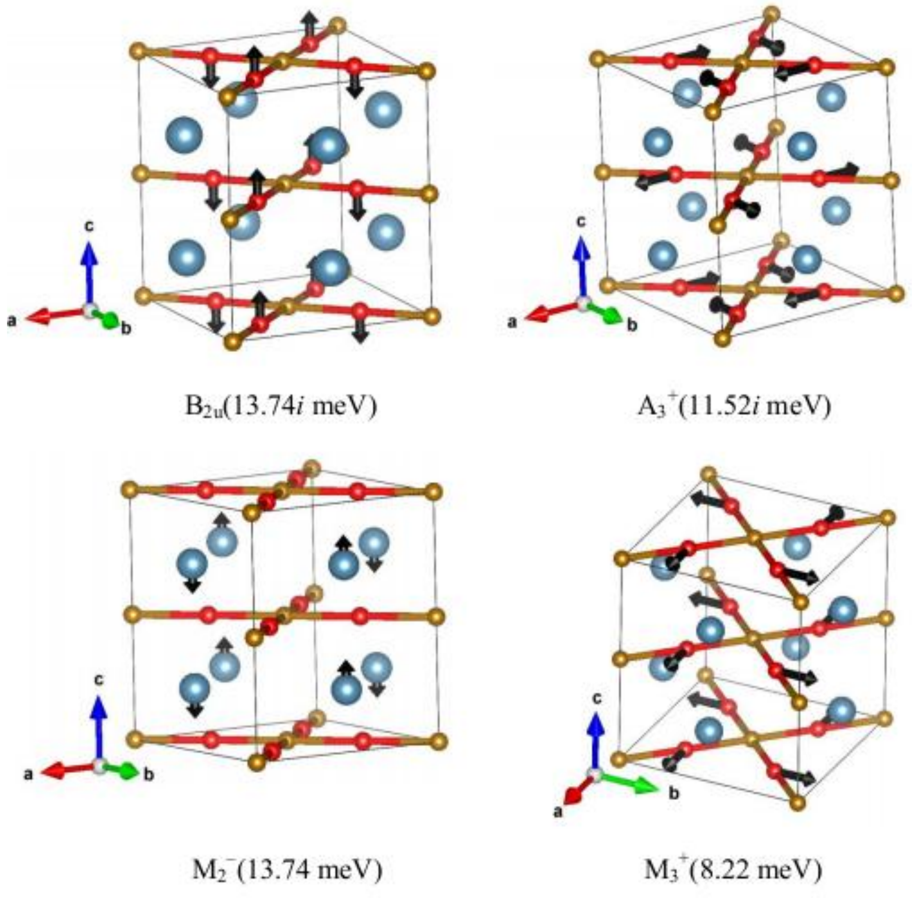

B_{2u}(13.74*i* meV)

A_3^+(11.52*i* meV)

M_2^-(13.74 meV)

M_3^+(8.22 meV)

FIG 5.6 *Polarization vectors of selected zone center modes of* $CaFeO_2$*in P4/mmmFor each mode, the assignment and frequency are indicated in meV units. The 'i' after the phonon energy indicates that mode is unstable. The length of the arrows is related to the displacement of the atoms. The absence of an arrow on an atom indicates that the atom is at rest. The number after the mode assignment gives the phonon frequency. Key: Ca, blue spheres; Fe, golden spheres; O, red spheres (1 meV=8.0585* cm^{-1}*).*

In order to obtain further insights into the structural instability in p-CaFeO$_2$, we have calculated the energy profiles (Fig. 5.7) of p-CaFeO$_2$ by exciting pairs of phonon modes simultaneously with different amplitude. The unstable modes A_3^+ and B_u will not give a minimum in the total energy at zero phonon distortion. One may expect some minima at finite distortion created by these unstable phonon modes. The calculated energy profile of B_u phonon mode with different distortion amplitude of A_3^+ phonon mode is shown in Fig. 5.7(a). As we increase the amplitude of any one of the mode, the energy profile of the other phonon mode transforms from a double-well potential to a single-well potential. However, the A_3^+ mode is found to stabilize with only a small amplitude of the B_u mode. The B_u phonon mode is also found to get stabilized at finite distortion resulting by A_3^+ mode. The energy profiles as obtained from simultaneous excitation of A_3^+ with M_3^+ and A_3^+ with M_2^- are shown in Fig. 5.7(b) and 5.7(c), respectively. One can see that the distortion in M_3^+ or M_2^- modes also stablizes the unstable A_3^+ mode. However, the required magnitude of distortion of M_2^- mode is much larger than that of M_3^+. In Fig. 5.7(d) and 5.7(e), we show the energy profiles as obtained from simultaneous excitation of B_u mode with M_3^+ and B_u mode with M_2^- mode respectively. The distortion of M_3^+ leads to a single minima for the B_u mode but at very high energy. On the other hand, the M_2^- mode does not stabilize the zone centre B_u instability as it remains a double-well even at large distortion of M_2^- mode. In conclusion, the B_u and the modes at M point show anharmonic coupling with the unstable mode at A point. The coupling between A_3^+ and B_u mode leads to stabilization of A_3^+ mode (Fig. 5.7(a)) prior to B_u. The stabilization of B_u at finite amplitude of A_3^+ and M_3^+ is not of any consequence (Fig. 5.7(a, d)) as it does not lead to a deeper minima in total energy. It is clear that any of the mode coupling involving only two modes as discussed above does not explain the observed distortion in CaFeO$_2$.

TABLE 5.4 *The calculated structures of d-*$CaFeO_2$ *(*$P\text{-}42_1m$*) and (√2×√2×1) super cell of p-*$CaFeO_2$ *(P4/mmm). The super cell (√2×√2×1) of p-*$CaFeO_2$ *is equivalent to the d-*$CaFeO_2$*. The distortion vector is obtained from the difference in atomic co-ordinates between d-*$CaFeO_2$ *and p-*$CaFeO_2$ *structures phases. The eigen vector of the unstable* B_u *and stable* M_3^+ *and* M_2^- *modes in the p-*$CaFeO_2$ *phase for the super cell is also given. A linear combination of Bu ,* M_3^+ *and* M_2^- *modes with appropriate weight factor is used to generate the observed distortion vector as given in the last column of the table.*

		P-42$_1$m CaFeO$_2$	**P4/mmm CaFeO$_2$**	**Distortion vector**	**B$_u$**	**M$_3^+$**	**M$_2^-$**	**0.25Bu+0.085M$_3^+$ +0.141M$_2^-$**
	a (Å)	5.550	5.622					
	b (Å)	5.550	5.622					
	c (Å)	3.443	3.234					
O1	*x*	0.720	0.750	0.030	0.000	0.354	0.000	0.030
	y	0.780	0.750	-0.030	0.000	-0.354	0.000	-0.030
	z	-0.120	0.000	0.120	0. 500	0.000	0.000	0.120
O2	*x*	0.280	0.250	-0.030	0.000	-0.354	0.000	-0.030
	y	0.220	0.250	0.030	0.000	0.354	0.000	0.030
	z	-0.120	0.000	0.120	0.500	0.000	0.000	0.120
O3	*x*	0.220	0.250	0.030	0.000	0.354	0.000	0.030
	y	0.720	0.750	0.030	0.000	0.354	0.000	0.030
	z	0.120	0.000	-0.120	-0.500	0.000	0.000	-0.120
O4	*x*	0.780	0.750	-0.030	0.000	-0.354	0.000	-0.030
	y	0.280	0.250	-0.030	0.000	-0.354	0.000	-0.030
	z	0.120	0.000	-0.120	-0.500	0.000	0.000	-0.120
Ca1	*x*	0.500	0.500	0.000	0.000	0.000	0.000	0.000
	y	0.000	0.000	0.000	0.000	0.000	0.000	0.000
	z	0.400	0.500	0.100	0.000	0.000	0.707	0.100
Ca2	*x*	0.000	0.000	0.000	0.000	0.000	0.000	0.000
	y	0.500	0.500	0.000	0.000	0.000	0.000	0.000
	z	0.600	0.500	-0.100	0.000	0.000	-0.707	-0.100
Fe1	*x*	0.000	0.000	0.000	0.000	0.000	0.000	0.000
	y	0.000	0.000	0.000	0.000	0.000	0.000	0.000
	z	0.000	0.000	0.000	0.000	0.000	0.000	0.000
Fe2	*x*	0.500	0.500	0.000	0.000	0.000	0.000	0.000
	y	0.500	0.500	0.000	0.000	0.000	0.000	0.000
	z	0.000	0.000	0.000	0.000	0.000	0.000	0.000

As mentioned above the amplitude mode analysis[31] indicates that the distortion in p-$CaFeO_2$ is induced by B_u, M_3^+ and M_2^- phonon modes. The calculated structures of d-$CaFeO_2$ (P-42_1m) and (√2×√2×1) super cell of p-$CaFeO_2$ (P4/mmm) is given in TABLE 5.4. The difference in the atomic coordinates of room temperature phase (P6_3*cm*) and the (√2×√2×1 super cell of the p-$CaFeO_2$ (P4/mmm) is a measure of the distortion required to stabilize the d-$CaFeO_2$ (P-42_1m). The eigen vectors of the unstable B_u and stable M point modes of p-$CaFeO_2$ (P4/mmm) for the super cell are given in Table 5.4. The eigen vector as obtained with appropriate weight of B_u (52%) and M_3^+ (18%) and M_2^- (30%) point modes is used to generate the observed distortion vector, which matches very well with the distortion vector. This clearly shows that the coupling between B_{2u}, M_3^+, and M_2^- point modes is able to explain the observed distortion in planer structure and stabilizes d-$CaFeO_2$. Usually the cell doubling in the plane may be expected due to a soft mode at the M(½½ 0) point. However, in the present case all the modes at the M-point are stable and instabilities are found at Γ and A point. We find that the stable M-point modes (M_3^+ and M_2^-) couple anharmonicity with the Γ point Bu phonon and result in the cell doubling in the a-b plane. It also turns out that the soft mode at the A-point does not have any role in inducing the distortion or the cell doubling.

We have also determined the energy barrier between the p-$CaFeO_2$ (P4/mmm) and the d-$CaFeO_2$ (P-42_1m) structures. We started with the calculated structure (TABLE 5.4) of p-$CaFeO_2$ (P4/mmm). The distortion vector as given in TABLE 5.4 is further used to obtain (Fig 5.8) the profile of the energy barrier. The energy barrier between the two structures is calculated to be 0.3 eV. The calculations clearly show that a minimum in the profile is obtained at unit distortion in the p-$CaFeO_2$, thus confirms the stability of d-$CaFeO_2$. Our ab-initio calculations for $SrFeO_2$ reveal that with increase of volume a B_u mode becomes unstable. This unstable mode is similar to that found in p-$CaFeO_2$ at ambient conditions.

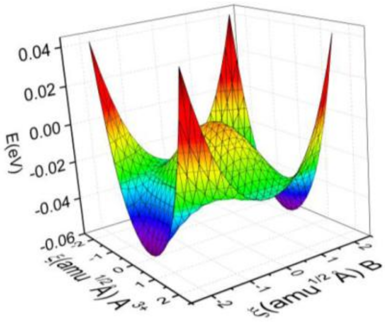

(a) A_3^+ and B_u modes

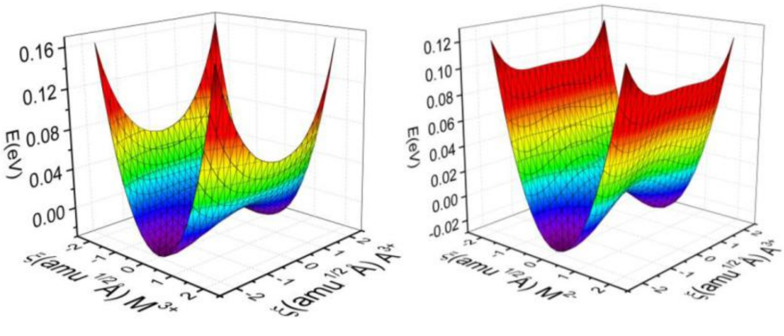

(b) M_3^+ and A_3^+ modes **(c) M_2^- and A_3^+ modes**

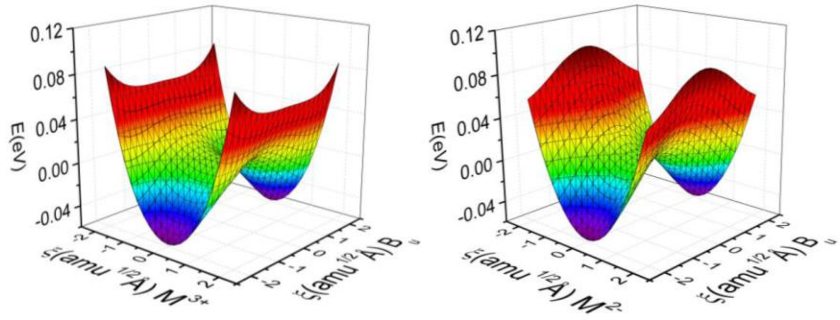

(d) M_3^+ and B_u modes **(e) M_2^- and B_u modes**

FIG 5.7 *The energy landscape of p-$CaFeO_2$ obtained by exciting the pair of phonons with different amplitude. (a) $A^{3+}$and B_u modes (b) M^{3+} and A^{3+} modes (c) M^{2-} andA^{3+} modes (d) $M^{3+}$and B_u modes and (e) $M^{2-}$and B_u modes. The energies E are per magnetic unit cell.*

We suggest that the distortion in $SrFeO_2$ as revealed from the phonon measurements at above 300 K is similar to that known in d-$CaFeO_2$ at ambient conditions. This is qualitatively in agreement with the nature of distortion reported [22] from an analysis of the total neutron scattering in $SrFeO_2$ at around 450 K.

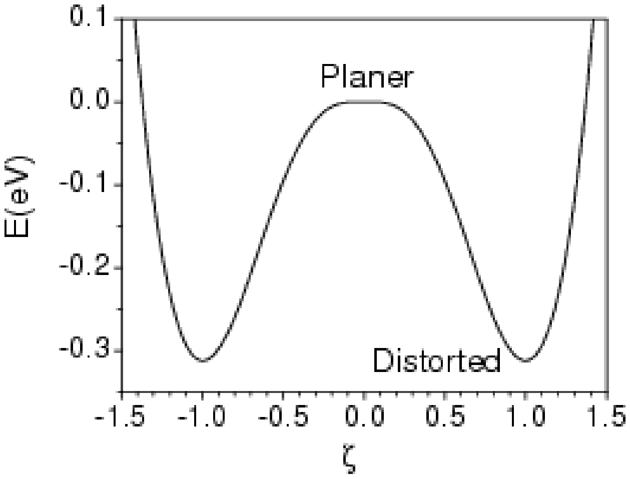

FIG 5.8 *Energy barrier from the p-$CaFeO_2$ (P4/mmm) to the d-$CaFeO_2$ (P-42_1m). ζ corresponds to the distortion vector as obtained from the difference in atomic co-ordinates of the d-$CaFeO_2$ and p-$CaFeO_2$ structures phases as given in TABLE 5.4. The energies E is per magnetic unit cell.*

5.2.4 Phase Transition from Distorted to Planer $CaFeO_2$ at High Pressure

At high pressure, the interlayer separation between FeO_4 planes reduces, which may stabilize the planer structure of p-$CaFeO_2$. The comparison of the distorted and planar structure (TABLE 5.4) at ambient pressure shows that difference in the two structures arises due to distortion in the atomic positions of the oxygen and calcium atoms in the p-$CaFeO_2$. The calculated x and z-coordinate of the oxygen and z-coordinate of the calcium atom in the d-$CaFeO_2$ as a function of pressure is shown in Fig. 5.9(a), which indicates that with increase of pressure the distorted structure finally transform to the p-$CaFeO_2$ (Fig. 5.9(a)) at around 20 GPa. In order to check the dynamical stability of the p-$CaFeO_2$ structure, we calculated the phonon dispersion relation in the entire Brillouin zone at 30 GPa. As shown in Fig. 5.9(b), all the phonon modes in p-$CaFeO_2$ are indeed dynamically stable. This suggests a second order phase transition to the distorted to planar structure.

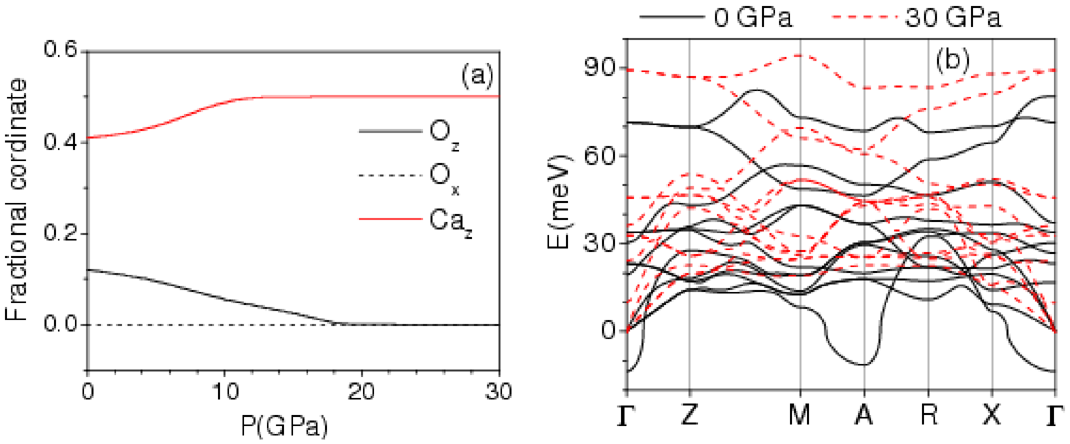

FIG 5.9 *(a) The calculated x and z-coordinate of the oxygen and z-coordinate of the calcium atom in the d-$CaFeO_2$ as a function of pressure. As given in Table 5.4 the oxygen and calcium atoms occupy the Wyckoff sites 4e(x+1/2, -x, -z) and (1/2 0 –z) respectively. (b) The calculated phonon dispersion of planer $CaFeO_2$ at ambient and 30GPa.*

5.2.5 Spin Phonon Coupling and Magnetic Exchange Interaction Parameters in Planar $SrFeO_2$ and $CaFeO_2$

The electronic structure calculations as reported in the literature[18] show a possibility of electromagnetic coupling in planar $BaFeO_2$ as well as distorted $CaFeO_2$. In addition, a significant change was shown in electronic contribution to the total density of states of different atoms with different magnetic configurations (A, C, G antiferromagnetic and ferromagnetic F). In A-type antiferromagnetic configuration Fe atoms interact ferromagnetically within a-b plane and antiferromagnetically to adjacent a-b plane. In C-type configuration the intraplaner interaction between Fe atoms is antiferromagnetic in nature but interplaner interaction is ferromagnetic. However in G-type configuration all Fe atoms interact antiferromagnetically with nearest Fe atoms. This motivated us to perform the phonon calculations of p-$CaFeO_2$ and $SrFeO_2$ in various antiferromagnetic magnetic configurations, namely, A, C, G as well as in the ferromagnetic (F) configurations. As shown in Fig. 5.10, we could not observe significant difference in the calculated phonon dispersion relations for p-$CaFeO_2$ in various magnetic configurations. The zone-centre and zone-boundary instabilities remained present in all the calculations while their magnitude of instabilities changed slightly. This shows that the p-$CaFeO_2$ structure is not dynamically stable in the above said magnetic structures.

TABLE 5.5 *Calculated lattice parameters and bond length of $CaFeO_2$ and $SrFeO_2$ in various magnetic configurations (A, C, G type antiferromagnetic and Ferromagnetic F).*

	$CaFeO_2$				$SrFeO_2$			
	G	C	A	F	G	C	A	F
a(Å)	3.975	3.976	3.994	3.993	4.042	4.042	4.061	4.061
b(Å)	3.975	3.976	3.994	3.993	4.042	4.042	4.061	4.061
c(Å)	3.234	3.238	3.229	3.232	3.497	3.499	3.487	3.488
Fe-O(Å)	1.987	1.988	1.997	1.996	2.021	2.021	2.031	2.031
Interlayer Separation(Å)	3.234	3.238	3.229	3.232	3.497	3.499	3.487	3.488

As mentioned above, $SrFeO_2$ is found dynamically stable with the G-type AFM ordering. We find that zone centre B_u mode for $SrFeO_2$ becomes unstable in FM and A-type spin configurations, while in C-type and G-type it is dynamically stable. In FM and A type configurations, the parallely aligned Fe moments within the layer result in a slightly larger

Fe-O bond length (2.03 Å) in comparison to the Fe-O bond (2.02 Å) in C and G type configurations with anti-parallelly aligned Fe moments (see Table 5.4).

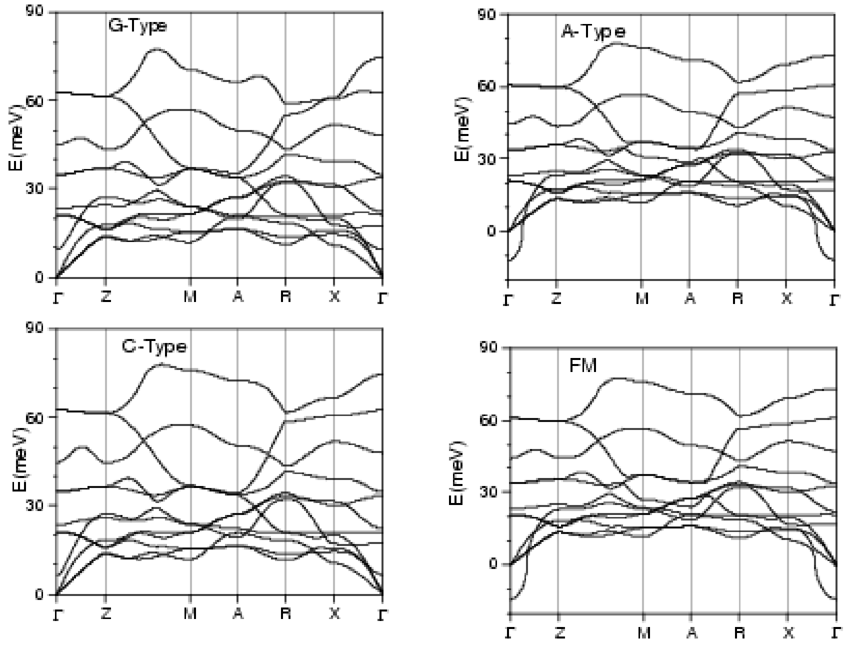

CaFeO₂

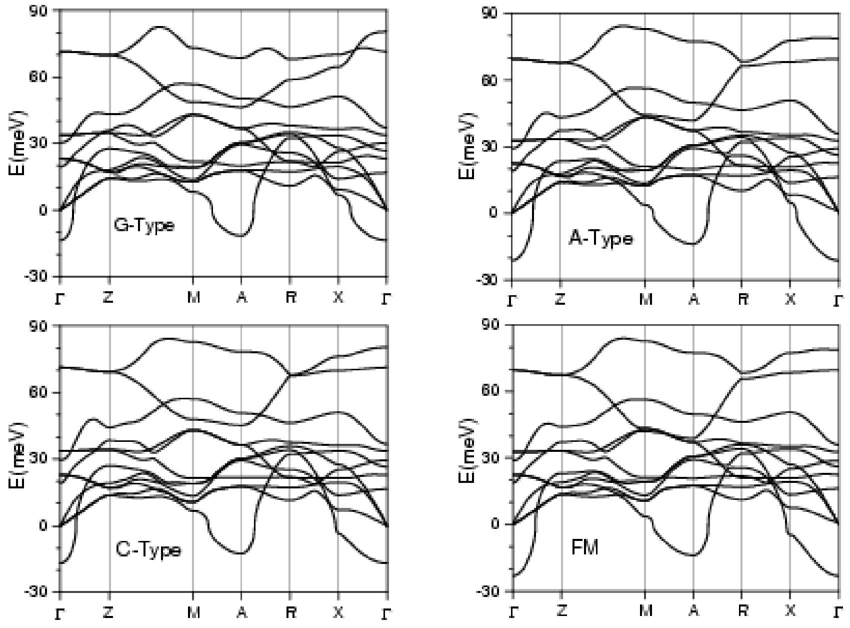

FIG 5.10 *Calculated dispersion relations of $SrFeO_2$(P4/mmm) and $CaFeO_2$(P4/mmm)including the A, C, G antiferromagnetic and FM configurations.*

The phonon spectra are also sensitive to the interlayer distances in the quasi two-dimensional systems. The calculations performed including the C type and G-Type structures on $SrFeO_2$ seem to result in a slightly larger interlayer separation (TABLE 5.5), in comparison to the A- and F-type configurations. Figure 5.10 shows that a small change in interlayer distance caused by different magnetic interaction gives significant influences on phonon spectra. These calculations suggest that nature of magnetic configurations have significant impact on the structural stability as well as anharmonicity of phonons. As mentioned above, the phonon spectra in $SrFeO_2$ change significantly with the change in magnetic configurations, implying a strong spin phonon coupling. However, phonons in p-$CaFeO_2$ show a weak dependence with change in magnetic configurations, indicating a weak spin-phonon coupling of phonons.

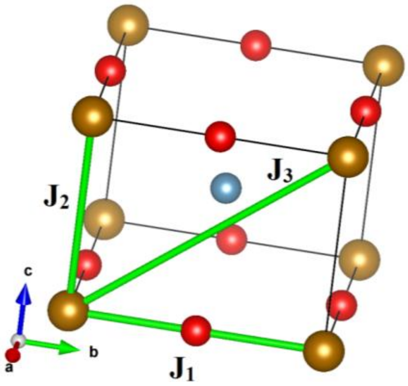

FIG 5.11 *The various J exchange interaction parameters in $SrFeO_2$ (P4/mmm) and p-$CaFeO_2$(P4/mmm).*

Analysis of the high-resolution neutron diffraction measurements on $SrFeO_2$ shows[22] that the exchange parameters are reduced significantly above 300 K along with the local distortion in the planer geometry. We calculated the exchange interaction parameters J_1, J_2, J_3 and J_4 for $SrFeO_2$ and $CaFeO_2$ (see Fig. 5.11). The calculated exchange parameters at different amplitudes of phonon distortion of B_u mode (Fig. 5.12)show that with the increase in the distortion amplitude of B_u phonon mode, the exchange parameters indeed reduce significantly, in consistent with the experiment[32]. At high temperature, the amplitude and population of low energy modes should be significantly large and hence the distortion involving out-of-plane oxygen motion (Fig. 5.6) would be enhanced.

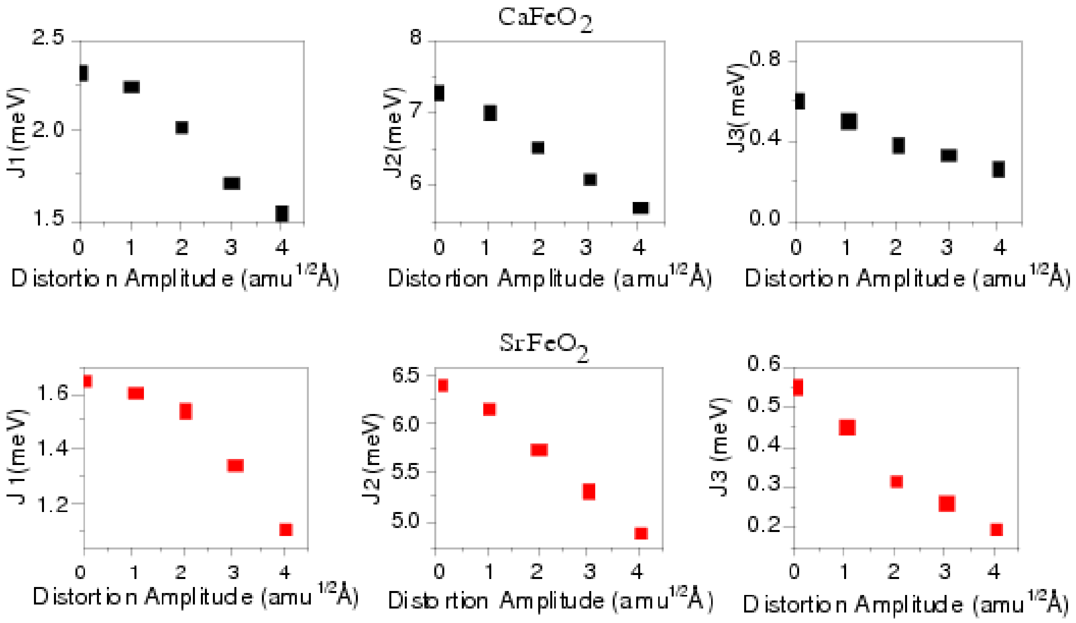

FIG 5.12 *The calculated magnetic exchange interaction parameters (J's) in $SrFeO_2$ (P4/mmm) and p-$CaFeO_2$(P4/mmm) compound at different amplitude of B_u phonon mode distortion.*

5.3 Conclusions

We have reported detailed measurements of the temperature dependence of the phonon density-of-states of $SrFeO_2$ in the antiferromagnetic phase (*P*4/*mmm*). The phonon spectrum shows anharmonic broadening above 300 K, which is consistent with the reported distortion of the planer structure.The phonon spectra of $SrFeO_2$ have been analysed based on detailed *ab-initio* lattice dynamical calculations in the magnetic state. Our calculations show that Fe magnetism is essential for stabilizing the *P4/mmm* structure of $SrFeO_2$. However the calculations carried out in the same space group for $CaFeO_2$ result in dynamically unstable structure. The lattice contraction in $CaFeO_2$ in compare to $SrFeO_2$ does not explain the presence of phonon instabilities, which may be due to difference in nature of bonding in $SrFeO_2$ and $CaFeO_2$. The anharmonic coupling of the unstable B_u mode with two stable zone boundary modes at the M point are shown to lead to the distortion in the planer structure (P4/mmm) and stabilization of d-$CaFeO_2$ (P-42_1m). These observations are consistent with the available experimental structural data. The spin exchange interaction parameters are found to decrease with increase in the distortion of the planer structure as described by the amplitude of B_u phonon mode. Calculations at high pressures predict that the undistorted planer $CaFeO_2$ would stabilize.

[1] R. M. H. C. W. Burnham, Americal Mineralogist **59**, 10 (1974).

[2] J. C. Grenier, A. Wattiaux, J. P. Doumerc, P. Dordor, L. Fournes, J. P. Chaminade and M. Pouchard, Journal of Solid State Chemistry **96**, 20 (1992).

[3] Y. Tsujimoto, C. Tassel, N. Hayashi, T. Watanabe, H. Kageyama, K. Yoshimura, M. Takano, M. Ceretti, C. Ritter and W. Paulus, Nature **450**, 1062 (2007).

[4] H. Peng, H. J. Xiang, S.-H. Wei, S.-S. Li, J.-B. Xia and J. Li, Physical Review Letters **102**, 017201 (2009).

[5] KawakamiT, TsujimotoY, KageyamaH, X.-Q. Chen, C. L. Fu, TasselC, KitadaA, SutoS, HiramaK, SekiyaY, MakinoY, OkadaT, YagiT, HayashiN, YoshimuraK, NasuS, PodlouckyR and TakanoM, Nat Chem **1**, 371 (2009).

[6] J. M. Pruneda, J. Íñiguez, E. Canadell, H. Kageyama and M. Takano, Physical Review B **78**, 115101 (2008).

[7] M. Rahman, Y.-z. Nie and G.-h. Guo, Inorganic Chemistry **52**, 12529 (2013).

[8] K. Masayoshi, K. Tomoko, S. Katsuya and K. Hiroshi, Journal of Physics: Conference Series **592**, 012041 (2015).

[9] S. Inoue, M. Kawai, Y. Shimakawa, M. Mizumaki, N. Kawamura, T. Watanabe, Y. Tsujimoto, H. Kageyama and K. Yoshimura, Applied Physics Letters **92**, 161911 (2008).

[10] T. Kawakami and H. Kageyama, Zeitschrift für Kristallographie Crystalline Materials, **225**, 504 (2010)

[11] K. Tomiyasu, H. Kageyama, C. Lee, M. H. Whangbo, Y. Tsujimoto, K. Yoshimura, J. W. Taylor, A. Llobet, F. Trouw, K. Kakurai and K. Yamada, Journal of the Physical Society of Japan **79**, 034707 (2010).

[12] T. Yamamoto, Y. Kobayashi, N. Hayashi, C. Tassel, T. Saito, S. Yamanaka, M. Takano, K. Ohoyama, Y. Shimakawa, K. Yoshimura and H. Kageyama, Journal of the American Chemical Society **134**, 11444 (2012).

[13] L. Seinberg, T. Yamamoto, C. Tassel, Y. Kobayashi, N. Hayashi, A. Kitada, Y. Sumida, T. Watanabe, M. Nishi, K. Ohoyama, K. Yoshimura, M. Takano, W. Paulus and H. Kageyama, Inorganic Chemistry **50**, 3988 (2011).

[14] T. Yamamoto, Z. Li, C. Tassel, N. Hayashi, M. Takano, M. Isobe, Y. Ueda, K. Ohoyama, K. Yoshimura, Y. Kobayashi and H. Kageyama, Inorganic Chemistry **49**, 5957 (2010).

[15] K. Matsumoto, D. Kan, N. Ichikawa, S. Hosokawa, H. Kageyama and Y. Shimakawa, Chemistry Letters **42**, 732 (2013).

[16] N. Z. Ali, J. Nuss, D. Sheptyakov and M. Jansen, Journal of Solid State Chemistry **183**, 752 (2010).

[17] P. Andrea, C. Monica, R. J. Mark, A. Giovanni, P. Werner and L. Carlo, Journal of Physics: Condensed Matter **27**, 225403 (2015).

[18] K. Yamauchi, T. Oguchi and S. Picozzi, Journal of the Physical Society of Japan **83**, 094712 (2014).

[19] N. Murakami, D. Kan, N. Ichikawa and Y. Shimakawa, Dalton Transactions **43**, 14596 (2014).

[20] H.-S. Lu, T.-Y. Cai, S. Ju and C.-D. Gong, The Journal of Physical Chemistry C **119**, 17673 (2015).

[21] C. Tassel, J. M. Pruneda, N. Hayashi, T. Watanabe, A. Kitada, Y. Tsujimoto, H. Kageyama, K. Yoshimura, M. Takano, M. Nishi, K. Ohoyama, M. Mizumaki, N. Kawamura, J. Íñiguez and E. Canadell, Journal of the American Chemical Society **131**, 221 (2009).

[22] K. Horigane, A. Llobet and D. Louca, Physical Review Letters **112**, 097001 (2014).

[23] G. Kresse and J. Furthmüller, Computational Materials Science **6**, 15 (1996).

[24] G. Kresse and D. Joubert, Physical Review B **59**, 1758 (1999).

[25] H. J. Monkhorst and J. D. Pack, Physical Review B **13**, 5188 (1976).

[26] J. P. Perdew, K. Burke and M. Ernzerhof, Physical Review Letters **77**, 3865 (1996).

[27] J. P. Perdew, K. Burke and M. Ernzerhof, Physical Review Letters **78**, 1396 (1997).

[28] S. L. Dudarev, G. A. Botton, S. Y. Savrasov, C. J. Humphreys and A. P. Sutton, Physical Review B **57**, 1505 (1998).

[29] K. Parlinksi, (2003)

[30] A. Sjolander, arkiv für Fysik **14**, (1958).

[31] http://www.cryst.ehu.es/,

[32] S. Mathi Jaya, R. Jagadish, R. S. Rao and R. Asokamani, Physical Review B **43**, 13274 (1991).

Chapter 6

Lattice Dynamics and Phase Transitions in Perovskites $NaNbO_3$ and $RMnO_3$ (R= Ca and Pr)

6.1 Introduction

The materials with perovskite structure have been a subject of intense numerical investigations by means of first-principles calculations [1-5]. Virtually, all perovskites exhibit high-symmetry (cubic) structure at high temperatures. Materials exhibiting ferroelectric/ piezoelectric properties are a subject of keen interest due to their potentially practical applications ranging from high density memories to advanced robotic technology (as sensor and actuator) [6-13]. Phonons have been known to play a key role in the understanding of structural phase transitions in ferroelectrics. Most of the ferroelectric transitions are governed by softening of phonon modes in the high symmetry phase.

Further, the perovskite with transition-metal oxides show a variety of interesting physical properties, such as dielectric, magnetic, optical, and transport properties [14-25]. The study of perovskite manganite $RMnO_3$ (R= Ca, La, Pr etc) has been of great relevance [20-33]. The cubic perovskite structure has unstable modes at T=0 and it is therefore subject to energy-lowering distortions like zone-center distortions and zone-boundary distortions involving rotations and/or tilting of the oxygen octahedral results in sequence of phase transition as a function of temperature and pressure. In this chapter, results obtained on perovskites $NaNbO_3$ and $AMnO_3$ (A= Ca and Pr) are given in sections 6.2 and 6.3 respectively.

6.2 $NaNbO_3$

Niobate based materials are environment friendly and appropriate for wide piezoelectric applications due to their piezo-response that is comparable to $Pb(Zr Ti)O_3$. One of the end members, $NaNbO_3$ is a well-documented antiferroelectric that also finds applications in high density optical storage, enhancement of non-linear optical properties, as hologram recording materials, etc [10-12, 34]. Relaxor type behavior in $NaNbO_3$ based solid solutions has also been reported [34]. Beyond the technological application, $NaNbO_3$ has been a rich model system for understanding of the mechanism of structural phase transitions. This system exhibits one of the most complex sequences of structural phase transitions in the perovskite family [35, 36]. Above 913 K, it has a paraelectric cubic phase (*Pm-3m).* On lowering the temperature it undergoes transition to a series of antiferrodistortive phases in this order: tetragonal (*T*2) *P4/mbm*, orthorhombic (*T*1) *Cmcm*, orthorhombic (*S*) *Pbnm*, orthorhombic (*R*) *Pbnm*, orthorhombic (*P*) *Pbcm* phases, and a rhombohedral *R3c* phase. Previous studies based on neutron diffraction in the temperature range 17 to 350 K [35] provided experimental evidence for the coexistence of the ferroelectric (FE) *R3c* phase and the antiferroelectric (AFE) phase (*Pbcm)* over a wide range of temperatures. This phase coexistence and the reported anomalous dielectric response are consistent with competing ferroelectric and antiferroelectric interactions.

The focus of our study is to correlate the specific phonon modes relevant to the observed structural distortions of antiferroelectric phase. We have calculated the phonon spectra of $NaNbO_3$ in antiferroelectric orthorhombic (*Pbcm*), ferroelectric rhombohedral (*R3c*) and cubic (*Pm-3m)* phases and identified the characteristic antiferroelectric Raman modes, which are responsible for stabilization of antiferroelectric phase. We have calculated the enthalpy as a function of pressure of various phases of $NaNbO_3$ and identified the mechanism of pressure driven phase transitions. We have also succeeded in assigning the Raman and infrared modes, which are essential for the understanding of the nature of structural phase transitions induced by the change of the temperature, pressure, and composition. We also report results of inelastic neutron scattering measurements of phonon spectra in different crystallographic phases of sodium niobate from 300 K to 1048 K. The results of inelastic neutron scattering experiment provide an opportunity to validate our calculations as well as important insights into the correlations between vibrational spectra and phase transitions.

The temperature dependent inelastic neutron scattering experiment on $NaNbO_3$ from 300 K to 1048 K was carried out using the IN4C spectrometer at the Institut Laue Langevin (ILL), Grenbole, France. The measurements were done in the neutron-energy-gain mode using the incident neutron energy of 14.2 meV (2.4 Å). Several inelastic runs were recorded on increase of temperature from 300 K to 1048 K. An energy cutoff of 1100 eV and 8×8×8 K-points mesh are found to be sufficient for an accuracy of 10^{-4} eV in total energy calculations. Table 6.1 compares the calculated and experimental structural parameters for both the phases. The calculated lattice parameters are found to be slightly overestimated as compared to the experimental ones, as expected from GGA calculations. Total energies and Hellmann-Feynman forces were calculated for *Pbcm, R3c and Pm-3m* phases using VASP. Phonon frequencies, Raman modes and dispersion relations were extracted from subsequent calculations using the direct method [37] as implemented in the PHONON software [38].

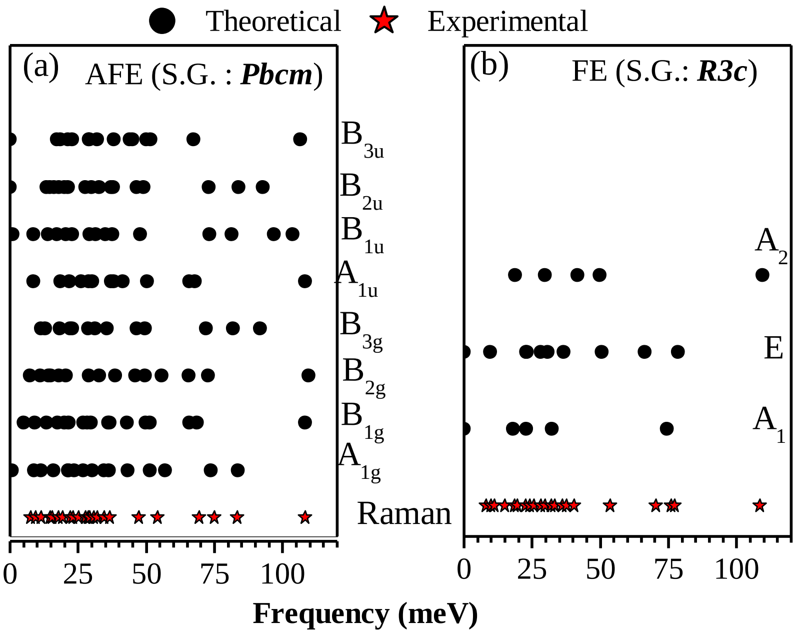

FIG 6.1 *Comparison of the calculated (filled circles) long-wavelength phonon frequencies with the available experimental data (stars)[17, 39, 40] for both the antiferroelectric (AFE) and the ferroelectric (FE) phases.*

At room temperature $NaNbO_3$ crystallizes in the orthorhombic phase (*Pbcm)* with 8 f.u. per unit cell (40 atoms). This leads to 120 phonon branches (3 acoustic modes + 117 optical modes). From the group theoretical analysis, the irreducible representations of the zone-centre optical phonons are $\Gamma_{optical} = 15A_g + 17B_{1g} + 15B_{2g} + 13B_{3g} + 13A_u + 14B_{1u} + 16B_{2u} + 14B_{3u}$, where the A_g, B_{1g}, B_{2g} and B_{3g} modes are Raman active, whereas the modes A_u are both Raman and infrared inactive. The modes B_{1u}, B_{2u} and B_{3u} are infrared active. Hence, 60 Raman active modes are expected in the orthorhombic phase (*Pbcm).* At low-temperature $NaNbO_3$ is rhombohedral *(R3c)* with 2 f.u. per unit cell (10 atoms), resulting in 30 phonon

TABLE 6.1 *Experimental [35] and ab-initio calculated structural parameters of* $NaNbO_3$ *in the orthorhombic, antiferroelectric phase (Pbcm) and in the rhombohedral, ferroelectric* *phase (R3c). The structural information of ferroelectric (R3c) phase compared with the result obtained by reference [5] (second row) with the Wu and Cohen version of GGA.*

Orthorhombic Antiferroelectric phase (*Pbcm*)						
	Experimental positional coordinates			Calculated positional coordinates		
Atoms	x	y	z	x	y	z
Na1	0.247	0.75	0.00	0.260	0.7500	0.000
Na2	0.227	0.789	0.25	0.259	0.796	0.250
Nb	0.242	0.282	0.131	0.243	0.279	0.125
O1	0.329	0.25	0.00	0.310	0.250	0.00
O2	0.208	0.278	0.25	0.191	0.227	0.25
O3	0.530	0.040	0.138	0.542	0.033	0.140
O4	0.975	0.489	0.107	0.960	0.456	0.110
	Lattice Parameters (Å) A_{orth}= 5.5012 (Å); B_{orth} = 5.5649 (Å), C_{orth}= 15.3972 (Å)			Lattice Parameters (Å) A_{orth}= 5.568 (Å); B_{orth}= 5.645 (Å), C_{orth}= 15.603 (Å)		

Ferroelectric Rhombohedral phase (*R3c*)						
	Experimental positional coordinates			Calculated positional coordinates		
Atoms	x	y	z	x	y	z
Na	0.272	0.272	0.272	0.273 0.272[a]	0.273 0.272[a]	0.273 0.272[a]
Nb	0.016	0.016	0.016	0.014 0.016[a]	0.014 0.016[a]	0.014 0.016[a]
O	0.320	0.183	0.747	0.312 0.318[a]	0.184 0.191[a]	0.749 0.749[a]
	Lattice Parameters (Å) a_{rhom}= 5.552 (Å), α=59.16 (deg)			Lattice Parameters (Å) a_{rhom}=5.637 (Å), α=58.94 (deg) a_{rhom}=5.570 (Å), α=59.15 (deg)[a]		

[a] Reference [5].

branches (3 acoustic modes + 27 optical modes). The irreducible representations of the zone-centre optical modes are: $\Gamma_{\text{optical}} = 5A_1 + 4A_2 + 9E$. The A_1 and the doubly degenerate E

modes are both Raman and infrared active, whereas the A_2 mode is both Raman and infrared inactive. Therefore, 23 Raman active phonons are expected in the rhombohedral phase ***(R3c)***.

A proper understanding of the functionality and phase transition behaviour of the materials requires that the structural information as obtained from diffraction techniques should be adequately complemented by spectroscopic investigations like Raman and infrared spectroscopies. The mode assignments from Raman and infrared spectroscopies are essential to understand the nature of phase transition as a function of temperature, pressure, and composition. The assignment of phonon modes also helps to identify the atomic motions which drive the observed phase transition(s). The computed zone centre phonon frequencies for both the antiferroelectric and ferroelectric phases are shown in Figure 6.1. As expected, the ferroelectric phase has less Raman modes than those found in the antiferroelectric phase.

6.2.1 Results and Discussion

6.2.1.1 Phonon Dynamics and Inelastic Neutron Scattering of $NaNbO_3$

Figure 6.2 depicts the evolution of inelastic neutron scattering (INS) spectra for $NaNbO_3$ at T= 303, 783, 838, 898, and 1048 K. The spectra correspond to different crystallographic phases. Five features (broad peaks centered on 19, 37, 51, 70 and 105 meV) can be easily identified. At 303 K, additional well resolved peaks below 37 meV are also observed. Their intensity decreases significantly with increasing temperature. Remarkably, the peak around 70 meV, shifts significantly towards lower energies with increasing temperature, while the others do not change in a noticeable way. At 783 K, a prominent change is observed and the spectra become more diffusive than that at 303 K. The variation of the INS spectra is associated with the occurrence of phase transitions. Prominent changes in the phonon spectra are usually expected across strong first order phase transitions, while weak first or second order phase transitions lead to minimal changes. Upon heating, sodium niobate undergoes a strong first order phase transition at 680 K. On the other hand, all the other phase transitions above 783 K are of a weak first or second order in nature. Thus, a prominent change is only observed in the phonon spectra at 783 K, as compared to that at 303 K. Further heating above 783 K leads to phonon spectra resembling each other.

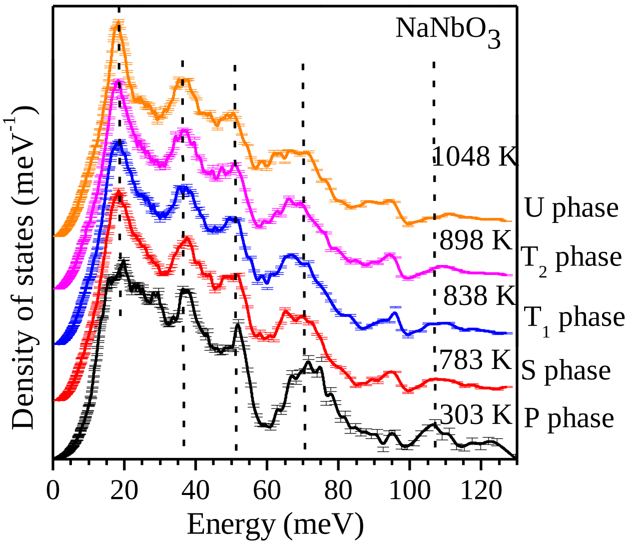

Fig 6.2. *The temperature dependence of the phonon spectra of NaNbO$_3$ as observed by neutron inelastic scattering.*

Figure 6.3 compares the experimental and calculated neutron-weighted phonon density of states of NaNbO$_3$, in the antiferroelectric phase. The calculations are found to be in fair agreement with the measurements. All the observed features are computationally well reproduced. Our ab-initio lattice dynamics calculations show that both the ferroelectric (***R3c***) and the antiferroelectric (***Pbcm***) phases are dynamically stable (all frequencies are real). All the calculations were performed at zero-temperature. The calculated free energies of ferroelectric (-7.8102 eV/atom) and antiferroelectric (-7.8082 eV/atom) phases are comparable. The small energy (~ 2 meV/atom) difference between the two phases could explain the coexistence of both the phases observed in neutron powder diffraction experiments [35]. R. Machado et al, [5] have also computationally investigated the relative phase stability of sodium niobate and reported the similar behavior.

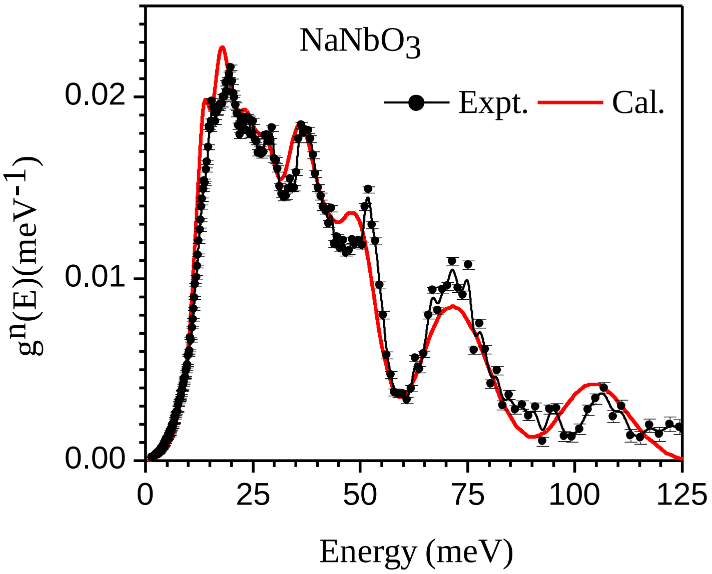

FIG 6.3 *The experimental (dotted line at 303 K) and calculated (solid line at 0 K) phonon spectra for NaNbO$_3$ in the antiferroelectric phase (**Pbcm**). The calculated spectra have been convoluted with a Gaussian of FWHM of 15% of the energy transfer in order to describe the effect of energy resolution in the experiment.*

Recently, Lu Jiang *et al* [41] have performed refinements of neutron diffraction data to determine the local structure by the pair distribution function (PDF) method. They reported that the ground states of NaNbO$_3$ in the low-temperature antiferroelectric and ferroelectric phases have the R3c symmetry, even though in the long range the system shows the *Pbcm* symmetry or the coexistence of two phases. They argued that this structure tends to form nano-twins with irregular spacing, resulting in the appearance of a long-range antiferroelectric *(Pbcm*) phase. As mentioned earlier, the ferroelectric phase (*R3c*) phase has slightly lower energy in comparison to antiferroelectric phase *(Pbcm*). This suggests that ferroelectric phase is most likely and consistent with the results of Lu Jiang et al. [41]. However, it is difficult to confirm the formation of nano twins with irregular spacing using theoretical calculation. Due to its structural complexity, we have not modeled the twin structure.

The ab-inito derived atomistic partial densities of states are shown in Figure 6.4. The oxygen atoms contribute dynamically in the whole spectral range, upto 120 meV, while Nb atoms mainly contribute upto 75 meV. The vibrations due to Na atom extend upto 40 meV. Computed partial density of state of Na reveals the presence of three peaks in antiferroelectric phase and two peaks for ferroelectric phase. It can also be seen that spread in the partial density of state associated with Na is more in antiferroelectric phase as compared to ferroelectric phase. It can be interpreted in terms of Na-O bond lengths. For the antiferroelectric phase, there are two types of sodium and four types of oxygen atoms, which result in significant variation in bond length (change in the force constant), and in turn result in more spread in the partial density of state. While in the ferroelectric phase, we have only one type of Na and O atom. In the ferroelectric phase Na atoms are shifted from centre of the oxygen cage and results in two different Na-O bond lengths. Similar interpretation also holds for partial density of states of niobium and oxygen atoms. It should be noticed that shorter bond lengths in ferroelectric phase (w.r.t antiferroelectric phase) results in the extending of the energy range of the total density of states. It is interesting to note that band gap in the phonon density of states for ferroelectric phase is larger as compared to that in antiferroelectric phase.

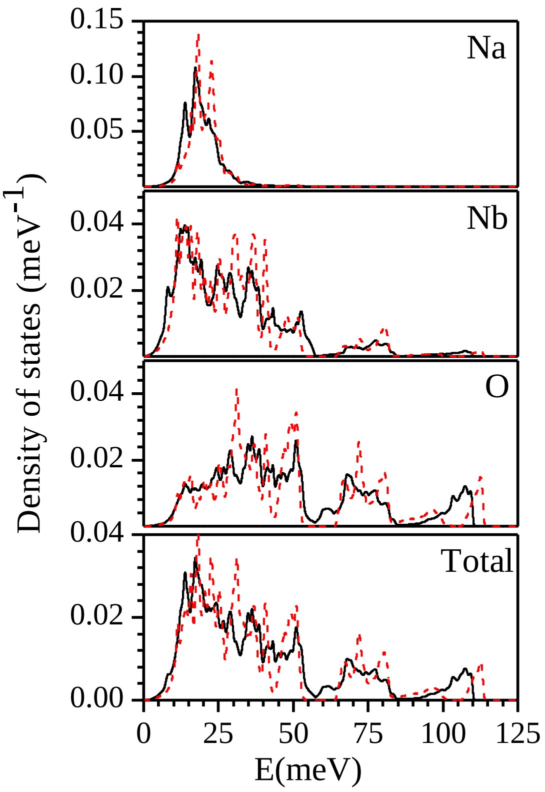

FIG 6.4 *The calculated partial density of states for various atoms and the total phonon density of states for NaNbO$_3$, in both the antiferroelectric orthorhombic (Pbcm) phase (solid line) and the ferroelectric rhombohedral (R3c) phase (dashed line).*

The structural phase transitions in Perovskite-type materials (ABO$_3$) originate from the competing interactions between different phonon instabilities occurring in the cubic phase. These transitions belong generally to two classes: ferrodistortive (FD) and antiferrodistortive (AFD)[6, 7, 13, 42]. The FD and AFD phase transitions are driven by zone centre ($q=0$) and zone- boundary phonons ($q\neq 0$), respectively. Known examples of these transitions are the cubic to tetragonal phase transition in BaTiO$_3$ and PbTiO$_3$, for the ferrodistortive case, and in SrTiO$_3$ and CaTiO$_3$ for the antiferrodistortive case [13, 42]. The evolution of these phase transitions depends on the condensation sequence of the soft modes M$_3$ and R$_{25}$. The zone boundary R$_{25}$ mode is three fold degenerate and the M$_3$ mode is nondegenerate. The triply degenerate R_{25} soft mode is made up of three components corresponding to the rotational degrees of freedom of the BO_6 octahedra around the three separate [001] axes. If one of the components condenses at the transition point, the resulting structure would be tetragonal *I4/mcm*, and the coupled condensation of the three components would lead to a rhombohedral *R3c* structure. However, when with successive phase transitions associated with both the M_3 and R_{25} soft modes, the sequence of the phase evolution depends in a complex way on the condensation sequence of the soft mode [13, 42].

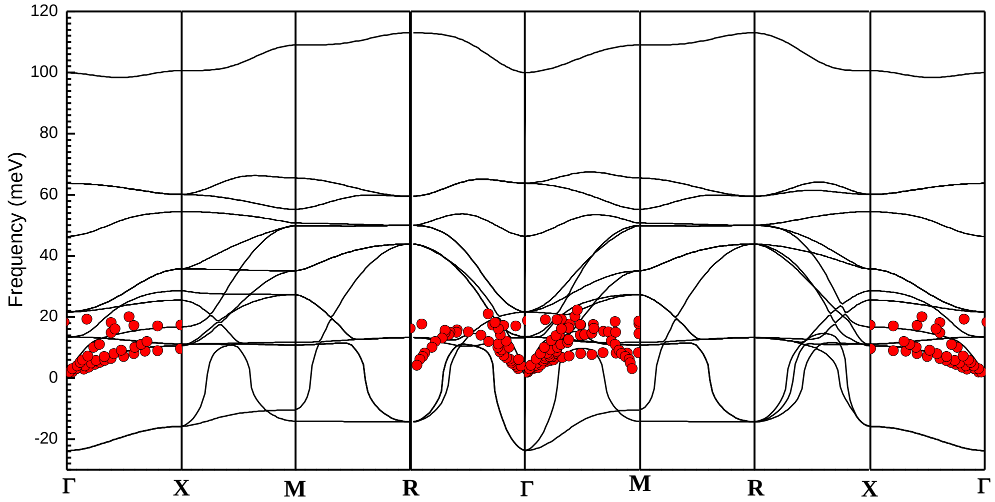

FIG 6.6 *Computed phonon dispersion relations for cubic phase* ***(Pm-3m)*** *of* $NaNbO_3$ *compared to reported experimental inelastic neutron scattering (INS) single crystal data (red circles) (Ref. [43]).*

Recently, Izumi and coworkers performed a detailed inelastic neutron scattering study in the cubic phase of $NaNbO_3$ [43]. Their measurements show gradual softening of the transverse acoustic (TA) phonon modes at the zone boundary points M (½ ½ 0) and R (½ ½ ½). This indicates instabilities of the in-phase and out-of-phase rotations of the oxygen octahedra around the [001] direction. The softening of these modes suggests low-lying flat transverse acoustic dispersion relations along the zone-boundary line M-R (T-line). As the temperature is decreased, these modes soften and become stable below the phase transition temperature. In order to detect these phonon instabilities using first principle technique, we have calculated the phonon dispersions from the zone centre (Γ) to the zone boundary points R and M (Figure 6.6).

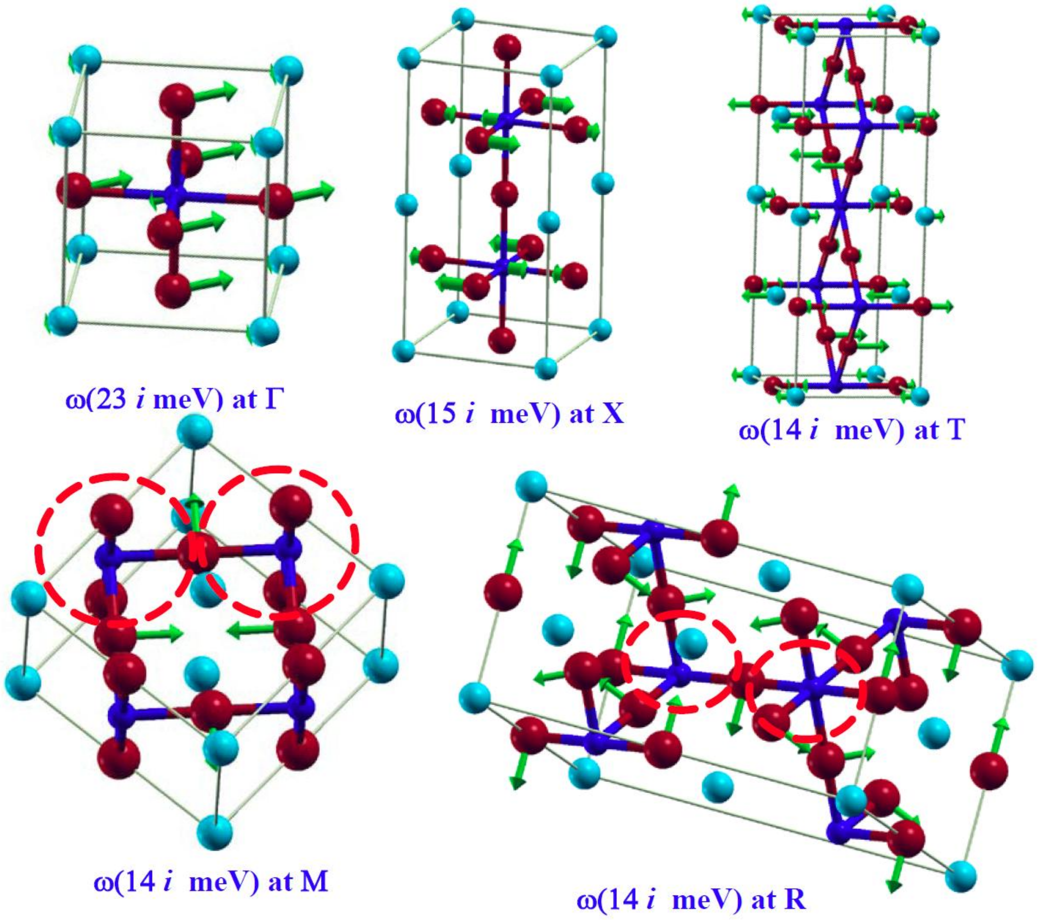
ω(23 *i* meV) at Γ

ω(15 *i* meV) at X

ω(14 *i* meV) at T

ω(14 *i* meV) at M

ω(14 *i* meV) at R

FIG 6.7 *Ab initio derived eigenvectors of selected zone-centre and zone-boundary unstable phonon modes at the Γ*, *M, R, T and X points for the cubic phase of NaNbO*$_3$*. The lengths of arrows are related to the displacements of the atoms. Key: Na, cyan; Nb, blue; O, brown.*

In general, we find a very good agreement between our calculations and R Machado *et al* [5], together with the experimental data from the literature [43]. Small deviations are expected as calculations were obtained at 0 K whereas inelastic neutron scattering data were acquired at in cubic phase (970 K).

From Figure 6.6 one can see that, in contrast to $SrTiO_3$ [44], the polar instability strength at the Γ point is stronger than the antiferrodistortive instabilities at the R and M points, and it extends over a wider region of the Brillouin zone. Further, the strength of the M and the R point instabilities are quite similar. Interestingly, the branches along the Γ-R and Γ-M directions, show dramatic changes when reaching the R and M points. When moving away from M to R, two unstable modes are detected. One of them is rather flat and the other one shows rapid stiffening and becomes stable. Moreover, one of the stable modes become unstable at **T** (½ ½ ¼) point. Our results are consistent with other theoretical works in the literature [5].

Above 950 K, $NaNbO_3$ occurs in the cubic phase. On decreasing the temperature, it transforms to a tetragonal phase (*P4/mbm*). The first structural transformation is from cubic to tetragonal structure, where the unit cell is doubled in the plane perpendicular to the rotation axes of the M_3 mode. By further lowering the temperature, condensation of the R_{25} phonon leads to the orthorhombic *Cmcm* (T_2) phase. Unstable phonon-branches along the M-R line contribute to the occurring successive phase transitions. These phonons play an important role in stabilizing the different phases (P, S and R) in $NaNbO_3$. The orthorhombic structures of the S, R and P phases result from the condensation of the phonon mode (q= ½, ½, g); with g= 1/12, 1/6 and 1/4. These orthorhombic phases originate from the modulation of the high symmetry cubic phase, associated with the phonon modes at q= (½, ½, g). Further, the freezing of all the R_{25} modes and a zone-centre phonon stabilizes the low-temperature ferroelectric rhombohedral phase. The detailed descriptions of the polar mode (responsible for ferroelectricity) and the rotational modes (R_{25} and M_3) are found to be similar to those reported by R Machado *et al* [5].

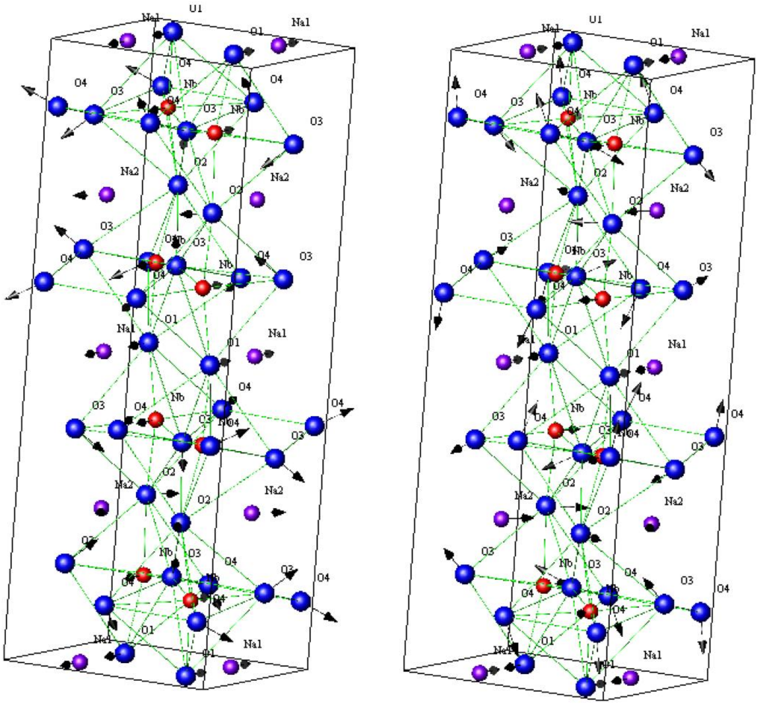

ω= 93 cm^{-1} ω= 129 cm^{-1}

FIG 6.8 *The eigenvectors of the two antiferroelectric modes, at (a) ω=93 cm^{-1} and (b) 129 cm^{-1} of NaNbO$_3$, induced by the folding of the T (q= ½ ½ ¼) and Δ (q= 0 0 ¼) points of the Brillouin zone under the cubic phase, respectively. (Key: Na: violet spheres; Nb: blue spheres; O: brown spheres).*

Deeper insights into phonon dynamics can be gained by performing an analysis of the eigenvectors corresponding to specific phonon modes, relevant to the present study. These are derived from our ab-initio calculations and are plotted in Figure 6.7. The eigenvector of the unstable Γ-point zone-centre phonon mode at ω =23*i* meV indicates clearly that niobium and oxygen atoms are moving in opposite directions. This leads to the formation of a dipole, and induces ferroelectricity. The eigenvectors corresponding to the unstable modes at M and R points (ω=14*i* meV) exhibit an in-phase and out phase rotation of the oxygen octahedra, leading to a doubling of the unit cell. The analysis of the eigenvector of the X-point zone boundary mode at $\omega=15i$ meV suggests that, similar to the zone centre mode, Nb and O atoms move in opposite directions within a layer of the basal plan, and this motion is anti-phased in an adjacent layer. This results in a zero total dipole moment in unit cell. The displacement patterns are therefore related to antiferroelectricity. The mode at the T-point having the phonon frequency $\omega=14i$ meV possesses an eigenvector displacement indicating a multiplication of the unit cell.

The antiferroelectric phase is found to accompany new super lattice reflections in powder neutron diffraction data [35, 36]. This is confirmed by the appearance of new Raman lines in Raman spectroscopy. These lines become active due to the folding of the corresponding specific zone-centre points, below the antiferroelectric phase transition temperature. Below the antiferroelectric phase transition, strong modifications of the Raman scattering patterns are observed [17, 39, 40, 45-47] accompanying the appearance of new Raman modes around 93 cm^{-1} and 123 cm^{-1}. Further, a sudden enhancement of the intensity of the bands within the two frequency ranges 150-300 cm^{-1} and 500-650 cm^{-1} are also noted. We have assigned the two lines at 93 cm^{-1} and 123 cm^{-1} as belonging to the A_{1g} irreducible representation, and we have identified them as originating from the folding of the T (93 cm^{-1}) and Δ (129 cm^{-1}) points of the Brillouin zone under the cubic phase. The eigenvectors corresponding to the two AFE modes of $NaNbO_3$, as extracted from our ab initio lattice dynamical calculations are shown in Figure 6.8. The mode at 93 cm^{-1} involves significant motions of Na, Nb and O, which are located at the sites 4d (¼+u, ¾+v, ¼), 8e (¼+u, ¼+v, ⅛+w) and (½ +*u*,0+*v*, ⅛+*w)*, respectively. However, the Raman mode at 129 cm^{-1} reflects a significant displacement of all the atoms.

6.2.1.2 High Pressure Behaviour

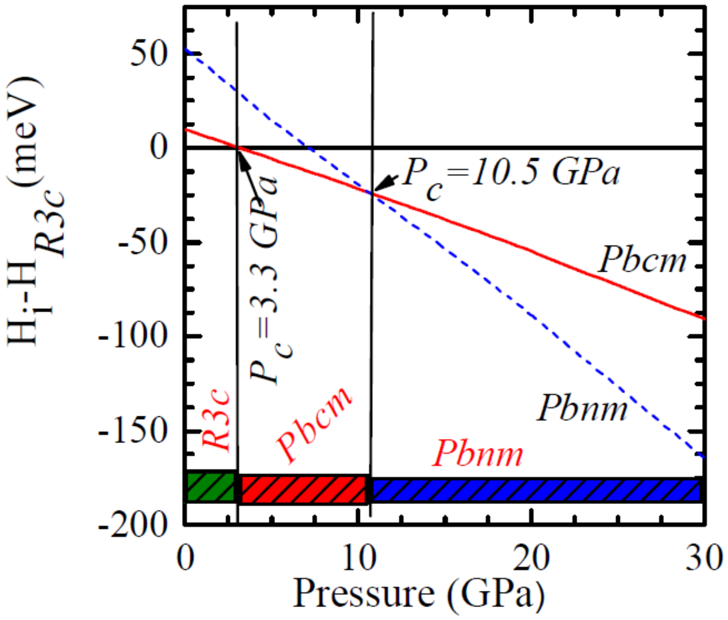

FIG 6.9 *Enthalpy difference (ΔH) between the indicated ferroelectric (R3c), antiferroelectric (Pbcm), and paraelectric (Pbnm) phases of $NaNbO_3$ as calculated using ab-inito DFT calculation.*

We have also studies the pressure driven phase transition in sodium niobate. Application of pressure modifies the structural parameters, such as the Nb–O bond length, Nb–O–Nb bond angles, and the distortion of the NbO_6 octahedra. Figure 6.9 depicts the computed pressure dependence of the difference in the enthalpy $\Delta H = H_i - H_{R3c}$ of various phases of sodium niobate. For the lower pressure (P_c=3.3 GPa), only ferroelectric (*R3c*) phase has the lowest enthalpy (ΔH), as it is the well-known ground state of $NaNbO_3$ at T=0 K. However at pressure above 3.3 GPa, the antiferroelectric phase (*Pbcm*) becomes favorable over the ferroelectric (*R3c*) phase. Further increasing the pressure above 10 GPa, the paraelectric phase (*Pbnm*) becomes favourable over the other two phases. Thus, the calculation predict (figure 6.5) that sodium niobate may undergo successive phase transitions from ferroelectric to antiferroelectric (at 3.3 GPa) to paraelectric (at 10.5 GPa) phases. The phase transition pressure is fairly close to experimental values (8 GPa) for antiferroelectric to paraelectric phase.

6.3 RMnO$_3$ (R= Ca and Pr)

$CaMnO_3$ crystallizes in the distorted orthorhombic structure (space group Pnma) and consists of single-valent Mn^{4+} ions and does not exhibit Jahn-Teller distortion. At ambient conditions, it is paramagnetic and at ~130 K it undergoes a G type antiferromagnetic (AFM) transition [48]. In high temperature x-ray diffraction study, H Taguchi *et al* [49, 50] showed that oxygen deficient $CaMnO_3$ undergoes orthorhombic to tetragonal phase at 1169 K and finally transforms in cubic phase at 1186 K. Doping of trivalent and tetravalent ions at Ca^{2+} site provides additional electrons into e_g orbital of Mn ions and causes a variety of phase transitions, e.g from collinear G-type AFM insulator to canted G-type AFM metal, collinear C-type AFM insulator etc. This suggests that we can tune the magnetic phase transition with a small amount of electron doping. For example, solid solution of (1-x)$CaMnO_3$- x$PrMnO_3$ ($Ca_{1-x}Pr_xMnO_3$) exhibits a variety of ground state, namely: G- AFM insulator, CE- type charge ordered state, CE-type AFM spins ordering, canted AFM state which consists a mixture of AFM and ferromagnetic (FM) clusters, depending on temperature and composition [49-55]. The other end member of solid solution, $PrMnO_3$ also crystallizes in the orthorhombic phase but it exhibits [32] a strong Jahn-Teller distortion of MnO_6 octahedral associated with the ordering of e_g orbital and undergoes A-type antiferromagnetic spin ordering below 95 K [32]. The difference in magnetic structure of $CaMnO_3$ and $PrMnO_3$ is attributed to different occupancy of d electron in Mn ions. Hence it is intriguing to study the role of magnetic interaction on lattice vibration.

The structural, physical and magnetic properties of $RMnO_3$ (R= Ca and Pr) were investigated by variety of experimental techniques [27, 56-62]. The physical properties of these materials are governed by a delicate interplay of charge, spin, orbital, and lattice degrees of freedom. To understand the relation among these interactions, first principles calculations have been performed in cubic and orthorhombic phases. Using a density functional theory approach within the local spin density approximation, S. Bhattacharjee *et al*, [63] have computed structural, dielectric and dynamical properties of orthorhombic phase of $CaMnO_3$. They have computed whole set of zone-center phonon modes and assignment of experimental data has been proposed. F.P. Zhang *et al* [60] had investigated geometry, ground state electronic structure and charge distributions of $CaMnO_3$. Effect of compressive and tensile strains on a magnetic phase transition in electron-doped $CaMnO_3$ was theoretically studied by H. Tsukahara *et al* [61]. Further the first principles calculations of structural, electronic and magnetic properties of the $PrMnO_3$ as well as the calculation of zone centre phonon modes in the cubic phase were reported by B. Bouadjemi [62].

Understanding of various functional properties of derived compounds $Pr_xCa_{1-x}MnO_3$ needs complete study of electronic and dynamical properties of the parent compound $CaMnO_3$ and $PrMnO_3$. In spite of various experimental and theoretical investigations, the temperature dependence of phonon spectra for $CaMnO_3$ and $PrMnO_3$ is still missing. In the present study, we report results of inelastic neutron scattering measurements of phonon spectra at different temperatures of $CaMnO_3$ and $PrMnO_3$. The interpretation and analysis of the observed phonon spectra have been performed using ab-initio phonon calculations. Previous first-principles calculations on $CaMnO_3$ were focused mainly on the electronic structure[60-63]. Here, we report a first-principles study of phonon dynamical properties of the ground-state orthorhombic phase in the entire Brillouin zone. We also investigated the effect of pressure on the structural distortions in orthorhombic phase of $CaMnO_3$ and

$PrMnO_3$. The calculated structure as a function of pressure in $PrMnO_3$ shows that suppression of Jahn-Teller distortion and insulator to metal transition occurs simultaneously. We provide the evidence that although tetragonal phase as reported in the literature is energetically favored over orthorhombic phase above 20 GPa, but it is found to be dynamically unstable.

Inelastic neutron scattering measurements were performed by Dr. Alexander I. Kolesnikov using the Fine Resolution Chopper Spectrometer (SEQUOIA) [64, 65] at the Spallation Neutron Source (SNS) at Oak Ridge National Laboratory. The data were collected using fixed incident neutron energy of 110 meV, which allowed for the measurement of excitations up to energy transfers of ~100 meV. The low temperatures scans (4-300 K) were carried out using the closed cycle helium refrigerator. For high temperature measurements up to 1250 K samples were heated in air. We have used furnace (called MiCAS) with a quartz tube insert that allows controlling the atmosphere of sample.

The calculation of phonon spectra in the *Pnma* space group has been performed using the first-principles density functional theory and both the local density approximation (LDA) or generalized gradient approximation (GGA) for $CaMnO_3$. However, for $PrMnO_3$, GGA has been used. The total energy calculations have been done using an energy cutoff of 1100 eV. A grid of 8×8×8 K-points was used according to the Monkhorst-Pack (MP) scheme [66]. We have used the G-type and A-type antiferromagnetic structures in orthorhombic phases for $CaMnO_3$ and $PrMnO_3$ respectively. The choice of magnetic structures is based on the previously reported configurations obtained from neutron diffraction measurements [32, 48, 67]. However in the tetragonal phase of $PrMnO_3$ the magnetic structure has not been known. So we have calculated the enthalpy of the tetragonal phase of $PrMnO_3$ including different antiferromagnetic configurations, namely A, C, G type, and ferromagnetic configurations. The calculations show that ferromagnetic structure is favored in comparison to the other structures. In the cubic phase G-type antiferromagnetic and ferromagnetic structures are adapted for $CaMnO_3$ and $PrMnO_3$ respectively. The supercell approach or direct method is used to calculate the phonon frequencies in entire Brillouin zone implemented in PHONON5.12 software [38].

The phonon calculations are performed in various magnetic and nonmagnetic configurations to see the effect of spin degrees of freedom on phonons. In the fully relaxed calculations the atomic coordinates and lattice parameter have been relaxed. However partially relaxed nonmagnetic calculation (PNM) refers to fix lattice parameter as used in magnetic calculations with relaxing the atomic coordinates. Hereafter, the labeling "FM" and "FNM" refer to fully relaxed magnetic and fully relaxed nonmagnetic calculation.

6.3.1 Results and Discussion

6.3.1.1 Temperature Dependence of Neutron Inelastic Spectra in Orthorhombic Phase of $CaMnO_3$

$CaMnO_3$ is known to undergo paramagnetic to antiferromagnetic (AFM) transition at ~ 130 K [48, 67]. Other transitions are observed from orthorhombic to tetragonal phase at 1169 K and then to cubic phase at 1186 K. The phonon spectra of $CaMnO_3$ (Figs. 6.10-12) were measured from 7 up to 1250 K, across the magnetic transition (~130 K) and the structural phase transitions at high temperatures**.** The neutron inelastic spectra were collected over wide range of momentum transfer (Q) from 0.5-7 $Å^{-1}$. The magnetic signal is expected to be more pronounced at low Q, and it decreases as Q increases, following the magnetic form factor. Hence we have integrated the inelastic scattering function S(Q,E) in two ranges, namely total Q range (0.5-7 Å^{-1}) and high Q (4-7 Å^{-1}), the later one represents mostly the contribution from the neutron scattering on phonons. The data collected at 7 K show intense peak at about 20 meV in the low Q data (Figs. 6.10, 6.11). The observed peak around 20 meV is largely contributed from magnetic excitations and shows strong Q dependence intensity (stronger at low-Q and weaker at high-Q). However as the temperature increases the contribution from spin excitation becomes weaker. Above the magnetic transition temperature (T_N=130 K) we also see that the intensity of peak at 20 meV is decreasing with increase in temperature up to 601 K (Fig. 6.12).

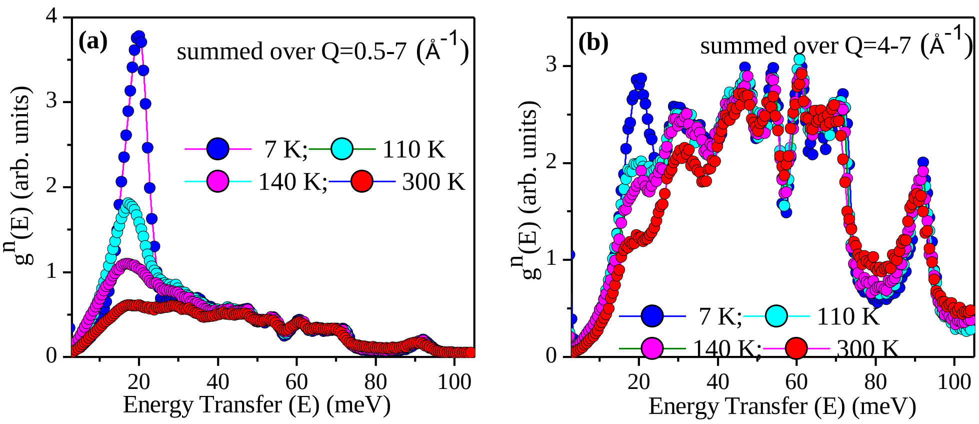

FIG 6.10. *The neutron inelastic spectra of CaMnO$_3$ at low temperatures, the data were summed over (a) Q=0.5-7 Å^{-1} and (b) Q=4-7 Å^{-1} respectively. The peak at ~20 meV is due to spin-wave excitations, not due to phonons (1 meV=8.0585 cm^{-1}).*

At temperatures 951 K and above the intensity does not change with increase in temperature. This indicates that the contributions from the paramagnetic scattering persist up to very high temperatures of 601 K. Fig. 6.11 illustrates the experimental S(Q,E) measured for CaMnO$_3$ in the low temperature range from 7 to 300 K. The data collected at 7 K clearly show the signature of spin-wave excitations which are probably gaped at Q=1.45 Å^{-1}, corresponding to Bragg peak (011) (the gap is not resolved with the current experimental setup, providing energy resolution ~2 meV at the elastic line).

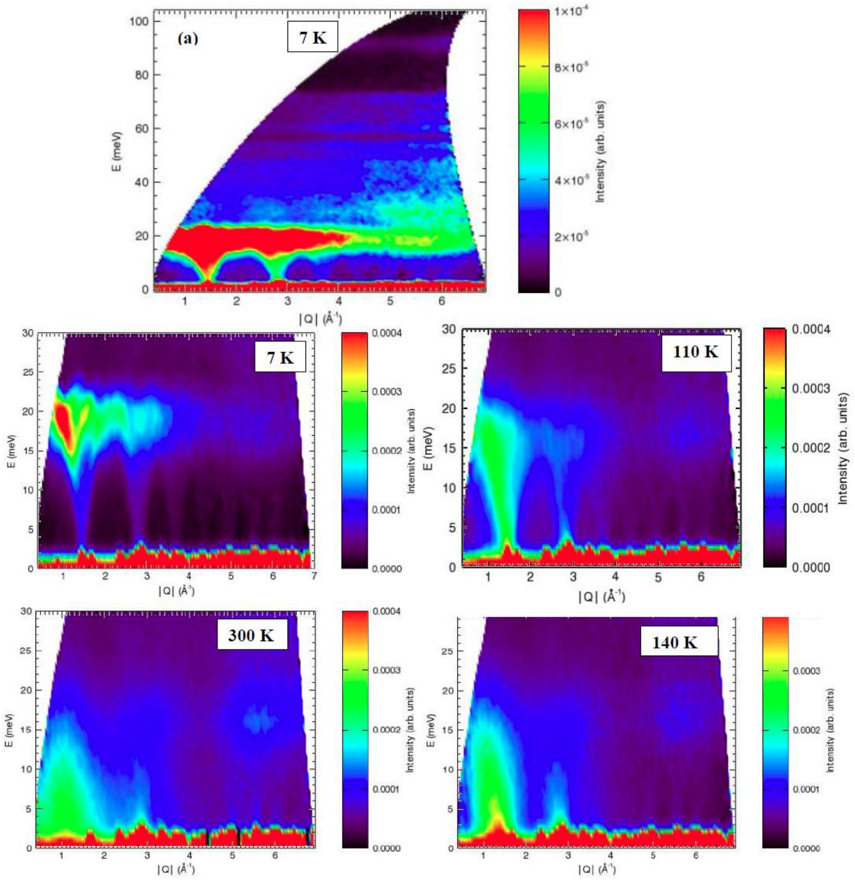

FIG 6.11. *The (Q,E) contour plot of S(Q,E) data for $CaMnO_3$ at T=7 K measured at SEQUOIA with incident neutron energy of 110 meV is shown at top. Strong intensity excitations at low temperatures (7 K and 110 K) below E=20 meV and Q=3.5 $Å^{-1}$ are due to magnetic spin-wave excitations. The excitations around 30, 45, 55, 60, 65, 70, and 90 meV are due to phonons (their intensities increase with increasing Q).*

Further we noticed that at higher temperature (T=110 K) the intensity of these excitations are strongly redistributed to lower energies, the peak position shifts from 19.5 meV at 7 K to 16.5 meV at 110 K. At $T>T_N$ (in paramagnetic state) at small Q values (Q<3.5 $Å^{-1}$) we observe spin-fluctuation excitations extended from elastic line up to ~20 meV. It is evident from figure 6.11 that the nature of neutron scattering intensity S(Q, E) changes above T_N from inelastic (due to well defined spin excitation) to quasielastic (due to stochastic spin-fluctuations) and the intensity also spreads over a broader range of Q. The intensity of these spin fluctuations corrected for the thermal population Bose factor leads to a peak in g(E), which is plotted in Figs. 6.10 & 6.12, that decreases with temperature increase.

The high temperature neutron inelastic spectra (Fig. 6.12) show strong modification with increasing temperature. In particular, the intensity of peaks below 40 meV decreases with increasing temperature up to 601 K while the peak around 90 meV shows significant shift towards lower energies with increasing temperature. The others peaks do not change in a noticeable way. We find that above 1101 K, a prominent change is observed in the neutron inelastic spectra, where they are found to be more diffusive as compared to the spectra at low temperatures. These changes in the phonon spectra may be associated with phase transitions in $CaMnO_3$ which transforms from orthorhombic to tetragonal phase at 1169 K, and finally to cubic phase at 1186 K [49].

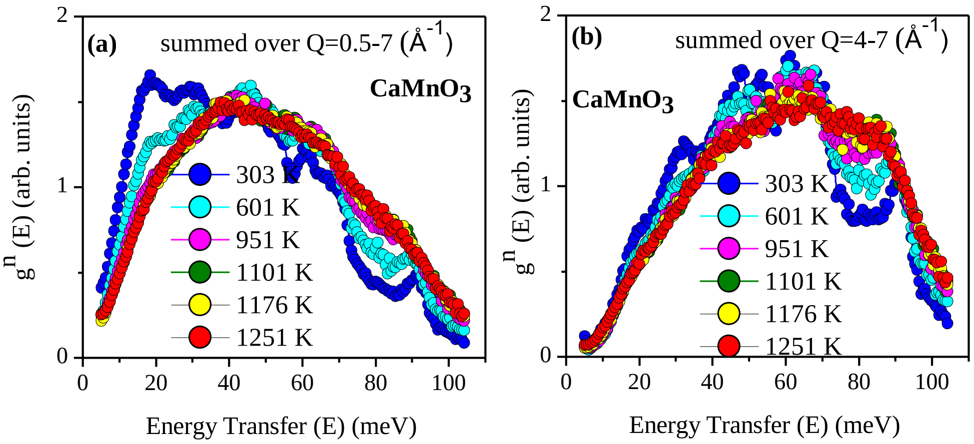

FIG 6.12. *The temperature dependence (above 300 K) of the neutron inelastic spectra of $CaMnO_3$, the data were summed over (a) Q=0.5-7 A^{-1} and (b) Q=4-7 A^{-1} respectively.*

6.3.1.2 Magnetic Ordering and Calculated Phonon Spectra in the Orthorhombic Phase of $CaMnO_3$

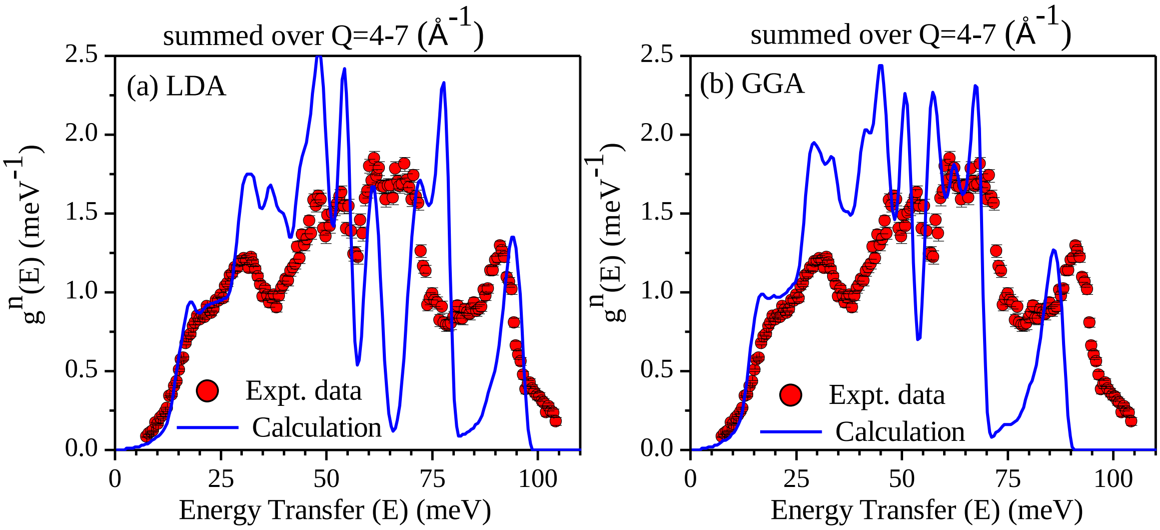

FIG 6.13. *Comparison between the experimental (T=300 K) and calculated neutron inelastic spectra of* $CaMnO_3$ *using (a) local density approximation and (b) generalized gradient approximation. Experimental data are summed over 4-7 Å*$^{-1}$*. The phonon calculations are carried out in the fully relaxed magnetic (FM) configuration. The calculated phonon spectra have been convoluted with a Gaussian of FWHM of 4.5 meV to account for the effect of energy resolution in the experiment.*

In order to analyze the experimental data, as stated above, first principle calculations have been performed. The fully optimized structure of $CaMnO_3$ in both the “FM” and “FNM” configurations using both the local density approximation (LDA) or the generalized gradient approximation (GGA) exchange correlation functional are summarized in Table 6.2. The calculated atomic positions are in good agreement with the experimental data. It can be seen that in both the LDA and GGA, the “FM” calculated structures are found to close to the experimental data [68]. The LDA calculated lattice constants are found to be underestimated by 2% in comparison to the experimental data, while GGA gives slight overestimation of about 1%. As will be shown latter in the paper, nonmagnetic structures are found to be dynamically unstable at T=0 K. The comparison between the experimental data and the calculated phonon spectra from both the LDA and GGA are shown in Fig. 6.13. It can be seen that all the observed features in the experimental data are fairly well reproduced by the calculations. It is evident from this figure that below 55 meV, phonon calculation in fully relaxed magnetic configuration using LDA gives better agreement with the experimental data in comparison to GGA. However, for the spectral range above 55 meV, the calculated phonon spectrum using GGA describes the experiment better than LDA. The high energy (> 75 meV) phonons are due to Mn-O stretching modes. The observed discrepancy could be understood in terms of bond lengths. As shown in TABLE 6.2, the LDA calculation underestimates the lattice parameters. The shorter bond lengths would shift the phonon spectra to higher energies in comparison to the experimental data. Similarly the slight overestimation of lattice parameter by GGA results in underestimation of the energies of the Mn-O modes in the calculation.

The atomistic contributions in the phonon spectra from the various calculations can be understood in terms of the partial density of states. The difference is primarily due to the nature of the chemical bonding in the magnetic and nonmagnetic configurations, as well as the related volume effect. The computed atomistic partial phonon density of states show (Fig. 6.14 (a)) that the contribution of the oxygen atoms spreads over the whole energy range, while the Mn atoms contribute mainly up to 75 meV. The contribution due to Ca atoms extends up to 50 meV. Above 75 meV, the dynamics is mainly due to the Mn-O stretching modes.

TABLE 6.2. *Comparison of experimental and theoretical structural parameters in the antiferromagnetic orthorhombic phase (space group: Pnma) of $CaMnO_3$. The Wyckoff sites of the atoms are given in the brackets. "FM", "FNM" and "PNM" refer to fully relaxed magnetic, fully relaxed non-magnetic and partially relaxed non magnetic calculations, respectively.*

Structural Parameters	Expt. [69]	Ref. [63]	This work					
			GGA			LDA		
			FM	PNM	FNM	FM	PNM	FNM
A_o (Å)	5.279	5.287	5.3380	5.3380	5.3148	5.2011	5.2011	5.189
B_o (Å)	7.448	7.498	7.4977	7.4977	7.4238	7.2933	7.2933	7.2386
C_o (Å)	5.264	5.235	5.2949	5.2949	5.2645	5.1396	5.1396	5.1084
Ca (4c)								
x	0.035	0.040	0.040	0.038	0.038	0.045	0.044	0.045
y	0.250	0.250	0.250	0.250	0.250	0.250	0.250	0.250
z	-0.009	-0.008	-0.008	-0.007	-0.007	-0.009	-0.008	-0.009
Mn (4b)								
x	0.00	0.00	0.00	0.00	0.00	0.00	0.00	0.00
y	0.00	0.00	0.00	0.00	0.00	0.00	0.00	0.00
z	0.500	0.500	0.500	0.500	0.500	0.500	0.500	0.500
O1 (4c)								
x	0.493	0.485	0.489	0.483	0.483	0.488	0.491	0.491
y	0.250	0.250	0.250	0.250	0.250	0.250	0.250	0.250
z	0.068	0.071	0.068	0.062	0.062	0.073	0.070	0.070
O2 (8d)								
x	0.290	0.287	0.288	0.287	0.287	0.290	0.290	0.29
y	0.030	0.036	0.035	0.032	0.033	0.031	0.036	0.037
z	-0.289	-0.288	-0.289	-0.288	-0.288	-0.289	-0.289	-0.289

It can be seen (Fig. 6.14 (a)) that the contributions of Ca and Mn are nearly the same in the calculations performed using LDA and GGA, while there are significant differences in the partial contributions from the O atoms. The difference in the calculated partial contribution is mainly in the stretching modes region which is very sensitive to the unit cell volume. The underestimation or overestimation of energy of modes is related to the calculated structures as given in TABLE 6.2. Results of the FM-GGA calculations are found to be close to the experimental data. Consequently in the following we adopt the GGA density functional.

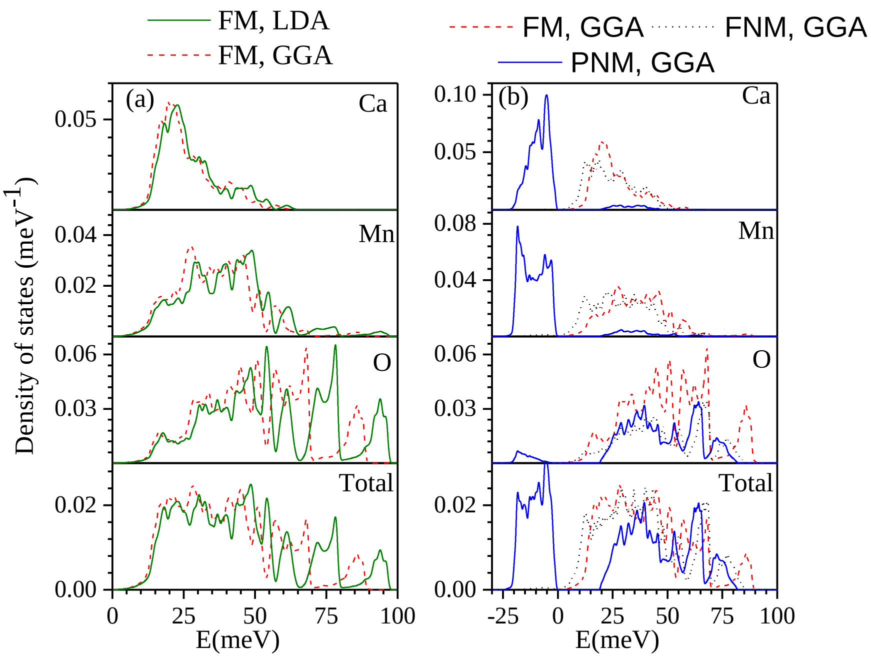

FIG 6.14. *(a) The calculated partial phonon density of states of various atoms in $CaMnO_3$ with in LDA and GGA approximations. (b) The calculated partial density of states of $CaMnO_3$ in various configurations with in* GGA. *"FM", "FNM" and "PNM" refer to fully relaxed magnetic, fully relaxed non-magnetic and partially relaxed non magnetic calculations, respectively. The energies of unstable modes in PNM-GGA are plotted as negative energies.*

To study the effect of magnetic interactions on the phonon spectra, the phonon spectra were calculated in three different configurations as said above (“FM”, “FNM”, and “PNM”) and shown in Figure 6.14 (b). It is evident from this figure that the phonon spectra calculated using PNM results in several unstable modes up to 25*i* meV. Similarly FNM calculations also results in unstable modes with slightly lower energy range (10*i* meV). The comparison of the FM and PNM calculations indicates that magnetic interactions are very important for obtaining the dynamically stable structure.

6.3.1.3 Temperature Dependent Neutron Inelastic Spectra and First Principle Studies in Orthorhombic Phase of $PrMnO_3$

The compound $PrMnO_3$ is isostructural to $CaMnO_3$; however, the magnetic structure is different. The Jahn-Teller transition in $PrMnO_3$ takes place at about 1050 K. It undergoes antiferromagnetic spin ordering below 95 K. Here we performed the measurements of neutron inelastic spectra of $PrMnO_3$ at two temperatures, 6 and 150 K. The experimental S(Q,E) data for $PrMnO_3$ (Fig. 6.15, at the bottom) collected at 6 K clearly shows the signature of spin-wave excitations at energies below 20 meV and Q<1.5 $Å^{-1}$, which significantly dissipate at 150 K. This behavior is similar to $CaMnO_3$, however the Q dependence is completely different. Fig. 6.15 (at the top) shows the phonon spectra, (a) summed over momentum transfer (Q)=1-7 $Å^{-1}$ and (b) Q=4-7 $Å^{-1}$. The data collected at 6 K show intense excitations with the peak maximum at about 17 meV. However above magnetic transition temperature the intensity at 17 meV peak is significantly suppressed but has contribution from phonons and paramagnetic fluctuations.

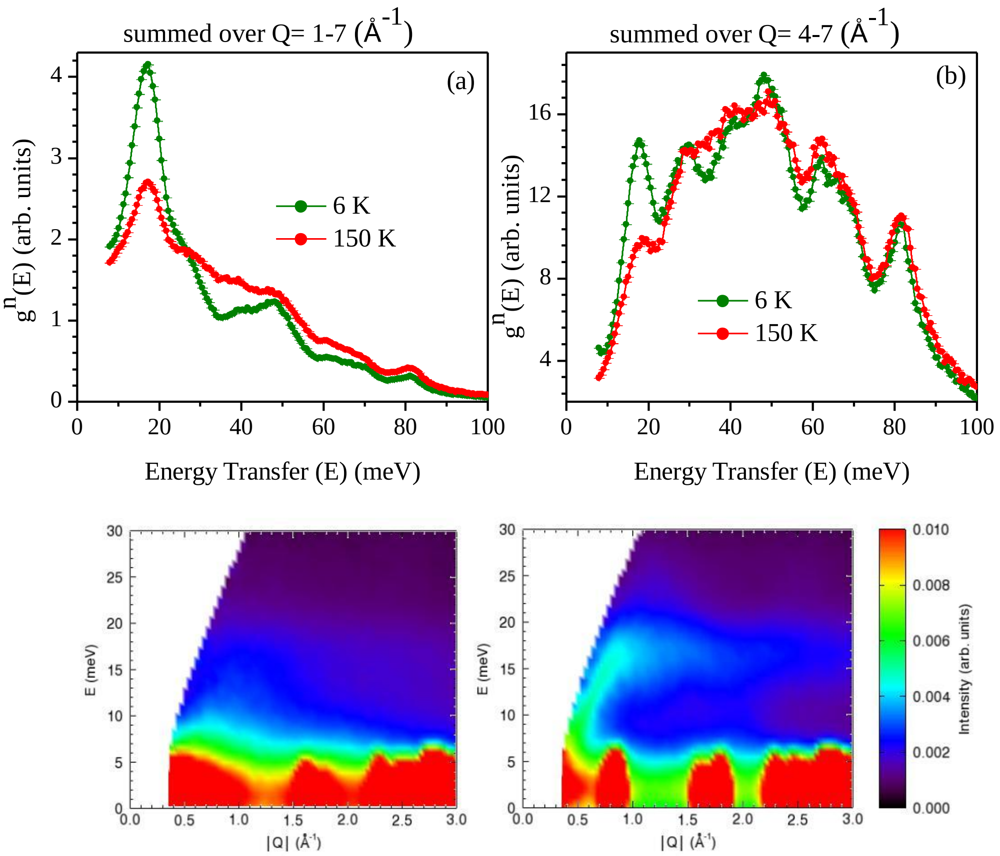

FIG 6.15. *Top panel: Temperature dependent neutron inelastic spectra of* $PrMnO_3$ *summed over various Q-range. Bottom panel: Contour plot of S(Q,E) spectra for* $PrMnO_3$ *measured at 6 K (right) and 150 K (left). A dispersed spin wave excitation is clearly seen below 20 meV and 1.5* A^{-1} *at 6 K. In 150 K spectra, weakly dispersed magnetic excitation around 15 meV is observed.*

It is remarkable to notice that in spite of similar structure, room temperature neutron inelastic spectrum (Fig. 6.13) of $CaMnO_3$ exhibits well-defined peaks in comparison to the data for $PrMnO_3$ (Fig. 6.16) at 150 K. The difference in the phonon spectra may be due to the difference in nature of interactions. The Jahn-Teller distortion is present in $PrMnO_3$, while such distortion is not there in $CaMnO_3$.

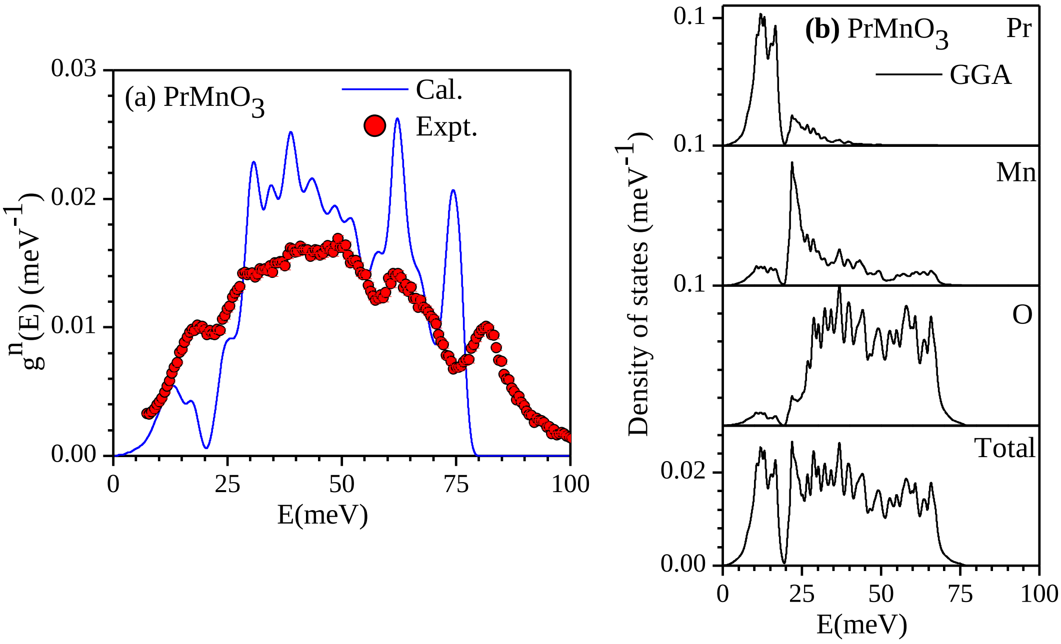

FIG 6.16. *(a) Comparison between the experimental (T= 150 K) and calculated phonon spectra in* $PrMnO_3$*. Experimental data are summed over 4-7 Å*$^{-1}$*. (b) The calculated partial phonon density of states of various atoms in* $PrMnO_3$*. The phonon calculations are carried out in the fully relaxed magnetic (FM) configuration in the generalized gradient approximation (GGA).*

The phonon calculations (Figs. 6.16 (a) and (b)) for $PrMnO_3$ are carried out only in the fully relaxed magnetic configuration using GGA exchange correlation functions. All the observed features are fairly well reproduced (Fig. 6.16(a)) by the computations. The computed atomistic partial density of states shows (Fig. 6.16(b)) that the contribution of the Mn and oxygen atoms spreads over the whole energy range up to 75 meV, while the contribution due to Pr atoms extends up to 50 meV. It should be noted that in the present case contributions due to the Mn-O stretching modes do not extend above 75 meV, while in $CaMnO_3$ the energy range of these modes is up to 90 meV. The comparison between the calculated and experimental phonon spectra shows that stretching modes are underestimated

(Fig. 6.16) in the phonon calculations. Further the calculations of zone centre phonon modes as shown in Fig. 6.12 also confirm the same.

6.3.1.4 High Pressure Phase Stability of $CaMnO_3$ and $PrMnO_3$

Pressure tunes the interplay between lattice and electronic degree of freedom to a much larger extent than any other parameter like temperature and magnetic field. In the present section, we discuss the effect of pressure on the structural distortions in the orthorhombic phase of $CaMnO_3$ and $PrMnO_3$. The main emphasis of this study are to investigate the pressure dependence of the Jahn-Teller distortion (if persist) and existence of insulator to metal transition at high pressure. Figure 6.17 shows the calculated pressure dependence of the equivalent pseudo-cubic lattice parameters for the orthorhombic phase of (a) $CaMnO_3$ and (b) $PrMnO_3$ using GGA and comparison with experimental data reported in the literature [28]. The computed bulk modulus for $CaMnO_3$ and $PrMnO_3$ are found to be 185.4 (Expt. 224 ± 25) GPa [28, 70-72] and 137.4 (Expt. 139±4) GPa [28], respectively. It is evident from the figure that compression is more anisotropic for $PrMnO_3$ as compared to $CaMnO_{3.}$ The pressure dependence of the Jahn-Teller distortion, which is evidenced by the spatial distribution of Mn-O bond length (d) and defined as $\Delta = (\frac{1}{6}) \sum_{n=1}^{6} [\frac{d_n - <d>}{<d>}]^2)$, along-with three Mn-O distances of the distorted MnO_6 octahedra, are shown in Fig 6.17 (c) and (d). It is interesting to notice that computed Jahn-Teller distortion using the above relation was found to be two-orders lower for $CaMnO_3$ in comparison to $PrMnO_3$, and could be considered as zero. This result is satisfying as $CaMnO_3$ is not known to possess [29] Jahn-Teller distortion.

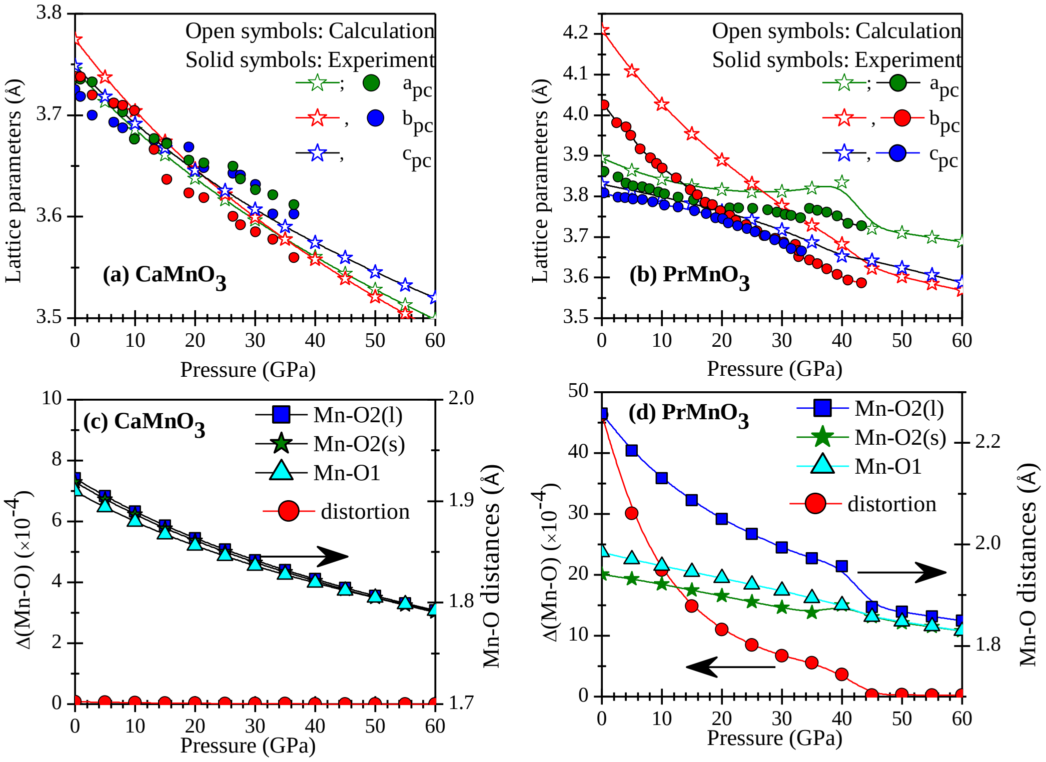

FIG 6.17. *(Color online) Pressure dependence of pseudocubic lattice parameters for (a) $CaMnO_3$ and (b) $PrMnO_3$ compared to reported experimental data for $CaMnO_3$ [70-72] and $PrMnO_3$ [28] respectively. Pressure dependence of Mn-O bond length and distortion of MnO_6 ochtahedra as calculated are shown in (c) $CaMnO_3$ and (d) $PrMnO_3$, respectively.*

The calculated variations of Mn-O distances are isotropic for $CaMnO_3$ and found to be highly anisotropic for $PrMnO_3$. On increasing pressure, long Mn-O2 (l) distance decrease faster than the other (Mn-O2(s) and Mn-O1) and becomes nearly equal at around 45 GPa. This nearly isotropic behavior of the Mn-O distance at high pressure is attributed to disappearance of Jahn-Teller distortion (similar to $CaMnO_3$). Basically, application of external pressure opens the Mn-O-Mn angles and in turn shortens the Mn-O bond lengths, leading to less distorted octahedra. The calculated Mn magnetic moment in the equilibrium structure at Mn site is 2.6 μ_B, which is in agreement with the experimental values of free

Mn^{3+} (3.0). We found that at about 45 GPa the Mn magnetic moment decrease to 1.0 μ_B which could be signature for insulator to metal transition.

Recently, Mota *et al.*[28] reported a high pressure study of orthorhombic rare-earth manganites using a combination of synchrotron x ray diffraction and Raman scattering technique. The authors observed change in the diffraction patterns of $PrMnO_3$ and disappearance of the Raman spectrum with pressure. The authors [28] suspected that the changes might be related to the structural phase transition from orthorhombic to tetragonal (*I4/mcm*) structure at 45 GPa. However the disappearance of Raman peak could also be due to metal to insulator transition. Hence the first principle simulation with pressure will help to overcome this ambiguity. Theoretically, we can predict the transition pressure by comparing the enthalpy as a function of pressure for different phases. Figure 6.18 (a) depicts the computed pressure dependence of the difference in the enthalpy $\Delta H= H_{ortho}-H_{tetra}$ of orthorhombic and tetragonal phases. We find that at low pressure (Pc=19 GPa) orthorhombic phase has the lowest enthalpy (ΔH), as it is the well-known ground state of $PrMnO_3$ at T=0 K. However at pressure above 19 GPa, the tetragonal phase becomes favorable over the orthorhombic phase. The value of the pressure is in agreement to pressure where shear strain becomes unstable (see Fig. 7 of ref.13). Mota *el al.* [28] reported that the strain analysis does not give any evidence for the suppression of the Jahn-Teller distortion at this pressure. If we recall Fig. 6.17 (d), we find that computed Jahn-Teller distortion decrease rapidly up to this pressure and then later it decreases slowly. Based on combined diffraction and Raman data, Mota *el al.* [28] reported that $PrMnO_3$ undergoes orthorhombic to tetragonal structural phase transition at around 45 GPa. As mentioned above the calculated pressure dependence of the enthalpy suggests that tetragonal phase is energetically favorable over orthorhombic phase above P= 19 GPa. In order to investigate the dynamical stability of tetragonal phase, we computed the phonon dispersion relation (Fig. 6.18 (b)) in the entire Brillouin zone at 30

GPa. The presence of unstable phonon modes in the tetragonal phase, clearly suggests that although tetragonal phase is energetically favor over orthorhombic phase, it is dynamically unstable. This rules out the possibility of orthorhombic to tetragonal phase transition in $PrMnO_3$ around 45 GPa.

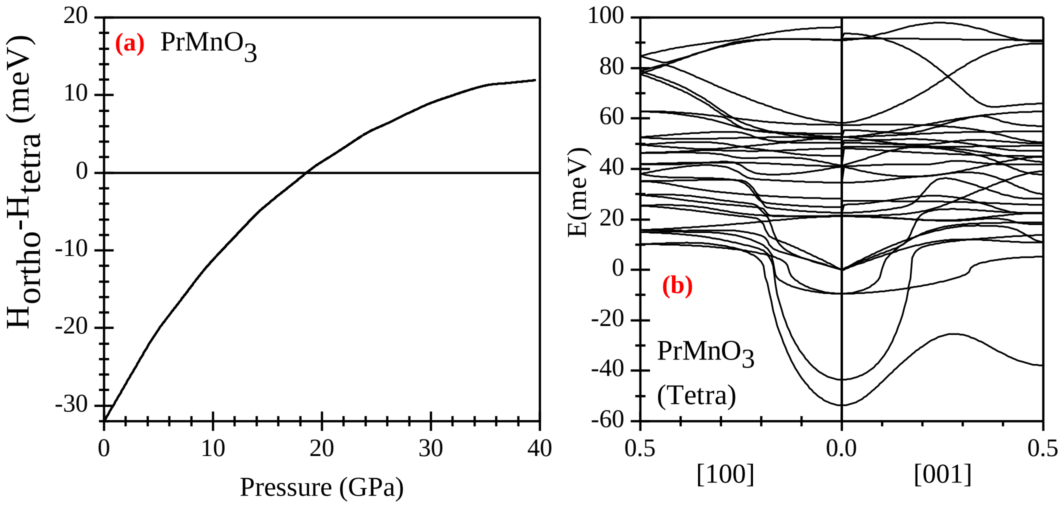

FIG 6.18. *(a) Enthalpy difference (ΔH) between the orthorhombic (Pnma) and tetragonal (I4/mcm) phases of $PrMnO_3$ as calculated using ab-inito DFT calculation. (b) The computed phonon dispersion relations for $PrMnO_3$ in tetragonal phase.*

As shown in Fig. 6.17 the suppression of Jahn-Teller distortion occurs at 45 GPa. Further we found that the magnetic moment at Mn site is also quenched at the same pressure. The suppression of the Jahn-Teller distortion is expected to decrease the volume at high pressures. Thus change in the volume of the unit cell in the experimental data at around 45 GPa may be associated with disappearance of Jahn-Teller distortion followed by insulator to metal transition. Our band structure calculation also suggests that $PrMO_3$ becomes poor metal above 45 GPa. The similar observation is also found in $LaMnO_3$ [73], which show the suppression of Jahn-Teller distortion and insulator to metal transition by application of pressure. In $LaMnO_3$, Jahn-Teller distortion and orbital ordering are known to be completely suppressed well below the insulator to metal transition. In contrast to $LaMnO_3$, in the present case, we notice that suppression of Jahn-Teller distortion and insulator to metal transition occurs simultaneously.

6.4 Conclusions

In $NaNbO_3$, We have reported inelastic neutron scattering measurements of the phonon density of states of sodium niobate as a function of temperature. The inelastic neutron scattering spectra are correlated to the various crystallographic phases of $NaNbO_3$, and show significant changes with increasing temperature. Upon heating, the spectra become more diffusive. The computed phonon density of states of $NaNbO_3$ is found to be in good agreement with our INS measurements. Using the calculations, we have identified the various soft phonon modes at specific points in the Brillouin zone that are associated with various phase transition as a function of temperature. Further, we have found that the characteristic antiferroelectric Raman modes, which appear below the antiferroelectric phase transition temperature, correspond to the A_{1g} symmetry and are due to the folding of the T (ω=95 cm^{-1}) and Δ (ω=129 cm^{-1}) points of the Brillouin zone, under the cubic phase.

In $RMnO_3$, we have reported inelastic neutron scattering measurements of the $CaMnO_3$ and $PrMnO_3$ in a wide temperature range up to 1251 K. The excitations at 20 meV and 17 meV are found to be associated with the magnetic origin for $CaMnO_3$ and $PrMnO_3$ respectively. The neutron inelastic spectra also show changes across the magnetic as well as structural phase transitions temperatures in both the compounds. Measurements show that in spite of similar structure the presence of Jahn-Teller distortion $PrMnO_3$ might results in broad peaks in the phonon spectra in comparison to $CaMnO_3$ where it exhibits well-defined peaks. Theoretical calculation for $PrMnO_3$ suggests that suppression of Jahn-Teller distortion and insulator to metal transition occurs simultaneously, which is in-contrast to $LaMnO_3$. We found that at high pressure above 20 GPa tetragonal phase in $PrMnO_3$ is energetically favored over orthorhombic phase, however it is found to be dynamically unstable.

[1] O. Diéguez, K. M. Rabe and D. Vanderbilt, Physical Review B **72**, 144101 (2005).

[2] R. D. King-Smith and D. Vanderbilt, Physical Review B **49**, 5828 (1994).

[3] W. Zhong, R. D. King-Smith and D. Vanderbilt, Physical Review Letters **72**, 3618 (1994).

[4] W. Zhong and D. Vanderbilt, Physical Review Letters **74**, 2587 (1995).

[5] R. Machado, M. Sepliarsky and M. G. Stachiotti, Physical Review B **84**, 134107 (2011).

[6] Y. Xu, Ferroelectric Materials and their Applicationsix (1991)

[7] J. L. G. F. L.G. Tejuca, Properties and Applications of Perovskite-Type Oxides. (Dekker, New York, 1992).

[8] E. Bousquet, M. Dawber, N. Stucki, C. Lichtensteiger, P. Hermet, S. Gariglio, J.-M. Triscone and P. Ghosez, Nature **452**, 732 (2008).

[9] T. Choi, Y. Horibe, H. T. Yi, Y. J. Choi, W. Wu and S. W. Cheong, Nat Mater **9**, 253 (2010).

[10] E. Valdez, C. B. de Araújo and A. A. Lipovskii, Applied Physics Letters **89**, 031901 (2006).

[11] E. Hollenstein, M. Davis, D. Damjanovic and N. Setter, Applied Physics Letters **87**, 182905 (2005).

[12] I. Y. Yu, P. Simon, E. Gagarina, L. Hennet, D. Thiaudière, V. I. Torgashev, S. I. Raevskaya, I. P. Raevskii, L. A. Reznitchenko and J. L. Sauvajol, Journal of Physics: Condensed Matter **17**, 4977 (2005).

[13] M. E. Lines and A. M. Glass, Principles and Applications of Ferroelectrics and Related Materials. (Oxford University Press, 2001, Oxford, 2001).

[14] S. Jin, T. H. Tiefel, M. McCormack, R. A. Fastnacht, R. Ramesh and L. H. Chen, Science **264**, 413 (1994).

[15] G. C. Milward, M. J. Calderon and P. B. Littlewood, Nature **433**, 607 (2005).

[16] D. Preziosi, M. Alexe, D. Hesse and M. Salluzzo, Physical Review Letters **115**, 157401 (2015).

[17] Y. F. Nie, P. D. C. King, C. H. Kim, M. Uchida, H. I. Wei, B. D. Faeth, J. P. Ruf, J. P. C. Ruff, L. Xie, X. Pan, C. J. Fennie, D. G. Schlom and K. M. Shen, Physical Review Letters **114**, 016401 (2015).

[18] C. Ulrich, G. Khaliullin, M. Guennou, H. Roth, T. Lorenz and B. Keimer, Physical Review Letters **115**, 156403 (2015).

[19] L. L. Lev, J. Krempaský, U. Staub, V. A. Rogalev, T. Schmitt, M. Shi, P. Blaha, A. S. Mishchenko, A. A. Veligzhanin, Y. V. Zubavichus, M. B. Tsetlin, H. Volfová, J. Braun, J. Minár and V. N. Strocov, Physical Review Letters **114**, 237601 (2015).

[20] L. Chaix, S. de Brion, S. Petit, R. Ballou, L. P. Regnault, J. Ollivier, J. B. Brubach, P. Roy, J. Debray, P. Lejay, A. Cano, E. Ressouche and V. Simonet, Physical Review Letters **112**, 137201 (2014).

[21] N. Ganguli and P. J. Kelly, Physical Review Letters **113**, 127201 (2014).

[22] Y. Jia, R. V. Chopdekar, E. Arenholz, A. T. Young, M. A. Marcus, A. Mehta and Y. Takamura, Physical Review B **92**, 094407 (2015).

[23] M. Hoffmann, V. S. Borisov, S. Ostanin, I. Mertig, W. Hergert and A. Ernst, Physical Review B **92**, 094427 (2015).

[24] A. Furrer, A. Podlesnyak and K. W. Krämer, Physical Review B **92**, 104415 (2015).

[25] Y. W. Windsor, S. W. Huang, Y. Hu, L. Rettig, A. Alberca, K. Shimamoto, V. Scagnoli, T. Lippert, C. W. Schneider and U. Staub, Physical Review Letters **113**, 167202 (2014).

[26] P. Barone, D. Di Sante and S. Picozzi, Physical Review B **89**, 144104 (2014).

[27] J. Hong, A. Stroppa, J. Íñiguez, S. Picozzi and D. Vanderbilt, Physical Review B **85**, 054417 (2012).

[28] D. A. Mota, A. Almeida, V. H. Rodrigues, M. M. R. Costa, P. Tavares, P. Bouvier, M. Guennou, J. Kreisel and J. A. Moreira, Physical Review B **90**, 054104 (2014).

[29] S. Bhattacharjee, E. Bousquet and P. Ghosez, Physical Review Letters **102**, 117602 (2009).

[30] U. Aschauer, R. Pfenninger, S. M. Selbach, T. Grande and N. A. Spaldin, Physical Review B **88**, 054111 (2013).

[31] N. Hamdad and B. Bouhafs, Physica B: Condensed Matter **405**, 4595 (2010).

[32] J. Hemberger, M. Brando, R. Wehn, V. Y. Ivanov, A. A. Mukhin, A. M. Balbashov and A. Loidl, Physical Review B **69**, 064418 (2004).

[33] L. Bocher, M. H. Aguirre, R. Robert, D. Logvinovich, S. Bakardjieva, J. Hejtmanek and A. Weidenkaff, Acta Materialia **57**, 5667 (2009).

[34] I. P. Raevski, S. I. Raevskaya, S. A. Prosandeev, V. A. Shuvaeva, A. M. Glazer and M. S. Prosandeeva, Journal of Physics: Condensed Matter **16**, L221 (2004).

[35] S. K. Mishra, N. Choudhury, S. L. Chaplot, P. S. R. Krishna and R. Mittal, Physical Review B **76**, 024110 (2007).

[36] S. K. Mishra, R. Mittal, V. Y. Pomjakushin and S. L. Chaplot, Physical Review B **83**, 134105 (2011).

[37] K. Parlinski, Z. Q. Li and Y. Kawazoe, Physical Review Letters **78**, 4063 (1997).

[38] K. Parlinksi, (2003)

[39] X. B. Wang, Z. X. Shen, Z. P. Hu, L. Qin, S. H. Tang and M. H. Kuok, Journal of Molecular Structure **385**, 1 (1996).

[40] Z. X. Shen, X. B. Wang, S. H. Tang, M. H. Kuok and R. Malekfar, Journal of Raman Spectroscopy **31**, 439 (2000).

[41] L. Jiang, D. C. Mitchell, W. Dmowski and T. Egami, Physical Review B **88**, 014105 (2013).

[42] A. D. Bruce and R. A. Cowley, Advances in Physics **29**, 219 (1980).

[43] I. Tomeno, Y. Tsunoda, K. Oka, M. Matsuura and M. Nishi, Physical Review B **80**, 104101 (2009).

[44] N. Choudhury, E. J. Walter, A. I. Kolesnikov and C.-K. Loong, Physical Review B **77**, 134111 (2008).

[45] S. J. Lin, D. P. Chiang, Y. F. Chen, C. H. Peng, H. T. Liu, J. K. Mei, W. S. Tse, T. R. Tsai and H. P. Chiang, Journal of Raman Spectroscopy **37**, 1442 (2006).

[46] E. Bouziane, M. D. Fontana and M. Ayadi, Journal of Physics: Condensed Matter **15**, 1387 (2003).

[47] R. J. C. Lima, P. T. C. Freire, J. M. Sasaki, A. P. Ayala, F. E. A. Melo, J. Mendes Filho, K. C. Serra, S. Lanfredi, M. H. Lente and J. A. Eiras, Journal of Raman Spectroscopy **33**, 669 (2002).

[48] M. Nicastro and C. H. Patterson, Physical Review B **65**, 205111 (2002).

[49] H. Taguchi, M. Nagao, T. Sato and M. Shimada, Journal of Solid State Chemistry **78**, 312 (1989).

[50] H. Yoshizawa, H. Kawano, Y. Tomioka and Y. Tokura, Physical Review B **52**, R13145 (1995).

[51] Z. Jirák, S. Krupička, Z. Šimša, M. Dlouhá and S. Vratislav, Journal of Magnetism and Magnetic Materials **53**, 153 (1985).

[52] Y. Tomioka, A. Asamitsu, H. Kuwahara, Y. Moritomo and Y. Tokura, Physical Review B **53**, R1689 (1996).

[53] C. Martin, A. Maignan, M. Hervieu and B. Raveau, Physical Review B **60**, 12191 (1999).

[54] M. v. Zimmermann, C. S. Nelson, J. P. Hill, D. Gibbs, M. Blume, D. Casa, B. Keimer, Y. Murakami, C. C. Kao, C. Venkataraman, T. Gog, Y. Tomioka and Y. Tokura, Physical Review B **64**, 195133 (2001).

[55] V. I. Anisimov, I. S. Elfimov, M. A. Korotin and K. Terakura, Physical Review B **55**, 15494 (1997).

[56] M. N. Iliev, M. V. Abrashev, J. Laverdière, S. Jandl, M. M. Gospodinov, Y. Q. Wang and Y. Y. Sun, Physical Review B **73**, 064302 (2006).

[57] M. Molinari, D. A. Tompsett, S. C. Parker, F. Azough and R. Freer, Journal of Materials Chemistry A **2**, 14109 (2014).

[58] E. S. Božin, A. Sartbaeva, H. Zheng, S. A. Wells, J. F. Mitchell, T. Proffen, M. F. Thorpe and S. J. L. Billinge, Journal of Physics and Chemistry of Solids **69**, 2146 (2008).

[59] R. Kajimoto, H. Mochizuki, H. Yoshizawa, S. Okamoto and S. Ishihara, Physical Review B **69**, 054433 (2004).

[60] F. P. Zhang, Q. M. Lu, X. Zhang and J. X. Zhang, Journal of Alloys and Compounds **509**, 542 (2011).

[61] H. Tsukahara, S. Ishibashi and K. Terakura, Physical Review B **81**, 214108 (2010).

[62] B. Bouadjemi, S. Bentata, A. Abbad, W. Benstaali and B. Bouhafs, Solid State Communications **168**, 6 (2013).

[63] B. Satadeep, B. Eric and G. Philippe, Journal of Physics: Condensed Matter **20**, 255229 (2008).

[64] G. E. Granroth, D. H. Vandergriff and S. E. Nagler, Physica B: Condensed Matter **385–386, Part 2**, 1104 (2006).

[65] G. E. Granroth, A. I. Kolesnikov, T. E. Sherline, J. P. Clancy, K. A. Ross, J. P. C. Ruff, B. D. Gaulin and S. E. Nagler, Journal of Physics: Conference Series **251**, 012058 (2010).

[66] H. J. Monkhorst and J. D. Pack, Physical Review B **13**, 5188 (1976).

[67] C. R. Wiebe, J. E. Greedan, J. S. Gardner, Z. Zeng and M. Greenblatt, Physical Review B **64**, 064421 (2001).

[68] M. V. Abrashev, J. Bäckström, L. Börjesson, V. N. Popov, R. A. Chakalov, N. Kolev, R. L. Meng and M. N. Iliev, Physical Review B **65**, 184301 (2002).

[69] K. R. Poeppelmeier, M. E. Leonowicz, J. C. Scanlon, J. M. Longo and W. B. Yelon, Journal of Solid State Chemistry **45**, 71 (1982).

[70] Y.-X. Liu, S. Qin, J.-Z. Jiang, T. Kikegawa and G.-H. Shi, Chinese Physics C **34**, 1025 (2010).

[71] W. Paszkowicz, S. Woodley, P. Piszora, B. Bojanowski, J. Piętosa, Y. Cerenius, S. Carlson and C. Martin, Appl. Phys. A **112**, 839 (2013).

[72] J. Piętosa, W. Paszkowicz, R. Minikayev, J. Nowak, C. Lathe and C. Martin, Powder Diffraction **26**, 262 (2011).

[73] I. Loa, P. Adler, A. Grzechnik, K. Syassen, U. Schwarz, M. Hanfland, G. K. Rozenberg, P. Gorodetsky and M. P. Pasternak, Physical Review Letters **87**, 125501 (2001).

Chapter 7

Phonons and Superionic Behavior in Battery Materials

7.1 Introduction

Plenty of research is going on to address the issue of energy storage for clean and sustainable energy. The discovery and exploitation of new high performance materials requires a greater fundamental understanding of their properties on the atomic scales, leading to major advances in rechargeable batteries for portable electronics, electric vehicles and large-scale grid storage. Also the issue of global warming and diminishing fossil-fuel reserves accelerate the search for efficient energy alternatives. The performance of energy storage devices depends crucially on the properties of their component materials. An excellent example of innovative materials science is the discovery of the rechargeable lithium battery.

In the area of energy, materials research based on computational methods now play a vital role in characterizing and predicting the structures and properties of complex materials on the atomic scale. The simulations will be able to predict the material properties at extreme conditions as well as supplement the experimental studies. In this chapter we have presented our work based on first principles simulations to understand the diffusion mechanism of Li ion in superionic conductor Li_2O and scope of diffusion in electrode materials $LiMPO_4$ (M=Mn, Fe).

7.2 Lithium Oxide (Li_2O)

Lithium oxide belongs to the class of superionics, which exhibit high ionic conductivity above 1200 K. In this case, Li ion is the diffusing species, while oxygen ions constitute the rigid framework. The material find large application is attributed to its high melting point, relatively low volatility and high Li atom density. At ambient conditions Li_2O occurs in the anti-fluorite structure with space group O^5_h (Fm3m)[1-3]. Oxygen ions are arranged in a FCC sublattice with lithium ions occupying the tetrahedral sites. We have performed the first principles lattice dynamics simulations at different volume corresponding to ambient and superionic regime. We have identified the phonon mode which might be responsible for superionic in the compound. Further, we have also carried out the barrier energy calculation for Li migration from one lithium site to adjacent lithium site along different direction.

For Li_2O, we have used the Quantum espresso[4] package for the *ab-initio* phonon calculations. Pseudopotential generated by using Perdew Burke Ernzerhof exchange correlation functional under generalized gradient approximation (PBE-GGA) [5, 6] and Perdew-Zunger correlation functional under local density approximation (PZ-LDA)[7] have been used. We have chosen 12×12×12 K mesh for self-consistent field calculations with energy cutoff of 280 and 120 Rydberg for GGA and LDA respectively, which is found to be sufficient for convergence of the order of meV.

7.2.1 Results and Discussion

7.2.1.1 Phonon Dispersion Relation

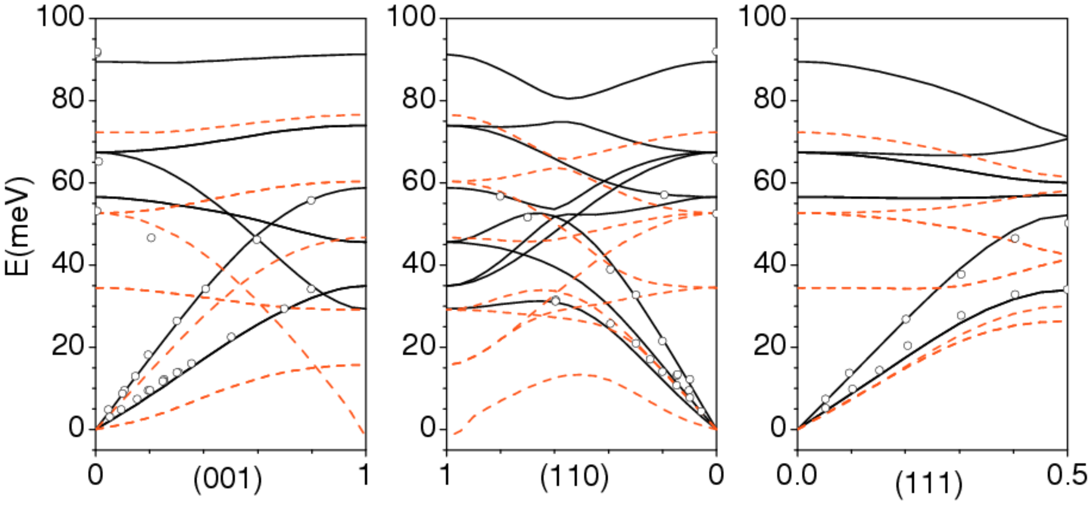

FIG 7.1 *Phonon dispersion from first principles density functional theory under generalized gradient approximation (GGA-DFT). The full and dashed lines correspond to calculations performed at a= 4.57 Å and a= 4.88 Å respectively. The open symbols correspond to reported experimental[8] data.*

Ab-initio phonon calculations have been carried out with both the LDA and GGA schemes. However qualitatively we did not get any substantial improvement using GGA. The computed values of Born effective charges for Li and O are 0.9 and -1.8 respectively, while the dielectric constant is 2.90. These are in agreement with previous reported[9, 10] values. Here we have shown (Fig. 7.1) calculated phonon dispersion relation at relaxed lattice parameter a = 4.57 Å (at 0 K) in GGA scheme. The phonon dispersion relation have been plotted after including the LO-TO splitting of the modes. The results are in good agreement with reported experimental data. The compound exhibits superionic transition in the vicinity of 1200 K. Hence we have performed phonon calculations at various unit cell parameters corresponding to superionic regime. As expected the phonon frequencies along all the three direction are found to soften with increase of volume. The softening is found to be small for all the modes except for the lowest transverse acoustic (TA) branch along [110] at zone boundary.

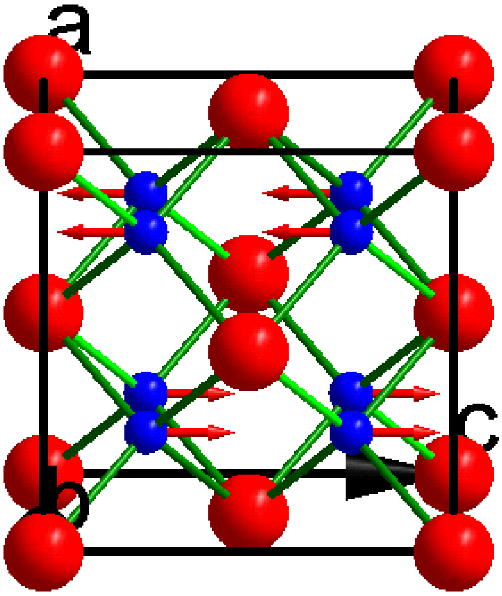

FIG 7.2 *Motion of individual atoms for zone boundary TA mode along [110] direction at lattice parameter corresponding to a= 4.88 Å. Key; O: red spheres, Li: blue spheres.*

The eigen vector of TA mode has been plotted (Fig. 7.2) corresponding to the unit cell parameter of a= 4.88 Å. We find that lithium atoms in the alternate layers move opposite to each other along [001] while oxygen's are at rest. Hence increasing the temperature could lead to migration of lithium ions from one site to another vacant site along [001] direction, which can easily be visualized from Fig. 7.2. Fig. 7.3 gives the change in the transverse acoustic frequency with increasing lattice parameter, as calculated from LDA and GGA schemes of *ab-initio* DFT. The lowest TA mode along [110] at zone boundary is found to soften sharply at volume in the superionic regime. At the superionic transition, some of the lithiums might just have sufficient energy to move from their ideal positions and start diffusing. It is possible that the softening of these modes might be the precursor to the process of diffusion. Fracchia[11] et al have also reported softening of zone boundary mode along [001] in Li_2O.

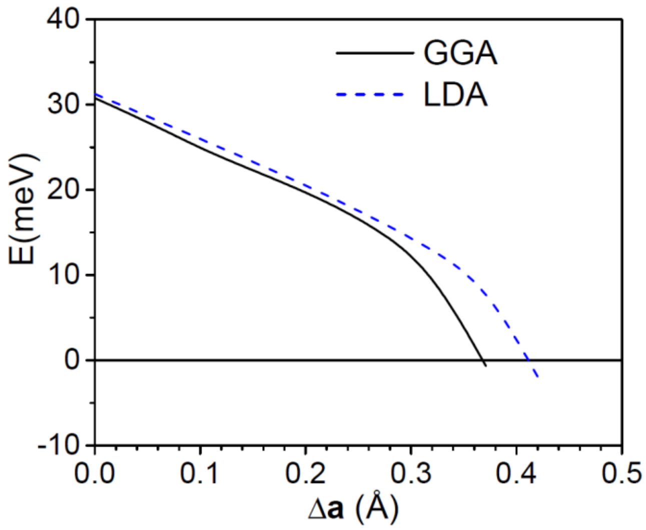

FIG 7.3 *Softening of zone boundary transverse acoustic (TA) phonon along [110]. Δ**a** correspond to difference in lattice parameter from equilibrium. The equilibrium value of lattice parameter, a in GGA and LDA calculations are 4.57 Å, and 4.45 Å respectively.*

7.3 $LiMPO_4$ (M=Mn, Fe)

At ambient conditions, $LiMPO_4$ (M= Mn , Fe) crystallize in olivine type (Fig. 7.4) orthorhombic Pnma[12] space group analogous to mineral Triphylite structure. $LiMPO_4$ are paramagnets above their Neel temperatures. In case of LiFePO4[13-15], below T_N= 50 K, Fe^{2+} spins align collinear with b-axis, while in $LiMnPO_4$ [16, 17] Mn^{2+} spins align along a-axis below T_N = 34 K. The structure comprises of discrete PO_4 tetrahdera and highly distorted oxygen octahedra about lithium and transition metal ion, M. The PO_4 tetrahdra are irregular, with two significantly different sets of O-O distances. Our interest in this study has been to understand the dynamics of these compounds and plausible role of phonons in triggering the lithium ion movement. We have studied phonons in the entire Brillouin zone, softening of phonons with increasing volume. Here I have calculated the phonon density of states and compared with the measured data[18]. The *ab-initio* calculations are in good agreement with the inelastic neutron scattering data.

For $LiMPO_4$, we have used the Vienna ab initio simulation package (VASP-5.2) [19, 20] along with the PHONON package for the phonon calculations. The volume dependence of zone centre and zone boundary phonon modes has been calculated using density functional perturbation theory implemented in VASP. The plane wave pseudo-potential has been used with maximum plane wave energy cutoff of 500 eV for these compounds. The integrations over the Brillouin zone has been performed on a 4×7×9 grid of k-points generated by Monkhorst [21] pack method. The generalized gradient approximation (GGA) exchange correlation given by Perdew Burke and Ernzerhof [6] with projected–augmented wave method has been used. First-principles calculations have been carried out for the ground states of A-type AFM structures of $LiMPO_4$. The on-site Hubbard interaction for the d-electrons has been taken care within the approach as introduced by Dudarev [22] et al. The value of the onsite interaction term U=4.3 eV for d electrons for Fe and Mn has been taken from previous studies [23] on $LiMPO_4$ (M=Mn, Fe). Phonon frequencies were extracted from subsequent calculations using the PHONON software[24].

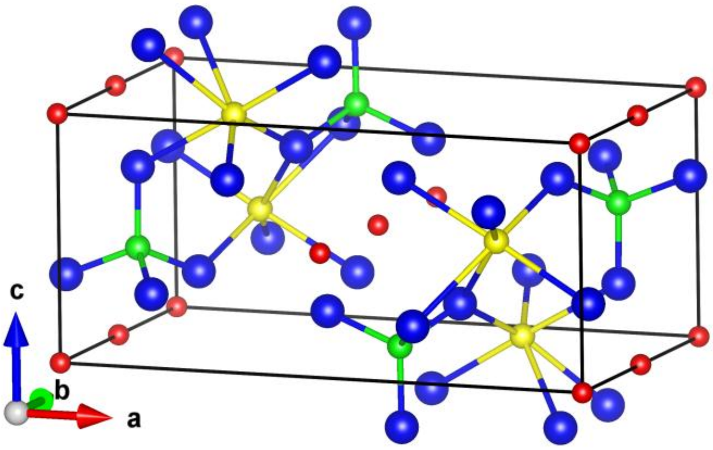

FIG 7.4 *Structure of* $LiMPO_4$ *(M=Mn, Fe) (orthorhombic Pnma space group) derived from xcrysden software at T = 0 K. Key; Li: Red spheres, M=Mn or Fe: Yellow spheres, P: Green spheres, O: Blue spheres.*

Density functional perturbation method (DFPT) [25] method can be used to calculate the phonon frequencies at any given specific q point, However in the force constant approach using the PHONON code one can obtain the phonons in the entire Brillouin zone, but it is very time expensive. DFPT method has been used to calculate the volume dependence of the zone-boundary and zone center modes specifically. These calculations have been used to identify the dynamically unstable regime. Later the force constant approach has been used for calculation of phonon spectra in the entire Brillouin zone at unit cell volumes corresponding to ambient as well as dynamically unstable regime. The results obtained from either method are identical except for the longitudinal optic modes that are not obtained in the DFPT method.

7.3.1 Results and Discussion

7.3.1.1 Phonon Density of States

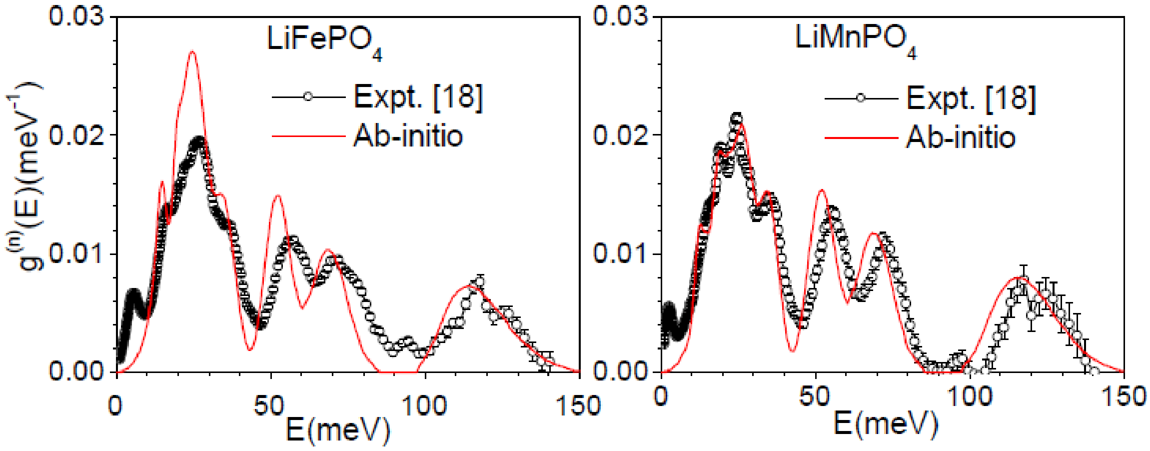

FIG 7.5 *The comparison of the calculated and experimental neutron inelastic scattering spectra for LiMPO$_4$ (M=Mn, Fe) available in the literature [18] at ambient pressure at 300 K. The ab-initio calculation is carried out at 0 K. The experimental spectra comprises of magnetic and phonon contribution, while computed results pertain to phonon contribution alone.*

The comparison between calculated phonon density of states and experimental measured neutron inelastic spectra is shown in Fig. 7.5 for LiFePO$_4$ and LiMnPO$_4$. The phonon spectrum extends up to 150 meV. The general characteristics of the experimental features are well reproduced by the calculations. The measurements are found to be in agreement with *ab-initio* calculations.

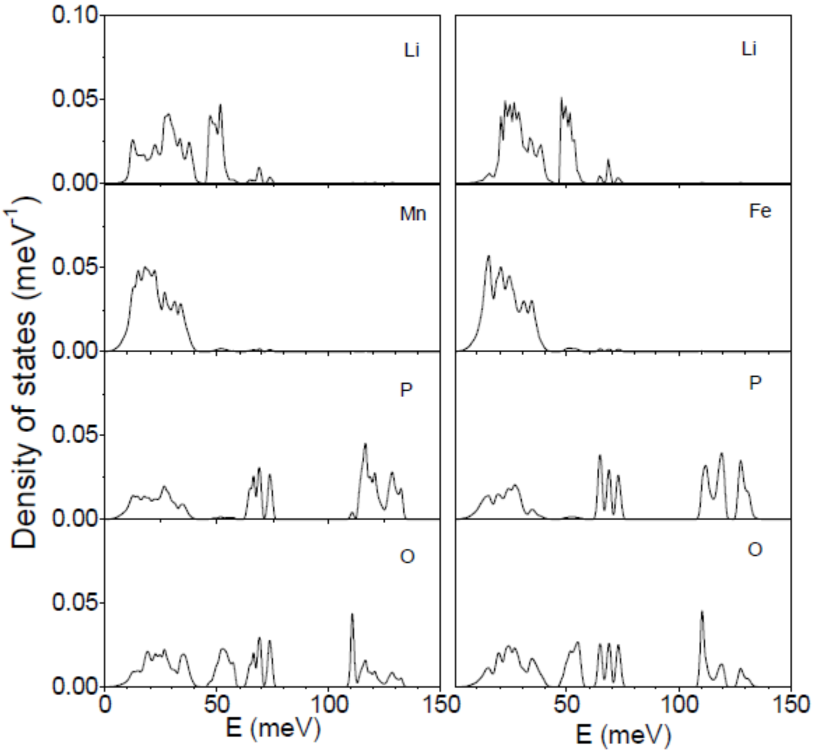

FIG 7.6 *The calculated partial densities of states in LiMPO$_4$ (M=Mn,Fe). The solid and dashed lines correspond to the calculations carried out using ab-initio.*

The parital contribution of the constituent atoms to the total phonon density of states in the two olivines computed using *ab-initio* calculations is shown in Fig. 7.6. We find that Fe/Mn ions contribute largely below 40 meV, while Li being lighter contributes up to 75 meV. The density found beyond 105 meV is only due to the stretching modes of the PO$_4$ polyhedra.

7.3.1.2 Behavior of Phonons with Volume

The phonon dispersion has been calculated along the high symmetry directions using *ab-initio* DFT method. Fig. 7.7 shows the calculations of phonon dispersion relations using the *ab-initio* method. The LO-TO (longitudinal optic and transverse optic) splitting of the modes has also been included while plotting the phonon dispersion relation. The phonon frequencies are usually expected to soften with increase of volume. The phonon frequencies of $LiMPO_4$ (M=Mn, Fe) have been calculated (Fig. 7.8) using *ab-initio* method as a function of volume. The phonon frequencies along all the three high symmetry direction are found to soften with increase of volume. However, the softening is found to be very large for one of the zone-centre (ZC) and zone- boundary (ZB) modes along [100] direction. The change in the phonon frequency with increasing volume (Fig. 7.9) has been plotted for these ZC and ZB modes. We find that in both the compounds the zone centre optic mode softens first, followed in quick succession by the zone-boundary mode with increasing volume.

For qualitative understanding of the atomic displacement in these unstable modes, we have plotted eigen vectors of both these modes (Fig. 7.10). In case of ZC mode at ambient volume the displacements of the Li atoms is maximum, while the amplitudes of other atoms are less but not negligible. The displacement of the lithium ions is only in the x-y plane. In the dynamically unstable regime, the amplitude of Li atoms has increased significantly. The Fe atoms are at rest, while the amplitude of P atoms decreased slightly and O atoms do not show any change. The component of displacement of Li atoms is non-zero along all the three directions but with the highest component along x direction.

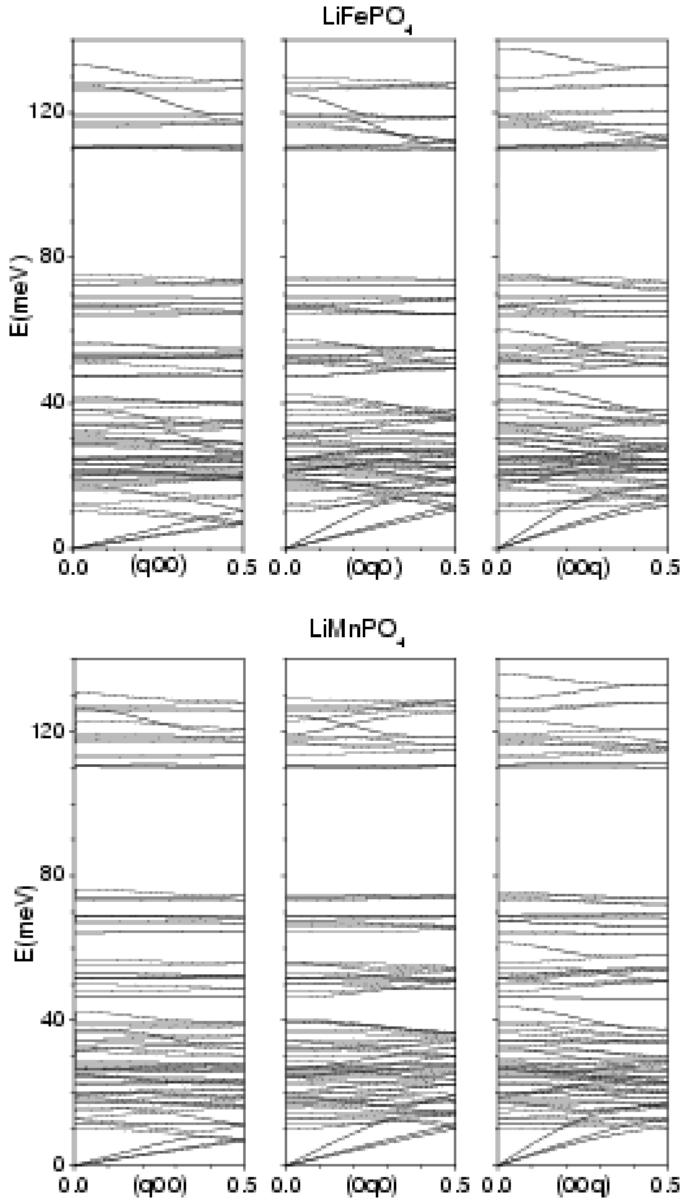

FIG 7.7 *The Calculated phonon dispersion for LiMPO$_4$ (M=Mn, Fe) from ab-initio density functional theory under generalized gradient approximation (GGA-DFT).*

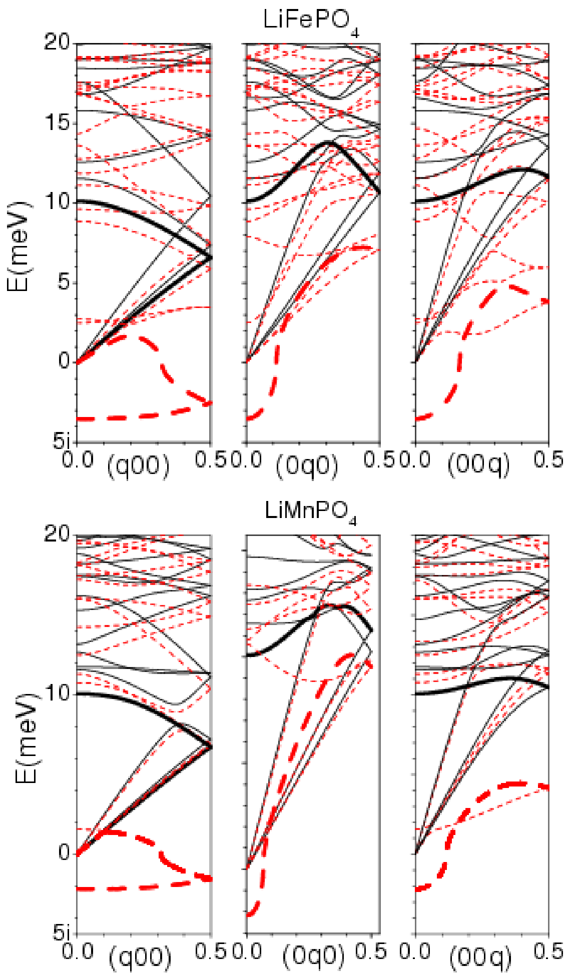

FIG 7.8 *The low-energy part of the phonon dispersion relation from ab-initio density functional theory under generalized gradient approximation (GGA-DFT). The full and dashed lines refer to the phonon dispersion corresponding to calculated unit cell parameters a=10.42(10.55) Å, b = 6.06 (6.17) Å, c = 4.75 (4.79) Å and a = 10.77 (10.66) Å, b = 6.20 (6.22) Å, c = 4.88 (4.83) Å for $LiFePO_4$ ($LiMnPO_4$). The zone-centre and zone-boundary phonon modes in $LiFePO_4$ and $LiMnPO_4$ soften at unit cell volume corresponding to the higher temperature. This region is hitherto defined by us as dynamically unstable regime. The thick lines shows the phonon branches undergoing large softening in the dynamically unstable regime.*

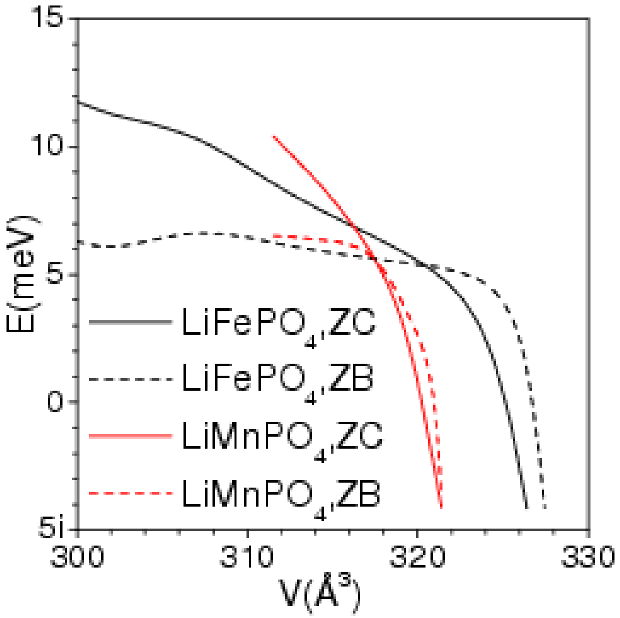

FIG 7.9 *Zone-boundary and zone-centre modes as a function of unit cell volume. The zone-centre and zone-boundary phonon modes in $LiFePO_4$ and $LiMnPO_4$ soften at unit cell volume corresponding to higher temperatures.*

For ZB mode (Fig. 7.10), all the atoms have finite displacement in the ambient regime. In case of lithium, there is no displacement along z-direction while the displacements along x and y directions are comparable. Here again movement is only in the x-y plane. While in the high temperature regime, the amplitude of Fe and P atoms have reduced substantially and there is a large increase in amplitude of Li atoms. It is interesting to note that Li atoms at the corners of the unit cell do not show any substantial change in amplitude. This behavior is different as compared to the ZC mode where amplitude of all Li atoms increased simultaneously. As far as O atoms are concerned, the amplitudes do not change. Careful analysis of the eigen vector of ZB mode also indicates that, there are non-zero components along all the three directions. The component along z-direction is least, while the largest component is along x-direction.

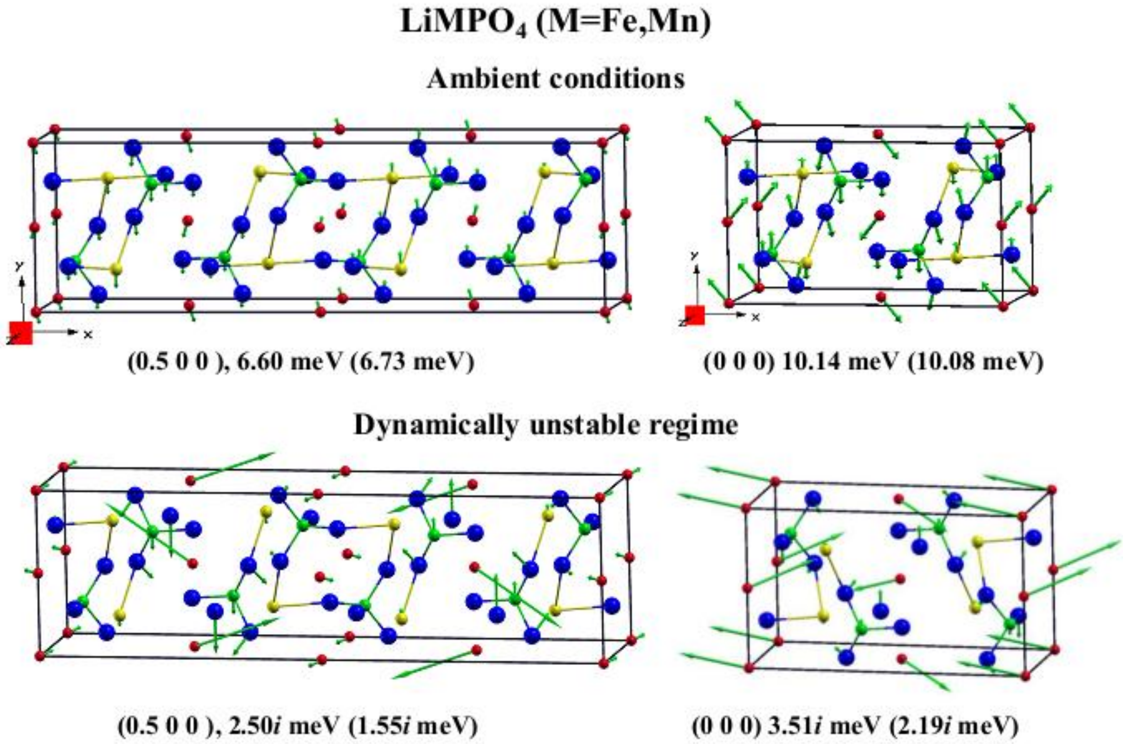

FIG 7.10 *Motion of individual atoms for zone boundary and zone centre modes at unit cell volumes corresponding to ambient and dynamically unstable region. The numbers after the mode assignments give the phonon energies of mode in Fe(Mn) compound. i after the phonon energy indicates that mode is unstable. A 2×1×1 super cell of the primitive unit cell is shown for zone boundary mode at (0.5 0 0). The zone-centre and zone-boundary phonon modes in LiFePO$_4$ and LiMnPO$_4$ soften at unit cell volume corresponding to higher temperatures. Key; Li: Red spheres, M=Mn or Fe: Yellow spheres, P: Green spheres, O: Blue spheres.*

From both the analysis we can see that at ambient temperature, the likely motion of lithium is in the x-y plane. If conducive conditions prevail, lithium might move in this plane. Earlier calculations and experimental observation [26-30] of thermal ellipsoids of lithium ions from neutron diffraction at ambient temperature have shown that lithium ions move along y-direction in a curved path. Hence as far as room temperature results are concerned our results are in agreement with previous observations. But, with substantial increase in temperature, we find that the scenario changes.

We find that $LiFePO_4$ shows softening (Fig. 7.8) at a higher volume in comparison with the Mn counterpart. The percentage change in volume for initiation of phonon instability in $LiMnPO_4$ is much lesser as compared to $LiFePO_4$. The phonon instabilities observed at higher volume may correspond to higher lithium MSD compared to the ambient volume. The main interest in these compounds stems from their use as battery materials. Lithium intercalation and subsequent delithiation are the main processes by which energy is transferred during its use as battery material. We have so far tried to unveil the role of phonons in the initiation of lithium movement crucial for the use of these materials as battery material.

7.4 Conclusions

Phonon dispersion along symmetry directions from ab-initio calculations is in good agreement with reported experimental data of Li_2O. We find that around the fast ion transition temperature, zone boundary TA phonon mode along [110] become unstable. This softening of the phonon could be a precursor to dynamical instability. This observation is corroborated by the eigenvector of this mode, and could be one of the factors leading to diffusion of lithium ions. We are able to relate the phonon softening with the ease of lithium movement at elevated temperature along [001] as against the other two high symmetry directions considered.

A first principles calculation of $LiFePO_4$ and $LiMnPO_4$ has been successfully used to understand the phonon dynamics. The calculated density of states is in excellent agreement with inelastic spectra of $LiMPO_4$ compounds as available in the literature. The phonon density of states calculated using first principles at volume corresponding to high temperature (> 1000 K) in $LiFePO_4$ and $LiMnPO_4$ suggests that there is a significant instability initiating in the Li sub-lattice. Analysis of the eigen vectors of these modes at 300 K suggest that if conducive conditions for Li movement from its lattice positions are available, the net displacement of Li atoms is in the x-y plane. But at higher temperature regime, the pattern of displacement suggests that lithium exhibits non-zero displacement along all the directions but with the highest component along x direction.

[1] R. Shah, A. De Vita, V. Heine and M. C. Payne, Physical Review B **53**, 8257 (1996).

[2] L. V. Azároff, Journal of Applied Physics **32**, 1658 (1961).

[3] Y. Duan and D. C. Sorescu, Physical Review B **79**, 014301 (2009).

[4] G. Paolo, B. Stefano, B. Nicola, C. Matteo, C. Roberto, C. Carlo, C. Davide, L. C. Guido, C. Matteo, D. Ismaila, C. Andrea Dal, G. Stefano de, F. Stefano, F. Guido, G. Ralph, G. Uwe, G. Christos, K. Anton, L. Michele, M.-S. Layla, M. Nicola, M. Francesco, M. Riccardo, P. Stefano, P. Alfredo, P. Lorenzo, S. Carlo, S. Sandro, S. Gabriele, P. S. Ari, S. Alexander, U. Paolo and M. W. Renata, Journal of Physics: Condensed Matter **21**, 395502 (2009).

[5] J. P. Perdew, K. Burke and M. Ernzerhof, Physical Review Letters **78**, 1396 (1997).

[6] J. P. Perdew, K. Burke and M. Ernzerhof, Physical Review Letters **77**, 3865 (1996).

[7] J. P. Perdew and A. Zunger, Physical Review B **23**, 5048 (1981).

[8] S. Hull, T. W. D. Farley, W. Hayes and M. T. Hutchings, Journal of Nuclear Materials **160**, 125 (1988).

[9] P. Sony and A. Shukla, Physical Review B **77**, 075130 (2008).

[10] P. Sony and A. Shukla, Physical Review B **73**, 165106 (2006).

[11] R. M. Fracchia, G. D. Barrera, N. L. Allan, T. H. K. Barron and W. C. Mackrodt, Journal of Physics and Chemistry of Solids **59**, 435 (1998).

[12] S. Geller and J. L. Durand, Acta Crystallographica **13**, 325 (1960).

[13] J. Li, V. O. Garlea, J. L. Zarestky and D. Vaknin, Physical Review B **73**, 024410 (2006).

[14] G. Liang, K. Park, J. Li, R. E. Benson, D. Vaknin, J. T. Markert and M. C. Croft, Physical Review B **77**, 064414 (2008).

[15] R. P. Santoro and R. E. Newnham, Acta Crystallographica **22**, 344 (1967).

[16] J. Li, W. Tian, Y. Chen, J. L. Zarestky, J. W. Lynn and D. Vaknin, Physical Review B **79**, 144410 (2009).

[17] A. Denis, Z. Andrej, D. Robert and J. Zvonko, Journal of Physics: Condensed Matter **16**, 5531 (2004).

[18] P. Goel, M. K. Gupta, R. Mittal, S. Rols, S. J. Patwe, S. N. Achary, A. K. Tyagi and S. L. Chaplot, Journal of Materials Chemistry A **2**, 14729 (2014).

[19] G. Kresse and D. Joubert, Physical Review B **59**, 1758 (1999).

[20] G. Kresse and J. Furthmüller, Computational Materials Science **6**, 15 (1996).

[21] H. J. Monkhorst and J. D. Pack, Physical Review B **13**, 5188 (1976).

[22] S. L. Dudarev, G. A. Botton, S. Y. Savrasov, C. J. Humphreys and A. P. Sutton, Physical Review B **57**, 1505 (1998).

[23] S. L. Shang, Y. Wang, Z. G. Mei, X. D. Hui and Z. K. Liu, Journal of Materials Chemistry **22**, 1142 (2012).

[24] K. Parlinksi, (2003)

[25] S. Baroni, P. Giannozzi and A. Testa, Physical Review Letters **58**, 1861 (1987).

[26] J. Sugiyama, H. Nozaki, M. Harada, K. Kamazawa, Y. Ikedo, Y. Miyake, O. Ofer, M. Månsson, E. J. Ansaldo, K. H. Chow, G. Kobayashi and R. Kanno, Physical Review B **85**, 054111 (2012).

[27] J. Sugiyama, H. Nozaki, M. Harada, K. Kamazawa, O. Ofer, M. Månsson, J. H. Brewer, E. J. Ansaldo, K. H. Chow, Y. Ikedo, Y. Miyake, K. Ohishi, I. Watanabe, G. Kobayashi and R. Kanno, Physical Review B **84**, 054430 (2011).

[28] S.-i. Nishimura, G. Kobayashi, K. Ohoyama, R. Kanno, M. Yashima and A. Yamada, Nat Mater **7**, 707 (2008).

[29] P. J. Baker, I. Franke, F. L. Pratt, T. Lancaster, D. Prabhakaran, W. Hayes and S. J. Blundell, Physical Review B **84**, 174403 (2011).

[30] G. K. P. Dathar, D. Sheppard, K. J. Stevenson and G. Henkelman, Chemistry of Materials **23**, 4032 (2011).

Chapter 8

Summary and Future Direction

8.1 Summary

The experimental and simulations studies on various compound presented in the thesis show that lattice dynamics calculations along with inelastic neutron scattering measurements can be successfully used to study the phonon properties as well as several thermodynamic properties of various novel compounds including negative thermal expansion materials and multiferroics. Properties of a material are related with the response of the material to external stimuli. Vibration of lattice in crystalline material changes on application of external stimuli, hence they also contribute to the physical properties of the material. Further, the vibrational frequencies are governed by the interatomic interaction between the atoms; hence it is important to know interaction between atoms. The author has used the state of the art density functional theory methods to compute the interaction between atoms in various crystalline materials. In order to validate the theoretical calculations, the author carried out measurements of phonon density of states from the polycrysatlline sample using time-of-flight spectrometers.

The density functional theory methods have been used to compute and analyze the various features of the vibrational excitations in the solids, such as: (i) the frequency of phonons as a function of the wavevector (i.e. the phonon dispersion relation), (ii) the polarization vector of the phonons, (iii) the frequency distribution of phonons, (iv) elastic constants (v) the thermodynamic properties of the solid such as the equation of state, specific heat, thermal expansion, *etc*. and (vi) the variation of phonon frequencies due to pressure (vii) effect of magnetic interaction on phonon frequencies etc. The calculations have also been very useful in the planning and execution of the experiments, and enabled microscopic interpretations of the observed experimental data. The outcome of the research included in this thesis can be summarized as:

(1) A comparative ab-initio DFT calculation of phonon spectra as well as thermal expansion behavior in M_2O and MCN (M=Ag, Au and Cu) is presented. We find that although low energy phonon modes of similar energies are present in all the M_2O compounds, the nature of bonding as well as open space in the unit cell are important in governing the thermal expansion behavior.

In MCN, we have identified the phonon modes responsible for the anomalous thermal expansion behavior. The nature of the chemical bonding is found to be similar in HT-CuCN and AgCN, which is significantly different from that in AuCN. The computed elastic constants and Born effective charges are in correlation with the difference in the nature of bonding in metal cyanides.

(2) The ab-initio DFT calculations of phonons modes of ZrW_2O_8 have been performed in the entire Brillouin zone. We have been able to explain the observed anomalous pressure as well as temperature variation of the energies of phonon modes. The increase of the frequency with temperature essentially results from the cubic and/or quadratic anharmonic part of the phonon potential, which is able to explain the temperature dependence of low energy modes as reported in the literature.

(3) We have performed measurements of neutron inelastic scattering spectra of the multiferroic material $GaFeO_3$ and $YMnO_3$ over a wide temperature range (50 -1300 K) covering all the relevant characteristic transition temperatures. $GaFeO_3$ does not undergo any

structural phase transition at high-temperature. However, the increase of the distortion amplitudes of the various polyhedral units might be at the origin of the gradual broadening of the stretching modes around 60 meV. The ab-initio phonon calculations highlighted unambiguously a spin-phonon coupling in $GaFeO_3$. The enthalpy calculations in various phases showed that the quenching of the Fe magnetic moment leads to the observed high pressure structural phase transition at 47 GPa.

In $YMnO_3$, the room temperature phase is found to be subject to a strong spin-phonon coupling. The calculated phonon dispersion relations in the entire Brillouin zone indicate phonon instability in the high-temperature ($P6_3/mmc$) hexagonal phases of $YMnO_3$, at the symmetry point K (1/3 1/3 0). Unstable phonon modes may lead to a stabilization of the low-temperature ($P6_3cm$) phase.

(4) We have reported detailed measurements of the temperature dependence of the phonon density-of-states of $SrFeO_2$ in the antiferromagnetic phase ($P4/mmm$). The phonon spectrum shows anharmonic broadening above 300 K, which is consistent with the reported distortion of the planer structure. Another isostructural compound $CaFeO_2$ shows strong coupling of the unstable B_u mode with two stable zone boundary modes at the M point leading to the distortion in the planer structure (P4/mmm) and stabilization of d-$CaFeO_2$ ($P\text{-}42_1m$). These observations are consistent with the available experimental structural data. The spin exchange interaction parameters are found to decrease with increase in the distortion of the planer structure as described by the amplitude of B_u phonon mode. Calculations at high pressures predict that the undistorted planer $CaFeO_2$ would stabilize.

(5) In piezoelectric $NaNbO_3$, We have measured inelastic neutron scattering measurements of the phonon density of states of sodium niobate as a function of temperature across the various phase transitions. Using the ab-intio DFT calculations, we have identified the various soft phonon modes at specific points in the Brillouin zone that are associated with various phase

transition as a function of temperature. The calculated enthalpy in various phase of sodium niobate indicate that that the orthorhombic structure with space group Pbcm could transform to the Pbnm structure at high pressure.

For antiferromagnetic RMnO3(R=Ca, Pr), the inelastic neutron scattering data (5 - 1250 K) obtained through collaborative experiments has been obtained and analysed. The measurements show that in spite of similar structure the presence of Jahn-Teller distortion $PrMnO_3$ might result in broad peaks in the phonon spectra in comparison to $CaMnO_3$ where it exhibits well-defined peaks. Theoretical calculation for $PrMnO_3$ suggests that suppression of the Jahn-Teller distortion and insulator to metal transition occurs simultaneously.

(6) A first principles calculation of $LiFePO_4$, $LiMnPO_4$ and Li_2O has been successfully used to understand phonon dynamics. The calculated phonon dispersion relation in Li_2O as a function of volume shows a zone boundary unstable phonon mode at volume corresponding to superionic regime. This softening of the phonon could be a precursor to dynamical instability. We are able to relate the phonon softening with the ease of lithium movement at elevated temperature along [001]. The calculated phonon density of states at volume corresponding to high temperature (> 1000 K) in $LiFePO_4$ and $LiMnPO_4$ suggests that there is a significant instability initiating in the Li sub-lattice. Analysis of the eigen vectors of these modes at 300 K suggest that if conducive conditions for Li movement from its lattice positions are available, the net displacement of Li atoms is in the x-y plane. But at higher temperature regime, the pattern of displacement suggests that lithium exhibits non-zero displacement along all the directions but with the highest component along x direction.

Besides the basic research activities the author also developed various post processing codes interfaced with VASP, Quantum Espresso and PHONON-5.2 software's. Author has also installed and tested various codes in ANUPAM supercomputing facility, BARC.

8.2 Future Direction

The experience gained during thesis work would be useful for studying the structure and dynamics of more complex technologically important solids. The calculated eigen vector of phonons is useful to study the phase transition behaviour of solids. The study of phonon anharmonicity and phonon-phonon interaction is a difficult but exciting field. It is difficult because we must consider how phonons interact with other phonons. In comparison, our understanding today about the vibrational thermodynamics of materials is based on the harmonic model in which phonons are independent, avoiding issues of anharmonic lattice dynamics. Phonon anharmonicity is an exciting topic because of its fundamental importance and broad applications. With the development of modern experimental techniques and the progress of the anharmonic phonon theories and computational methodologies, we are in a position to study the relation between the phonon anharmonicity and many important thermodynamic properties of materials. We can study the anharmonity of phonon and their effect on thermodynamic properties using ab-initio molecular dynamics. The ab-initio molecular dynamics technique is a powerful technique but it limited because it is computationally very expensive. Now days the supercomputers are very powerful and one can perform such massive calculation.

On the other hand of experimental activity, the author is also involved in design a new triple axis spectrometer at Dhruva. We are planning to measure phonon dispersion relation of various multiferroic materials using time of flight technique and triple axis spectrometer. Our aim is to investigate the spin-phonon coupling and their role in multiferroicity. In battery materials also we are planning to measure the dispersion relation at around superionic temperature. These measurements may provide the information about the nature of diffusion in ionic material.